

THESIS / THÈSE

DOCTOR OF SCIENCES

Processing of transparent YAG and BaTiO₃ ceramics by SPS

Moronta Perez, Rosa

Award date:
2018

Awarding institution:
University of Namur

[Link to publication](#)

General rights

Copyright and moral rights for the publications made accessible in the public portal are retained by the authors and/or other copyright owners and it is a condition of accessing publications that users recognise and abide by the legal requirements associated with these rights.

- Users may download and print one copy of any publication from the public portal for the purpose of private study or research.
- You may not further distribute the material or use it for any profit-making activity or commercial gain
- You may freely distribute the URL identifying the publication in the public portal ?

Take down policy

If you believe that this document breaches copyright please contact us providing details, and we will remove access to the work immediately and investigate your claim.



UNIVERSITY OF NAMUR
FACULTY OF SCIENCES
Namur, Belgium

Processing of transparent YAG and BaTiO₃ ceramics by SPS

Author: ROSA MORONTA PEREZ

Members of the jury:

Pr. LAURENT HOUSSIAU (President)

Pr. PAOLA PALMERO

Dr. CLAUDE ESTOURNES

Dr. PHILIPPE AUBRY

Pr. OLIVIER DEPARIS

Dr. FRANCIS CAMBIER

Dr. LAURENT BOILET (Co-supervisor)

Pr. LUC HENRARD (Supervisor)

Doctoral Thesis January 2018



UNIVERSITÉ
DE NAMUR
UNIVERSITY OF NAMUR
FACULTY OF SCIENCES
Namur, Belgium



BELGIAN CERAMIC RESEARCH
CENTRE
Mons, Belgium

Processing of transparent YAG and BaTiO₃ ceramics by SPS

Ph. D. supported by the Walloon Region (DG06) and the ESF
First DOCA program (Convention ECV320600FD017F/1217883)

Author: ROSA MORONTA PEREZ

Members of the jury:

Pr. LAURENT HOUSSIAU (President)
Pr. PAOLA PALMERO
Dr. CLAUDE ESTOURNES
Dr. PHILIPPE AUBRY
Pr. OLIVIER DEPARIS
Dr. FRANCIS CAMBIER
Dr. LAURENT BOILET (Co-supervisor)
Pr. LUC HENRARD (Supervisor)

Doctoral Thesis January 2018

Acknowledgments

Je tiens tout d'abord à remercier la Région Wallonne (DG06) qui a financé ce projet dans le cadre du programme First DoCA (First Doctorat Centre Agréé, n° convention ECV320600FD017F/1217883) et les directeurs du BCRC pour avoir eu confiance en moi pour mener à bout ce projet.

Mes remerciements vont ensuite à mon promoteur du BCRC, Laurent Boilet, pour être toujours là pour m'aider, pour ses conseils et son engagement. Il est aussi devenu un bon ami que j'espère toujours garder. Merci Laurent pour tout.

Un grand merci aussi à mon promoteur de l'Université de Namur, Luc Henrard, pour avoir suivi mon travail si éloigné de ses thématiques habituelles, pour sa disponibilité et sa gentillesse.

Je remercie également Philippe Aubry pour avoir suivi mon travail depuis le début, pour m'avoir aidé et encouragé et Jean-Pierre Erauw qui m'a aidé lors de mes doutes sur le SPS, pour les simulations et a pris le temps de relire certaines parties du manuscrit pendant son temps libre et m'a fait des remarques constructives et judicieuses.

Mes remerciements vont aussi aux autres membres du comité d'accompagnement: Francis Cambier et Olivier Deparis pour avoir accepté de suivre ce projet, pour leur lecture attentive du manuscrit et leurs commentaires et corrections.

Ma gratitude va également aux autres membres du jury qui ont accepté d'évaluer ce travail : Paola Palmero qui m'a accueillie chaleureusement au sein de son laboratoire à Turin, Claude Estournès qui m'a fait l'honneur d'assister à ma soutenance et, enfin, Laurent Houssiau qui a accepté d'assurer la présidence du jury.

Un tout grand merci aussi à Védi Dupont, pour son assistance technique lors des essais SPS et sa bonne humeur.

Ma gratitude va également à mes collègues, chercheurs, techniciens et personnels administratifs, lesquels m'ont aidée et accompagnée pendant ces quatre années et avec lesquels j'ai passé des bons moments.

Por último, no puedo olvidar a mi familia y a Antonio, por su apoyo incondicional y sus consejos, ni a mis amigos, tanto de España como los que he encontrado en Mons, que me han animado, escuchado y soportado este tiempo, especialmente a Patri por estar siempre pendiente a pesar de la distancia.

J'espère n'avoir oublié personne, mais si c'est le cas, ils connaissent ma petite tête. Merci à tous ceux qui ont participé, de près ou de loin, à l'avancée de ce projet.

Table of contents

Abstract.....	5
List of symbols and abbreviations	7
List of publications and presentations	9
Introduction	11
Chapter I - Literature review	15
1.1. Transparent ceramics	17
1.1.1. Fundamental aspects and transparency conditions	17
1.1.2. Production of transparent ceramics	20
1.1.2.1. Influence of powder properties and powder conditioning	21
1.1.2.2. Sintering of transparent ceramics	22
1.2. Yttrium aluminium garnet	35
1.2.1. Structure, properties and applications	35
1.2.2. Synthesis	37
1.2.3. Transparent YAG ceramics	39
1.3. Barium Titanate.....	41
1.3.1. Structure	41
1.3.2. Properties and applications	43
1.3.3. Effect of strontium substitution	47
1.3.4. Transparent BT and BST ceramics.....	50
1.4. Conclusions	52
Chapter II – Experimental procedures and finite element modelling	55
2.1. Powder conditioning	57
2.1.1. Dispersion	57
2.1.2. Solvent removal.....	57
2.2. Sintering and post-treatments	57
2.2.1. Spark Plasma Sintering.....	57
2.2.2. Hot Isostatic Pressing	58
2.3. Physico-chemical characterizations	59
2.3.1. Granulometric measurements.....	59
2.3.2. X-Ray Diffraction	59

2.3.3.	Specific surface area.....	60
2.3.4.	Trace-level elemental analysis.....	60
2.3.5.	Raman spectroscopy	60
2.3.6.	TGA/DTA.....	60
2.3.7.	Archimedes's method	60
2.3.8.	Permittivity measurements	61
2.4.	Microstructural characterisation.....	62
2.5.	Optical characterisation.....	62
2.6.	Finite Element Modelling to simulate temperature distribution in SPS	64
Chapter III – Yttrium Aluminium Garnet		67
3.1.	YAG-S	69
3.1.1.	Powder synthesis and characteristics	69
3.1.1.1.	Precipitant concentration influence	70
3.1.1.2.	Characterisation of the synthesized powder	73
3.1.2.	Sintering and transparency improvement	74
3.1.2.1.	Sintering behaviour	74
3.1.2.2.	Influence of SPS parameters on density, microstructure and visual aspect of the samples	75
3.1.2.3.	Influence of pre- and post-treatments on the optical transmission.....	80
3.1.3.	Conclusions on YAG-S powder	84
3.2.	YAG-B.....	85
3.2.1.	Powder characteristics	85
3.2.2.	Sintering and transparency improvement	87
3.2.2.1.	Sintering behaviour	87
3.2.2.2.	Influence of SPS parameters on density, microstructure and visual aspect of the samples	87
3.2.2.3.	Influence of pre- and post-treatments on the optical transmission.....	91
3.2.3.	Conclusions on YAG-B powder	98
3.3.	YAG-N	98
3.3.1.	Powder characteristics	99
3.3.2.	Sintering and transparency improvement	100
3.3.2.1.	Sintering behaviour	100

3.3.2.2.	Influence of SPS parameters on density, microstructure and visual aspect of the samples	101
3.3.2.3.	Influence of pre- and post-treatments on the optical transmission.....	105
3.3.3.	Conclusions on YAG-N powder	109
3.4.	Conclusions chapter III.....	109
Chapter IV – Barium Titanate		113
4.1.	Powders characterisations	115
4.1.1.	Barium titanate	115
4.1.2.	Barium strontium titanate	117
4.2.	Processing dense ceramics with controlled microstructure.....	119
4.2.1.	Barium titanate	120
4.2.1.1.	Sintering behaviour	120
4.2.1.2.	Influence of SPS parameters on density, microstructure and visual aspect of the samples	121
4.2.1.3.	Powder deagglomeration	130
4.2.1.4.	Conclusions	133
4.2.2.	Barium strontium titanate	134
4.2.2.1.	Sintering behaviour	134
4.2.2.2.	Influence of SPS parameters on density, microstructure and visual aspect of the samples	135
4.2.2.3.	Effect of powder deagglomeration	141
4.2.2.4.	Conclusions	142
4.3.	Functional properties	142
4.3.1.	Optical properties.....	142
4.3.2.	Dielectric properties.....	147
4.4.	Conclusions chapter IV.....	158
General conclusions		161
References.....		165
List of figures		177
List of tables		183
Appendix A - Technical information from the suppliers		185

Abstract

The purpose of this work was to elaborate Yttrium Aluminium Garnet (YAG) and Barium Titanate (BT) ceramics with a high level of transparency and to investigate to what extent functional properties (optical and dielectric) were linked to the powder characteristics and the sintering parameters.

Three different YAG powders (two commercial and a home-synthesized one) were densified by Spark Plasma Sintering (SPS). The role of the physico-chemical characteristics of the powders (purity, agglomeration state and stoichiometry) on the sintering and the optical transmission was investigated. Depending on the powder type, different pre-treatments and/or post-treatments were necessary to increase both homogeneity and optical transmission of densified parts. In the case of agglomerated powders, dispersion by ultrasonication was efficient and led to better homogeneity and higher optical transmission. Post-treatments such as annealing and post-hipping in air were helpful to reduce oxygen vacancies and residual porosities and improved the optical transmission of the ceramics. The detrimental effect of impurities (sulphur), even in a quantity as low as 50 ppm, on optical transmission, was evidenced. The YAG powder with the lowest agglomeration degree and the highest purity resulted in the highest values of optical transmission. 70% real in-line transmission at the wavelength of 600 nm was obtained under SPS conditions of 50 MPa at 1500°C and after addition of 0.2% Lithium Fluoride.

Concerning barium titanate and barium strontium titanate powders, black and opaque samples were obtained after Spark Plasma Sintering. However, optimisation of SPS parameters (with prior dispersion by ball mixing in the case of BT powder) led to fully dense samples with grain size under 1 μm . These two conditions were necessary to achieve translucent ceramics after a suitable air annealing treatment. These samples presented the highest values of transmission obtained so far: total forward transmission values reached 35% and 41% at 600 nm, for barium titanate and barium strontium titanate, respectively. Ceramics with full density and homogeneous grain size around 1 μm provided the highest permittivity values with low dielectric losses, after air annealing.

Keywords: YAG, BaTiO₃, SPS, transparent ceramics, optical properties, permittivity

Résumé

Cette thèse vise à élaborer des céramiques transparentes de grenat d'yttrium et d'aluminium (YAG) et de titanate de baryum (BT) et à investiguer la relation entre les propriétés fonctionnelles (optiques et diélectriques) des céramiques frittées et les caractéristiques des poudres et paramètres de frittage.

Trois poudres de YAG différentes (deux commerciales et une synthétisée) ont été densifiées par Spark Plasma Sintering (SPS). Le rôle des caractéristiques physico-chimiques des poudres (pureté, agglomération et stœchiométrie) sur le frittage et la transmission optique des échantillons a été investigué. De plus, différents pré-traitements et/ou post-traitements ont été optimisés en fonction du type de poudre afin d'améliorer l'homogénéité et la transmission optique des céramiques obtenues. Dans le cas de poudres agglomérées, une dispersion par ultrasons a été efficace pour augmenter l'homogénéité et la transmission optique. Des post-traitements de recuit sous air et de post-hipping ont permis de réduire la quantité de lacunes d'oxygène et de porosités résiduelles, et ainsi d'améliorer la transmission optique des céramiques. L'effet néfaste des impuretés (soufre), même en quantités très faibles (50ppm) sur la transmission optique a été mis en évidence. Les meilleurs résultats de transmission optique ont été obtenus avec la poudre de YAG la moins agglomérée et de plus haute pureté: une transmission en ligne de 70%, mesurée à une longueur d'onde de 600 nm, a été obtenue après frittage SPS à 1500°C, sous 50 MPa, et avec l'addition de 0.2% LiF.

Après frittage SPS des poudres de titanate de baryum et de titanate de baryum et de strontium (BST), des échantillons noirs et opaques ont été obtenus. Néanmoins, l'optimisation des paramètres SPS (avec une dispersion préalable dans le cas de la poudre de BT) a conduit à des échantillons complètement denses, avec une microstructure composée de grains de taille inférieure au micron. Ces deux conditions ont conduit à l'obtention de céramiques translucides après un recuit sous air optimisé. Les échantillons présentent les meilleurs résultats de transmission optique obtenus jusqu'à présent, dans la littérature, avec des valeurs de transmission totale de 35% et 41% (à 600 nm), pour des céramiques de BT et de BST, respectivement. Les céramiques complètement denses, de microstructure homogène contenant des grains de taille proche de 1 μm , présentent les valeurs de permittivité les plus élevées et après recuit des pertes diélectriques faibles.

Mots clé: YAG, BaTiO₃, SPS, céramiques transparentes, propriétés optiques, permittivité

List of symbols and abbreviations

SPS:	Spark Plasma Sintering
YAG:	Yttrium Aluminium Garnet, $Y_3Al_5O_{12}$
BT:	Barium Titanate, $BaTiO_3$
ST:	Strontium Titanate, $SrTiO_3$
BST:	Barium Strontium Titanate
YAP:	Yttrium Aluminium Perovskite, $YAlO_3$
YAM:	Yttrium Aluminium Monoclinic, $Y_4Al_2O_9$
PZT:	Lead zirconate titanate, $Pb(Zr,Ti)O_3$
AHC:	Ammonium bicarbonate, NH_4HCO_3
HP:	Hot Pressing
HIP:	Hot Isostatic Pressing
SEM:	Scanning Electron Microscopy
TEM:	Transmission Electron Microscopy
FEM:	Finite Element Modelling
TFT:	Total Forward Transmission
RIT:	Real in-line Transmission
XRD:	X-Ray Diffraction
BET:	Brunauer-Emmett- Teller method
ICP:	Inductively Coupled Plasma
XRF:	X-Ray Fluorescence
XPS:	X-Ray Photoelectron Spectroscopy
EDS:	Electron Dispersive Spectroscopy
US:	Ultrasonication
ϵ :	Permittivity
td:	Tangent delta (Dielectric loss)
Tc:	Curie temperature

C: Cubic phase (in XRD)

T: Tetragonal phase (in XRD) or transmission in optical measurements

TGA: Thermogravimetric Analysis

DTA: Differential Thermal Analysis

ρ : Density

λ : Wavelength

t: Thickness

n: Refractive index

GB: Grain Boundary

EPR: Electron Paramagnetic Resonance

d10, d50, d90: these values refer to the values where the cumulative volume curve crosses 10%, 50% and 90% on the Y axis (the diameter of the particles). For instance, d10 means that particle size of 10% of the volume of particles show a diameter under d10.

List of publications and presentations

Publications:

Moronta Perez, R.; Boilet, L.; Aubry, P.; Palmero, P.; Henrard, L.; Deparis, O.; Lardot, V.; Cambier, F. "Improving Optical Transmission of Spark-Plasma-Sintered YAG Ceramics: Effect of Powder Conditioning and Post-Treatments", accepted on Oct. 13, 2017 in *Journal of Ceramic Science and Technology*.

Presentations:

Moronta Perez, R.; Boilet, L.; Aubry, P.; Lardot, V.; Henrard, L.; Deparis, O.; Cambier, F. "Elaboration de YAG transparent par frittage SPS". *Journée Technique Céramiques Transparentes*, 20 January 2015, Paris (France). (Poster).

Moronta Perez, R.; Boilet, L.; Aubry, P.; Lardot, V.; Palmero, P.; Henrard, L.; Deparis, O.; Cambier, F. "Processing transparent YAG ceramics by SPS". *European Ceramic Society Conference*, 25 June 2015, Toledo (Spain). (Oral).

Moronta Perez, R.; Boilet, L.; Aubry, P.; Lardot, V.; Palmero, P.; Henrard, L.; Deparis, O.; Cambier, F. "Spark Plasma Sintering of YAG ceramics: Research of transparency". *Annual Meeting of the Belgian Ceramic Society Conference*, 26 October 2015, Mons (Belgium). (Oral).

Moronta Perez, R.; Boilet, L.; Aubry, P.; Lardot, V.; Palmero, P.; Henrard, L.; Deparis, O.; Cambier, F. "Attempts to improve the optical transmission on spark plasma sintered YAG ceramics". *International Conference and Exposition on advanced ceramics and composites*, 26 January 2016, Daytona Beach (USA). (Poster).

Moronta Perez, R.; Boilet, L.; Aubry, P.; Lardot, V.; Palmero, P.; Henrard, L.; Deparis, O.; Cambier, F. "Unraveling the aspects affecting transparent YAG ceramics". *Annual Meeting of the Belgian Ceramic Society Conference*, 16 December 2016, Mol (Belgium). (Oral).

Moronta Perez, R.; Boilet, L.; Aubry, P.; Lardot, V.; Henrard, L.; Deparis, O.; Cambier, F. "High permittivity BaTiO₃ ceramics prepared by SPS". *European Ceramic Society Conference*, 11 July 2017, Budapest (Hungary). (Oral).

Introduction

Transparent polycrystalline ceramics combine good optical properties and, compared to single crystals, higher mechanical properties and lower manufacturing costs. These ceramics are already used in a wide range of applications such as: optical fibres, armouring, lightning, laser systems and jewellery.

However, obtaining a transparent polycrystalline ceramic requires a careful control of its microstructure. In fact, any defect inside the material can induce scattering or absorption, and thus a decrease in the optical transmission. Hence, impurities, pores and secondary phases with refractive indexes different from the ceramic material will be preferably avoided. Therefore, the use of an ultra-pure powder is required. Moreover, particles with homogeneous size and shape and powder free of agglomerates are recommended in order to obtain a fully dense specimen, free of defects.

Together with excellent powder characteristics, advanced sintering techniques are required to reach the extreme densities needed to obtain transparent ceramics. Between the different sintering techniques, Spark Plasma Sintering (SPS) was retained in this thesis work. SPS combines uniaxial pressure and heating by Joule effect, and offers the possibility of sintering powders up to full density at lower temperatures (and with shorter dwell times) compared to conventional sintering. This enables avoiding grain growth and lowering the energy consumption. However, SPS often implies the use of graphite tooling and sintering under vacuum atmosphere. This process can lead to a darkening of the samples, limiting their optical properties. In the literature, this behaviour is attributed to graphite contamination and/or formation of oxygen vacancies. Different solutions have been explored during this research to avoid or limit this darkening.

The main goal of this thesis was to investigate to what extent functional properties (optical and dielectric) of a polycrystalline ceramic are linked to powder characteristics and sintering parameters. Additionally, determining the way powder pre-treatments and post-treatments of the sintered compacts influence their final properties was aimed.

To reach these goals, a partnership was necessary. This thesis is indeed the result of the collaboration between the Belgian Ceramic Research Centre (Mons, Belgium), the University of Namur (Belgium) and the Politecnico di Torino (Italy).

A major field of research at the Belgian Ceramic Research Centre is the investigation of densification of ceramics. Better understanding of reaction mechanisms as well as studying new processes or formulating slurries or green bodies with different additives or treatments to achieve the required density are different examples among the main research activities of the Centre. Thanks to this expertise, this thesis was the opportunity to develop high densified materials and open new opportunities in the field of transparent ceramics. Higher densifications are difficult but in order to obtain transparent ceramics, you have to go one step further and achieve total full densification which is another challenge. The Politecnico di Torino had already synthesized powders for transparent ceramics and was consequently an ideal partner in the frame of this thesis. Its previous experience in the field of transparent ceramics was a great starting point for this work. Eventually,

the University of Namur allowed numerous characterizations and more particularly optical measurements, which are the ultimate test for transparent ceramics.

Throughout the thesis, the following aspects will be addressed:

- a better understanding of the influence of the physicochemical characteristics of the starting powder on the sintering behaviour and functional properties of the ceramics;
- the study of the relative influence of each SPS parameter (temperature, pressure, heating rate ...) on microstructure (homogeneity and grain size) and optical transparency;
- the analysis of the effect of pre-treatments (dispersion, additives) and post-treatments (annealing) on the sought functional properties.

Two different materials have been investigated during this work: Yttrium Aluminium Garnet and Barium Titanate. The first ceramic material, known as YAG ($\text{Y}_3\text{Al}_5\text{O}_{12}$), is one of the most widely studied transparent ceramics. A lot of research in YAG has been made and, for instance, its application, when doped with rare earth ions, is well-known in lasers. However, many applications yet use single crystals due to the difficulties of processing free-defect transparent polycrystalline ceramics. In the literature, very different transmission values can be found regarding YAG ceramics, but the origin of these differences remains unclear. This thesis aims to shed light on the origin of these differences, if they arise from the characteristics of the powders or from the sintering process. Thus, the influence of the starting powder and sintering conditions on the final optical properties of the sintered samples has been analysed throughout this work. The second ceramic material, barium titanate (BaTiO_3) has been rarely studied as a transparent ceramic in the literature, but the same procedures discussed in the case of YAG have been applied to increase its transparency. Furthermore, barium titanate, owing to its recognized dielectric, ferroelectric and piezoelectric properties, appears suitable for electro-optic devices and for substituting more toxic, lead-based electronic components as $\text{Pb}(\text{Zr},\text{Ti})\text{O}_3$ (PZT). For this reason, a study of the influence of grain size on the dielectric properties has been also carried out. Transparent barium titanate polycrystalline ceramics offer very promising perspectives in the research of environmentally friendly electric components. The objectives were thus to obtain polycrystalline samples with a higher degree of transparency than previous works and to evaluate its permittivity.

This thesis is structured in four chapters:

Chapter I reviews the existing literature about the fundamental aspects of transparency and the different features that have to be considered in the processing of a transparent ceramic. It also describes SPS and its application to elaborate transparent ceramics. Finally, the main properties and applications of YAG and BaTiO_3 are discussed.

Chapter II describes the experimental procedures used in the fabrication and characterisation of YAG and Barium Titanate ceramics. This chapter also introduces the procedure followed in the finite element simulation of the thermal distribution inside the SPS tooling.

Chapter III presents the results concerning the first material: YAG. Three different powders are studied. For each powder, the sintering behaviour is analysed and related to the powder characteristics. The effect of the SPS parameters, pre- and post-treatments on the optical properties of the sintered ceramics is also described.

Finally, Chapter IV focuses on the processing of barium titanate and its doping with strontium. The first part of this chapter concerns the processing of dense ceramics with a controlled microstructure by SPS. The second part describes the characterizations of the optical and dielectric properties.

Chapter I - Literature review

Table of contents

1.1. Transparent ceramics	17
1.1.1. Fundamental aspects and transparency conditions	17
1.1.2. Production of transparent ceramics	20
1.1.2.1. Influence of powder properties and powder conditioning	21
1.1.2.2. Sintering of transparent ceramics	22
1.2. Yttrium aluminium garnet	35
1.2.1. Structure, properties and applications	35
1.2.2. Synthesis	37
1.2.3. Transparent YAG ceramics	39
1.3. Barium Titanate.....	41
1.3.1. Structure	41
1.3.2. Properties and applications	43
1.3.3. Effect of strontium substitution	47
1.3.4. Transparent BT and BST ceramics.....	50
1.4. Conclusions	52

1.1. Transparent ceramics

Transparent polycrystalline ceramics combine good optical properties and, compared to single crystals, higher mechanical properties and lower manufacturing costs. They appear in the 1960s [1] and a continuous development to improve their properties has been done since that time. Nowadays, they are used as laser hosts, infrared windows/domes, lamps envelopes and transparent armours. However, processing conditions leading to transparency are very narrow and a combination of different parameters must be taken into account in order to maximize optical transparency. Generally speaking, the concentration of defects in the ceramics (impurities, secondary phases, residual porosity ...) must be as low as possible. A brief insight into the main phenomena that affect light transmission and the production of transparent ceramics is given in the following section.

1.1.1. Fundamental aspects and transparency conditions

Simply stated, a solid material will appear “transparent” to the eye if an object situated far behind it is distinctly seen. If this object is not clearly seen and only scattered light is observed, the material will be called “translucent”.

Visible light (wavelength $\approx 400\text{-}800$ nm) is just a small part of the electromagnetic spectrum. Every electromagnetic wave that passes through an object undergoes different phenomena: reflection, absorption, scattering and transmission in different proportions. Equation 1.1 shows these phenomena, where T , A , R and S are, respectively, the intensity of the transmitted, absorbed, reflected and scattered light, normalized to the incident intensity (I_0).

$$1 = T + A + R + S \quad \text{Equation 1. 1}$$

In order to improve the transmission of a sample, the other phenomena must be minimised.

- **Reflection**

Each material is characterized by a refractive index, n , that describes the ratio between the speed of light in vacuum (c) and the speed of light in the material (V):

$$n = \frac{c}{V} \quad \text{Equation 1. 2}$$

Considering an interface, as a light wave passes from one material to another one with a different refractive index, a reflection happens at the interface and part of the incident light is returned to the first material. The reflectance, R , represents the fraction of the incident light intensity that is reflected. When we consider a light wave propagating in the air ($n=1$) and arriving perpendicular to a planar surface, the reflectance is given by the following expression:

$$R = \left(\frac{n-1}{n+1}\right)^2 \quad \text{Equation 1. 3}$$

Considering the reflection losses at the two surfaces of a planar film at normal incidence [2], [3], we obtain the total reflectance R_s

$$R_s = \frac{2R}{1+R} \quad \text{Equation 1. 4}$$

This coefficient is unique for each material and allows calculating the maximum transmission (T_{max}) in a material without any contribution of absorption or scattering (equation 1.5).

$$T_{max} = 1 - R_S = \frac{2n}{(n^2+1)} \quad \text{Equation 1.5}$$

The refractive index of a material depends on the wavelength, so does the maximum transmission value. Therefore, materials with a refractive index almost constant in the desired wavelength region are preferred for optical applications.

Regarding the materials studied in this thesis, YAG is a well-known optical material and it shows an almost wavelength independent refractive index in the visible-near infrared range. Barium titanate (and strontium titanate) presents lower optical transmission, and its refractive index varies according to the wavelength region.

Figure 1.1 depicts the refractive index variation of these materials as a function of the wavelength [4].

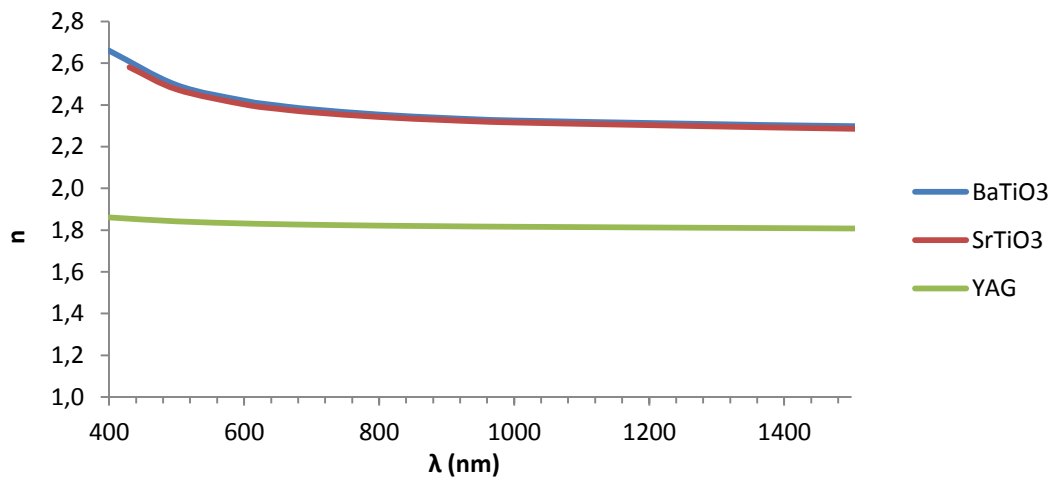


Figure 1.1. Wavelength dependence of the refractive index of pure YAG, BaTiO₃ and SrTiO₃ in the visible and near infrared region.

- **Absorption**

When the electromagnetic wave propagates through a real material, it can transfer energy. The material can absorb part of this energy ([3], [5], [6]). Absorption arises from several sources and even ppm volume fractions of defects can lead to opacity. Impurities act as absorption centres, hence high purity powders must be employed. Charged defects, such as antisites (when atoms of different type exchange positions) and vacancies, can trap electrons or holes generating absorption at short wavelengths ($\lambda < 400$ nm) [7]. Including the absorption phenomena into an absorption coefficient (α), the transmission (T) can be written as follows:

$$T = (1 - R_S)e^{-\alpha t} \quad \text{Equation 1.6}$$

where R_S is the total reflection coefficient; α , the absorption coefficient and t , the material thickness.

- **Scattering**

Scattering of light is the deviation of light rays from its straight path. In the case of ceramic materials, the sources of scattering are numerous, but the most important ones are the surface roughness, the presence of pores and secondary phases, with a refractive index different from the material, and the grain boundaries (Figure 1.2).

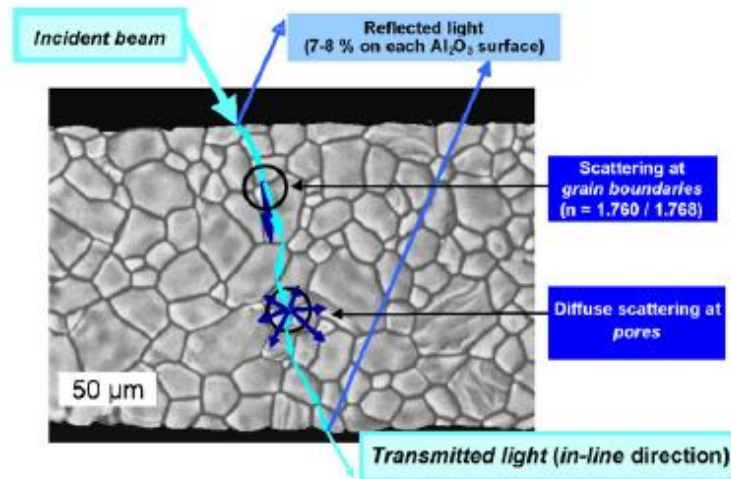


Figure 1.2. Light transmission through a polycrystalline ceramic [8].

Surface roughness can be suppressed by mirror-polishing the surfaces. However, real ceramics inevitably have a certain value of roughness.

Impurities or secondary phases scatter light and, consequently, decrease the in-line optical transmission. Moreover, pores, with a refractive index different from the one of the ceramic material, also scatter light, so that transparency can only be achieved for ceramics with full density. Grain boundaries have an influence in the case of birefringent materials, with anisotropic refractive index, but in the case of ceramics with a cubic structure this component can be neglected.

Grouping all the scattering sources into a global scattering coefficient, β , the expression of the transmission (T) becomes [9] :

$$T = (1 - R_s)e^{-(\alpha+\beta)t} \quad \text{Equation 1. 7}$$

Considering ceramics prepared from high purity powders, carefully polished, and with an isotropic structure, porosity represents the major contribution to scattering and an approximation to its contribution is presented next.

Porosity is a main source of scattering in transparent ceramics, the most detrimental being pores with the same size as the transmitted wavelength. The refractive index of the pores ($n \approx 1$ if they are filled with air) is usually very different from that of the matrix. Considering spherical pores with an homogeneous radius, the contribution of porosity to the scattering coefficient (γ_p) can be calculated as a function of the volume fraction of porosity, p , mean pore radius, r_p , and the scattering cross section of one spherical pore, $C_{sca,p}$ ([2], [10], [11]) :

$$\gamma_P = \frac{p}{\frac{4}{3}\pi r^3} C_{sca,p} \quad \text{Equation 1. 8}$$

$C_{sca,p}$ can be calculated using Mie scattering theory [12]. It mainly depends on the pore radius and a minimum of transmission is observed when pore size is close to the wavelength of the incident light.

Figure 1.3 illustrates the calculated transmission through a YAG polycrystalline ceramic as a function of the pore size. It is also worth to note the influence of the volume fraction of porosity. For example, a ceramic can have a transmission reduction of 30% with an increase of the porosity volume fraction from 0.01% to 0.05%.

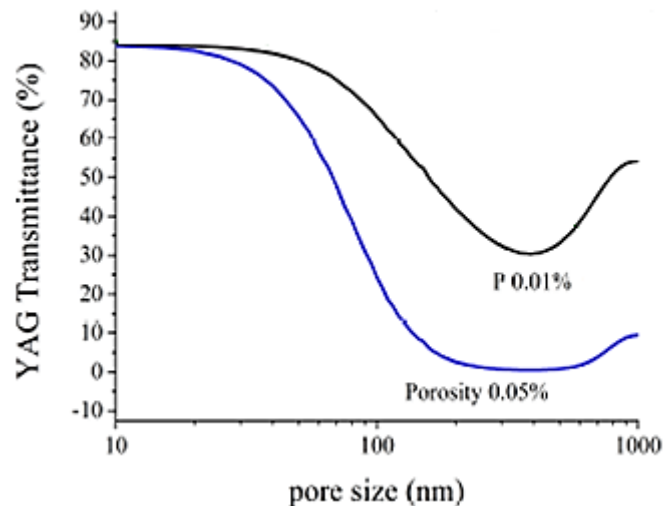


Figure 1.3. Calculated transmission through a polycrystalline ceramic ($\lambda=600$ nm) [11].

Diminishing volume fraction of porosity and pore size reduces greatly the scattering and thus pore concentration and size reductions are among the main goals of transparent ceramics processing.

1.1.2. Production of transparent ceramics

Production of transparent ceramics with nearly the same optical characteristics as those of single crystals has been an issue since their appearance in the 1960s. In order to reach the extreme densities necessary to obtain transparent ceramics, advanced sintering techniques are required, together with excellent powder characteristics and careful green body forming. Figure 1.4 shows the difficulties and interactions between variables in the production of transparent ceramics. In the following section, different aspects of the manufacturing of transparent ceramics are described.

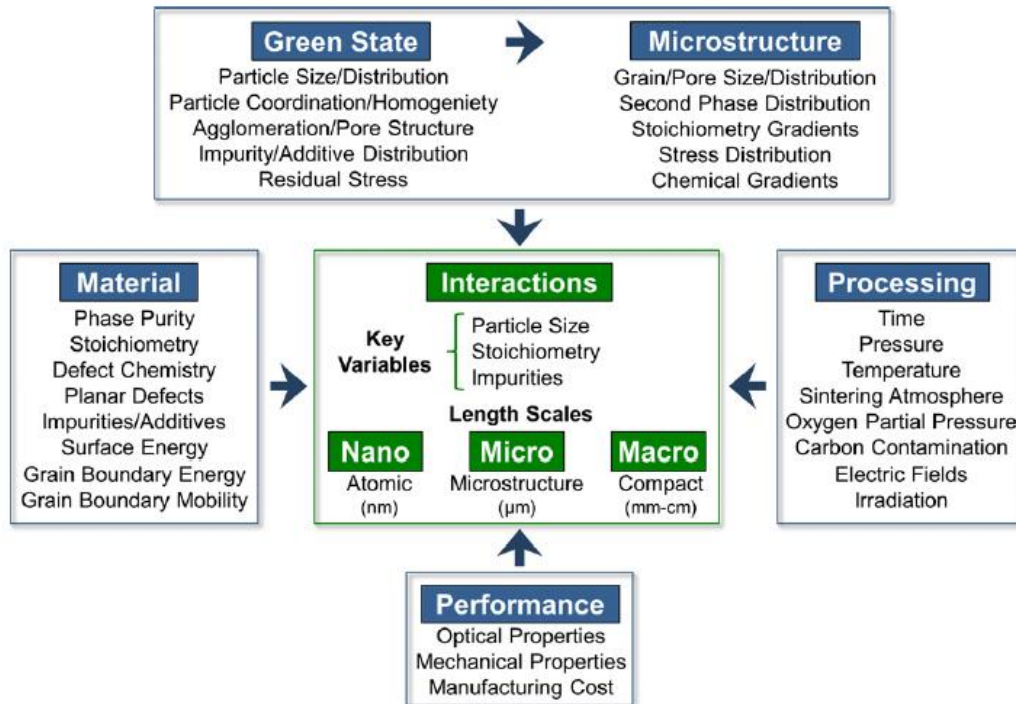


Figure 1.4. Fabrication variables in transparent ceramics [7].

1.1.2.1. Influence of powder properties and powder conditioning

Starting powders are a main issue in transparent ceramics. Desired characteristics are phase purity, controlled stoichiometry, homogeneous size and shape particles and powder free of agglomerates in order to lead to a homogeneous microstructure without defects that disturb optical transmission.

- **Purity and stoichiometry**

Impurities and secondary phases, even at ppm level, scatter and absorb light and, consequently, decrease the optical transmission. Hence, ultra-high purity powders (>99.9%) and stoichiometric ones are desirable in order to obtain transparent ceramics. Impurities can result from the synthesis process, incomplete removal of precursors, binders, or processing fluids [13]. The removal of the latter requires different temperatures but a previous thermal treatment can lead to grain growth and agglomeration of the powders.

Most impurities segregate at particle surfaces and reside at grain boundaries. Their effect on grain boundaries depends on the composition. Some can restrict grain growth by solute drag, other can enhance surface diffusion or densification. However if these impurities have a similar refractive index than the matrix, they can also be helpful to achieve dense samples and quite transparent ceramics.

- **Particle size and shape, size distribution and agglomeration**

The green-body state determines the sintering activity and it is profoundly influenced by particle size [14]. Defect-free, homogeneous, highly coordinated green bodies with narrow pore-size distributions can be obtained with high-purity nanopowders. Then sintering forces alone allow these green bodies to achieve high densification (>95%) at temperatures up to 200°C lower than less optimal bodies.

With additional pressure, full density has been reached without additives while exhibiting high transparency and nanometer-sized grains [7].

Smaller particles result in smaller green-body interparticle porosity. However, small size and high surface area increase susceptibility to agglomeration from weak attractive forces. High surface area powders also provide more residence sites for adsorbed gases, water and impurities, and may be more susceptible to chemical reactions. Nanometer-sized powders are also more expensive, are cumbersome to handle and are difficult to disperse. From Krell et al, a balance between small particle size, avoiding agglomeration and attaining high green-body particle coordination and homogeneity leads to an optimal particle size [14].

- **Agglomeration - dispersion**

Smaller particles are especially prone to agglomeration and make it difficult to obtain an optimal green body. Dense agglomerates sinter differentially. These differential sintering enlarges inter-agglomerates porosity inducing stresses that can cause cracking. Moreover, these dense agglomerates form solid skeletons (even during calcining) that limit particle rearrangement during consolidation and sintering [7]. Agglomerates are best dealt with before green-body formation, and are typically broken down by mechanical milling, ultrasonic or acoustic methods, or removed by sieving. Several works have focused on dispersion: Spina et al. [11] compared mechanical milling and ultrasonication of YAG, and privileged ultrasonication over mechanical milling because the use of alumina and zirconia balls added impurities to the powder and decreased final optical transmission. Suarez [15], [16] pointed out the influence of freeze-drying after dispersion as an effective method to avoid powder agglomeration.

Gong et al. [17] also used freeze-drying as drying method: they observed that powders with irregular particle shape and wide particle size distribution lead to dislocations and scattering centres in the sintered ceramics.

The best case, although difficult to achieve in practice, is forming soft agglomerates that can be broken by sintering stresses alone.

1.1.2.2. Sintering of transparent ceramics

Several sintering techniques can be used for the production of transparent ceramics. The most well-established is vacuum sintering [18], [19], [20]. However, the complete removal of porosity needs high temperatures and long dwell times. In order to reduce time and temperature conditions, other techniques have appeared: these techniques add external driving forces (pressure and/or electrical field) to the temperature and dwell effect in order to attain full density while limiting grain growth. Sintering techniques in this group are Hot Pressing (HP) [21], Hot Isostatic Pressing (HIP) [22], [23], microwave sintering [21], [24], [25] and Spark Plasma Sintering (SPS) [26], [27], [28], [29].

Spark plasma sintering (SPS) combines uniaxial pressure and heating by Joule effect, and offers the possibility of sintering powders up to full density at lower temperatures compared to conventional sintering. This enables avoiding grain growth and lowering the energy consumption. SPS is the main sintering technique used in this PhD thesis, so it will be detailed in the following section.

- **Spark Plasma Sintering**

The name “Spark plasma sintering” comes from the hypothesis of pulsed current inducing plasma between particles, but this hypothesis is still not well recognized among the SPS experts. This is why other names e.g. «Pulsed Electric Current Sintering» (PECS), or «Field Assisted Sintering Technique» (FAST) are also used to refer the same sintering technique. However, SPS remains the most popular denomination.

The concept of compacting metallic materials to a relative high density (relative density > 90%) by an electric discharge process was originally proposed by Inoue in the 1960s [30]. Sumitomo was the first company (1991) to fabricate SPS equipments and then other companies appeared as well in Europe and USA [31].

The basic configuration of a SPS unit is shown in Figure 1.5. It consists of a uniaxial pressure device, in which a water-cooled punches serve as electrodes, a water-cooled reaction chamber, a pulse DC generator and a position- and temperature-regulating system.

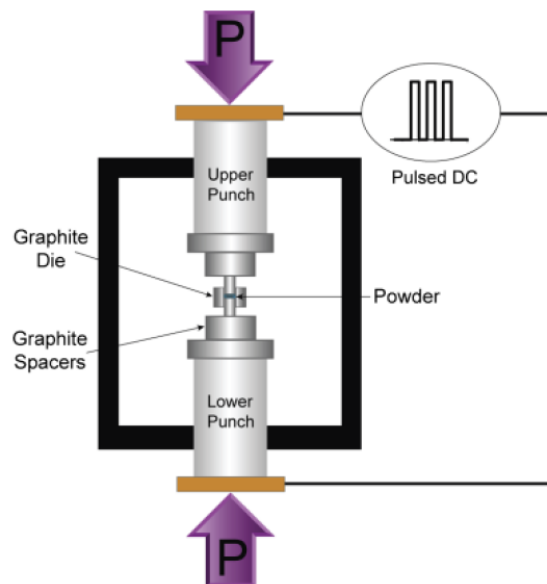


Figure 1.5. Basic configuration of a typical SPS set-up [32].

SPS resembles the Hot Pressing (HP) process in several aspects, i.e. the precursor powder (green body) is loaded in a die (generally in graphite), and a uniaxial pressure is applied during the sintering process. However, a major advantage of SPS technology is the way the compact is heated. Instead of external heating source, heating is accomplished directly by the electrical current by Joule effect. Depending on the sample’s electrical properties, the current generates Joule heat inside the die and possibly the powder compact. In the case of a conductive sample, current goes through the sample and enhances mass transport through electromigration, point defect generation and enhanced defect mobility [32]. However, for non-electrically conductive samples, as alumina, the current inside the samples could be neglected (Figure 1.6). The current passes through the die and punches and heats the sample, so no mass transport should be directly linked to the current. The electrical resistivity of alumina ($10^{14} \Omega \cdot \text{cm}$) is much bigger than the one of graphite ($1.6 \cdot 10^{-3} \Omega \cdot \text{cm}$), so the current passes from one punch to another via the die. Hence, the role of the electrical current would

differ substantially depending on the electrical resistivity of the material. This way of heating allows the application of very high heating rates (up to 400°C/min), hereby minimising the low temperature diffusion mechanisms that result in coarsening of the powder compact. Furthermore, as compared to HP, high cooling rates can also be obtained, preserving the high temperature microstructure and reducing the overall time of sintering process.

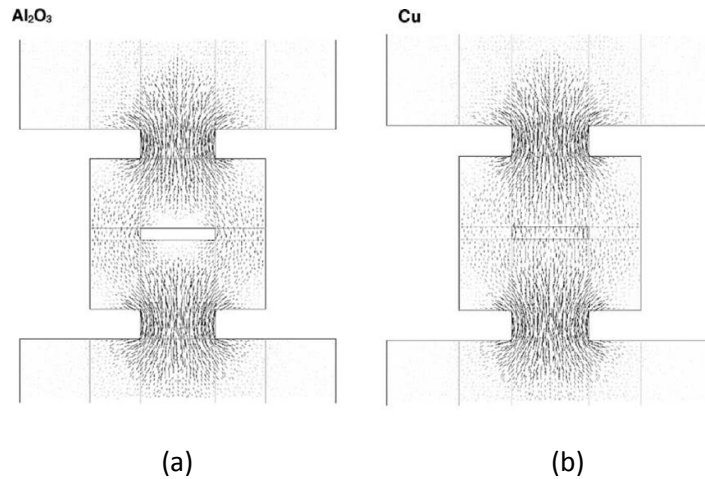


Figure 1.6. Electrical current distribution during SPS of two samples: (a) alumina (insulating); (b) copper (conductive) [33].

This high heating rate and the applied pressure (which allows decreasing the processing temperature usually by 100°C or even 500°C) permit to achieve fully dense samples with fine-grained microstructures.

These advantages were attractive in the development of transparent ceramics, when decrease of porosity (and pore size) leads to a decrease of scattering. The research on transparent ceramics by SPS started with the works of Chaim et al. [34] and Kim et al. [35].

In the last years, various transparent ceramics have been obtained by SPS: MgAl₂O₄ [14], [36], [37], YAG [34], [20], Al₂O₃ [38], [39], MgO [19] and BaTiO₃ [40] for example.

The following section will briefly describe the influence of SPS parameters observed in the literature, in the field of transparent ceramics.

- **Influence of SPS parameters**

Temperature, dwell time and heating rate

Temperature and dwell time are common for all the sintering techniques and in general, temperature should be high enough and dwell long enough to achieve full density. However, high temperatures and long dwell times lead to grain growth and, frequently, to pore coalescence that are inappropriate to achieve good optical transmission [41].

The influence of the sintering temperature in SPS on the transparency of ceramics has been studied extensively [9], [34], [36]. All works agree that the increase of the temperature leads to a microstructure coarsening and a diminution of the porosity.

Chaim et al. [34] studied the effect of temperature on YAG samples. They performed SPS cycles between 1250 and 1500°C, and observed an increase of the relative density from 83 to 99.6%. Grain size increased as the temperature increased as well (Figure 1.7).

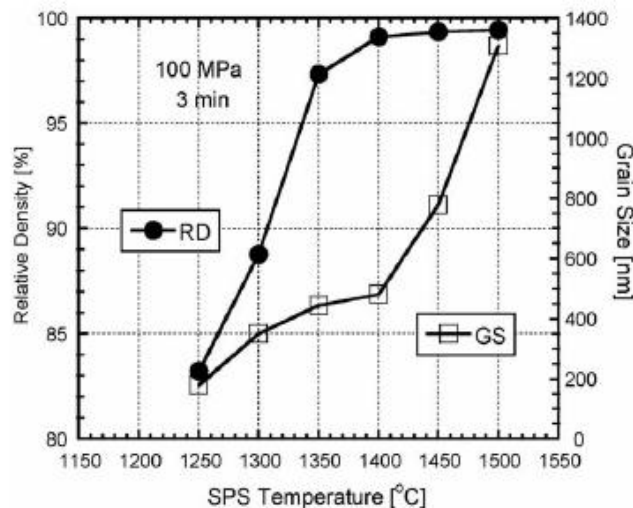


Figure 1.7. YAG relative density and mean grain size versus SPS temperature [34].

Morita et al. [36] also studied the effect of the SPS temperature, between 1275 and 1500°C, on $MgAl_2O_4$ samples (Figure 1.8). They observed an increase of the grain size from 0.4 to 1.2 μm . Porosity gradually decreased from 0.5% to 0.05% up to 1400°C, and above this it took an almost constant value $\leq 0.1\%$. Microstructures showed a residual pores decrease from 1275 to 1325°C. Above 1350°C, grain growth is faster and the density of residual pores is lower but the number of pores > 300 nm increases with the temperature. They remarked as well that fine particles precipitated during sintering at higher temperatures. These two effects explained the decrease in transparency at higher temperatures.

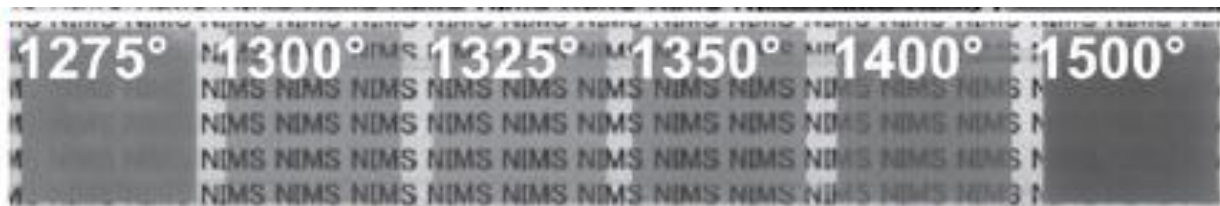


Figure 1.8. Appearance of $MgAl_2O_4$ samples sintered by SPS at different temperatures at 10°C/min [36].

The effect of dwell time has also been amply studied [34], [42], [43]; it appears less influential than temperature, even if, as the dwell time is increased, the porosity decreases but grain growth happens as well. For example, Aman et al. [43] have studied the influence of several parameters on the sintering of Al_2O_3 by SPS. Figure 1.9 reflects the effect of the dwell on the relative density and grain size. The increase of dwell time from 5 to 20 min increases the density from 97.6 to 98.7% of relative density (with grain size of 1.2 and 1.9 μm , respectively). Extension to the dwell up to 1 hour

leads to a significant grain growth ($3.1 \mu\text{m}$) and above all, a decrease of relative density, attributed to pore coalescence.

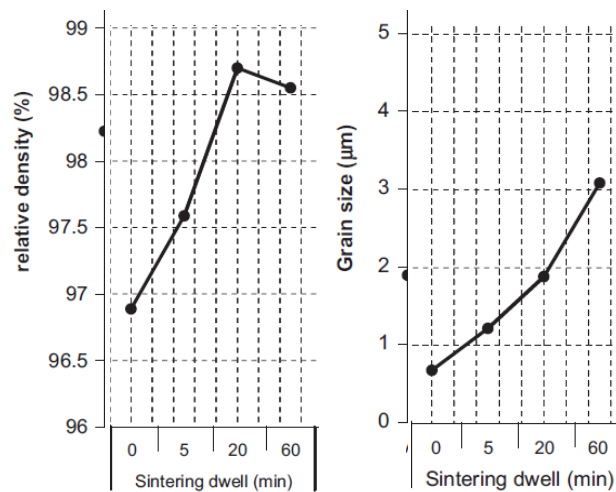


Figure 1.9. Effect of sintering dwell on relative density and grain size on Al_2O_3 samples [43].

Spark Plasma Sintering allows using high heating rates such as $400^\circ\text{C}/\text{min}$, but many researchers have obtained better transmission results using slower heating rates ($10^\circ\text{C}/\text{min}$) [11], [38], [44], [45]. In fact, high heating rates can impede porosity to close and disappear completely [10], [38].

Morita et al. [36] studied the influence of heating rate, from 2 to $100^\circ\text{C}/\text{min}$, on the relative density, microstructure and transparency of spinel samples. Samples were sintered under 80 MPa, using 1300°C as sintering temperature and a dwell of 20 minutes. All samples showed a relative density $>99\%$ regardless the heating rate, but the maximum densification rate increased with heating rate and shifted towards higher temperature ranges. Regarding the microstructure, grain size remained almost constant around $0.4 \mu\text{m}$, but porosity increased from 0.03% to 1% with the heating rate. Furthermore, pore size changed with the heating rate. At $2^\circ\text{C}/\text{min}$, few fine pores $<100 \text{ nm}$ were still observed at grain boundaries. At higher heating rate, pore size and quantity increased. Regarding the optical transmission, heating rate $\leq 10^\circ\text{C}/\text{min}$ led to a good optical transmission, but increasing rates deteriorated the transmission, and finally at $100^\circ\text{C}/\text{min}$ the sample is opaque (Figure 1.10)

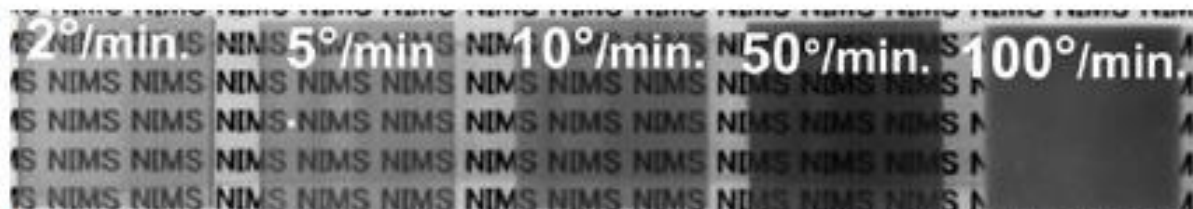


Figure 1.10. Appearance of MgAl_2O_4 samples sintered at different heating rates up to 1300°C for 20 minutes [36].

In addition, there are other thermal issues that can affect the transmission of the samples. Indeed, possible temperature gradients inside the compacts have to be taken into account, especially for nonconductive samples, to get a homogeneous sample after sintering. Size and shape of tooling, contact between different parts in SPS also modify the temperatures distribution inside the samples [15], [46].

In the case of conductive samples, most authors agree that the central part of the sample presents slightly higher temperatures, although the temperatures gradient magnitude varies depending on the SPS conditions [47], [48].

On the contrary, several works have used Finite Element Modelling (FEM) to simulate temperature gradients for insulating materials but, depending on the geometry of the tooling, the results were opposed [47], [48]. Vanmeensel et al. [48] modelled the SPS temperature gradient in ZrO_2 samples (Figure 1.11). ZrO_2 is a good electrical insulator, at least at low temperature; hence the current is forced to flow through the die. However since the sample was small compared to the tool and graphite has a good thermal conductivity, heat is quickly transferred to ZrO_2 resulting in a quite homogeneous temperature distribution, with central part slightly colder than the centre of the sample.

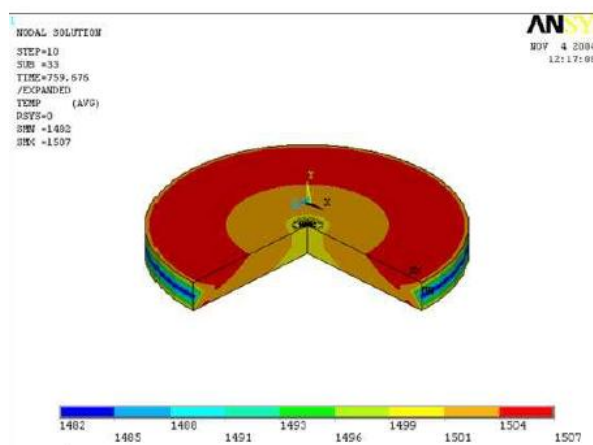


Figure 1.11. Temperature distribution inside a ZrO_2 sample (40 mm diameter) [48].

Munoz et al. [47] simulated the SPS behaviour taking into consideration a graphite tooling, and an alumina sample of 19 mm (Figure 1.12). However, in this case, thermal gradients were slightly higher and above all, contrary to the previous example, the central part of the sample presented slightly higher temperatures.

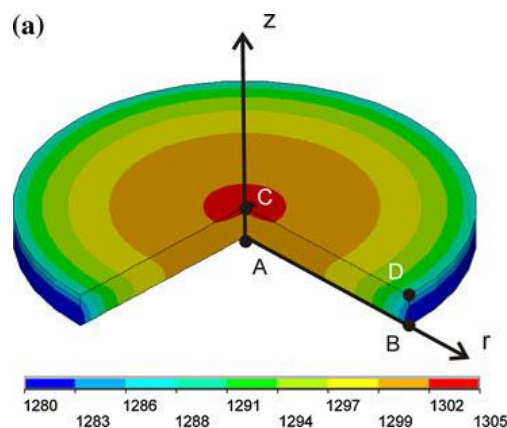


Figure 1.12. Temperature distribution in an alumina sample (19 mm diameter) [47].

Furthermore, most cases did not consider the use of a graphite felt to minimize the heat losses during heating and they did not take into account the porosity inside the samples.

These two examples concerning FEM simulations on thermal gradients show that it is not possible to take a general conclusion. Each SPS configuration (composition, diameter and thickness of the sample; tooling material, thickness of the die ...) represents a particular case.

Pressure

Pressure application allows obtaining fine and homogeneous microstructures at lower temperatures than conventional sintering. SPS allows as well the use of different pressures during sintering according to each material.

Some works have obtained an improvement in the optical transmission after applying the pressure at different temperatures [49], [50].

Morita et al. [50] studied the influence of the pressure schedule on spinel samples. They used a high heating rate (100°C/min) and a sintering temperature of 1300°C for 20 min. The pressure (80 MPa) was applied at different temperatures and this change had a strong impact on the optical transmission of the samples (Figure 1.13). When pressure is applied at 1300°C, in-line transmission reaches 35% at 550 nm. However, they observed a reduction of the transparency, as the loading temperature decreased, and they attributed this result to the increase of pore density and size. Loading at temperatures $\leq 1100^\circ\text{C}$ results in numerous large pores of size > 100 nm, resulting in a decrease of the transparency of the samples.

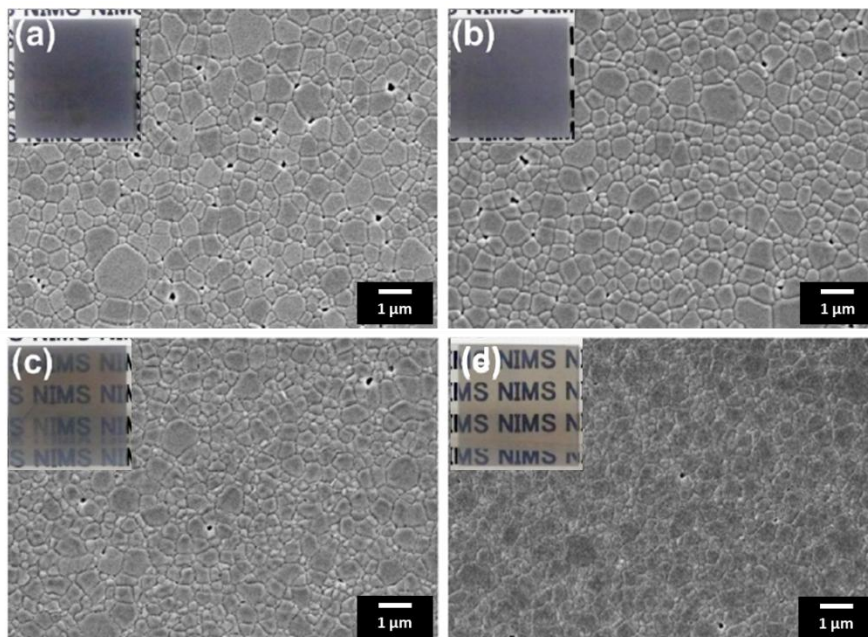


Figure 1.13. Microstructures and images of MgAl_2O_4 samples as a result of pressure application at different temperatures: (a) 1000°C; (b) 1100°C; (c) 1200°C and (d) 1300°C [50].

When the pressure is applied at higher temperature, densification takes place through the plastic deformation and diffusion processes, and thereby, the high densities can be attained irrespective of the heating rates. On the contrary, at lower temperatures, pressure induces strong inter-particle bonds, which enhance the formation of large closed pores between the particles. Once the large

closed pores are formed, they are difficult to remove in the later stages because further sintering for long times and/or at high temperatures results in grain growth accompanied by coalescence of the pores.

Marder et al. observed an influence of the pressure on the density of YAG when applying pressures between 2 and 100 MPa: the higher pressure used during heating by SPS to 1400°C, resulted in denser specimen, i.e. 71% versus 99% for 2 and 100 MPa pressure, respectively [51].

However, other publications have not found major influence in the transparency or microstructure of sintered samples as a function of the applied pressure between 50 and 100 MPa [45], [37], [7].

Works considering pressures above 100 MPa have found better results of transparency on spinel [37], alumina [52] or YAG [53]. However, application of such high pressures implies either a decrease of the sample diameter or the use of tools in other material than graphite.

In the case of addition of sintering aids, applying the pressure after the melting point of the sintering aid favours its volatilization and elimination before porosity is closed [54]. Meir et al. showed, indeed, in the case of SPS sintering of spinel with addition of lithium fluoride, that application of pressure at relatively low temperature may impede the elimination of residual LiF due to early closure of the pores. Thus, in order to achieve effective cleaning of the carbon residue and subsequent elimination of the LiF additive, it is mandatory to maintain an open pore system when the partial pressure of LiF is high.

Moreover, pressure application can cause gradients of density inside the sample. In uniaxial pressing, friction forces appear between sample and die and leads to density gradients [55]. These density gradients lead to inhomogeneous compaction and differential sintering. They can be reduced by decreasing the thickness to diameter ratio (L/D), as shown in Figure 1.14.

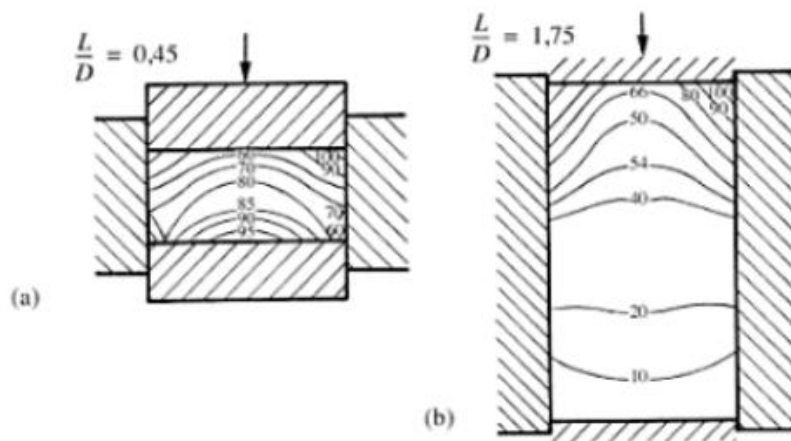


Figure 1.14. Density gradient in uniaxial pressing of ceramic powder for different L/D ratios [56]

Several works have used Finite Element Modeling (FEM) to evaluate pressure gradients during SPS.

Marlot [57] observed that pressure gradients were different using drilled or undrilled punches. According to her results, the use of drilled punches led to a stress gradient 3 times larger (Figure

1.15). This stress gradient was considered to explain the core-shell aspect of YAG ceramics after sintering by SPS with a pressure of 70 MPa.

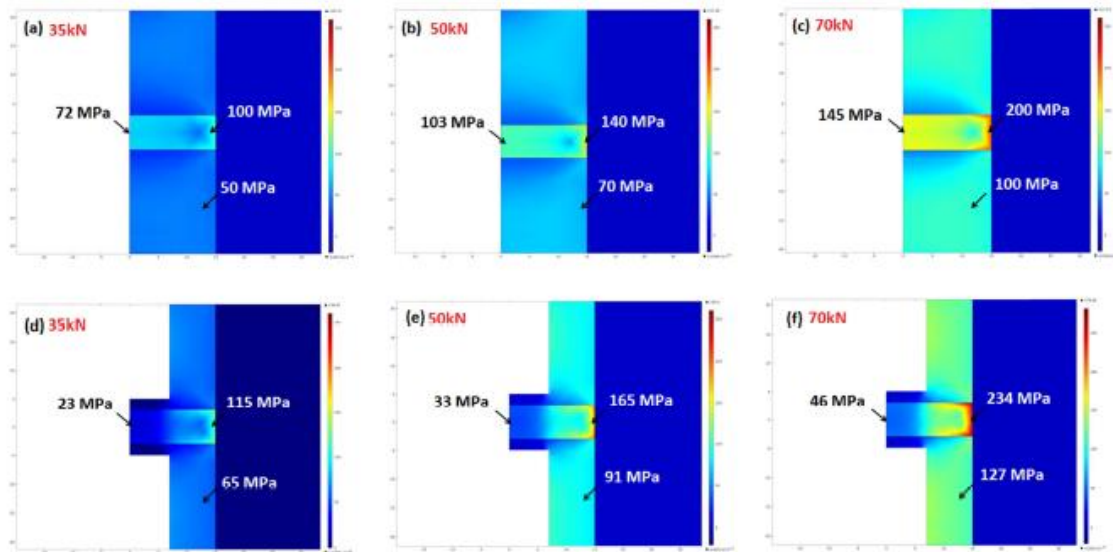


Figure 1.15. Von Mises stress distribution inside a YAG sample using (a-c) a full punch and (d-f) a drilled punch [57].

Munoz et al. [47] observed that contrary to the temperature gradient, pressure gradients were more pronounced in the case of conductive samples due to the thermal expansion of copper compared to the graphite. In the case of alumina, lower gradients were observed in the radial axis and were almost negligible in the axial one (Figure 1.16). Maximum compression was observed in the centre of the sample (39 MPa). [47]

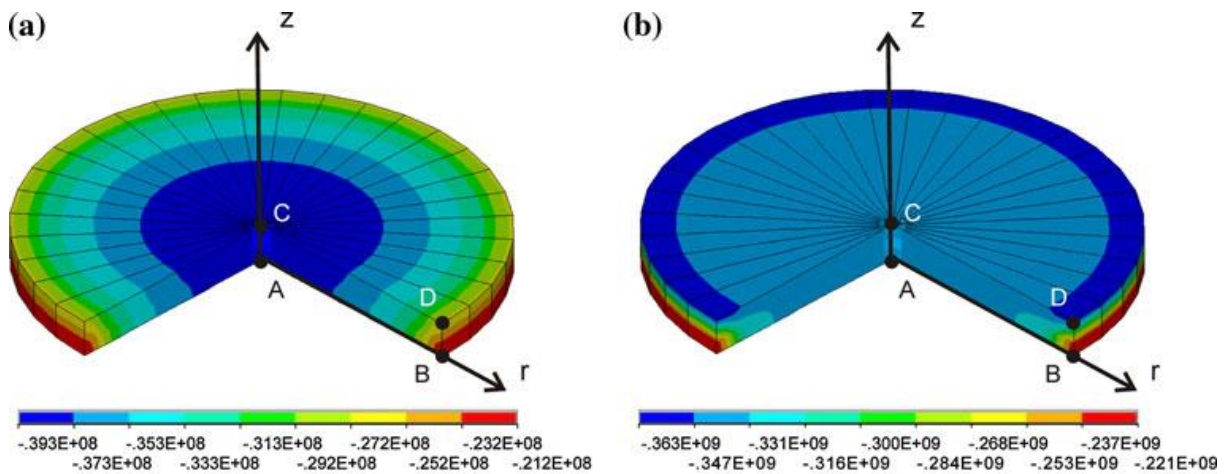


Figure 1.16. Hydrostatic stress distribution inside the a) alumina and b) Cu samples [47].

- **Darkening issue.**

Frequently, transparent ceramics produced by SPS show a darkening that lowers its transparency. This darkening is attributed to carbon contamination due to the graphite tooling, but also to the formation of oxygen vacancies inside the oxide materials under vacuum atmosphere.

Jiang et al. [58] observed that the colour of sintered alumina samples became greyer as the sintering temperature increased, owing to oxygen vacancies created in the reducing environment of the SPS chamber. Similarly, Zhang et al. [59] obtained yellowish-brown cubic-YSZ materials, which progressively darkened by increasing the SPS temperature. Grey colour and dark spots were also observed by Meir et al. in spinel [54], ascribed to carbon contamination from the SPS graphite dies. A further contribution is given by the work of Bernard-Granger et al. [60]: by means of electronic microscopy, graphite particles of about 20 nm in size, homogeneously dispersed inside a spinel matrix were observed, responsible for the dark/brown colour of the samples. However, Lee et al. [23] reported a grey appearance for pressureless, vacuum sintered YAG samples, supporting the hypothesis that oxygen vacancies rather than carbon contamination induced the darkening of the samples.

Several works have observed an increasing darkening while increasing heating rate, temperature, or applied pressure (Figure 1.17). In some cases, a core-shell aspect appeared according to the apparition of gradients inside the samples.

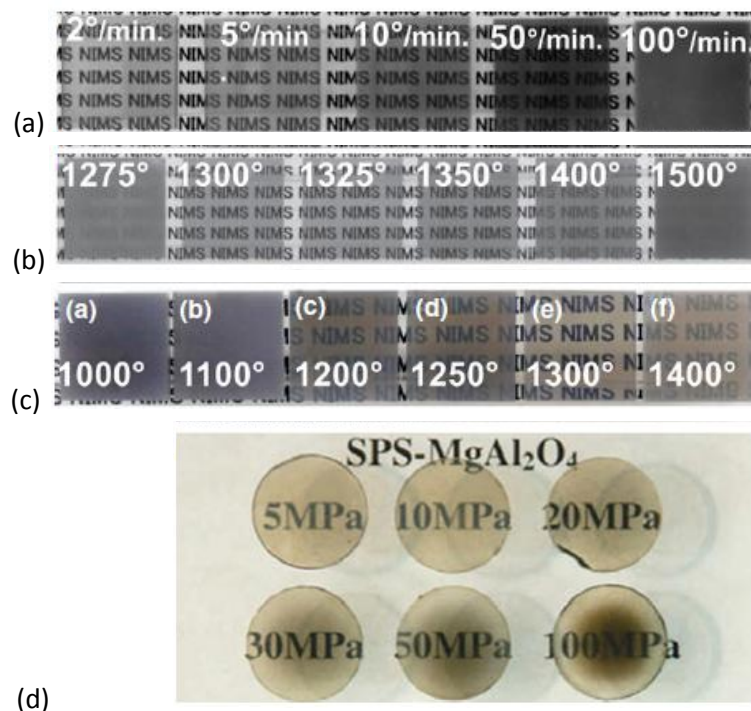


Figure 1.17. Influence of SPS parameters on the darkening of $MgAl_2O_4$ SPS specimens : a) heating rate [10], b) sintering temperature [36], c) temperature of pressure application [50], d) applied pressure [61].

In order to avoid (or at least limit) this darkening, pre-treatment of the powder, by addition of additives as LiF, have been proved to be useful. Post-annealing treatments are also frequently used to reduce the darkening of the SPS samples.

Pre-treatment of the powder: LiF addition

Lithium fluoride (LiF) is a commonly used additive in order to improve the optical transmission of spinel and YAG [42], [54]. LiF melts at $\sim 850^\circ\text{C}$ forming a liquid phase acting as sintering aid. Li and F cations segregate at grain boundaries and increase grain-boundary mobility and surface diffusion. This causes an important grain growth, that is why lithium fluoride is mainly used on cubic ceramics where grain size does not directly affect transparency.

A cleaning effect has also been attributed to LiF, and especially in SPS, it may help getting rid of carbon contamination caused by the graphite tooling (Equation 1.9). Moreover, LiF may also improve transparency by eliminating some other impurities as S, Fe or Ca (Equation 1.10 explains the reaction with sulphur). Indeed, fluorine reacts with these impurity cations to form volatile compounds, whose volatilization temperature is below the sintering temperature of the ceramic [7].



Meir et al. [54] studied the effect of LiF on spinel ceramics. The presence of 1 wt% LiF promoted the formation of spinel and accelerated its densification. LiF-doped samples showed better optical transmission than un-doped ones. In order to achieve effective cleaning of the carbon residue and subsequent elimination of the LiF additive, it is mandatory to maintain an open pore network when the partial pressure of LiF is high. They propose a reaction between the carbon residues and the LiF vapour to form a volatile $(\text{CF})_n$. Li atoms will be incorporated to the spinel lattice and give rise to oxygen vacancies. These oxygen vacancies will promote grain growth as well.

Frage et al. [62], [42] observed the same effect of LiF addition in YAG samples. A higher optical transparency in 0.25 wt% LiF-doped YAG was obtained compared to undoped ones (71% vs 20% at 500 nm, see Figure 1.18). They demonstrated the effectiveness of this additive in reacting with the carbon contamination, removing it as volatile species and restoring the light transmittance. However, they also measured the content of Li and F species in YAG specimens after sintering and their results suggest that major fraction of LiF is retained in the matrix. Li most likely incorporated as a cation substitute and F substituted for oxygen.

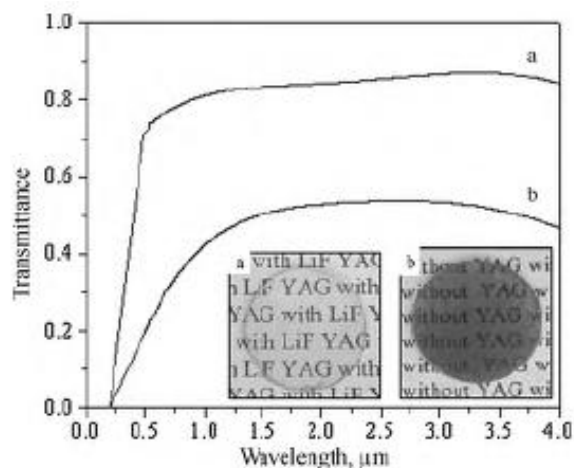


Figure 1.18. Optical transmission of YAG specimens (a) with LiF; (b) without LiF [62].

Anyway, to work effectively, LiF must be evenly distributed and must leave the compact as it has a different refractive index. Moreover, LiF can be trapped if too high concentration is used. Excess or trapped LiF accumulates at grain boundaries and triple junctions and results in scatter and possibly restricted grain size [7].

Post-treatments : annealing in air and post-hipping

The most used treatment in order to remove the darkening observed after SPS is annealing in air. Several authors observed darkening reduction in different materials as alumina [58], zirconia [59] or YAG [11] after annealing the samples in air.

Spina et al. [11] showed the benefits to optical transmission of air annealing at moderate temperatures (Figure 1.19) in YAG specimens, with an increase of transmission from 57 to 66% at 600 nm. The grey colour is less intense after annealing at 800°C during 1 hour due to the reduction of oxygen vacancies.



Figure 1.19. YAG samples after SPS (15 min, 1350 °C, 74 MPa) before annealing (left), and after air annealing at 800°C for 1h (right) [11].

Within the same research group, Palmero et al. [41] studied by XPS the presence of oxygen vacancies after annealing at different temperatures (Table 1.1). According to their results, oxidation state of Y and Al increased and oxygen vacancies decreased till 900°C. Annealing at higher temperatures led to a decrease of the optical transmission, this effect being attributed to a microstructural change at high temperatures, coalescence of colour centres and tiny pores leading to new or larger defects.

Table 1.1. Surface chemical composition (at.%) of as-sintered and annealed YAG samples [41].

Sample	Al (at.%)	Y (at.%)	O (at.%)	C (at.%)	Y/Al
US as-sintered	11.13	7.94	35.36	45.58	0.71
US annealed 600°C	14.32	9.86	45.44	30.37	0.69
US annealed 900°C	13.60	10.01	47.27	29.12	0.74
US annealed 1200°C	14.38	9.81	48.51	27.30	0.68

The same article shows that carbon contamination represents only a small contribution to the samples darkening. After annealing at 600°C, there is a significant diminution of the carbon content but optical transmission in the visible range is almost unchanged (Figure 1.20).

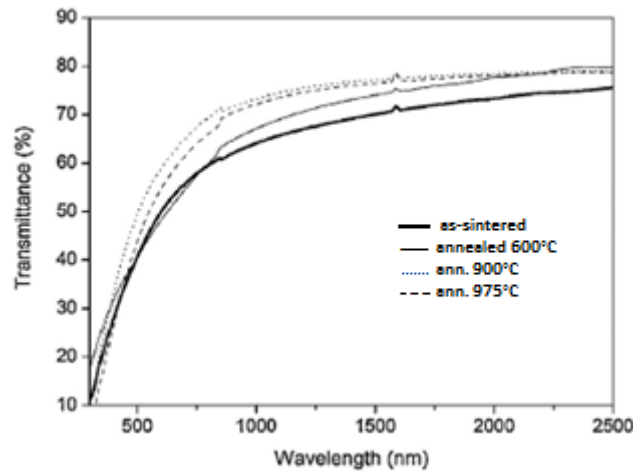


Figure 1.20. Optical transmission of as-sintered and annealed YAG samples [41].

Hot isostatic pressing (HIP) is difficult to employ directly on ceramics due to the encapsulation and high temperatures needed for sintering. But, in case of transparent ceramics, it has been used as post-treatment after conventional or vacuum sintering (including SPS) when samples reach densities over 92% (so with only close porosity) or to restore oxygen vacancies with post-hipping in oxidative atmosphere.

Lee et al. [23] obtained transparent ceramics with the addition of SiO_2 , but there was an obvious improvement of the transmission of the samples after HIP post-treatment, with the reduction of the large pores content (Figure 1.21).

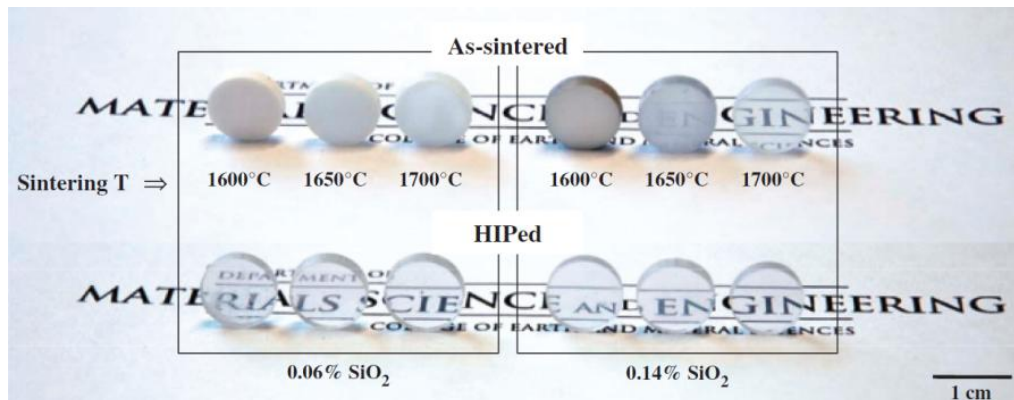


Figure 1.21. 1% Nd:YAG specimens doped with 0.06 and 0.14 wt% SiO_2 , sintered for 2 h at the temperatures showed above and subsequently hot isostatic pressed at 1750°C for 2 h in 200 MPa Ar [23].

Zhang et al. [63] fabricated transparent Nd:YAG ceramics by vacuum sintering, and then performed several post-treatments: annealing in air and hot isostatic pressing under argon. They observed a marked variation in the optical properties of the samples with these different post-treatments (Figure 1.22). The first annealing compensates oxygen vacancies generated during vacuum sintering. The post-HIP in Ar improves the transmission because it reduces the remaining pores. In order to further eliminate oxygen vacancies samples are re-annealed at different temperatures. Re-annealing at 1250°C slightly increases transmittance but an increase in the re-annealing temperatures reduced the transmittance of the samples. The microstructure of the samples was analysed and no

differences in grain size were revealed, but some intergranular pores were observed in the samples before HIP. After HIP no pores were observed, but after re-annealing at temperatures over 1350°C some pores were visible again. This effect was associated to residual small pores that could not be removed by HIP and are not visible by SEM. These pores coalesce at higher annealing temperatures resulting in loss of transmission (Table 1.2.)

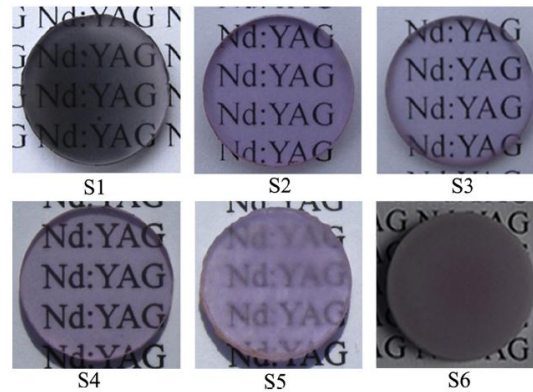


Figure 1.22. Nd:YAG samples vacuum sintered at 1780°C (S1), S1+annealing at 1450°C (S2), S2+ HIP at 1700°C (S3), S3+annealing at 1250°C (S4), S3+annealing at 1350°C (S5), S3+annealing at 1450°C (S6) [63].

Table 1.2. Sintering and post-treatment conditions, grain, pore size and porosity of the 2 at.% Nd:YAG samples [63].

Samples	Vacuum sintering	Annealing	HIP	Re-annealing	Grain size G (μm)	Pore size D (μm)	Porosity V (%)
S1	1780 °C, 20 h	–	–	–	9.95	0.38	0.0015
S2	1780 °C, 20 h	1450 °C, 20 h	–	–	10.03	0.39	0.0015
S3	1780 °C, 20 h	1450 °C, 20 h	1700 °C, 2 h, 200 MPa	–	9.97	–	–
S4	1780 °C, 20 h	1450 °C, 20 h	1700 °C, 2 h, 200 MPa	1250 °C, 10 h	10.05	–	–
S5	1780 °C, 20 h	1450 °C, 20 h	1700 °C, 2 h, 200 MPa	1350 °C, 10 h	10.12	0.17	0.021
S6	1780 °C, 20 h	1450 °C, 20 h	1700 °C, 2 h, 200 MPa	1450 °C, 10 h	9.98	0.19	0.056

1.2. Yttrium aluminium garnet

Yttrium aluminium garnet, known as YAG ($\text{Y}_3\text{Al}_5\text{O}_{12}$), is one of the most widely used transparent ceramics. When doped, its applications as laser and scintillation material are well-known [64], [65], [66] and thanks to its high strength and hardness, it is also suitable as structural ceramic [67].

1.2.1. Structure, properties and applications

YAG ($\text{Y}_3\text{Al}_5\text{O}_{12}$) is a mixed oxide of yttrium and aluminium, which present a cubic structure (cc) and 80 atoms/ primary cell (160 atoms/ cubic cell). The crystalline structure is shown at Figure 1.23. This structure is at the origin of its hardness and good thermal conductivity that makes it suitable for laser purposes. Moreover, its thermal expansion coefficient is isotropic and avoids stresses at grain boundaries.

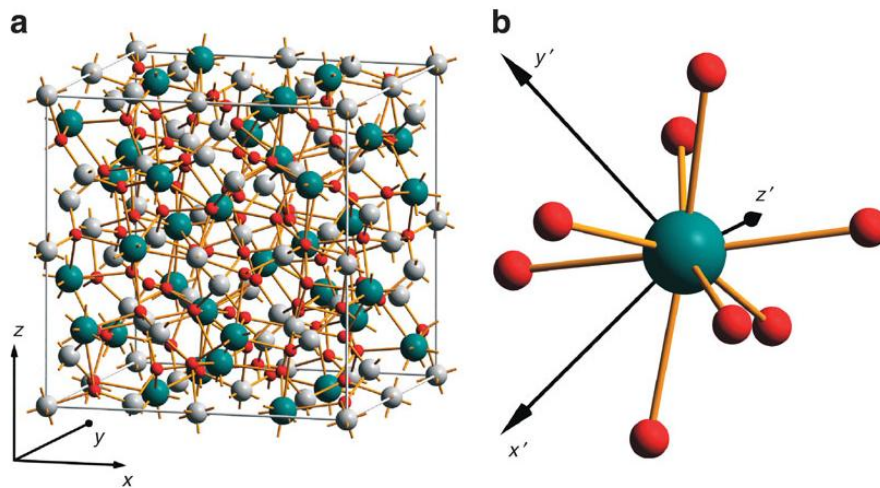


Figure 1.23. (a) YAG unit cell. Green, white and red sites correspond to yttrium, aluminium and oxygen, respectively. (b) Surrounding of yttrium atom. [68]

If we consider the phase diagram $\text{Al}_2\text{O}_3\text{-Y}_2\text{O}_3$, we observe 3 intermediate stable compounds with different stoichiometry. In addition to YAG, there are YAP (YAlO_3) and YAM ($\text{Y}_4\text{Al}_2\text{O}_9$) [69] (Figure 1.24). YAP (yttrium aluminium perovskite) presents an orthorhombic structure and YAM (yttrium aluminium monoclinic) crystallises in a monoclinic structure. A hexagonal phase has also been found (YAH (YAlO_3)) in some synthesized powders [70].

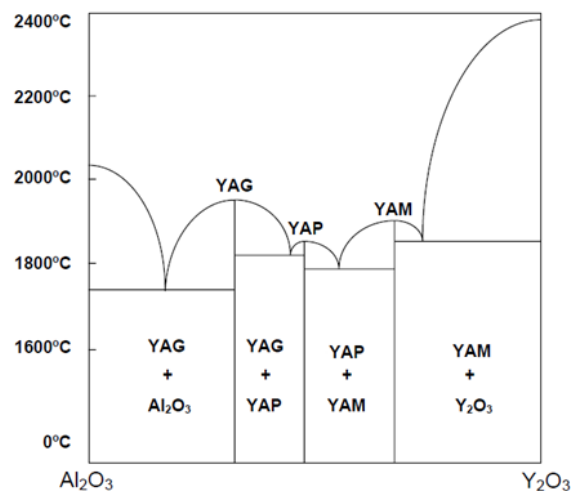


Figure 1.24. $\text{Al}_2\text{O}_3\text{-Y}_2\text{O}_3$ phase diagram.

Main characteristics and physico-chemical properties of a YAG single crystal are shown in Table 1.3 [71], [72].

Table 1.3. Physical and chemical properties of YAG (300K)

Density (g/cm ³)	4.55
Molar mass (g/mol)	593.7
Melting temperature (K)	2238
Refractive index, n	1.83 (à 628nm) 1.82 (à 1060nm)
dn/dT (K ⁻¹)	8.9·10 ⁻⁶ (à 1060nm)
Transmission window (µm)	0.21-5.5
Thermal expansion coefficient (K ⁻¹)	7.8·10 ⁻⁶
Thermal diffusivity (cm ² /s ²)	0.041
Specific heat capacity, Cp (J/kg·K)	590
Thermal shock resistance (W/m)	800-1100
Thermal conductivity, k (W/m·K)	11.2
Young modulus (GPa)	335
Mohs hardness	8.5
Dielectric constant	11.7

Fully dense polycrystalline YAG is a widely used transparent material for harsh environments, withstanding high temperatures (melting point 1940°C [51]) and corrosive conditions. Excellent high temperature strength, low creep rate and good mechanical properties make of YAG an oxide ceramic with outstanding functional and mechanical properties [70].

Therefore, YAG can be used as substrate for dielectric components, prisms and mirrors, as a part of discharge lamps, high intensity lamps as well as active medium for the production of lasers [64], [73], [74], [75], when doped with rare earths and transition metals. In this sense, it can be doped with Yb³⁺ (Yb:YAG) for diode-laser [76], [65], with Er³⁺ (Er:YAG) widely used in medical applications [77], with Eu³⁺ (Eu:YAG) used as cathode ray tube [78] and with Nd³⁺ (Nd:YAG) used as laser material [79], [66], [42]. Nd:YAG is one of the most popular laser materials.

1.2.2. Synthesis

There are several synthesis routes in order to produce pure YAG, the most frequently used being solid state reaction [80], [81], solvothermal [82], sol-gel [83], [84], and coprecipitation [79], [66], [85].

Solid state reaction is the easiest and the most used synthesis method at large scale. Precursors are generally yttrium and aluminium oxides, Y₂O₃ and Al₂O₃ [18], [23], [86], [20]. This method needs usually thermal treatments at higher temperatures [18], [86] and long-time dwells compared to the other methods.

Solvothermal method. This technique combines pressure and temperature simultaneously in an autoclave. Solvent can be water or any organic solvent. The use of organic solvents instead of water limits the temperature and pressure. Usually, more agglomerated powders are obtained and these liquids are generally toxic to the environment. However, pure YAG powders have been prepared this way [87], [88].

Sol-gel method. This method is widely used in order to synthesize oxide nanoparticles. It uses organic or inorganic precursors that form a gel and a 3D interconnected lattice after hydrolysis and polycondensation in an organic solvent. The following steps are drying and calcination to obtain the nanoparticles. Usually the advantage is a good chemical homogeneity, and the obtaining of metastable compounds at lower temperatures [74], [84]. Nevertheless, agglomerated powders are also obtained by this method [89].

Precipitation synthesis. This method is also common for the synthesis of YAG powders. It is usually carried out in two steps: during the first step a solution of the metallic salts precipitate in the presence of a solution containing the precipitant salt; the second step is usually the precipitate calcination which decomposes into the desired oxide.

Regarding the addition of the metallic salts there are two methods of precipitation: a) direct-strike: precipitant is added into the metallic solution and b) reverse-strike: metallic salts solution is added to the precipitant. Reverse-strike precipitation allows simultaneous formation of the aluminium and yttrium precursors and a better control of the pH. This method leads to better stability and homogeneity of the precursors and it is generally used [90]. The pH must be controlled and almost constant (~ 8) to assure the formation of yttrium and aluminium hydroxides [15]. When pH oscillates too much the Y:Al ratio can be different of 3:5 and lead to the formation of secondary phases [91]. Reverse-strike co-precipitation has been retained for the synthesis of pure YAG during the experimental part and is discussed next.

Fabrication of YAG powders is a complex process. Many factors, such as reaction temperature, final pH value, period of ageing, precipitant concentration and metallic salts solution, would affect composition, morphology and final properties of the precursor. Moreover, the calcination process is also another important factor that affects sintering properties of the YAG powder [92].

In reverse-strike co-precipitation, YAG is synthesized from solutions of yttrium and aluminium chlorides or nitrates. Salts solution ease controlling Y:Al ratio. Both chlorides and nitrates are indeed hygroscopic and accidental absorption of water can affect the Y:Al ratio.

Precipitant influence was studied by Li et al. [75]. Ammonium bicarbonate, AHC (NH_4HCO_3) or ammonium hydroxide (NH_4OH) are frequently used precipitants. They showed that AHC lead to precursors crystallizing to pure YAG at 900°C , a lower temperature than using ammonium hydroxide. Also Sang et al. recommended using AHC instead of ammonia [91] or urea ($(\text{NH}_2)_2\text{CO}$) [79] because AHC facilitates obtaining less agglomerated powders.

Regarding the influence of other factors, reaction temperature, precipitant concentration, pH and dripping speed have also been considered by different researches [57], [75], [93], [94], [95], [96]. Generally speaking, dripping speed of 5 ml/minute, pH around 8 and AHC concentration of 0.5M are recommended values in order to obtain spherical pure YAG powders. Reaction temperature has also an influence on the crystallization path [96], low temperatures between 5 and 25°C led to pure YAG, but when 60°C is used, secondary phases appear.

1.2.3. Transparent YAG ceramics

YAG ceramics have been extensively studied, and there are examples in the literature of transparent YAG ceramics prepared by different sintering techniques (vacuum sintering, SPS, HIP, HP, microwave ...). Table 1.4 describes the main characteristics of some recent publications about transparent doped and un-doped YAG.

Table 1.4. State of the art of transparent YAG ceramics.

Material	Powder/ type of synthesis	Sintering technique	Additives	%T@600nm, 1mm	%T@1000nm, 1mm	Grain size (μm)	Reference
YAG	co-precipitation; US	SPS+annealing	no	72	81	0.3	[11]
YAG	co-prec+lyophilisation	SPS	no	51 (@680nm)	64	0.4	[16]
YAG	commercial Nanocerox 50nm	SPS	no	48	60	0.2	[62]
YAG	commercial Nanocerox 50nm	SPS	0.25%LiF	79	82	1.7	[62]
Nd:YAG	solid state reaction, BM	Vacuum sint+anneal	2%at Nd	79	Not reported	30.3	[97]
Nd:YAG	solid state reaction, BM	Vacuum sint+anneal	0.8%Nd; 0.5%TEOS	74 (@700nm, thickness unknown)	Not reported	20.0	[18]
Yb:YAG	solid state reaction, BM	Vacuum sint+anneal	0.8%Yb; 0.5%TEOS	58 (@700nm, thickness unknown)	Not reported	12.0	[18]
YAG	commercial Tal Mats 34nm	SPS	no	5	Not reported	0.5	[34]
Er:YAG	solid state reaction, BM	Vacuum sint+anneal	1%Er;0.5%TEOS	84 (@400nm)	85 (@1800nm)	7.0	[98]
Cr, Nd:YAG	solid state reaction, BM	Vacuum sint+anneal	0.1%atCr;1%atNd; 0.5%wTEOS; CaO	72	78	10.0	[86]
Nd:YAG	commercial Nanocerox 50nm	SPS	1%Nd:YAG	Not reported	75	0.5	[42]
Nd:YAG	commercial Nanocerox 50nm	SPS	1%Nd:YAG; 0.25%LiF	Not reported	83	3.0	[42]
YAG	solid state reaction, BM	Vacuum sint+anneal	MgO; TEOS	81	84	10-50	[20]
Nd:YAG	solid state reaction, BM	microwave	9.8%Y ₂ O ₃ ;0.5%TEOS	Not reported	69	25.0	[65]
Nd:YAG	solid state reaction, BM+spray drying	Vacuum sint +HIP	1%Nd; 0.06%SiO ₂	80	84	2.0	[23]
YAG	lyophilisation+BM	Vacuum sint +HIP	2%Nd; SiO ₂ (<3000ppm)	Not reported	Not reported	10.0	[99]
Nd:YAG	Commercial Nanocerox 50 nm	HPSPS	1%Nd; 0.25%LiF	80 (@550 nm)	81	1.2	[53]

US: Ultrasounds

BM: Ball milling

HPSPS: High Pressure SPS

As observed in Table 1.4, YAG ceramics prepared by SPS show high values of optical transmission and presenting microstructures with small grain sizes, compared to YAG ceramics obtained by vacuum or microwave sintering.

Concerning transparent YAG ceramics obtained by SPS, Figure 1.25 shows the most relevant results of optical transmission. The SPS parameters were different in each publication: pressures between 50 and 100 MPa, heating rates between 2 and 100°C/min, temperatures between 1300 and 1400°C and dwell times between 3 and 120 minutes.

The best optical transmission values were obtained by Frage et al. [62] with a 0.25% LiF doping, they measured 79% RIT at 600 nm wavelength. Regarding undoped YAG ceramics, the highest values at 600 nm was obtained by Spina et al. [11] who measured 72% RIT.

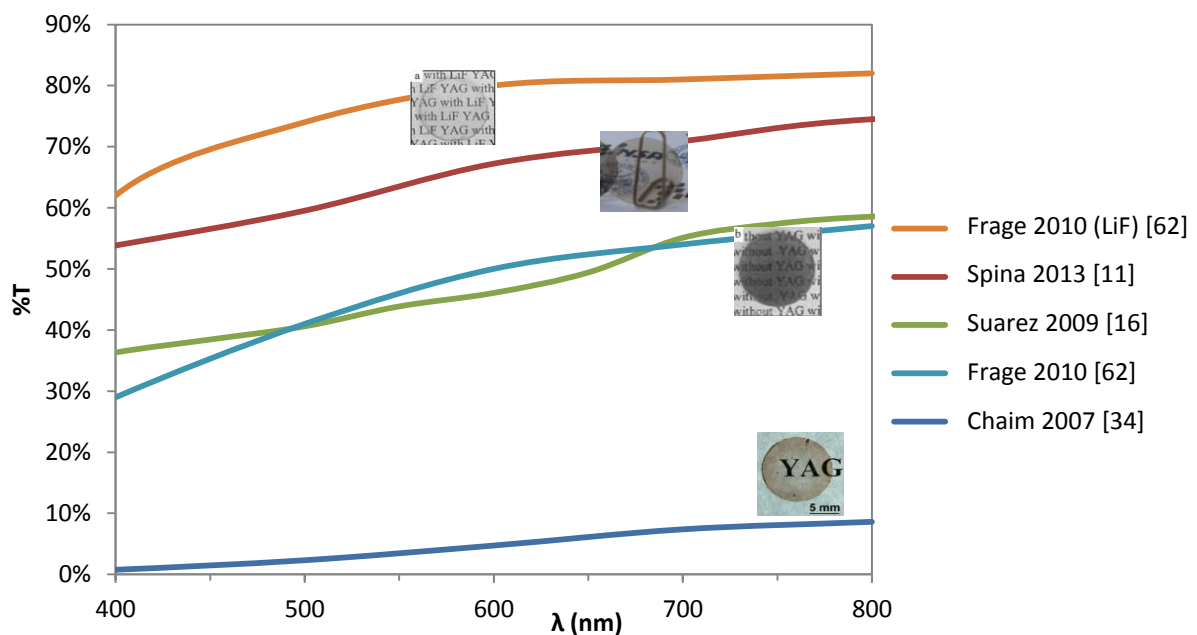


Figure 1.25. Optical transmission of transparent YAG ceramics prepared by SPS.

1.3. Barium Titanate

The interest in ferroelectric ceramics dates back from the early 1940s when the high dielectric constant of barium titanate ceramics was recognized. Since then, many efforts have been made to develop high-dielectric-constant capacitors, piezoelectric transducers, positive-temperature-coefficient devices, electro-optic light valves, and ferroelectric thin-film memories [100].

1.3.1. Structure

BaTiO₃ (BT) belongs to the perovskite family ABO₃. Its unit cell is shown at Figure 1.26. The structure consists in a corner-linked network of oxygen octahedra, with Ti⁴⁺ ions occupying the B sites within the octahedra and the Ba²⁺ ions located at the interstitial A positions [101], [102]. BT has a ferroelectric behaviour at room temperature and up to the Curie temperature (T_c) near from 134°C in single crystals (but T_c is very dependent on the crystalline purity).

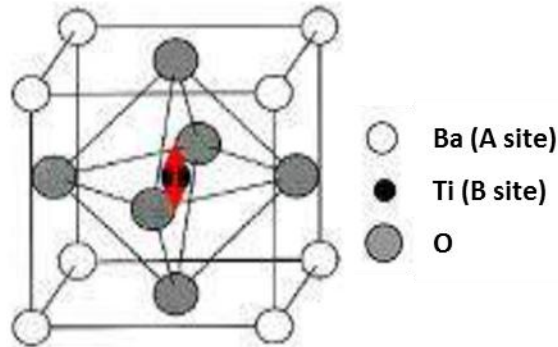


Figure 1.26. Unit cell of BaTiO_3 [103].

In a polycrystal T_C is around 120°C . Above it, BaTiO_3 becomes paraelectric and change its structure to cubic, non-polar and non- piezoelectric. The cubic structure is stable up to 1460°C when a hexagonal structure appears.

At lower temperatures, below 5°C , there is a new structural change with an orthorhombic symmetry. This phase is also ferroelectric but the spontaneous polarisation direction is different from that of the tetragonal phase. Finally, at -90°C there is a transition to rhombohedral structure.

Figure 1.27 illustrates crystallographic changes of BT, with the temperatures ranges of stability and dotted lines delineate the original cubic cell.

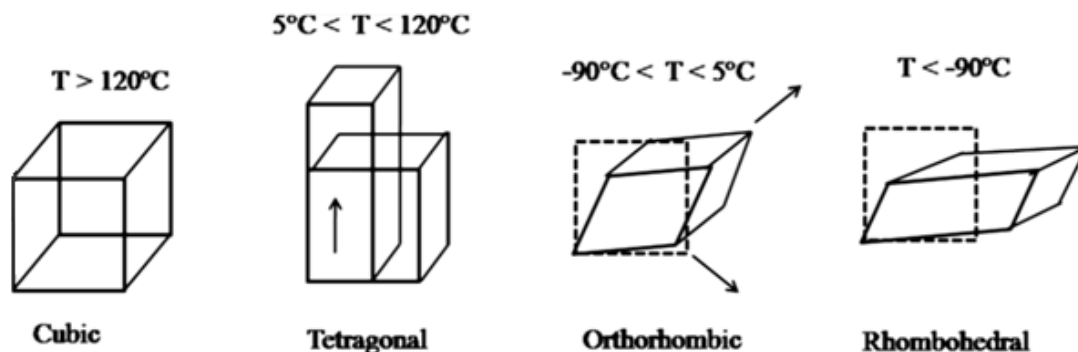


Figure 1.27. Unit cells of the four phases of BaTiO_3 .

BaO-TiO₂ phase diagram

The barium oxide (BaO) - titanium dioxide (TiO_2) phase diagram contains several phases. Between them, BaTiO_3 is the one of interest here. The presence of secondary phases inside the BaTiO_3 ceramics has a strong influence on the properties, so a careful control of the stoichiometry of the samples must be made.

Several stable compounds exist at room temperature: $\text{Ba}_6\text{Ti}_{17}\text{O}_{40}$, $\text{Ba}_4\text{Ti}_{13}\text{O}_{30}$, BaTi_4O_9 and $\text{Ba}_2\text{Ti}_9\text{O}_{20}$ [104]. Among the intermediate phases, only Ba_2TiO_4 and BaTiO_3 have been correctly identified and described ([104], [105], [106], [107], [108]).

Figure 1.28 illustrates the BaO-TiO_2 phase diagram. It is noticeable the high amount of compounds and the difficulty on obtaining a pure BaTiO_3 phase.

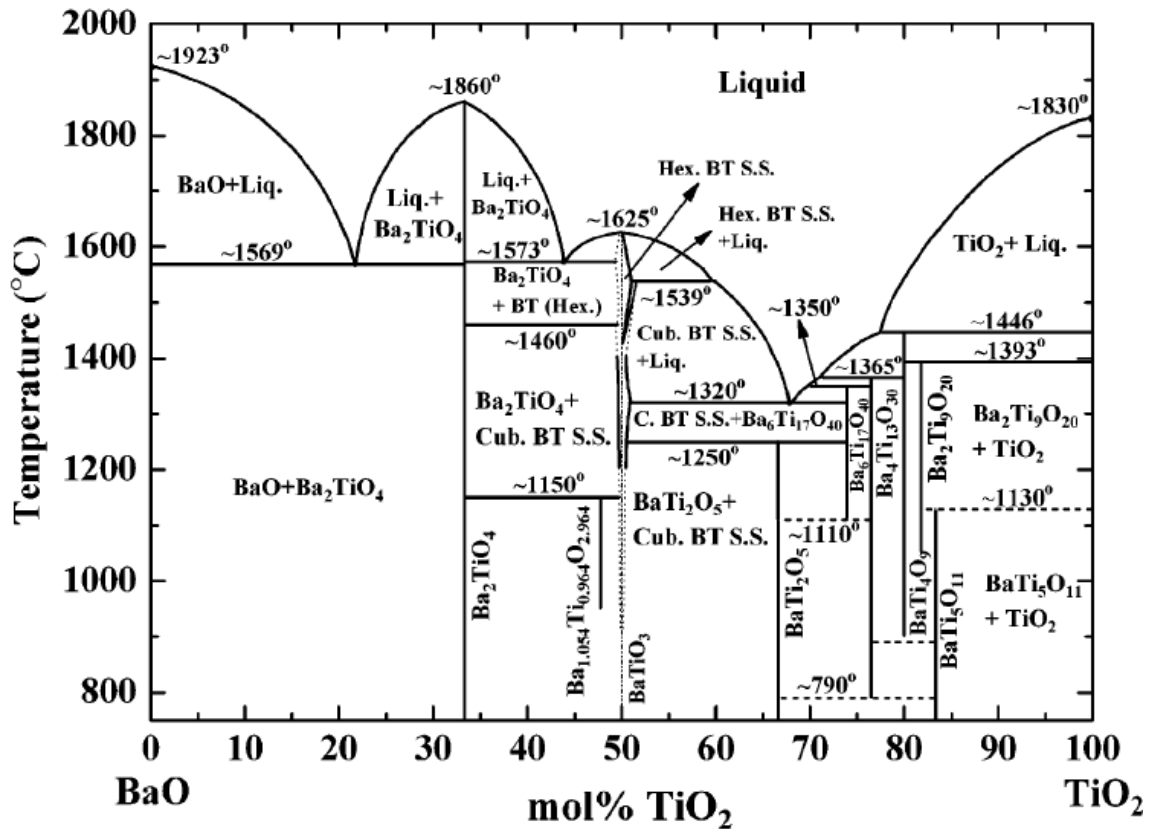


Figure 1.28. BaO-TiO₂ phase diagram [105].

1.3.2. Properties and applications

Barium titanate is the first ferroelectric ceramic and a good candidate for a variety of applications due to its excellent dielectric, ferroelectric and piezoelectric properties [102]. It can achieve a dielectric permittivity up to 10000 and a piezoelectric constant (d_{33}) up to 788 pC/N in textured ceramics [109].

Main characteristics and physico-chemical properties of BaTiO₃ ([110], [111], [4]) are summarized in Table 1.5.

Table 1.5. Physical and chemical properties of BaTiO₃ (300K)

Density (g/cm ³)	6.02
Molar mass (g/mol)	233.2
Melting temperature (K)	1898
Refractive index, n	2.66 (à 400 nm) 2.38 (à 700nm)
Thermal expansion coefficient (K ⁻¹)	$6.17 \cdot 10^{-6}$
Thermal diffusivity (mm ² /s ²)	1.03
Specific heat capacity, Cp (J/kg K)	434
Thermal conductivity, k (W/m.K)	2.61
Young modulus (GPa)	67
Mohs hardness	5

BaTiO₃ was the first material used for manufacturing dielectric ceramic capacitors and still nowadays it is widely used as part of multilayer ceramic capacitors (MLCC). It is suitable for this application due to its high permittivity and low dielectric loss [112].

The values of permittivity depend on intrinsic factors inherent to the sample: synthesis route, purity, dopants density, grain size, etc. and also extrinsic factors as temperature or frequency. Typical values of BaTiO₃ permittivity at room temperature are quite variable, ranging from 500 to 10000 [102].

Ceramics with grain size over 1 μm, sintered by conventional sintering in air, present a classical behaviour of BaTiO₃ permittivity (Figure 1.29). The temperature dependence of permittivity shows peaks when there is a change in structure. The main peak is observed with the tetragonal-cubic phase transition, around 130°C at the Curie temperature (T_C).

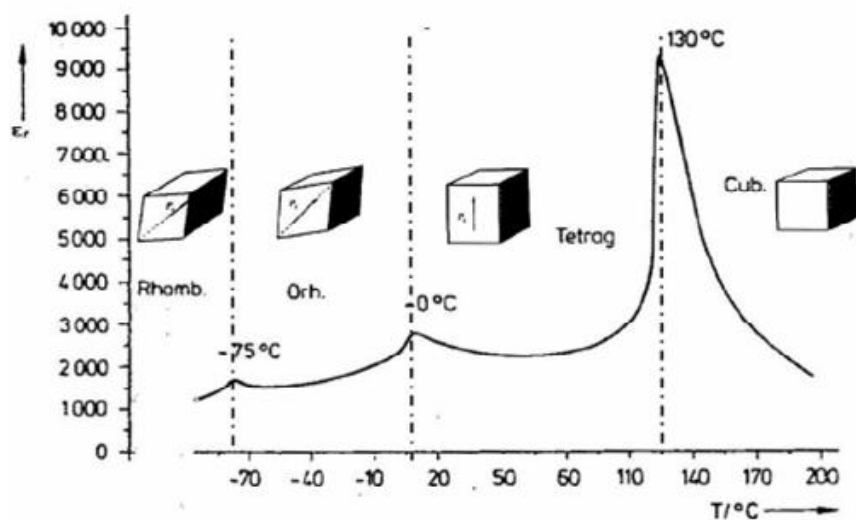


Figure 1.29. Permittivity of BaTiO₃ as a function of temperature [113].

In the last few years, ceramic capacitors have experienced drastic miniaturization and extensive investigations have been performed to reveal the role of the microstructure in defining the functional properties [114], [115], [109].

The influence of microstructure on permittivity was studied on different grain size ranges.

For example, Artl et al. showed that permittivity of ceramics with grain size larger than 10 μm is almost constant (size independent): for instance, coarse-grained ceramics (20 - 50 μm) of pure BT showed permittivity values in the range 1500-2000 at room temperature [116].

Kim et al. [117] reported in their work the influence of grain size on permittivity. They prepared samples by two step sintering and obtained samples with grain sizes from 0.86 to 10 μm but relative densities between 83-95%. They found that the samples with grain size of 0.86 μm presented the highest permittivity values and that permittivity decreased as the grain size increased (Figure 1.30).

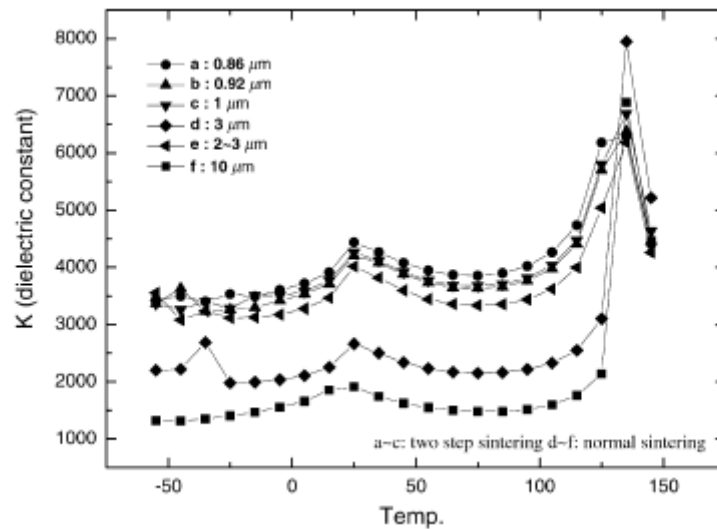


Figure 1.30. Temperature dependence of permittivity of BaTiO_3 with various grain sizes [117].

Influence of smaller grains sizes (nanometric or submicronic) was also studied. For example, Zhao et al. [118] prepared BaTiO_3 samples by SPS with grain sizes in the range 50 - 300 nm and then annealed them in air for 1-10 h at 700-800°C. They also prepared coarser ceramics with grain sizes between 500 to 1200 nm by conventional sintering. All the samples showed a density around 97%. They observed a reduction of tetragonal distortion in the case of smaller grain size and a decrease in T_c (Figure 1.31a). At the same time, they observed a decrease in the permittivity values (Figure 1.31b).

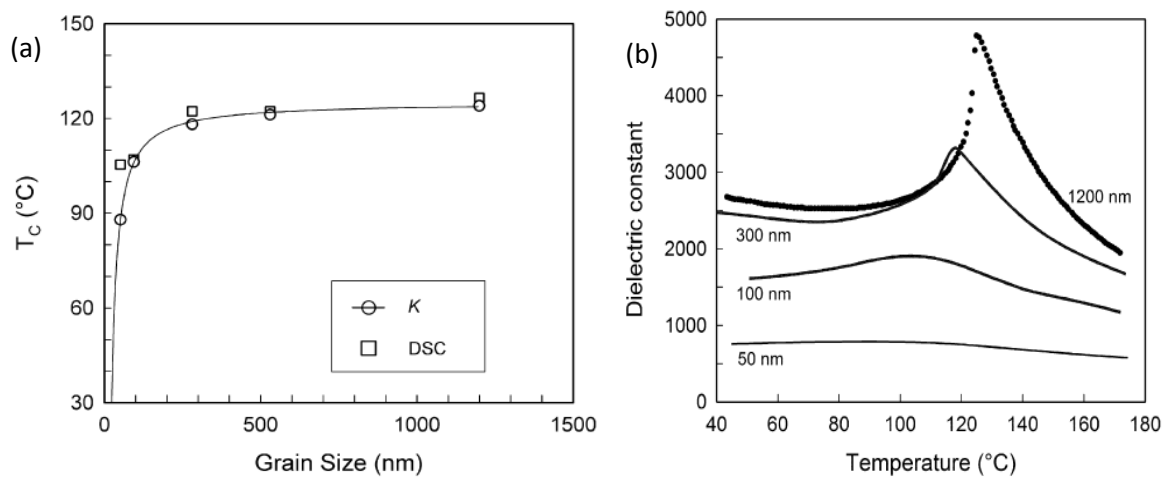


Figure 1.31. a) Curie temperature of BaTiO_3 ceramic as a function of grain size. b) Permittivity at 104 Hz as a function of temperature.

Huan et al. [119] also found a maximum in the permittivity values for grains size of around 1.28 μm and a decrease of the Curie temperature for decreasing grain sizes (Figure 1.32). They prepared BaTiO_3 samples by two step sintering.

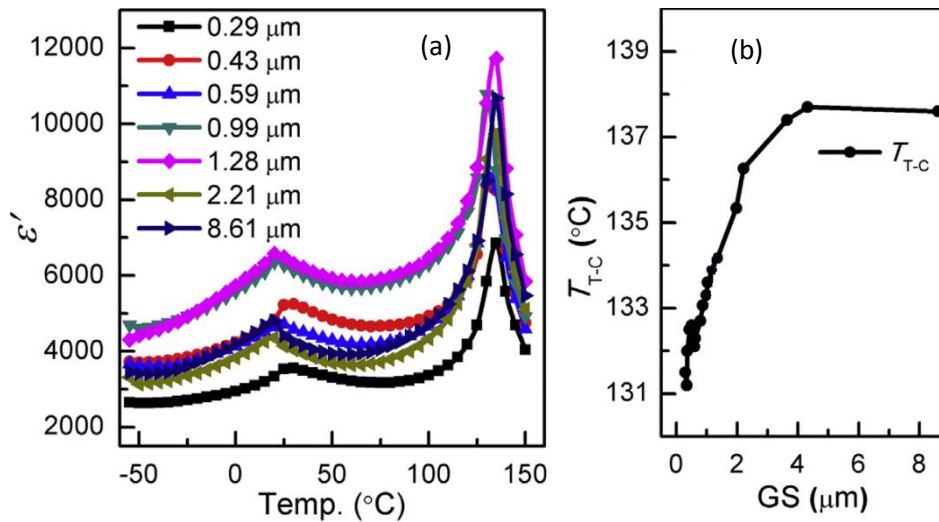


Figure 1.32. (a) Permittivity at 103 Hz as a function of temperature of BT ceramics with different grain sizes (b) T_c evolution as a function of grain size (GS).

Regarding the physical origin of the maximum value of the permittivity, usually associated with a grain size $\sim 1 \mu\text{m}$, two alternate theories based on internal residual stress and domain wall motion have been developed over the past decades. Recently, Ghosh et al. [120] confirmed the domain wall contribution to the permittivity. There is an increase of 90° domain wall motion when grain size approaches $1 \mu\text{m}$. Then, when grain size is lower, the behaviour of BT ceramics with different grain sizes is attributed to the grain boundaries density. Grain boundaries are characterised by a lower permittivity compared to the ferroelectric grain cores. So, when the grain boundaries density is very high the permittivity decreases [112].

Contrary to these results, Guillemet-Fritsch et al. [121] and Valdez-Nava et al. [122] obtained colossal permittivity in BaTiO_3 ceramics prepared by SPS with grain sizes between 250-300 nm. Furthermore, no peak at the Curie temperature was observed (Figure 1.33).

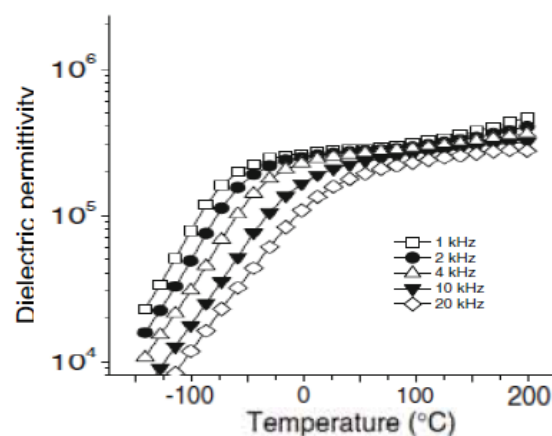


Figure 1.33. Variation of relative permittivity as a function of temperature for undoped BaTiO_{3-x} measured at various frequencies [122].

This behaviour was explained by an interfacial polarisation involving polarons due to the presence of Ti^{3+} ions. Vacuum sintering in SPS generates oxygen vacancies and electrons; to compensate the charge imbalance, there is a reduction of Ti^{4+} to Ti^{3+} .



Han et al. [123], [124] deepened in the study of BT colossal permittivity and proposed a model. Induced oxygen vacancies and electrons can be localized charge carriers in the grain or at the grain boundary under the applied electric field and generate different types of polarisation. Summarizing, permittivity inside polycrystalline samples is a combination of BLC (barrier layer capacitance), thanks to the insulating surface, interfacial polarization at grain boundaries (insulating) and hopping polarizations in semiconducting grains by a large number of induced charge carriers. The contributions are outlined in Figure 1.34.

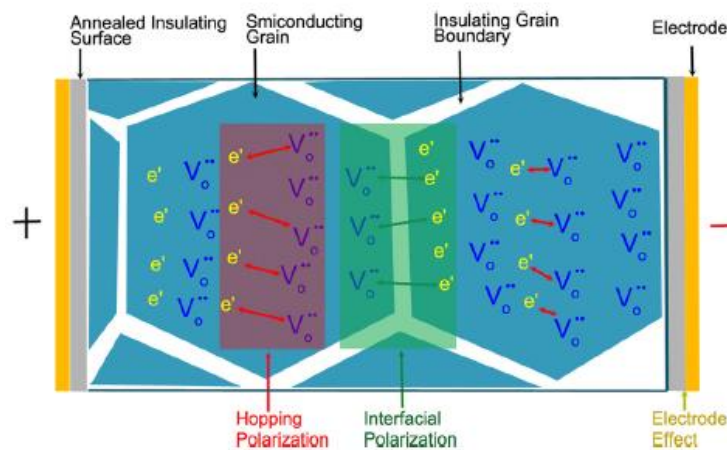


Figure 1.34. Interfacial and hopping polarization model for colossal permittivity of BT ceramics [123].

1.3.3. Effect of strontium substitution

In $BaTiO_3$, substitution can shift the temperature of ferroelectric to paraelectric transition (Curie temperature) to lower or higher values. In some conditions, T_c will be affected by the frequency of the applied field (relaxor behaviour) [101].

An example of A-site substitution is $Ba_{1-x}Sr_xTiO_3$ (BST) where Sr^{2+} substitutes Ba^{2+} . This substitution shifts the temperature region where ferroelectric properties are present while values of permittivity remain relatively large.

The properties of $Ba_{1-x}Sr_xTiO_3$ depend dramatically on the level of substitution. For instance, the Ba-rich BST compounds have tetragonal lattice and are ferroelectric and also piezoelectric, while Sr-rich BST compounds are cubic and paraelectric at room temperature. Figure 1.35 shows the lattice parameter of $Ba_{1-x}Sr_xTiO_3$ compounds as a function of composition at room temperature: BST compounds are tetragonal with c/a ratio greater than 1 when $x < 0.3$ [125].

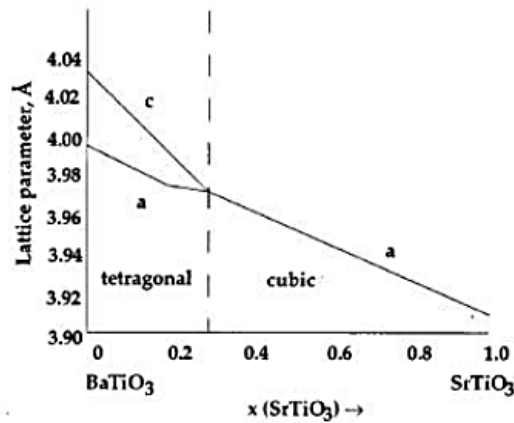


Figure 1.35. Phase diagram lattice parameter of BST as a function of composition [125]

Moreover, substituting barium by strontium results in a decrease of the Curie temperature as illustrated in Figure 1.36. It is well established that T_C of BaTiO_3 decreases linearly with the amount of Sr^{2+} in place of Ba^{2+} . In $\text{Ba}_{1-x}\text{Sr}_x\text{TiO}_3$ ceramics, T_C varies from 120°C to -240°C , depending on composition.

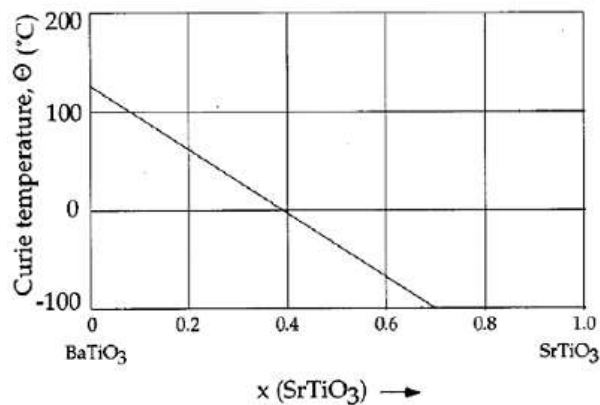


Figure 1.36. Curie temperature of BST as a function of composition [125].

$\text{Ba}_{1-x}\text{Sr}_x\text{TiO}_3$ (BST) is one of the most favourable electronic materials due to its adjustable Curie temperature and high dielectric, pyroelectric properties [126].

Regarding the permittivity of BST ceramics, there is a large dependence of results on the synthesis route, stoichiometry, homogeneity, purity, density, grain size, etc [127], [109], [117].

Hungria et al. [128] sintered BST ceramics with a Sr relative content from 0 to 1 by SPS. They observed a decrease of the permittivity when increasing Sr ratio, and also an extinction of the phase transition peak (Figure 1.37).

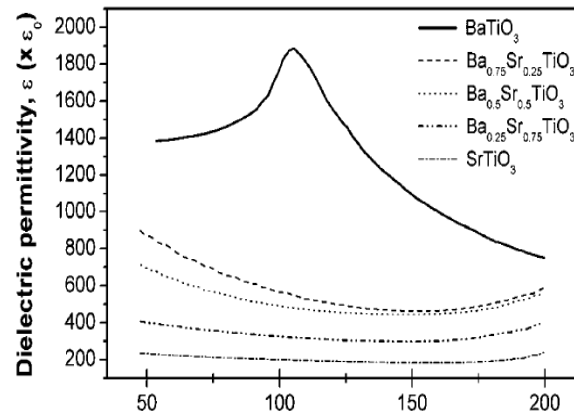


Figure 1.37. Temperature dependence of the permittivity of various BST compositions [128].

Mudinepalli et al. [129] prepared BST ceramics with a Sr ratio of 0.2 by conventional sintering. They observed an increase of the permittivity when increasing the grain size from 86 to 123 nm. They observed in all cases a phase transition peak, but Curie temperature was shifted to lower temperatures, from 80°C to 70°C, when decreasing grain sizes (Figure 1.38).

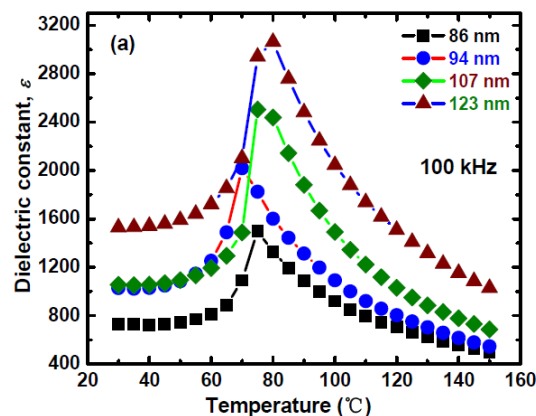


Figure 1.38. Temperature dependence of the permittivity of BST ($x=0.2$) with different grain sizes [129].

Moreover, Dupuis et al. [130] found colossal permittivity in BST ($x = 0$ to 1) associated to the same polarization that appears in the case of pure BaTiO_3 (Figure 1.39). The samples prepared by SPS, presented densities over 98% and grain sizes between 115 and 500 nm. The decrease of the permittivity value as the Sr-content increases was attributed to a decrease of the hopping contribution.

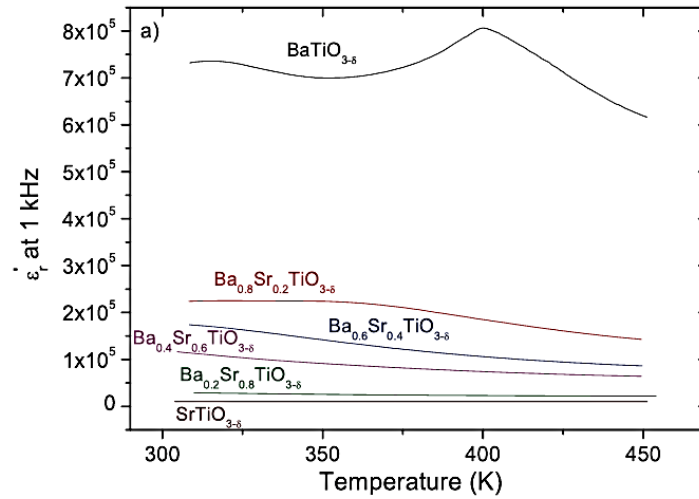


Figure 1.39. Temperature dependence of the permittivity of various BST compositions [130].

All the results show that the dielectric properties of BT and BST are very variable and can be adapted according to the application. However, relative influence of grain size and density remain, in some studies, still unclear.

1.3.4. Transparent BT and BST ceramics

In the literature, only few references are related to transparent/translucent BaTiO_3 or $\text{Ba}_{1-x}\text{Sr}_x\text{TiO}_3$ ceramics. Most researches on BT and BST ceramics are focused on their ferroelectric properties. Nevertheless, many of them have focused on the control of the grain size and the achievement of full density, since even small amounts of residual porosity produce a decrease of permittivity and an increase of dielectric loss [112]. Table 1.6 summarizes some of the works on BST nanometric ceramics.

Table 1.6. Examples of dense titanates (barium and strontium) with nanometric grain size [114].

Material	Grain size	Sintering method
BaTiO ₃	50–1200 nm	SPS
BaTiO ₃	50 nm	SPS
BaTiO ₃	50 nm	SPS
BaTiO ₃	30 nm	SPS
BaTiO ₃	<50 nm	SPS
BaTiO ₃	50 nm	SPS
BaTiO ₃	20–100 nm	SPS
BaTiO ₃	20 nm	SPS
BaTiO ₃	30–100 nm	LTHPS
BaTiO ₃	35 nm	TSS
BaTiO ₃	15–100 nm	SPS
BaTiO ₃	8–100 nm	TSS
BaTiO ₃	8 nm	TSS
BaTiO ₃	15–100 nm	SPS
BaTiO ₃	15 nm	SPS
BaTiO ₃	40–1700 nm	Multi-anvil pseudo-isostatic hot pressing (8 GPa)
BaTiO ₃	60 nm	High pressure sintering (5 GPa)
BaTiO ₃	35 nm	HIP
BaTiO ₃	30 nm	Three step high pressure assisted sintering
BaTiO ₃	30 nm	Three step high pressure assisted sintering
BaTiO ₃	30 nm	Pressure assisted sintering
BaTiO ₃	30 nm	High pressure assisted sintering
SrTiO ₃	50 nm	SPS

Acronyms: SPS (spark plasma sintering); LTHPS (low temperature|high pressure sintering); TSS (two step sintering); HIP (hot isostatic pressing).

The first publications considering some degree of transparency on BT appeared in 1985. Yamamura et al. [131] prepared BaTiO₃ samples by Hot-Pressing in flowing oxygen with a density up to 99%. The maximum obtained transmittance was 28% at 870 nm wavelength for a 1.07 mm- thick sample (Figure 1.40), but no pictures of the samples were shown. They observed that translucency appeared in specimens with relative density above 97% and small grain size below 1 μm .

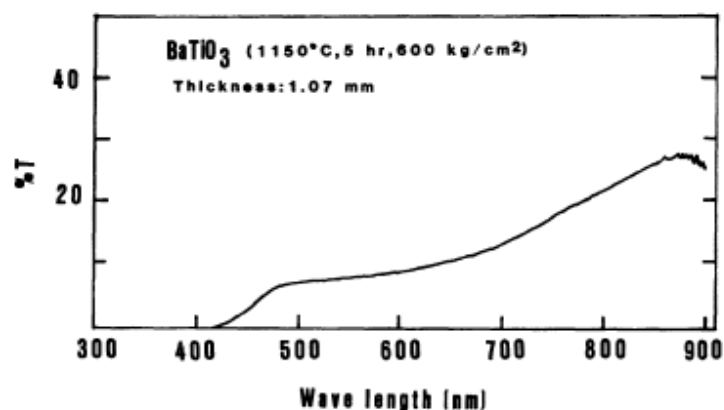


Figure 1.40. Transmittance as a function of wavelength for hot-pressed BT [131].

No more publications concerning translucent BT appeared until the 2000s. Shimooka et al. [132] produced translucent BaTiO₃ by sol-gel and conventional sintering at 1100°C in oxygen (Figure 1.41). They observed that the pore size inside their samples was lower than 10 nm. The sample presented

an amber colour may be due to the light absorption edge of BT located around 3.0 - 3.2 eV. Surprisingly, these authors reported a relative density of 85%, making these results questionable.

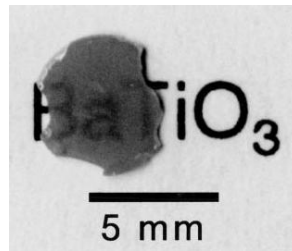


Figure 1.41. Appearance of a translucent BT ceramic: thickness = 0.34mm [132].

Recently, two publications [40], [133] have shown encouraging results of translucent ceramics, and both used SPS as sintering technique.

Liu et al. [40] prepared translucent BaTiO_3 and SrTiO_3 by SPS (Figure 1.42). They used commercial powders as starting powders and apply quite high pressure, 200 MPa. The heating cycle was a heating rate of $100^\circ\text{C}/\text{min}$ up to 900°C in the case of BT and up to 950°C in the case of ST. Dwell time was 3 minutes in both cases. The optical transmission of the samples (0.85 mm of thickness) was 40% for BT and 20% for ST at 1000 nm wavelength.

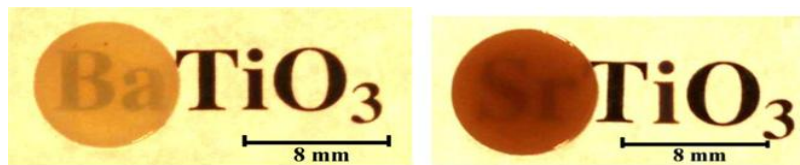


Figure 1.42. Appearance of BT and ST translucent samples [40].

Wu et al. [133] prepared $\text{Ba}_{1-x}\text{Sr}_x\text{TiO}_3$ powders with $x=0.6$ and 0.7 by solid state reaction and sintered them by SPS. SPS conditions were 50 MPa pressure, a heating rate of $100^\circ\text{C}/\text{min}$ up to 900°C , $40^\circ\text{C}/\text{min}$ up to 980°C and $20^\circ\text{C}/\text{min}$ up to 1000°C and a dwell of 5 minutes. The optical transmission of these samples (0.3 mm of thickness) was 74% at 633 nm (Figure 1.43).



Figure 1.43. Appearance of BST translucent samples [133].

1.4. Conclusions

This state of the art highlights the major importance of avoiding scattering phenomena to obtain a ceramic material with high transparency level. Above all, the presence of residual porosity, even in a small amount, is detrimental to the optical transmission. Powders characteristics (high purity, low agglomeration degree) are also essential. Moreover, despite its numerous benefits, Spark Plasma Sintering can cause a darkening of the samples, attributed to the presence of oxygen vacancies and/or graphite contamination. Some treatments (mostly LiF addition and annealing in air) are cited

in the literature to avoid (or limit) this darkening. However, the relative influence of powders characteristics and sintering conditions in the loss of optical transmission remains sometimes unclear.

YAG is a widely investigated transparent material and several works have already treated the achieving of transparency on it. In contrast, BaTiO₃ has been scarcely studied as a transparent material and less insight into its obtaining exists.

Chapter II – Experimental procedures and finite element modelling

Table of contents

2.1. Powder conditioning.....	57
2.1.1. Dispersion	57
2.1.2. Solvent removal.....	57
2.2. Sintering and post-treatments	57
2.2.1. Spark Plasma Sintering.....	57
2.2.2. Hot Isostatic Pressing	58
2.3. Physico-chemical characterizations	59
2.3.1. Granulometric measurements.....	59
2.3.2. X-Ray Diffraction	59
2.3.3. Specific surface area.....	60
2.3.4. Trace-level elemental analysis.....	60
2.3.5. Raman spectroscopy	60
2.3.6. TGA/DTA	60
2.3.7. Archimedes’s method	60
2.3.8. Permittivity measurements	61
2.4. Microstructural characterisation.....	62
2.5. Optical characterisations	62
2.6. Finite Element Modelling to simulate temperature distributions in SPS.....	64

In this chapter, the experimental procedures used in this thesis are described. These procedures are focused on the fabrication and characterisations of transparent ceramics.

If no other notice, the measurements were performed at the BCRC, in Mons.

2.1. Powder conditioning

2.1.1. Dispersion

Ultrasonic dispersion of the powders was performed in water with a 19 mm diameter ultrasonic probe Sonics Vibra-cell (750W). The parameters were: amplitude, $A= 80\%$ and, pulse of 30 seconds on/ 30 seconds off. In order to avoid the slurry heating this pulse was chosen and the container was surrounded with ice.

Dispersions in non-aqueous suspensions were performed in a Turbula type T2F. For this dispersion method, powders were mixed in a solvent and zirconia balls of 2 mm were added. The ratio balls/suspension was equivalent in volume.

2.1.2. Solvent removal

In order to remove solvents after dispersion two methods were used: freeze-drying and rotavapor.

Before lyophilisation, dispersed suspensions (performed using water as solvent) were frozen in liquid nitrogen (-40°C). Then, they were placed in a freeze-dryer (HETO, FD8-55) for 24 hours at 0.1 mbar to recover dry powders.

Freeze drying limits the use of solvent to water. Other solvents as ethanol or isopropanol need lower temperatures and there were incompatible with our freeze drying equipment, so in this case, solvents were removed in a rotavapor at 70°C .

After drying, powders were placed in a furnace at 110°C overnight.

2.2. Sintering and post-treatments

2.2.1. Spark Plasma Sintering

The sintering technique used in this thesis is Spark Plasma Sintering (SPS). We used a model HPD10 from FCT (Germany). A scheme of SPS is presented in Figure 2.1. Powder is placed between two graphite punches and inside a 20-mm diameter graphite die (R7710 grade from SGL society). Mass powder was calculated to obtain final samples with around 3 mm thickness.

In order to assure a good physical, electrical and thermal contact, a graphite foil (0.35mm-thickness) was placed between the sample and the die and the punches.

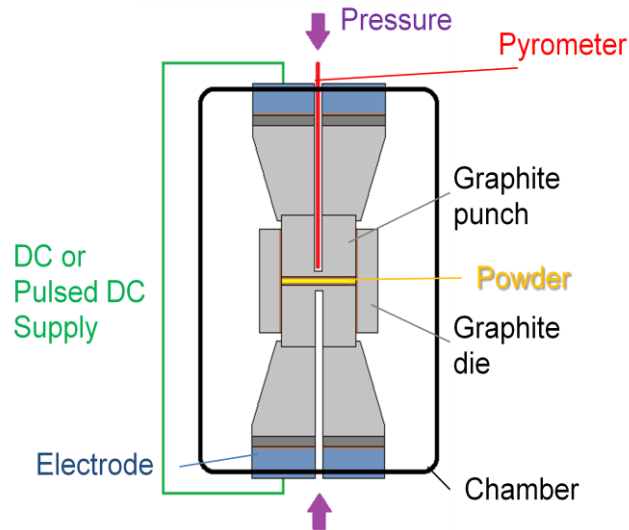


Figure 2.1. SPS design.

Then, to prevent heat losses and to minimise temperature gradient from the centre to the perimeter of the sample the graphite die is surrounded by a thermally isolating graphite felt.

A CFC (Carbon Fibres Composite) disc is placed between the truncated cone-shaped piece and the electrode: its role is to increase the electrical resistivity and to diminish the appearance of cracks inside the sintered sample.

The SPS chamber is under low vacuum (10 Pa). The two cylindrical pistons are drilled, and the temperature of the sample is measured, above 450°C, through an axial pyrometer passing in the top hole of the matrix. Below 450°C, the temperature is controlled by the power provided by the equipment. All the essays were made under direct current (DC).

To easily compare the different assays, recorded shrinkage data were transformed into relative density evolution, taking into account the initial and final densities, initial and final distances between punches and the theoretical density of each ceramic material. Thermal expansion of the system (sample and graphite tooling) was obtained by applying the same sintering cycle on the already-sintered sample and subtracted to the shrinkage data.

On the different curves representing sintering versus time, 0 second corresponds to the time when pyrometer temperature reaches 500°C.

The cooling rate was fixed to 150°C/min with an applied pressure of 50 MPa in YAG samples. However LiF doped- YAG samples and BT and BST samples are more brittle, and they cracked during cooling due to stresses during thermal contraction. In order to prevent the fracture of these samples, at the end of the dwell the pressure was released completely and the electric current was switched off.

2.2.2. Hot Isostatic Pressing

For completing samples densification, some pre-sintered samples underwent a hot isostatic pressing (HIP) cycle. Experiments were performed in a GPS VITEK HIP equipped with a platinum furnace,

under Ar/O₂ atmosphere (80/20 vol.%). The cycle was a heating rate of 5°C/min up to final temperature and isostatic pressure of 120 MPa for 1 h.

2.3. Physico-chemical characterizations

2.3.1. Granulometric measurements

Agglomerates/particle size distribution between 0.01 and 2000 μm was acquired with a laser particle size analyzer (Malvern Mastersizer 2000, UK), using water as standard dispersion medium. Some measurements were performed in a different solvent as isopropanol for barium titanate dispersions.

Granulometric curves presented in this manuscript correspond to the average of at least three measurements. Refractive indexes of YAG and BST were taken into account to calculate respective particle sizes.

2.3.2. X-Ray Diffraction

Phase compositions were identified by X-ray diffraction (Miniflex 600 Rigaku) operating with Cu Kα radiation (1.541874 Å). Diffractograms were recorded in a scan range of 2θ from 10 to 90 degrees with a step increment of 0.02°.

X-Ray Diffraction technique uses the Bragg's law:

$$2d \sin(\vartheta) = n\lambda \quad \text{Equation 2.1}$$

where d is the spacing between diffracting planes, ϑ is the incident angle, λ is the radiation wavelength and n is an integer. The constructive or destructive interference between waves reflected by diffraction planes will lead to an interference (diffraction) pattern.

The diffraction pattern depends from the crystalline phase and from the material analysed. It is thus possible to associate each pattern to a well-defined material. A semi-quantitative phase analysis was performed taking into account the relative peaks intensities, using the reference intensity ratio (RIR) method.

In the case of the Al₂O₃-Y₂O₃ system, the different patterns used in the characterisation are collected in table 2.1.

Table 2.1. PDF cards used for the Al₂O₃-Y₂O₃ system.

Phase	PDF Card
YAG	33-0040
YAP	33-0041
YAM	34-0368
Y ₂ O ₃	41-1105
θ-Al ₂ O ₃	23-1009
h-YAlO ₃	74-1334

In the case of BaO-SrO-TiO₂ system, the PDF Cards used in the XRD analysis are collected in table 2.2.

Table 2.2. PDF cards used for the BaO-SrO-TiO₂ system.

Phase	PDF Card
BaCO ₃	41-0373
BaTiO ₃ (C)	79-2263
	79-2265
BaTiO ₃ (T)	75-1169
Ba _{0.8} Sr _{0.2} TiO ₃ (C)	15-2711
Ba _{0.8} Sr _{0.2} TiO ₃ (T)	06-0820

2.3.3. Specific surface area

Specific surface area of powders was analysed using the BET (Brunauer-Emmett-Teller) method with a Micromeritics FlowSorb III 2310 at 77K with N₂ as adsorbate gaz. Degassing in vacuum at 150°C was performed prior to measurement and each measurement was repeated 3 times.

2.3.4. Trace-level elemental analysis

Trace-level elemental analysis was performed using inductively coupled plasma optical emission spectrometry (ICP-OES VARIAN 720-ES).

2.3.5. Raman spectroscopy

Phase analysis and Curie temperature for Ba_xSr_{1-x}TiO₃ were also evaluated by Raman spectroscopy. Raman spectra measurements (400–2000 cm⁻¹) were carried out, in Materia Nova (Mons, Belgium), using a Bruker Senterra spectrometer equipped with a CCD detector and a He-Ne laser (532 nm) at 10 mW.

2.3.6. TGA/DTA

Simultaneous TGA-DTA, Thermogravimetric (TG) and Differential Thermal Analysis (DTA) were performed in a Netzsch STA 409C, on powdered samples of about 150 mg, up to 1300°C in static air, with a heating rate of 5°C/min. (These measurements were performed at Politecnico di Torino, Italy).

These measurements record mass variations (TG) and thermal variations (DTA) while heating compared to an inert material (in our case an empty crucible). This allows determining at which temperatures volatile species leave the analysed material or phase transformations take place.

2.3.7. Archimedes's method

Densities of all samples were measured by the water immersion method. Theoretical densities of YAG, BaTiO₃ and Ba_{0.8}Sr_{0.2}TiO₃ were 4.55 g cm⁻³, 6.02 g cm⁻³ and 5.84 g cm⁻³, respectively, and used to evaluate the densification ratio.

The uncertainty of measured density was estimated to ± 0.2% in our samples.

When the sample is too dense, the measurement is also somewhat approximate, because the difference between the weights in air and in water is small, and the relative error increases. Larger samples, whose weight is higher, can partially reduce this problem.

Archimede's formula is:

$$\rho_{app} = \frac{m_{air}}{(m_{air} - m_{water})} \rho_{water} \quad \text{Equation 2. 2}$$

where ρ_{app} is the sample density, m_{air} the sample mass in air, m_{water} the sample mass in water and ρ_{water} is the density of water at the temperature of the measurement.

This method is not appropriate for measuring highly porous samples, because it overestimates the density of specimens presenting open porosity. Indeed, during the immersion in deionised water, the liquid penetrates into the sample and leads to an increased weight.

Hence, a measurement of the wet sample (m_{wet}) was performed, and the open porosity (OP) and corrected density (ρ_c) were estimated using the following equations:

$$OP = \frac{(m_{air} - m_{wet})}{(m_{wet} - m_{water})} \quad \text{Equation 2. 3}$$

and

$$\rho_c = \frac{m_{air}}{(m_{air} - m_{wet})} \rho_{water} \quad \text{Equation 2. 4}$$

2.3.8. Permittivity measurements

Permittivity measurements were performed with a HP4284A LCR meter, in the “Laboratoire des Matériaux Céramiques et Procédés Associés (LMPCA, Maubeuge, France). The frequency range analysed was from 200 Hz to 100 kHz. AC Level was 1V and DC Bias was 0V.

In order to make the electrodes, silver paste was applied on the surfaces of the samples. The system used to characterise the capacitor was the parallel plate method (Figure 2.2).

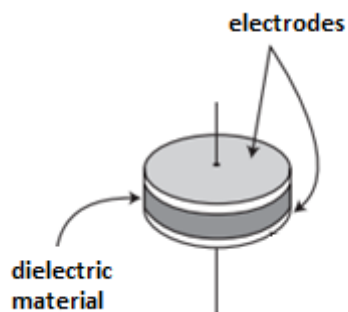


Figure 2.2. Parallel plate capacitor

Permittivity describes the interaction between a material and an electric field, i.e. the polarisation of the material.

The capacitance and dielectric loss of the samples were measured and transformed to permittivity value taking into account the thickness and surface of the samples using equation 2.5:

$$\epsilon_r = \frac{d \cdot C}{\epsilon_0 \cdot S} \quad \text{Equation 2. 5}$$

with ϵ_r material permittivity, C measured capacitance (F), ϵ_0 vacuum permittivity ($8.8419 \cdot 10^{-12}$ F/m), d, sample thickness (m) and S, electrode surface (m^2).

Capacitance (C) characterizes a capacitor and describes the charge quantity that can be accumulated on the surface of the dielectric material. This charge quantity is proportional to the voltage applied to the electrodes:

$$Q = C \cdot V \quad \text{Equation 2. 6}$$

where Q is the accumulated charge (C) and V is the voltage (V).

Furthermore, an effective capacitor must present low dielectric losses. Dielectric loss is obtained by the tangent delta or dissipation factor and represents the ratio between the imaginary part (ϵ'') and the real part (ϵ') of the permittivity (Equation 2.7), therefore the ratio between the dissipated power and the accumulated power at a specific frequency.

$$\text{Tan delta} = \frac{\epsilon''}{\epsilon'} \quad \text{Equation 2. 7}$$

2.4. Microstructural characterisation

For microstructure evaluation, YAG sintered samples were mirror-polished with a diamond paste down to 1 μm and then thermally etched in air at 100°C below the sintering temperature. Microstructural observations of BaTiO₃ and BaSrTiO₃ samples were generally performed on fracture surfaces. Before analysis, a fine gold coating was applied on the surfaces by sputtering. Powders and microstructures were observed with a field-emission scanning electron microscope (JEOL 7500F) equipped with JED 2300 Microanalysis system for elemental analysis (at Namur University).

Grain size of the samples was measured using the linear intercept method (ASTM E112-23 standard). A minimum of 150 grains in several parts of the samples in the SEM images were analysed. In the case of fracture surfaces this method gives only an approximate value.

2.5. Optical characterisation

The optical transmittance spectrum of the samples was measured within the wavelength region of 400-1500 nm using a double-beam spectrophotometer UV-visible (Perkin-Elmer Lambda 750S) at Namur University, and the results were extrapolated, following the Beer-Lambert law, to a thickness of 1 mm using the following equation [65]:

$$T = T_{max} \cdot \left(\frac{T_s}{T_{max}} \right)^{(d/d_s)} \quad \text{Equation 2. 8}$$

where T is the transmission at 1mm thickness, T_{max} the maximum transmission for a perfect material, (see Figure 2.3), T_s is the measured transmission of the sample, d and d_s are 1-mm normalized thickness and the sample thickness, respectively.

The maximum transmission of YAG is quite constant due to its refractive index that is almost constant in the wavelength region under study. BT and BST refractive indexes vary more with the wavelength (from 66 to 72% in the visible range) and in order to correct the thickness, the maximal transmission at each wavelength was considered.

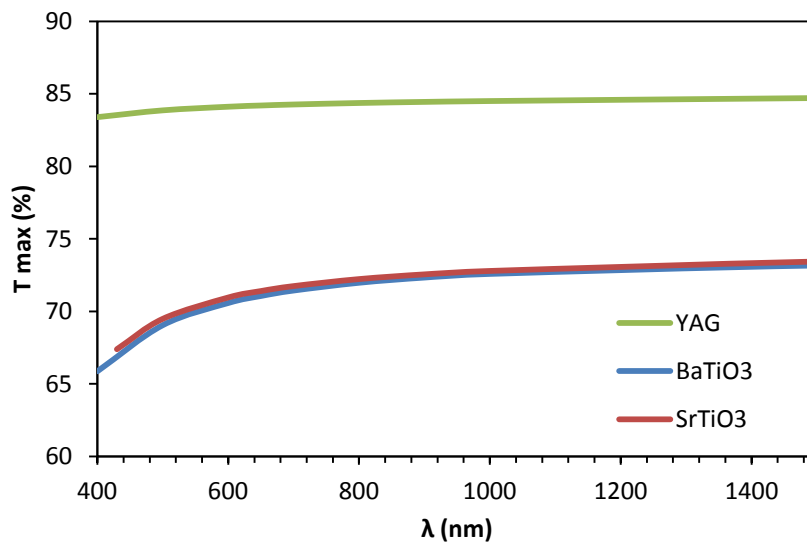


Figure 2.3. Maximal theoretical transmission of YAG and BST ceramics.

This spectrophotometer allows measuring both real in-line transmission (RIT) and total-forward-transmission (TFT). For TFT measurements, the sample is placed close to the detector, which collects all the light going out the sample, so both in-line transmitted and forward scattered light. On the contrary, for RIT measurements, the sample is situated ~ 1 m far from the detector, which collects only the light transmitted in a very narrow solid angle, excluding the scattered light [2].

Setups for both transmission measurements are illustrated in Figure 2.4.

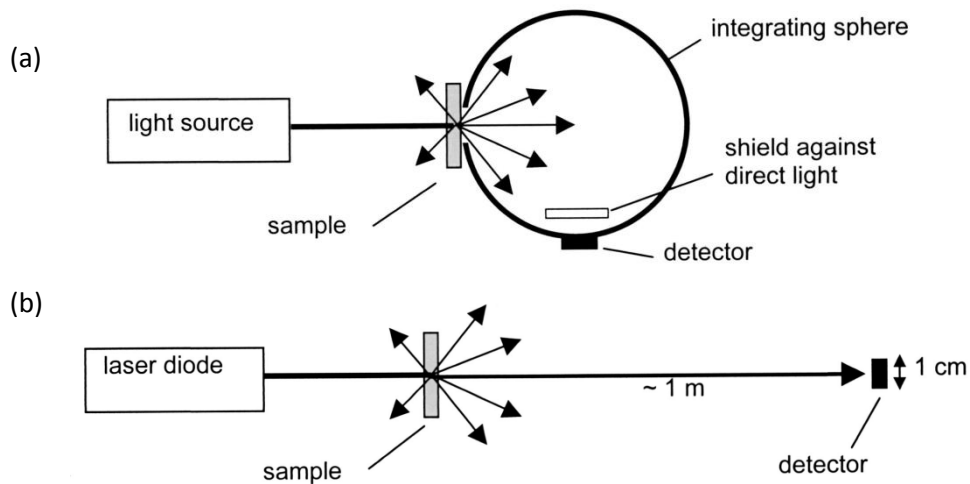


Figure 2.4. Measurement setup for (a) total forward transmission (TFT) and (b) real in-line transmission (RIT) [2].

Absorption measurements were also performed on the samples as a function of the wavelength. This spectrophotometer allows also this measurement by locating the sample inside the integrating sphere, slightly tilted (-8°) to avoid the reflection losses to be considered as absorption.

Backward scattering and reflection were not measured and considered as transmission losses.

2.6. Finite Element Modelling to simulate temperature distribution in SPS

For the purpose of estimating the temperature gradient within the compact at the end of the dwell period, BCRC has developed a simple coupled 2D axisymmetric electro-thermal model implemented in the Comsol Multiphysics code. The model incorporates a numerical PID temperature controller so that the whole system totally mimics the working of the SPS equipment. The temperature profile of the thermal cycle is thus used as entry parameter, and the current density injected at the upper electrode is adapted accordingly. The used thermal boundary conditions take into account the "unbalanced" thermal exchange with the cooling system at the top and bottom electrodes; the presence of the insulating felt around the die is modelled by adjusting locally the emissivity of the graphite. Temperature dependent characteristics for the various components of the tool system (copper, graphite, CFC spacer ...) have been used. For the YAG compact, following data were considered:

Table 2.3. Physical properties of YAG (300K) [71].

Density (g/cm^3)	4.55
Molar mass (g/mol)	593.7
Specific heat capacity, C_p ($\text{J/kg}\cdot\text{K}$)	590

Table 2.4. Thermal and electrical conductivity of YAG [134], [51].

T (°C)	Thermal conductivity, k (W/K m)	Electrical conductivity, σ (Ω cm) ⁻¹
20	10.5	-
200	6.7	-
400	-	$1 \cdot 10^{-10}$
500	-	$1 \cdot 10^{-9}$
600	4.6	$1 \cdot 10^{-7}$
1000	3.2	$1 \cdot 10^{-3}$

To obtain the thermal and electrical conductivity values at higher temperatures, two procedures were followed: one, considering the values at 1000°C constant and a second one, making extrapolations to the desired temperatures. The results obtained by the two methods lead to similar temperature distributions.

The steady state temperature gradients reached after 15 minutes holding during the dwell temperature were calculated for a 3 mm thick YAG compact, with constant density and 20 mm diameter.

The dimensions of the graphite tooling considered are the ones used experimentally.

A scheme of the ensemble appears on Figure 2.5.

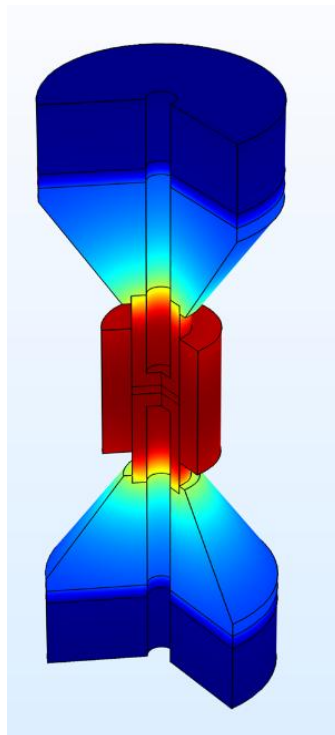


Figure 2.5. Representation of the SPS ensemble (tooling + sample) used for FEM modelling

Chapter III – Yttrium Aluminium Garnet

Table of contents

3.1. YAG-S	69
3.1.1. Powder synthesis and characteristics	69
3.1.1.1. Precipitant concentration influence	70
3.1.1.2. Characterisations of the synthesized powder	73
3.1.2. Sintering and transparency improvement.	74
3.1.2.1. Sintering behaviour.	74
3.1.2.2. Influence of SPS parameters on density, microstructure and visual aspect of the samples	75
3.1.2.3. Influence of pre- and post-treatments on the optical transmission.....	80
3.1.3. Conclusions on YAG-S powder	84
3.2. YAG-B.....	85
3.2.1. Powder characteristics	85
3.2.2. Sintering and transparency improvement	87
3.2.2.1. Sintering behaviour	87
3.2.2.2. Influence of SPS parameters on density, microstructure and visual aspect of the samples	87
3.2.2.3. Influence of pre- and post-treatments on the optical transmission.....	91
3.2.3. Conclusions on YAG-B powder.....	98
3.3. YAG-N	98
3.3.1. Powder characteristics.....	99
3.3.2. Sintering and transparency improvement	100
3.3.2.1. Sintering behaviour	100
3.3.2.2. Influence of SPS parameters on density, microstructure and visual aspect of the samples	101
3.3.2.3. Influence of pre- and post-treatments on the optical transmission.....	105
3.3.3. Conclusions on YAG-N powder	109
3.4. Conclusions.	109

Literature data on transparent ceramics show that final transparency of a spark plasma sintered compact depends on different factors: some depend on the powder (mainly purity and agglomeration degree) and some are linked to the sintering conditions (oxygen/vacancies, graphite contamination ...). However, the relative influence of these factors remains sometimes unclear. Moreover, transparency is conditioned to the absence of porosity and so the sintering cycle has to be carefully optimised.

In this chapter, three YAG powders, with different physicochemical properties, are studied for comparison: one powder synthesized under laboratory conditions by co-precipitation (YAG-S) and two different commercially available powders (YAG-B and YAG-N). The study of different YAG powders allows the analysis of the powder characteristics influence in the obtaining of transparent compacts, using the same SPS equipment and graphite tooling.

For each powder, the influence of SPS parameters on densification and microstructure of the sintered samples is discussed and related to the physicochemical properties of the powder. According to the results, different pre-treatments of the powder and/or post-treatments of the sintered ceramics are evaluated. Finally, the optical properties of the sintered compacts prepared from each powder are measured and compared. In order to characterise better the optical transmission of the samples, two different optical measurements are performed: real in-line transmission and total forward transmission. These measurements allow distinguishing between the scattered light and the transmitted light without deviations.

3.1. YAG-S

Powders suitable for transparent ceramics are not easily available. When available they are expensive and frequently only available in small quantities. Moreover, YAG synthesis has been broadly studied and in this section a co-precipitation synthesis has been carried out.

3.1.1. Powder synthesis and characteristics

During this thesis work, YAG was synthesized by reverse-strike co-precipitation. This powder will be called YAG-S thereafter. The route followed was based on the Ph.D. thesis of Giulia Spina at the Politecnico di Torino (Italy) [70].

The reverse strike method consists in the addition of the salts solution into the precipitant solution. For this synthesis, the salts solution was an aqueous solution of chlorides of yttrium and aluminium. Chlorides are widely used in the reverse strike precipitation of YAG and several works have obtained pure YAG powders with the use of these salts [70], [57]. Furthermore, they were preferred from nitrates, due to the highest temperature needed to crystallize YAG and the detrimental effect of remaining nitrates impurities on the transparency [15]. $YCl_3 \cdot 6H_2O$ and $AlCl_3 \cdot 6H_2O$ powders were used because they are more stable than non-hydrated products [70]. Ammonium hydrogen carbonate (AHC) was used as precipitant; this reagent has been found to be a good choice for the synthesis of stoichiometric and low agglomerated YAG powders [75], [79], [91]. The technical data of the reactants can be found in appendix A. Both the chlorides and the AHC solution were separately aged

overnight under magnetic stirring and then the salt solution was dripped into the AHC one at a speed of 3 ml/min. Once the dripping was finished, the obtained suspension remained under magnetic stirring overnight in order to age the precipitated YAG precursor. Then the slurries of the YAG precursor were washed 5 times in deionised water and twice in pure ethanol. The washings were carried out by centrifuging the suspensions at 3800 rpm for 30 minutes. The supernatant was removed and the precipitate was redispersed in new water or ethanol according to the washing step.

The last slurry dispersed in ethanol was then placed into an oven at 70°C during 24h to evaporate the remaining solvent and to obtain a dry, easily crushed YAG precursor. This precursor was crushed within an agate mortar and calcined to promote the decomposition of the carbonates and to obtain pure YAG.

Two molarities of AHC were used (0.5M and 1M) in order to evaluate the influence of the precipitant concentration on the purity of the produced powder. Table 3.1 shows the quantities of reagents used during the synthesis.

Table 3.1. Quantities of reagents used in YAG synthesis (for 25 g of YAG).

	Reagent (g)	Deionized water (g)	Molarity (M)
YCl₃.6H₂O	38.33	1000	0.2*3/5
AlCl₃.6H₂O	50.84	0	0.2
AHC	118	3000	0.5
AHC	236	3000	1

3.1.1.1. Precipitant concentration influence

After this type of coprecipitation, the mechanism to form the precursor is the competition between hydroxide and carbonate anions, combining with metal cations, and usually the co-precipitated precursor is identified as $(\text{NH}_4)\text{Al Y}_{0.6}(\text{OH})_2(\text{CO}_3)_{1.9} \cdot n\text{H}_2\text{O}$ [91].

The evolution of the YAG precursor with the temperature (in air atmosphere) was studied by XRD for the two concentrations of precipitant.

For AHC 0.5M, the evolution is presented in Figure 3.3: diffractograms were obtained after thermal treatments, firstly during 1 hour at 500°C to remove the carbonates and then during 30 minutes at the final temperature (heating and cooling rates were 5°C/min). At temperatures below 800°C, an amorphous phase is observed. Then, between 800 and 1000°C, crystallization of YAG happened. For temperatures higher than 1000°C, this YAG phase was stable and no other phases were detected with increasing temperature up to 1350°C. The presence of pure YAG in the final powder implies a high homogeneity of the distribution of Y and Al cations in the as-synthesised product.

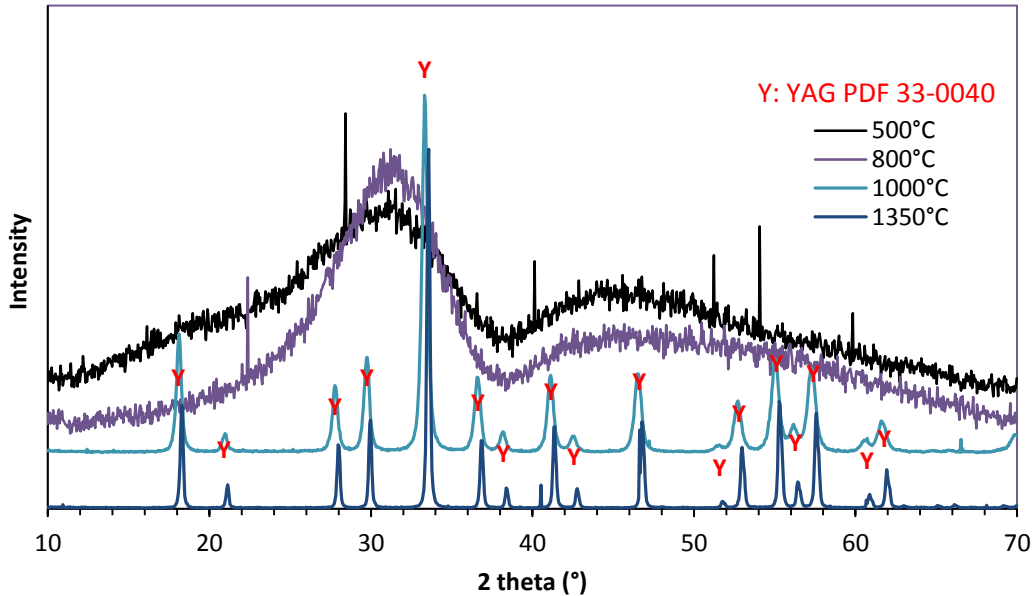


Figure 3.1. XRD evolution with temperature of YAG precursor from co-precipitation in AHC 0.5M.

In contrast, when AHC 1M was employed, after drying at 70°C, the precursor resulted in a mixture of already crystalline species, with mainly carbonates and hydrated hydroxides species among the numerous peaks. After thermal treatment (see Table 3.2), this powder followed a different phase development and at 600°C the powder presented a large quantity of YAP and YAM, as intermediate species. Even at 1350°C, Al_2O_3 , Y_2O_3 and YAM were still present (Table 3.2 and Figure 3.4). However, other publications [91] obtained pure YAG with higher concentrations of precipitant. Some other authors have already found a similar influence of the precipitant: for example, Wang et al. [95], ascribed the formation of stable secondary phases with the use of a higher precipitant concentration. Under higher precipitant concentration conditions, yttria particles are flake-shaped and of micron size, while with a lower precipitant concentration, yttria particles are spherical and smaller than 100 nm. The oversized yttria particles result in a decrease of the homogeneity at low temperature, therefore temperature for YAG formation is elevated, above 1350°C.

Table 3.2. Phases present in YAG precursor powders from co-precipitation in AHC 1M after thermal treatment at 600°C, 1000°C and 1350°C.

Compound	Composition (semi-quantitative) %		
	600°C	1000°C	1350°C
YAG ($\text{Y}_3\text{Al}_5\text{O}_{12}$)	0	64	82
Y_2O_3	50	21	4
YAM ($\text{Y}_4\text{Al}_2\text{O}_9$)	24	15	9
YAP (YAlO_3)	20	0	0
$\Theta\text{-Al}_2\text{O}_3$	0	0	5

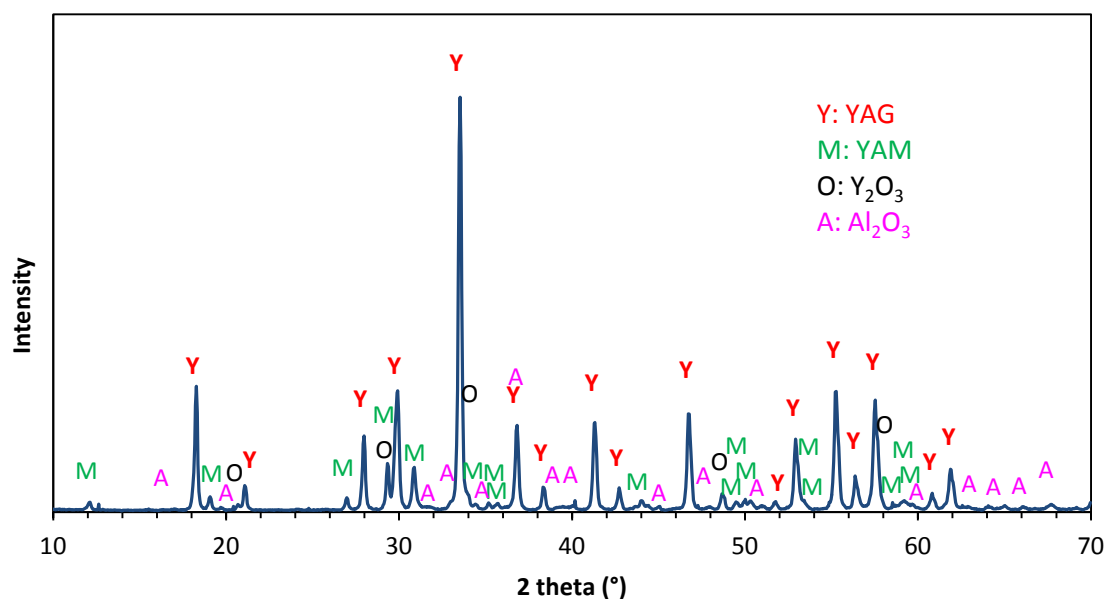


Figure 3.2. XRD of synthesized YAG from co-precipitation in AHC 1M treated at 1350°C for 30 minutes.

Thermogravimetric and Differential Thermal Analyses (TG-DTA) were performed on the precursors obtained from the two precipitant concentrations after drying at 70°C (Figure 3.1 and 3.2) using a heating rate of 5°C/min from room temperature up to 1250°C. Figure 3.1 describes the thermal behaviour of the precursor obtained with a precipitant concentration of 0.5M.

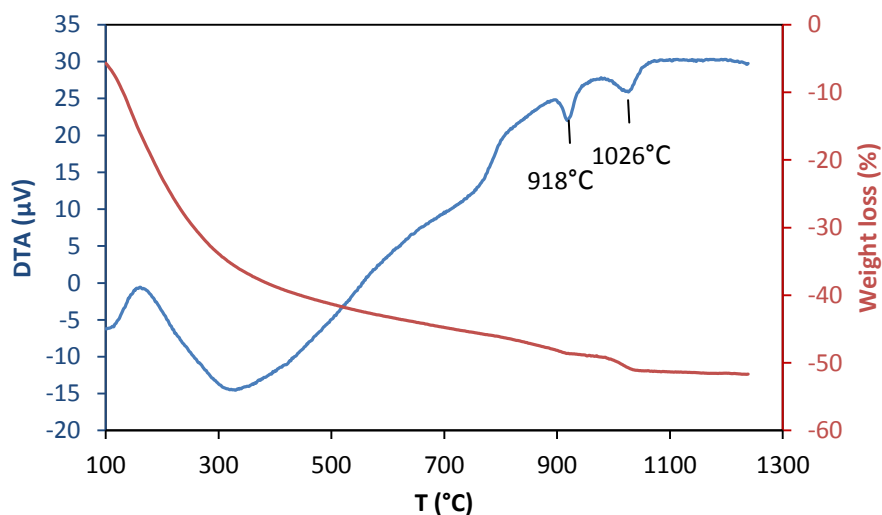


Figure 3.3. TG-DTA of YAG precursor from co-precipitation in AHC 0.5M.

YAG precursor undergoes a total weight loss about 50%. Larger mass loss (75% of the total mass loss) occurs below 400°C and it is assigned to dehydration and decomposition of the by-products. Then, between 900°C and 1050°C two exothermic peaks appear: these two peaks have been previously ascribed to the crystallisation of the intermediate hexagonal-YAlO₃ and then to its conversion to YAG, respectively [96].

Figure 3.2 shows the TG-DTA curves of the as-dried YAG precursor from co-precipitation in AHC 1M. In this case, a higher total weight loss (around 60%) is observed, certainly due to the higher amount of carbonates. Two exothermic peaks are also present in the high temperature DTA range, but less pronounced and presenting different onset temperatures than previously. This difference is attributed to the presence of different intermediate species; the first peak is attributed to the partial reaction of the different species to form YAP, the second peak to the transformation of YAP into YAG.

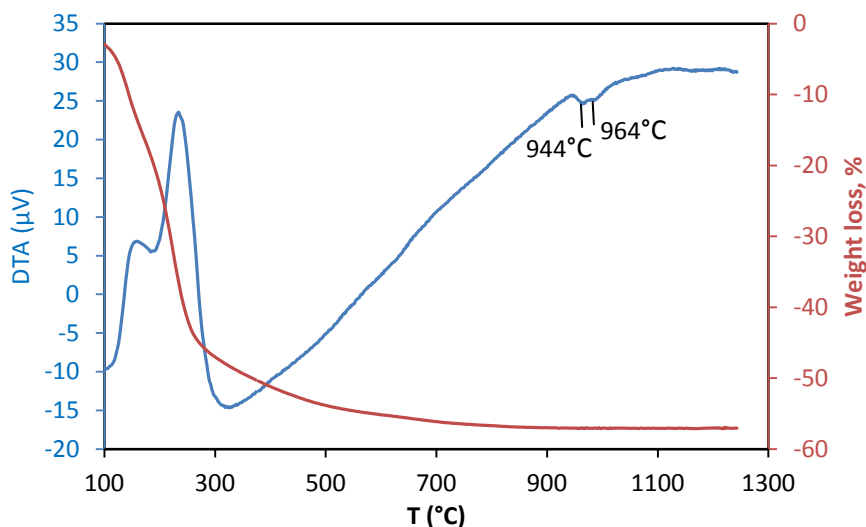


Figure 3.4. TG-DTA of YAG precursor from co-precipitation in AHC 1M.

According to these results, the study was pursued with YAG powders synthesized in 0.5M AHC, higher precipitant concentration leading to the presence of secondary phases, like YAP and YAM. Calcination temperature was fixed to 1000°C, the lowest temperature that allowed pure YAG phase, in order to retain a small particle size and the reactivity of the powder.

3.1.1.2. Characterisation of the synthesized powder

After thermal treatment at 1000°C to obtain pure YAG phase, YAG-S powder was observed by SEM, (Figure 3.5). This powder seems agglomerated, but its primary particles are spherical, with a diameter around 50 nm.

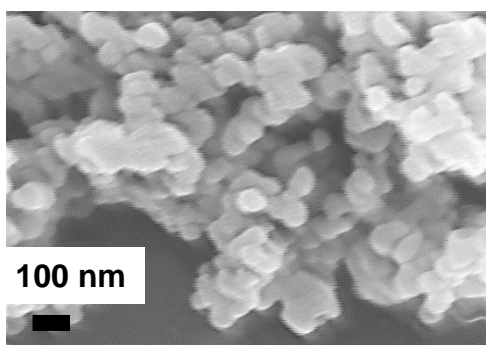


Figure 3.5. SEM images of the synthesized YAG powder calcined at 1000°C.

A specific surface area of 46.5 m²/g was measured using the Brunauer-Emmett-Teller method (BET).

The primary particle size of 28 nm calculated from Equation 3.1 is in fairly good agreement with SEM observations.

$$\phi_{BET} = \frac{6 \times 10^3}{\rho \times S_{BET}} \quad \text{Equation 3.1}$$

where ρ is YAG density, 4.55 g/cm³, ϕ_{BET} is the particle diameter and S_{BET} is the specific surface area.

The particle size distribution of the powder was analysed by laser granulometry. Figure 3.6 shows that, despite a small primary particle size, YAG-S is composed of agglomerates with a broad size distribution. The mean size of the agglomerates is around 180 μm .

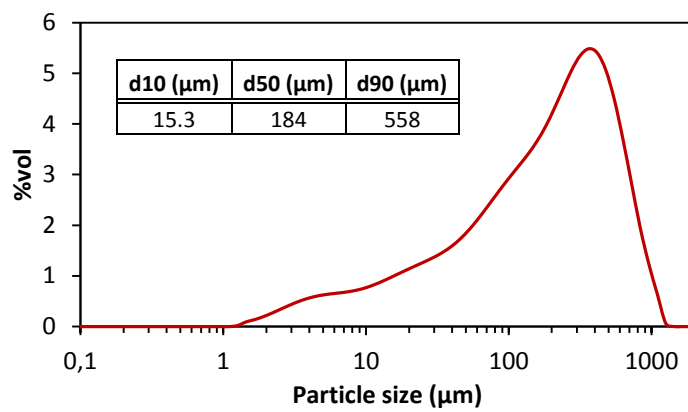


Figure 3.6. Frequency distribution (vol %) versus particle size of synthesized YAG powder.

An analysis of the impurities in the YAG-S powder was done by ICP (Inductively Coupled Plasma) and detected impurities (Cl, Si, Ca, Mg) were below 10 ppm.

3.1.2. Sintering and transparency improvement

3.1.2.1. Sintering behaviour

The sintering behaviour of YAG-S powder was evaluated by following the shrinkage of a powder compact sintered in the SPS equipment at a heating rate of 20°C/min from 500 to 1650°C under a pressure of 50 MPa, the latter applied during the whole sintering cycle. The resulting calculated evolution of the relative density is reported in Figure 3.7.

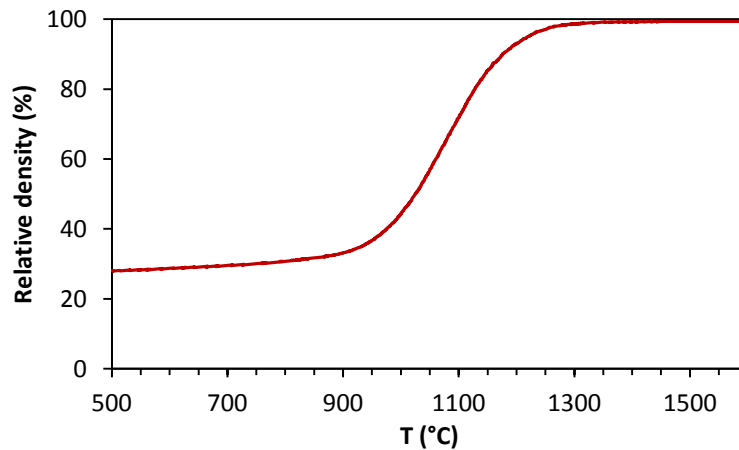


Figure 3.7. Relative density of YAG-S powder as a function of the temperature (heating rate 20°C/min, pressure 50 MPa).

Due to its high specific surface area, green density of YAG-S is low (around 30%). YAG-S powder is quite reactive: the onset of sintering occurs at $\sim 900^{\circ}\text{C}$ and reaches near full density at around 1300°C .

The sintered sample exhibits a dark appearance. XRD semi-quantitative analysis shows that at 1650°C , YAG-S is composed of pure YAG phase (see Figure 3.8).

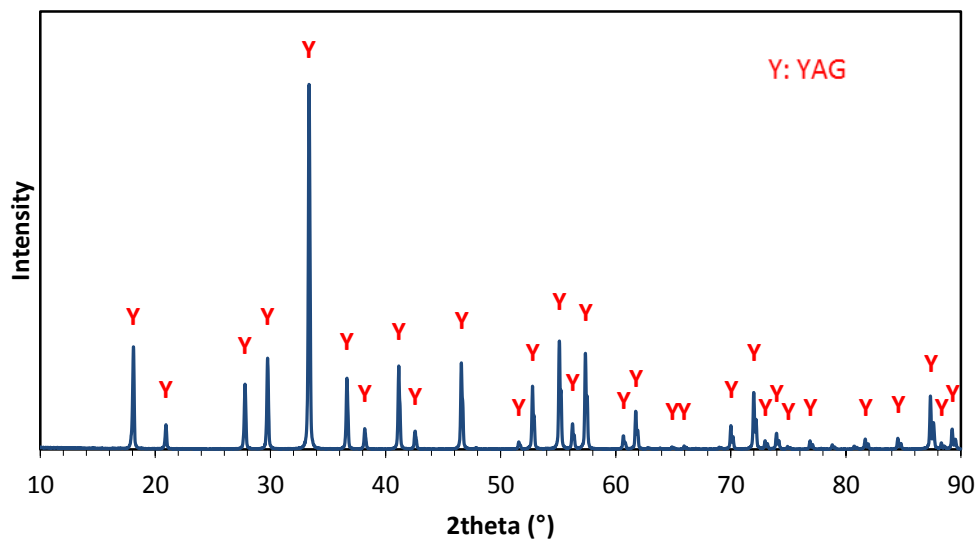


Figure 3.8. XRD of YAG-S after SPS at 1650°C .

3.1.2.2. Influence of SPS parameters on density, microstructure and visual aspect of the samples

The co-precipitation synthesis took a long time: 15 days to obtain 25 g of powder, therefore the amount of synthesized powder available was limited. This powder was synthesized at the Politecnico di Torino in Italy and an exhaustive study of the influence of all SPS parameters was not possible as a too large volume of synthesized powder would have been needed. Hence, we mainly focused on the influence of the temperature and studied to some extent the effect of other parameters (pressure, dwell time and heating rate) on the transparency of the samples.

- **Temperature influence**

The densification curve on Figure 3.7 shows that YAG-S powder reaches almost full densification at 1300°C. The effect of sintering temperature was therefore studied between 1200 and 1325°C.

To reduce the sintering time, a first quick heating rate (100°C/min) was used up to 1100°C (close to the maximum densification rate) followed by a slower one (10°C/min) up to the final temperature, to achieve high densification. The isothermal step was fixed to 15 min and the pressure (50 MPa) was applied during the whole sintering cycle.

The choice of these parameters was based on the sintering behaviour showed on Figure 3.7 and some preliminary cycles.

Figure 3.9 displays the sintering curve for a sample sintered at 1300°C. We observe that the green density is low, around 30% and relative density increases quickly between 1000 and 1200°C. When the heating rate is reduced, the sample has already reached 75% of relative density. Finally, at the beginning of the dwell, relative density is already close to 100%.

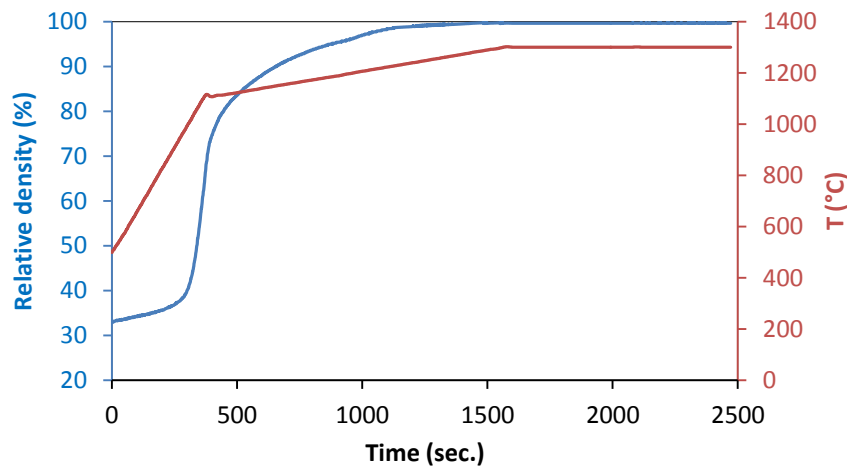


Figure 3.9. Sintering curve of a YAG-S sample sintered at 1300°C.

Figure 3.10 shows pictures of the sintered samples, related microstructure and final densities of YAG-S samples sintered at 1200°C, 1250°C, 1300°C and 1325°C .

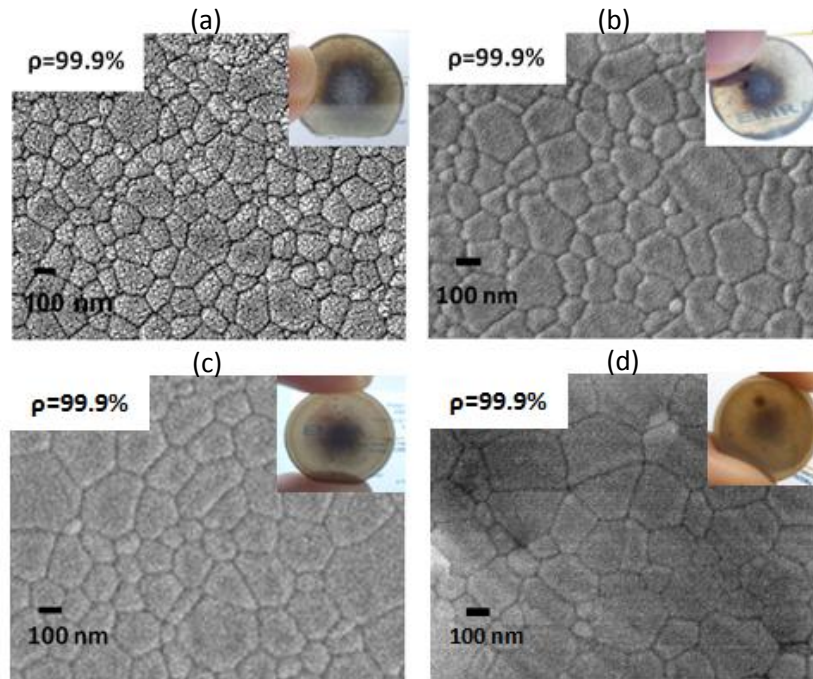


Figure 3.10. Scanning electron micrographs of YAG-S sintered at: (a) 1200°C, (b) 1250°C, (c) 1300°C, (d) 1325°C under a pressure of 50 MPa.

YAG-S reached almost full density for all tested temperatures and only YAG phase was detected by XRD. However, the samples showed a core-shell aspect, with an opaque central part (hereafter denoted as the core or centre) and a more transparent outer part (the shell). At temperatures higher than 1300°C, the opaque centre diminished but, unfortunately, so did the visual transparency of the outer part. This loss of transparency at higher temperatures has been also observed previously in transparent ceramics, and was attributed by several authors to pore coarsening [36], [11] and precipitation of fine particles. Nevertheless, regarding the microstructure of the sample sintered at 1325°C, we did not observe larger pores or secondary phases compared to the rest of the samples. At microstructural level, grain size increased slightly reaching values around 200 nm with the increase of temperature from 1200°C to 1325°C.

This core-shell aspect could be attributed to a difference in terms of density between the core and the peripheral part that could be induced by gradients of temperature. This effect could be amplified by the presence of agglomerates that avoid a uniform sintering. This aspect has been also reported previously in literature [57], [47], [48].

In our case, no difference in terms of residual porosity and grain size is observed between the peripheral part and the centre of the samples that could explain the differences in colour (Figure 3.11). Other works considering core-shell ceramics did not find differences in the microstructure either [61], [57].

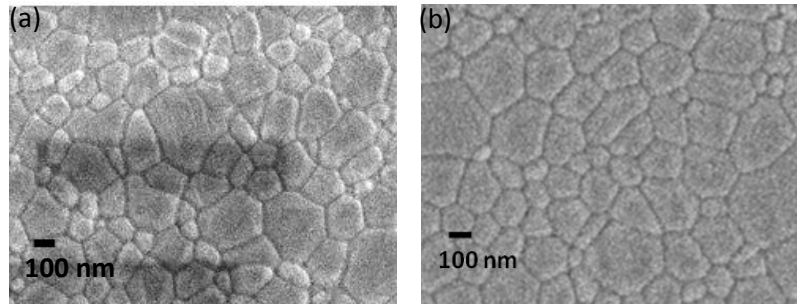


Figure 3.11. SEM images of (a) the core and (b) the shell of a sample sintered at 1300°C.

- **Thermal distribution simulations.**

To evaluate if temperature gradients could explain this core-shell aspect (even if the microstructure of the sample seems homogeneous), finite element modelling was performed to estimate the difference of temperature between the centre and the external part of a sample densified by SPS at 1300°C (see details in chapter 2).

The steady state temperature gradients reached after 15 minutes holding time at 1300°C have been calculated for a 3 mm thick YAG compact. The results are summarized in following figures. Figure 3.12 shows the overall temperature distribution of the SPS system. It is noticeable that the tooling is water refrigerated and high temperatures are only localized around the sample.

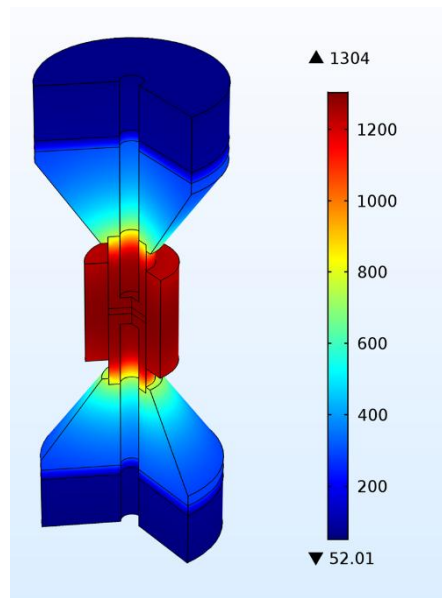


Figure 3.12. Temperature distribution in our SPS ensemble: tooling + sample (dwell temperature = 1300°C).

Figure 3.13 illustrates the temperature distribution within the YAG sample. At 1300°C the temperature gradient is very small, only 4°C between the peripheral part of the sample and the centre.

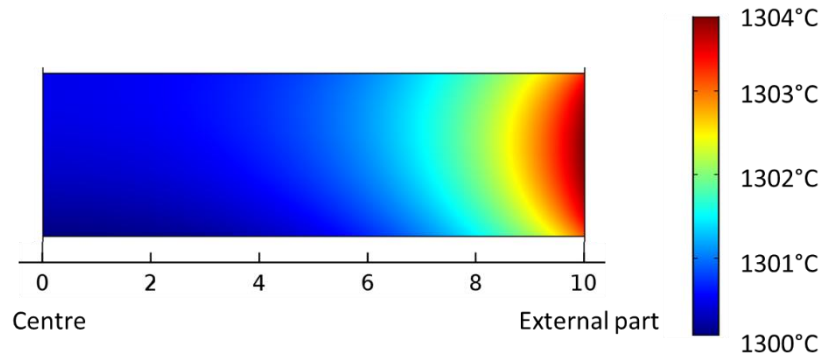


Figure 3.13. “Half view” temperature distribution in a YAG sample at dwell temperature = 1300°C.

Higher dwell temperatures were also simulated, but small differences were found between the peripheral and the central part as well. For instance, 1450°C of dwell temperature lead also to a gradient of 4°C.

- **Dwell time, pressure and heating rate influences.**

The influences of dwell time (isothermal step between 5 and 60 min at 1300°C) and of the applied load (between 30 and 70 MPa) were also studied for YAG-S powder, but no effect was observed, neither in terms of homogeneity of the samples nor in evolution of the microstructure. The effect of the pressure application mode was also investigated, but unlike Morita’s results [50], application of the pressure during the heating step or dwell time (whatever tested temperature) did not lead to any significant difference on final density or visual appearance of the samples.

On the contrary, heating rate influenced a lot the appearance of the samples. Three heating rates were applied from 1100°C to 1300°C: 2.5°C/min, 10°C/min and 100°C/min. Heating rates of 100°C/min led to opaque and whitish samples (due to residual porosity), with relative density around 99.5% (Figure 3.14); slower heating rates led to more transparent samples with 99.9% relative density, but the core-shell aspect was still present.



Figure 3.14. Sample sintered at 1300°C with a heating rate of 100°C/min.

Many reasons have been proposed to explain colorations and heterogeneity of translucent ceramics after sintering: graphite contamination [62], oxygen vacancies [11], [135], impurities [7], residual porosity [136], agglomerates [137], temperature or stress gradient during sintering [49], [57].

In our case, effect of temperature gradient has to be ruled out, since the core and the outer part show the same microstructure and simulations have confirmed that difference of temperature between core and shell was very low. The powder impurity level being very low, this hypothesis can also be ruled out.

The presence of pressure gradients is also possible, and can lead to tiny gradients of porosity. We observed that the use of different pressures did not affect significantly the grain size of the samples, so these gradients are possible even if the microstructure is homogeneous. Furthermore, the presence of pores < 50 nm is hard to evaluate due to the limited resolution of our SEM equipment. Kim et al. [9] showed the presence of pores under 50 nm in alumina samples only detectable by TEM, but sufficient to reduce dramatically the optical transmission. Unfortunately, our FEM simulations did not take into account the applied load on the model, so the existence of a pressure gradient cannot be confirmed this way.

Combined presence of agglomerates and stress gradients could also explain the core-shell aspect. In fact, Marlot et al. [57] used FEM simulations to evidence a lower pressure in the centre of the samples, and the pressure gradient inside the samples was exacerbated by the use of drilled punches as in our case. Agglomerates will likely remain at the core of the samples and generate a larger amount of porosity.

Darkening could be associated to oxygen vacancies attributed to sintering under vacuum and/or to graphite contamination [62], [11], [135] coming from the graphite tooling.

In order to verify these hypotheses and to improve the optical transmission of the samples, we investigated the effectiveness of different treatments (deagglomeration, air annealing and post-hipping).

3.1.2.3. Influence of pre- and post-treatments on the optical transmission

- **Deagglomeration of the powder.**

As observed previously, YAG-S powder is agglomerated, with a large size distribution of agglomerates. The presence of these agglomerates, certainly appearing during the calcination step of the initial nanometric powder, can lead to heterogeneous packing during pressing and potential formation of residual porosity during sintering. Moreover, agglomerates can lead to dislocations in compact samples and scattering centres in sintered ceramics [17].

In order to address the issue related to the critical influence of agglomeration in optical transmission, we aimed at developing YAG-S powders characterized by a finer and narrower particle size distribution. To disperse the powder, ultrasonication (US) using water as solvent was chosen. This method gives generally better results and lower pollution degree than other routes such as ball milling [11].

In Figure 3.15 agglomerate size distribution as function of the dispersion time is presented. Larger agglomerates disappear quickly in the first minutes of US dispersion. After that, it takes longer to

reduce the particle size. After 45 min of dispersion, particle size is between 0.1 and 10 μm , and no other evolution was observed for longer dispersion times.

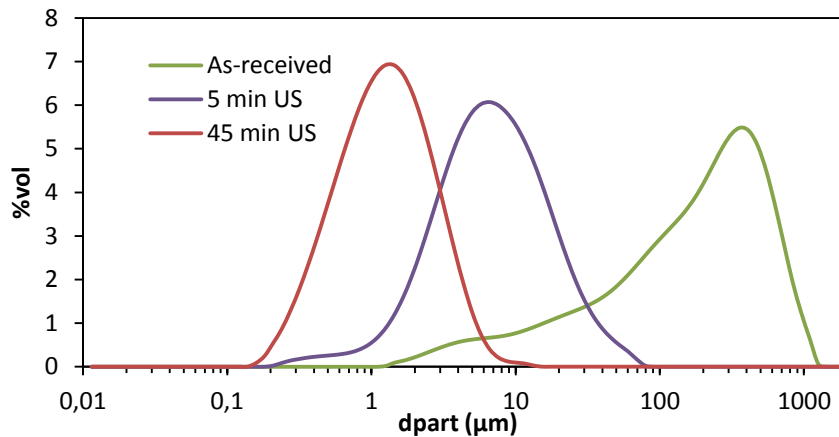


Figure 3.15. Frequency distribution (vol %) versus particle size of YAG-S as-received; after 5 min and 45 min of US dispersion.

After dispersion, the solvent was eliminated by freeze drying, this method leading to less reagglomeration of the powders than other standard processes such as drying in an oven or rotavapor [16]. Anyway, a partial reagglomeration occurred but the particle size distribution appeared narrower than the starting one (between 1 and 100 μm).

Deagglomerated powders were sintered by SPS with the same sintering cycle as the one used for the non-deagglomerated powder (1300°C, 50 MPa, dwell 15 min). No significant differences were observed between both sintering curves, except an increase of 4% in the green density, indicating the partial efficiency of ultrasonic dispersion to break some agglomerates. No differences in the microstructure of the sintered compacts were observed (Figure 3.16).

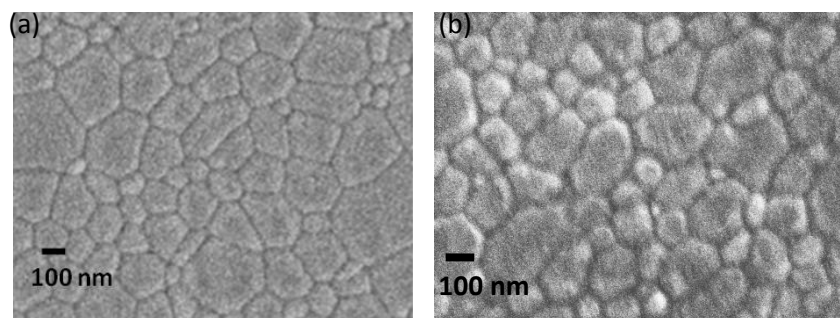


Figure 3.16. SEM images of YAG-S samples sintered at 1300°C before (a) and after deagglomeration (b).

In Figure 3.17, polished samples are compared. Sample obtained after powder deagglomeration was more homogeneous, with a less coloured core. This highlights the effect of conditioning on the optical homogeneity of the samples and confirms the observations of others researches like Suarez et al. [16], [138]. According to them, deagglomeration improves green body package and the homogeneity of the sintered samples. However, our samples still presented a high level of darkening so in the following section the effect of air annealing will be evaluated and its influence on the transmission discussed.

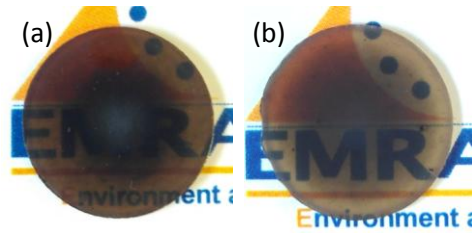


Figure 3.17. Samples of YAG-S sintered by SPS at 1300°C without (a) and after deagglomeration of the powder by US (b) (thickness 1.5 mm).

- **Conventional annealing.**

Annealing in air should remove the oxygen vacancies and possible graphite contamination present in the samples after SPS. After sintering at 1300°C, YAG samples were submitted to different air annealing conditions going from 900°C to 1150°C and lasting from 15 minutes to 24 hours with a heating rate of 5°C/min.

Figure 3.18 shows the appearance of YAG-S samples before and after some of these annealing conditions. Thermal treatments at low temperatures (below 1000°C) did not have a great impact on the samples. Treatments at higher temperatures reduced the darkening of the samples. However after treatments at too high temperature and long dwell time (1150°C – 24 hours), a decrease of the optical transmission was also detected. High temperature annealing is detrimental to optical transmission due to microstructural changes, grain growth and coalescence of tiny pores into larger ones [41].

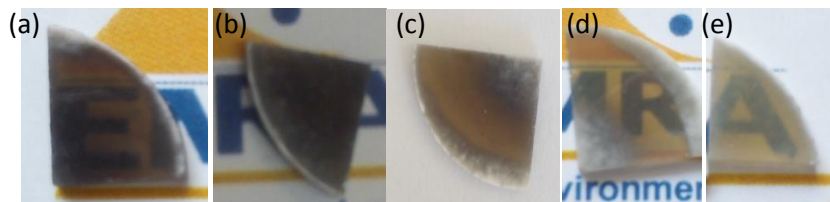


Figure 3.18. Appearance of YAG-S samples (a) before annealing and after annealing at (b) 900°C 1h (c); 1050°C 12h (d) 1100°C 24h (e); 1150°C 24h.

The most effective annealing conditions were 1100°C during 24 hours. As shown in Figure 3.19, the darkening was reduced and the sample was more homogeneous, even if a residual coloration remained.



Figure 3.19. Sample sintered at 1300°C after annealing at 1100°C 24h.

- **Post-hipping.**

Annealing in air allows partial oxygen vacancies and graphite removal but does not eliminate the eventual presence of remaining porosity. To address this issue, Hot Isostatic Pressing (HIP) post-treatments were performed on several SPS samples in an O₂/Ar atmosphere (20/80 vol%). The applied isostatic pressure was 120 MPa and the temperature 1250°C with an isothermal step of 1 hour.

Figure 3.20 shows a sample first sintered by SPS at 1300°C and then post-hipped. The sample presents a more homogeneous and transparent aspect. It seems that the high pressure and the oxygen pressure were enough to restore oxygen vacancies and eliminate remaining porosities inside the sample.



Figure 3.20. YAG-S sample sintered by SPS at 1300°C and post-treated by HIP at 1250°C for 1 h.

- **Optical transmission.**

Optical transmission measurements were performed on YAG-S samples prepared from deagglomerated powders. Before deagglomeration, samples were inhomogeneous and their centre was opaque. Consequently, transmission values were very low and not representative of the samples.

In order to characterise the optical transmission of the samples, TFT (Total Forward Transmission) and RIT (Real In-line Transmission) were measured as described in the experimental section.

As depicted in Figure 3.21, samples after SPS showed 23% TFT at 600 nm and only 12% RIT even if we can clearly read through the sample (Figure 3.17b). These low values of transmission are due to the great amount of absorption in this sample (confirmed by absorption measurements). The sample presented a dark brown colour owing to the probable presence of oxygen vacancies and graphite inclusions generated during SPS. Thus, most of the incident light was absorbed by the sample.

After annealing in air at 1100°C during 24 hours, some of the oxygen vacancies and graphite were removed, hence, an increase in the optical transmission was observed. TFT and RIT values at 600 nm were 40% and 21%. At this wavelength, ~20% of the light is scattered forward, which represent 10 % more in samples after annealing than in those without. The increase of the scattered light indicates an increase of the amount or size of the scattering centres, so pore coalescence has probably started.

Samples after HIP showed the highest values of transmission over the whole visible range. TFT value at 600 nm was 67% and it increased up to 74% at 800 nm. RIT value reached 52% at 600 nm and 62%

at 800 nm. Therefore, ~10% of light transmitted is scattered forward due to defects in the microstructure of the sample: pores, secondary phases, dislocations ... that remain after the HIP post-treatment. HIP has reduced the scattering centres, but not removed them completely. This sample presents still a brownish colour, indicating light absorption that prevents transmission to reach higher values.

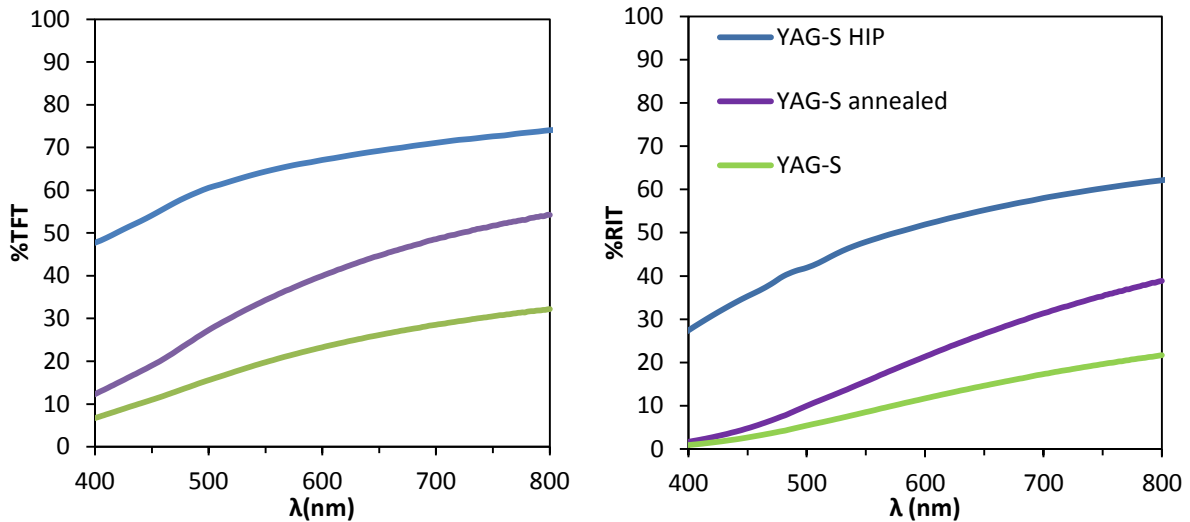


Figure 3.21. TFT and RIT values of YAG-S samples after deagglomeration, annealing and post-hip.

3.1.3. Conclusions on YAG-S powder

YAG-S powder was synthesized in this thesis by a co-precipitation method. This powder was pure YAG phase, with small primary particles (< 100 nm) but largely agglomerated.

The influence of SPS parameters was studied. The minor influence of dwell time and pressure has been shown, whereas the obligation to use slow heating rates has been highlighted. Ceramics with relative density of at least 99.9% were obtained.

Unfortunately, no homogeneous and transparent ceramic was obtained: with the best optimized sintering conditions, ceramics were quite transparent, but presented a core-shell aspect, with a darker and opaque core and a more transparent shell. Presence of temperature gradients, explaining this visual aspect, has been ruled out, both by comparison of the microstructure and simulations.

A significant influence of the powder agglomeration degree has been demonstrated. Samples prepared with deagglomerated powders were more homogeneous, even if a core-shell aspect remained.

A further improvement was attained with post-treatments. The darkening was partially removed with conventional annealing in air, owing to the restoration of oxygen vacancies and potential graphite removal. Finally, post-hipping in an oxidative atmosphere allows obtaining homogeneous and transparent samples by eliminating (or at least largely reducing) the residual porosities.

From these results, the core-shell aspect is attributed to residual porosities in the core, caused by the presence of pressure gradients and amplified by the agglomeration state of the powder that can imply differential sintering. This hypothesis will be investigated through the two other YAG powders.

3.2. YAG-B

In order to compare the behaviour of the synthesized powder with a commercial one, an analysis of a common commercial YAG powder used for transparent ceramics was performed and also its response to SPS was evaluated.

3.2.1. Powder characteristics

YAG-B is a commercial powder from Baikowski, which is a well-known provider of high purity powder for optical applications. This powder comes from a synthesis based on sulphate precursors (see technical information from the supplier in appendix A).

Several analyses have been performed on this powder in order to check the provider's data.

First, the powder has been observed by SEM in order to identify the morphology and size of the particles (Figure 3.22). Primary particles are spherical, with a diameter around 200 nm, but the powder presents coarse agglomerates, with size up to 150 μm .

The specific surface area has also been measured by the BET method. The BET area value is 6.7 m^2/g , close from the data of the provider (7.8 m^2/g). Using equation 3.1, the particle size was estimated in around 200 nm, in agreement with the SEM observations.

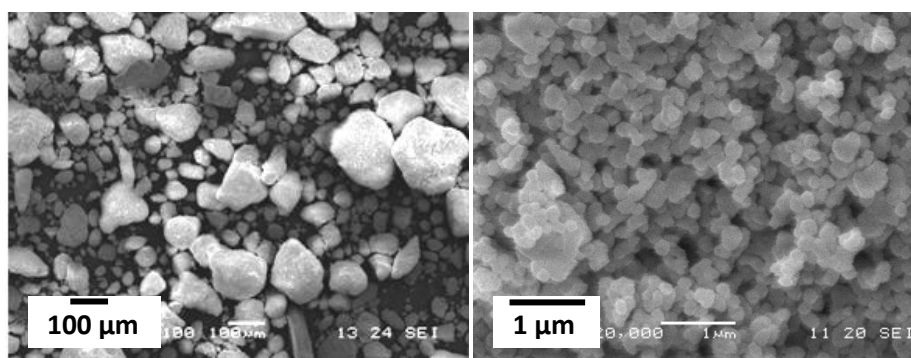


Figure 3.22. SEM Images of YAG-B

The granulometry of the powder has been analysed with a laser diffractometer in order to quantify the agglomeration state of the particles (Figure 3.23). We observe at Figure 3.23 that the powder is agglomerated: mean size of agglomerates (d_{50}) is around 160 μm (in agreement with SEM observations of the powder) and agglomerates size distribution is broad.

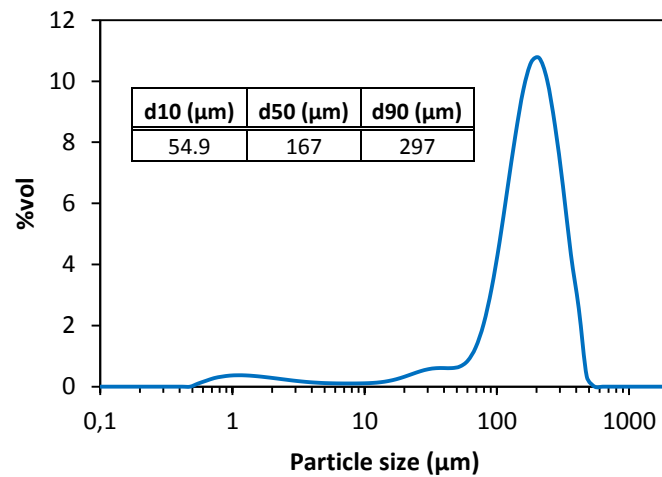


Figure 3.23. Frequency distribution (vol %) versus particle size of Baikowski YAG powder

The XRD analysis of YAG-B powder (Figure 3.24) shows yttrium aluminium garnet (YAG, $Y_3Al_5O_{12}$) as the main phase and the presence of secondary phases of yttrium aluminium monoclinic (YAM, $Y_4Al_2O_9$) and yttrium oxide (Y_2O_3) in very low quantity (<4 wt%). These secondary phases mean an incomplete reaction or non-stoichiometry of the powder.

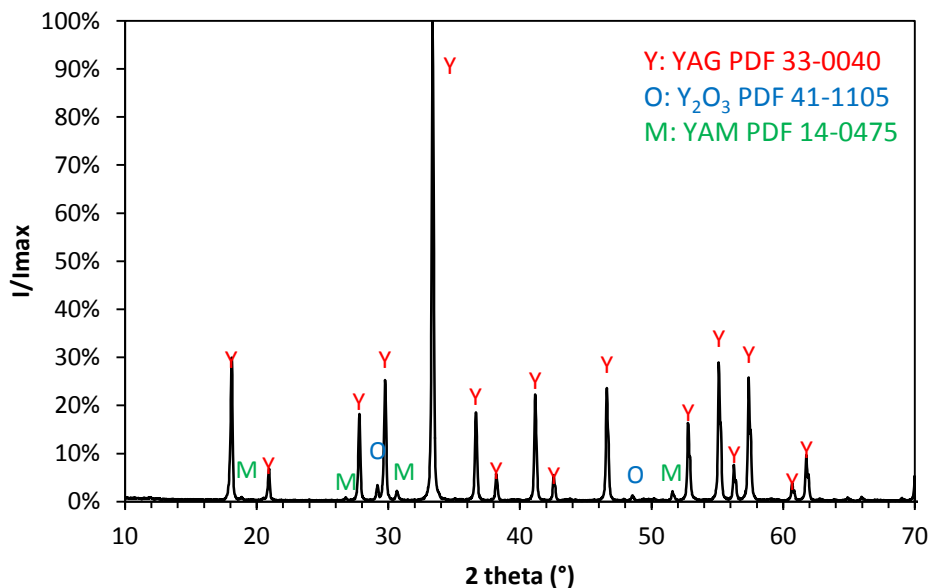


Figure 3.24. XRD of YAG-B powder.

An analysis of the impurities in the YAG-B powder was done by ICP (Inductively Coupled Plasma). The main impurity observed is sulphur in a quantity of 550 ppm, likely coming from the sulphates used for the synthesis. The presence of this high amount of sulphur was not mentioned on the supplier's analysis report. Sulphur impurities have been associated with a yellowish colour in YAG samples [57] and with an inhomogeneous grain growth [139]. The other impurities (including Si, Ca, Na, K, Fe, Zr or Mg) are below 10 ppm.

3.2.2. Sintering and transparency improvement

3.2.2.1. Sintering behaviour

The sintering behaviour of the YAG-B powder was evaluated by following the shrinkage of a powder compact in the SPS equipment. The same heating cycle as the one used for YAG-S powder was selected: a heating rate of 20°C/min from 500 to 1650°C and a pressure of 50 MPa applied during the whole sintering cycle. The calculated relative density as a function of the temperature is reported in Figure 3.25.

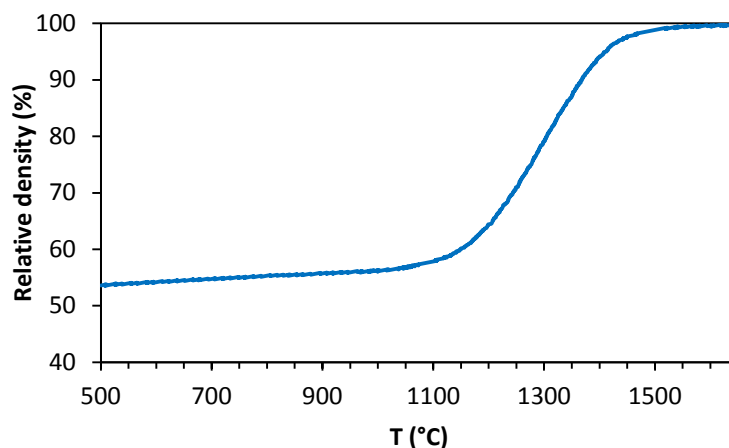


Figure 3.25. Relative density of YAG-B powder as a function of the temperature (heating rate 20°C/min, pressure 50 MPa).

Green density of YAG-B powder is around 53% (higher than that of YAG-S in agreement with YAG-B lower specific surface area). The onset of sintering occurs at around 1150°C (900°C for YAG-S) and full density is attained at ~1500°C (1300°C for YAG-S). These differences can be also attributed to the specific surface area and particle size of YAG-B, lower surface area and larger particle size involving the need of higher temperatures to achieve full densification.

After this cycle, the sample exhibits a dark appearance and 99.9% relative density. XRD semi-quantitative analyses showed that at 1650°C, YAG-B mainly consists of YAG phase, around 99.5 wt%, with traces of YAP (YAlO_3) and YAM ($\text{Y}_4\text{Al}_2\text{O}_9$). According to the $\text{Al}_2\text{O}_3 / \text{Y}_2\text{O}_3$ phase diagram (showed in Figure 1.24), the transformation of Y_2O_3 and YAM phases into YAG implies the presence of alumina in the starting powder. However, XRD analyses did not reveal the presence of alumina phases: either these phases are amorphous or their content is lower than the instrumental detection limit.

3.2.2.2. Influence of SPS parameters on density, microstructure and visual aspect of the samples

The YAG-B powder was available in bigger quantity than YAG-S. Thus, a more detailed evaluation of the SPS parameters could be performed and correlated with the properties of the final sintered compact: sintering temperature, dwell time, heating rate, pressure and pressure schedule.

- **Temperature influence**

The effect of sintering temperature on YAG-B was evaluated between 1350°C and 1450°C. Based on the sintering curve (Figure 3.25) and some preliminary tests, the SPS cycles were as follows: a first rapid heating step at 100°C/min up to 1100°C, followed by a step at a lower heating rate of 50°C/min up to the final temperature and a 15-min long isothermal step. The pressure (50 MPa) was applied during the whole sintering cycle. The cooling rate was fixed to 150°C/min.

Figure 3.26 shows images of the sintered samples, related microstructure and final densities. SEM micrographs show a decrease of intergranular porosity and a slight grain growth with the increase of the sintering temperature. At 1450°C, relative density reaches 99.4% and the mean grain size is around 400 nm. In addition, we can observe an increasing darkening of the samples, while increasing temperature and density.

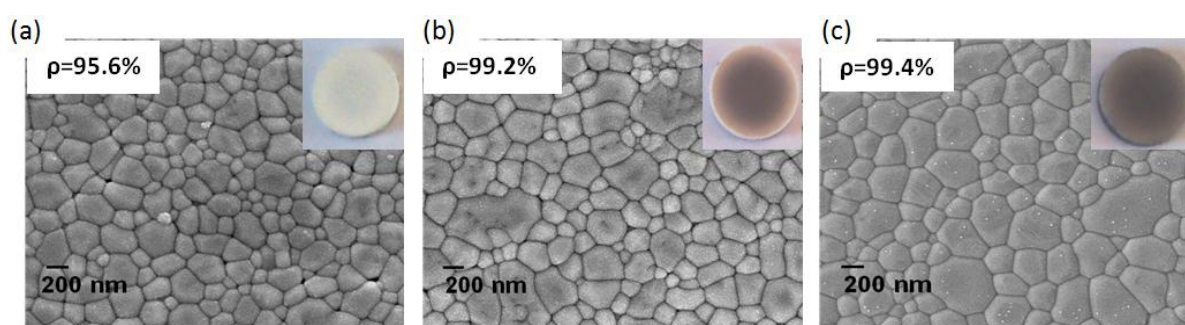


Figure 3.26. Scanning electron micrographs of YAG-B sintered at (a) 1350°C, (b) 1400°C and (c) 1450°C under a pressure of 50MPa.

A core-shell aspect is also observed on the sample sintered at 1400°C. However, as in the case of YAG-S powder, no difference in terms of microstructure is observed between the core and the shell of the sample (Figure 3.27).

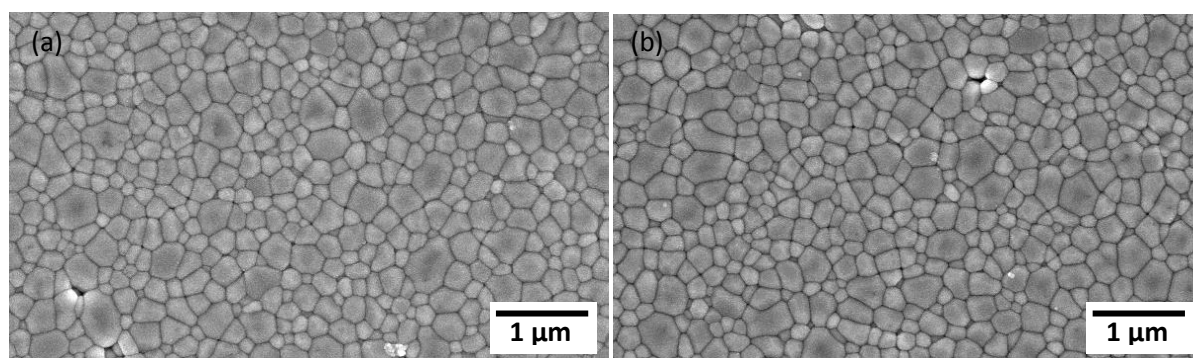


Figure 3.27. Microstructure of a sample sintered at 1400°C for 15 min: (a) core; (b) shell

Table 3.3 shows the evolution of phase composition as a function of the sintering temperature. Higher temperatures lead to a decrease of secondary phase content (YAP and YAM) in favour of YAG phase. However, even at 1450°C, the evolution is not complete as already observed in the XRD of the sample sintered at the highest temperature of 1650°C.

Table 3.3. Evolution of the phase composition of YAG-B as a function of the sintering temperature (pressure 50 MPa, dwell time 15 minutes). XRD semi-quantitative analysis, in wt%.

	% YAG	% YAM	% YAP
1350 °C	96.5	1.5	2.0
1400 °C	96.8	0.2	3.0
1450 °C	98.9	0.3	0.8

Besides the presence of traces of YAM and YAP, YAG-B also presents a non-negligible amount of sulphur coming from the synthesis route. In samples sintered by SPS at 1450°C, sulphur content decreased to 150 ppm. The residual presence of sulphur may inhibit both densification and phase transformation into pure YAG (which is incomplete even at 1650°C). At 1450°C the low quantities of YAP and YAM should have already reacted, taking into consideration that YAG formation should be completed even in the case of solid state reaction sintering at temperatures around 1500°C [140].

Presence of YAM, YAP or Y_2O_3 phases in the sintered ceramics may also be due to the sintering process, SPS, with thermal cycles too rapid to allow complete reactions into pure YAG.

All these aspects (presence of sulphur and secondary phases, too rapid sintering process) may explain the opacity of the samples. These hypotheses will be checked in the following sections.

- **Pressure and load schedule influence**

The pressure influence was also evaluated. Pressures from 30 MPa up to 70 MPa were tested (70 MPa was the limiting pressure owing to the mechanical characteristics of the graphite tooling). The sintering cycle was: a first heating rate of 100°C/min up to 1100°C, then as second heating rate of 50°C/min up to 1400°C followed by a 15-min isothermal step. The cooling rate was fixed to 150°C/min.

Figure 3.28 shows pictures of the sintered samples and their final relative density: darkening and density increased with the rise in pressure (the same effect was observed with the increase of temperature). At the microstructural level, apart the high porosity amount observed on the sample sintered with 30 MPa pressure, no real difference in terms of grain size was observed whatever applied pressure.

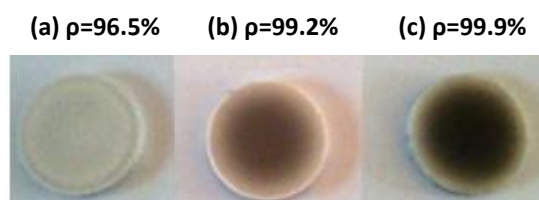


Figure 3.28. Samples sintered at 1400°C with a pressure of a) 30 MPa; b) 50 MPa and c) 70 MPa.

Moreover, Figure 3.28 shows that all samples present a core-shell aspect with a darker core and a lighter shell. Pressure gradients could be at the origin of this core-shell appearance, but, as in the

case of YAG-S powder, no difference of microstructure was observed between the centre and the external part of all samples.

The effect of load schedule was also evaluated: pressure was applied at different moments of the sintering cycle, at 1100°C or at the beginning of the dwell at 1400°C. However, no difference in terms of homogeneity or density was observed.

- **Dwell time influence**

The influence of different dwell times on the density, appearance and microstructure was also analysed. Three dwell times were compared: 5, 15 and 25 minutes for a SPS cycle of 100°C/min up to 1100°C, then 50°C/min up to 1400°C. A pressure of 50 MPa was applied during the whole cycle and the cooling rate was fixed to 150°C/min. In Figure 3.29, the aspect and density of the samples are compared. The same evolution that appeared with the increase of temperature or pressure is observed: the density increases as we extend the dwell time and an increasing darkening appears. However, even after a dwell of 25 minutes, density remains relatively low.

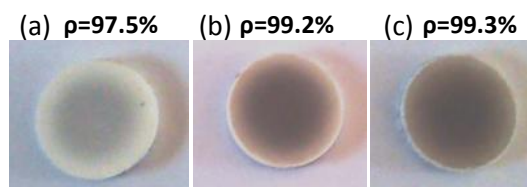


Figure 3.29. Samples sintered at 1400°C with a dwell time of a) 5min; b) 15min and c) 25min.

This increasing darkening has been observed previously in the literature; most authors [59], [11] attributed this effect to the sintering atmosphere. Vacuum sintering leads to oxygen vacancies formation, generating a grey colour of the samples. Other explanations [60], [54] attribute the darkening to the graphite contamination owing to the use of graphite tooling during SPS. But, darkening also appeared in vacuum sintered samples without the use of graphite tooling [23]. Moreover, graphite contamination and oxygen vacancies could not explain the core-shell aspect.

Concerning the cause of the core-shell aspect, temperature gradients were ruled out, but it can be associated with the presence of pressure gradients inside the samples. In contrast to the temperatures, the pressures investigated did not affect the grain size of the samples. Therefore, a pressure gradient will not affect grain size either but it might have an effect on the colour of the samples.

- **Heating rate influence**

Heating rate was also tested on YAG-B using a SPS cycle of 100°C/min up to 1100°C and then different heating rates (between 10 and 80°C/min) up to 1400°C, with an isothermal step of 15 minutes. Unfortunately no improvement on the appearance of the samples was found (Figure 3.30).

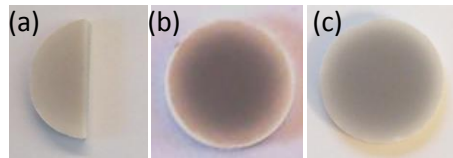


Figure 3.30. Samples sintered at 1400°C with heating rates of (a) 10°C/min; (b) 50°C/min and (c) 80°C/min.

3.2.2.3. Influence of pre- and post-treatments on the optical transmission

In the previous section, the influence of SPS parameters was studied, but no transparent ceramics were obtained. Therefore, we investigated the efficiency of powder treatments (deagglomeration, LiF addition) and post-sintering treatments (air annealing and post-hipping) to improve the optical transmission of the samples.

- **Deagglomeration**

Several authors have emphasized the influence of the ceramic powders deagglomeration on the optical transmission of sintered ceramics [16], [11].

Ultrasonication (US) using water as solvent was the dispersion method selected in order to remove agglomerates. No dispersant was used in order to avoid impurities addition and also, the need of a thermal treatment after dispersion to remove the dispersant.

As previously described, Figure 3.31 shows that YAG-B as-received presents a large particle size distribution. Deagglomeration is very effective during the first minutes of US, indicating that larger agglomerates are relatively soft. Nevertheless, for longer dispersion times, particle size evolves slowly and agglomerates are still present.

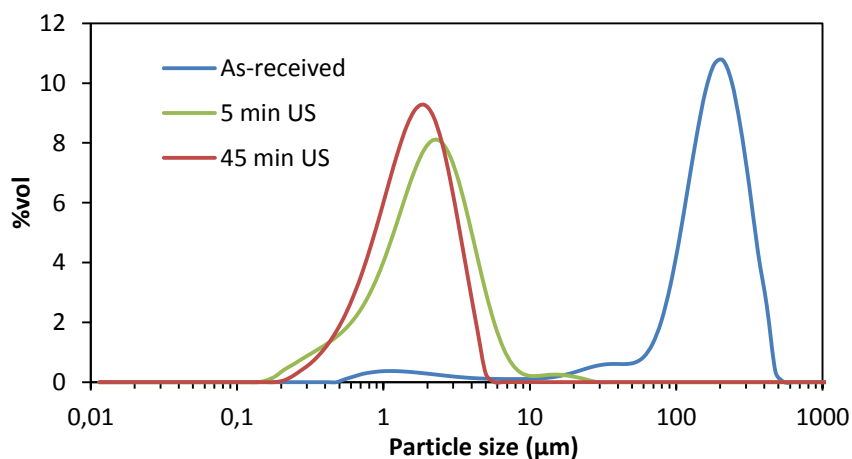


Figure 3.31. Frequency distribution (vol %) versus particle size of YAG-B as-received; after 5 min US and after 45 min US.

After 45 minutes of dispersion, mean agglomerate size is around 2 µm. Even if a re-agglomeration of the powders occurs after freeze drying, the size distribution (between 0.1 and 100 µm) appears narrower than the starting one.

Deagglomerated powders were sintered by SPS at 1450°C for 15 minutes but no significant differences were observed on the sintering curves or in the sintered samples. Polished samples are shown in Figures 3.32. Deagglomeration of YAG-B powder did not cause any relevant effect on the sample visual aspect or on its density, both samples presented 99.4% relative density, with the same phase composition (secondary phases still present).

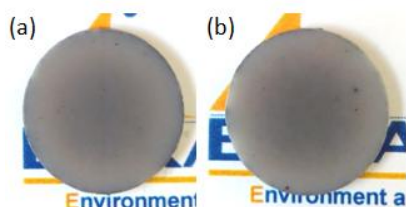


Figure 3.32. Samples sintered at 1450°C and 50MPa (a) without dispersion and (b) dispersed 45 minutes by US and then freeze-dried.

- **Post-treatments**

As we stated in the previous section, the increasing darkening of the samples could be associated to oxygen vacancies and graphite contamination. In this case, these two defects should be removed with a post-treatment in presence of oxygen. We have performed two kinds of annealings: a simple annealing in air and a post-hipping in O₂/Ar atmosphere.

However, conditions of annealing are very sensitive: temperature must be high enough to compensate oxygen vacancies, but a too high temperature can also lead to pores or vacancies coalescence and consequently to a loss of the optical transmission [11].

- **Conventional annealing**

In order to determine the optimal conditions of post-annealing, YAG samples with different levels of darkening were submitted to annealing conditions going from 900°C to 1150°C and lasting from 15 minutes to 24 hours. A reduction of the darkening was observed at higher temperatures but no changes on the density nor in the composition (mineralogical phases) of the sample were measured.

Figures 3.33a and b show an example of YAG-B sintered by SPS at 1450°C before and after annealing at 1150°C for 12 hours. We observed a reduction in the darkening of the sample but the transparency of all annealed samples remained very low.

- **Post- Hipping**

Annealing in air should remove oxygen vacancies and graphite, at least partially. However it does not eliminate the remaining porosity. Therefore, several SPS samples were submitted to a post-treatment by Hot Isostatic Pressing (HIP) in an O₂/Ar atmosphere (20/80 vol%). Annealing in oxygen in addition to the application of higher pressures could eliminate further oxygen vacancies and remove the eventual remaining porosity at the same time. The chosen cycle was a heating rate of 5°C/min to 1350°C with a dwell time of 1 hour and 120 MPa of pressure. This temperature was higher than the one used to YAG-S owing to the higher SPS sintering temperature.

All samples after HIP presented a relative density close to 100%, even the ones with initial density around 96%, confirming the efficiency of post-hipping to reduce porosity. Unfortunately, concerning the visual aspect, only a reduction of the darkening was observed and no transparent ceramics were obtained (Figure 3.33c).

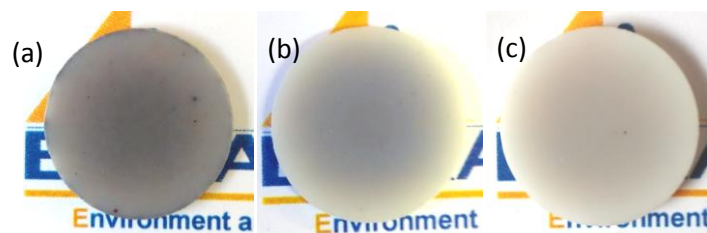


Figure 3.33. YAG-B samples after deagglomeration and SPS cycles at 50 MPa, 1450°C 15 min (a) without post-treatment; (b) after annealing at 1150°C for 12h and (c) after post-HIP at 120 MPa, 1350°C 1h (thickness 1.5 mm)

An analysis of the visual aspect of the samples offered a qualitative measurement of their transparency but optical transmission measurements were performed to have a quantitative and more detailed analysis.

The optical transmission of some YAG-B samples was characterised. Most of them presented very low values because they were opaque, even the ones after post-HIP treatment, and RIT values were under 1% for all visible and near-infrared wavelengths.

Figure 3.34 exhibits TFT measurements of the best samples before and after post-treatments.

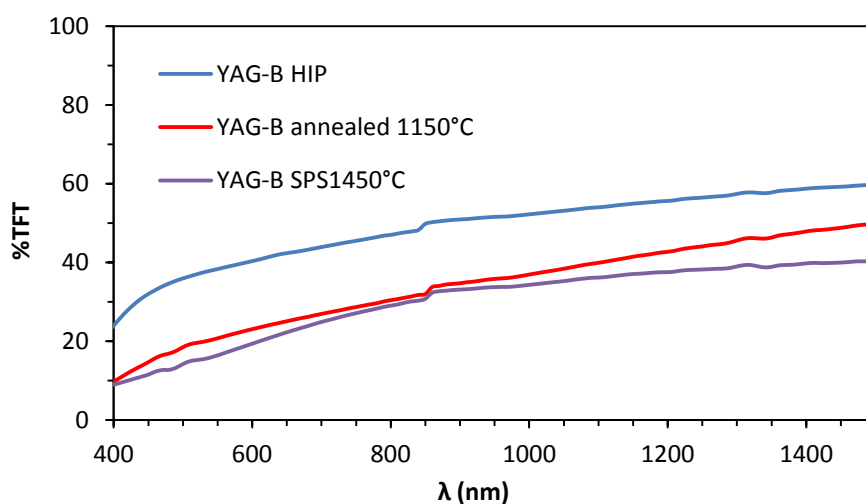


Figure 3.34. Total Forward Transmission of YAG-B samples before and after post-treatments.

TFT values of as sintered YAG-B samples are under 30% for all the visible wavelengths; annealing and mostly post-HIP treatments improve the transmission of the samples but values remain quite low, below 50%. Best results are obtained after HIP: this sample shows a transmission of 40% at 600 nm wavelength.

- **LiF addition**

Lithium fluoride (LiF) added in very low quantities to YAG has resulted in transparent [42], by forming a liquid phase that acts as a sintering aid. Moreover, some researches [7] point out that LiF may also improve transparency by eliminating some impurities as C, S, Fe or Ca. Fluorine reacts with these impurity cations to form volatile compounds. Hence, it appeared interesting to evaluate the LiF effect on this powder, considering that YAG-B powder contains a quite important amount of sulphur.

A LiF powder from Acros Organics (see product specifications in appendix A) was employed. It presented a cubic structure and purity >99.98%. The morphology of the powder is shown on Figure 3.35.

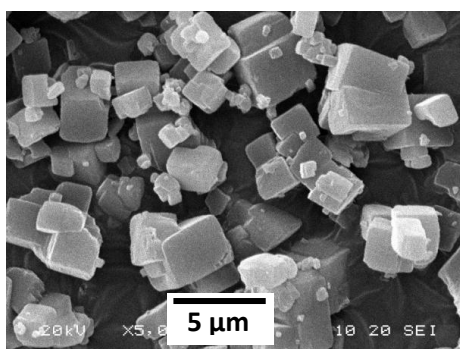


Figure 3.35. SEM image of LiF powder.

LiF mean particle size is around 2 μm . To get a good mixing between LiF and YAG powder, lithium fluoride was added into a YAG aqueous suspension, in very low concentration (0.1 - 0.3 wt%) and ultrasonicated for 45 minutes. The mixture was then freeze dried.

- **Optimisation of LiF concentration**

In order to determine the optimal quantity of LiF, three concentrations were evaluated: 0.1, 0.2 and 0.3 wt%. The same SPS cycle as in LiF-free samples was applied (50 MPa, 1400°C, 15 min dwell), but the cooling rate was modified in order to prevent the fracture of the samples. At the end of the dwell, the pressure was removed and free cooling rate was used ($\sim 50^\circ\text{C}/\text{min}$). In Figure 3.36, the evolutions of the relative density during sintering are compared. We observed a significant influence of LiF in densification from 0.1 wt%. Densification starts at lower temperatures and the maximum density is attained earlier as well. This behaviour is more pronounced with the increase of LiF concentration.

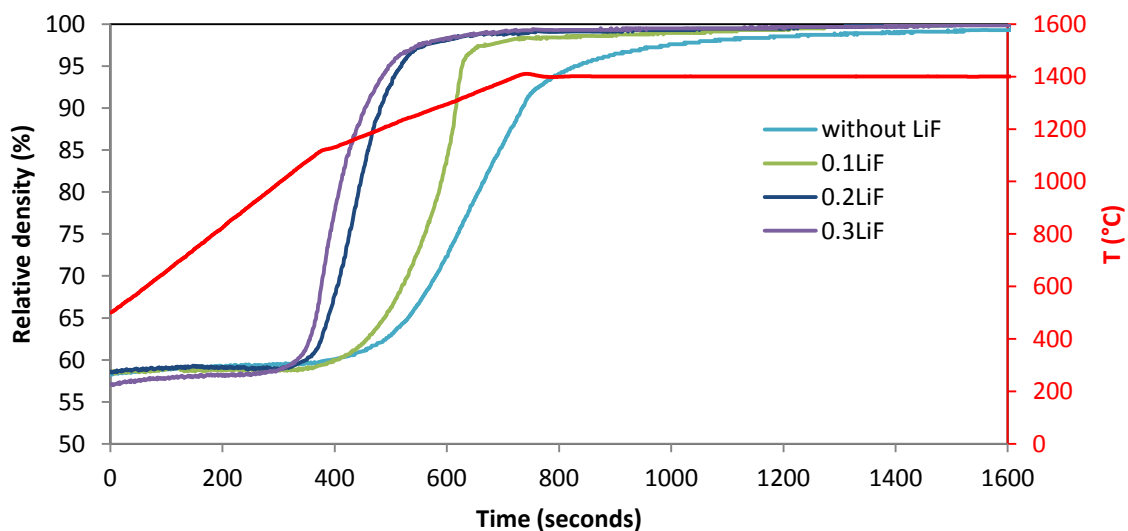


Figure 3.36. Density evolution during SPS for different LiF concentrations.

All three samples attained 100% relative density after sintering and the only phase detected by XRD was YAG (Figure 3.37).

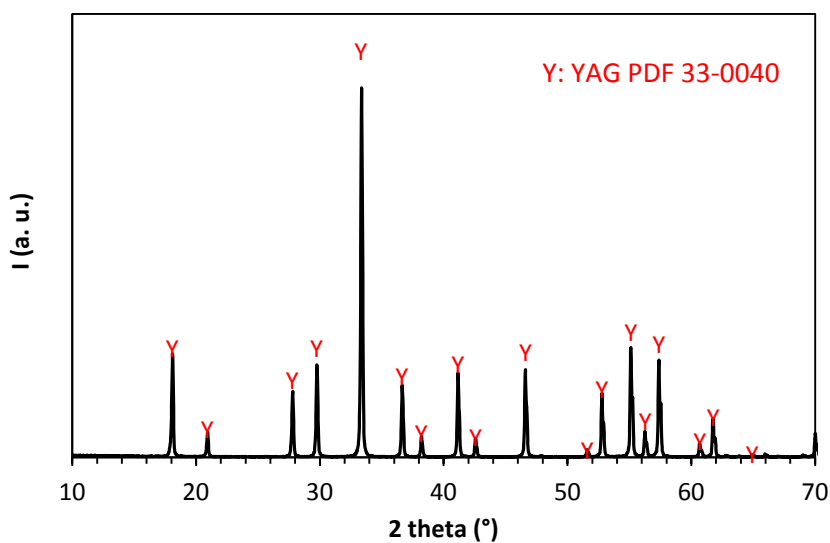


Figure 3.37. XRD of YAG-B-0.2LiF sintered at 1400°C.

Sample with 0.2 wt% of LiF presented the highest optical transmission values in the visible and near infrared regions (Figure 3.38). For example, total forward transmission at 600 nm reaches 60% with addition of 0.2 wt% LiF. This value was much higher than the one of non-doped YAG-B samples after HIP.

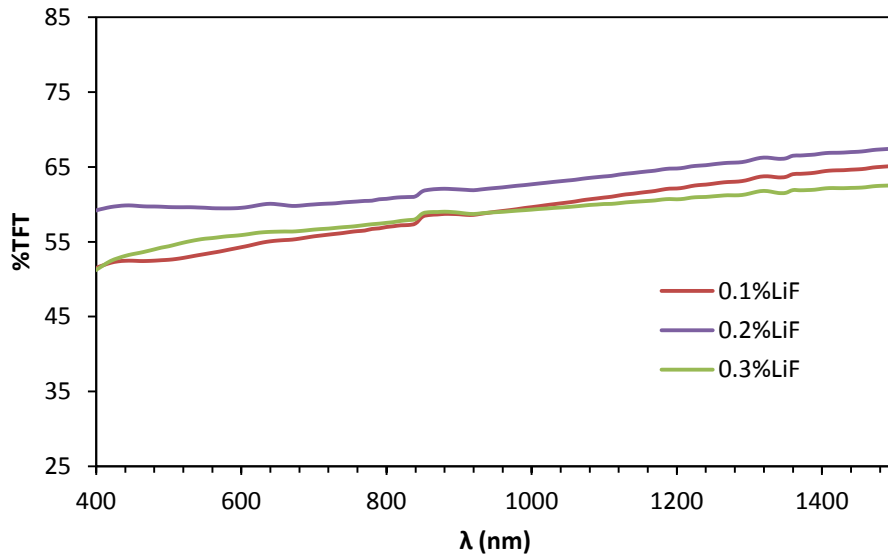


Figure 3.38. Optical transmission (TFT) of SPS samples of YAG-B with different LiF concentrations.

This additive concentration was thus fixed to 0.2 wt% and an optimization of the optical transmission was performed by modifying the SPS parameters (temperature, heating rate, pressure and dwell time):

- The decrease of the sintering temperature from 1400 to 1300°C implied an important decrease of the optical transmission (around 50% at 600 nm); contrariwise, increasing temperature to 1450°C improved transmission up to 70%. However, for temperatures higher than 1450°C, a decrease of TFT was measured, certainly due to the formation of porosities with the grain growth;
- The influence of dwell time was investigated for a sintering temperature of 1450°C: increasing the dwell time from 5 to 15 min increases the TFT value from 49 to 70%, respectively. The use of longer dwell times did not lead to any improvement of the optical transmission;
- The increase of the applied pressure implied an improvement of the optical transmission: 59 vs 70%, for 30 and 50 MPa respectively; higher pressures led to values of TFT similar than those at 50 MPa;
- The effect of heating rate was weak: optical transmission varied only from 70 to 61% for heating rates between 20°C/min and 80°C/min.

Finally, between the different tested sets of SPS parameters, the best optical transmission was obtained for a sintering at 1450°C during 15 min, a pressure of 50 MPa and a heating rate of 50°C/min.

Figure 3.39 shows the microstructure of a sample sintered under these conditions: we can observe a relevant increase of the grain size from 0.4 μm (non-doped sample) to around 6 μm (LiF-doped sample), confirming the huge effect of LiF addition on grain growth [42]. XRD measurement shows that the sample is pure YAG phase, indicating the correct stoichiometry of elements in the starting powder and the effect of LiF to complete transformation of intermediate phases (YAP and YAM) into YAG. This effect of LiF to complete reactions was also reported by Meir et al. [54] on spinel.

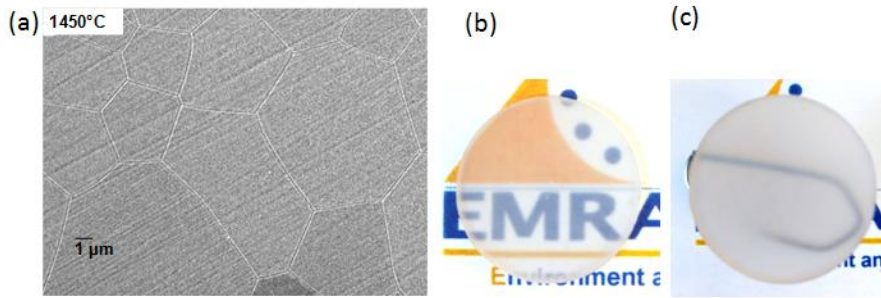


Figure 3.39. (a) Scanning electron micrograph and images of 0.2%LiF doped- YAG-B SPSed sample (1450°C, 50 MPa) (b) placed on the text and (c) 15 mm above it (1mm-thick).

Concerning the visual aspect of the sample (Figure 3.39), LiF addition has also a remarkable effect on YAG-B, as the sample shows a homogeneous and colourless aspect. In Figure 3.39b, the sample placed on the text shows a transparent appearance. However, transparency of the same sample placed 1.5 cm above the text (Figure 3.39c) appears to be very low.

Optical measurements on this sample showed no absorption. RIT and TFT values are shown in Figure 3.40. LiF-doped sample presented higher values of total transmission (close to 70% in the whole visible range) but its RIT were also close to 0. As this sample presented no absorption, difference between RIT and TFT values is caused by light scattering.

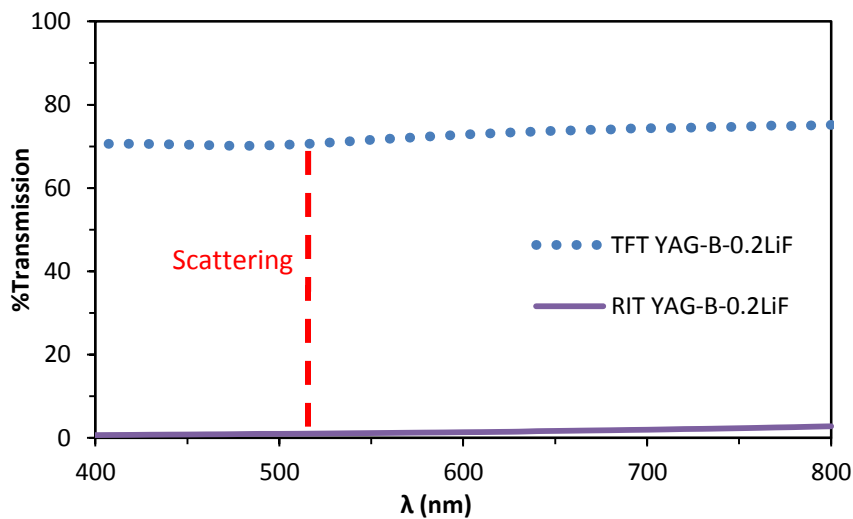


Figure 3.40. RIT and TFT values of 0.2%LiF doped- YAG-B sample

Different reasons might be proposed to explain this strong scattering: residual porosities (not observed by SEM), LiF trapping on grain boundaries and/or triple points (ICP and XPS analysis on the samples have in fact revealed some traces of lithium and fluorine, but these are too low to be observed by SEM or detected by EDX analysis).

Meir et al. [54] showed that the rates of densification and LiF evaporation have to be controlled simultaneously by the applied pressure regime. Application of the pressure at low temperature may impede the elimination of residual LiF due to early closure of the pores. So, in an attempt to clarify if LiF was the main source of scattering, we also applied the pressure at different points of temperature

(1100°C and 1450°C). However, our experiments revealed no differences in terms of transmission or in the detected quantity of Li after these changes.

Finally, we also considered the residual amount of sulphur present in the LiF doped YAG-B sample. Sulphur was initially present at 550 ppm in YAG-B, after SPS it has already decreased (to 150 ppm after SPS at 1450°C). LiF addition promoted a further decrease down to 40 ppm, but this content might be still sufficient to explain the lack of transparency.

3.2.3. Conclusions on YAG-B powder

YAG-B powder is characterized by the presence of secondary phases (YAM and Y_2O_3) in relevant content, and also of a large amount of sulphur impurities (~ 550 ppm).

After powder deagglomeration, optimisation of the SPS parameters and post-treatments (annealing in air and post-hipping), no transparent or translucent ceramic was obtained. Even after sintering at high temperature, densification was incomplete and secondary phases were still detected by XRD measurements.

At least, two reasons can be proposed to explain this behaviour:

- Spark Plasma Sintering implies short cycles (high heating rates and short dwell times), and may not allow a complete conversion of intermediate phases into pure YAG;
- The presence of sulphur may slow down densification of YAG powder.

The addition of an optimised amount of LiF (0.2 wt%) accelerated densification, allowed a complete transformation of YAM and Y_2O_3 in pure YAG phase and led to transparent ceramics. The content of sulphur was strongly reduced by LiF addition. However, transparent ceramics were also characterized by an important scattering. This scattering may be due to undetected residual porosities, trapping of Li and/or F at grain boundaries or residual amount of sulphur.

To conclude between all these hypotheses, another commercial powder was also evaluated in this thesis.

3.3. YAG-N

YAG-N is a commercial powder from Nanocerox. This YAG powder is one of the most quoted commercial powder in the literature on transparent YAG ([62], [42], [53]). It is synthesized by Flame Spray Pyrolysis (FSP). During this synthesis, metalloorganic alcohol solutions are pulverised and fired in air or oxygen. The resulting precursor particles are then cooled down quickly to preserve their stoichiometry and nanosize dimensions. However, this high purity powder is very expensive (9000 \$/kg), and only small quantities were available: so the number of parameters studied to get transparent samples was reduced to the most influent ones determined previously.

3.3.1. Powder characteristics

Several characteristics of YAG-N were measured and compared to the supplier's data (see appendix A). The powder was observed by SEM, in order to identify the morphology and size of the primary particles (Figure 3.41). The powder is agglomerated but its primary particles are spherical, with diameter ranging from 20 to 200 nm.

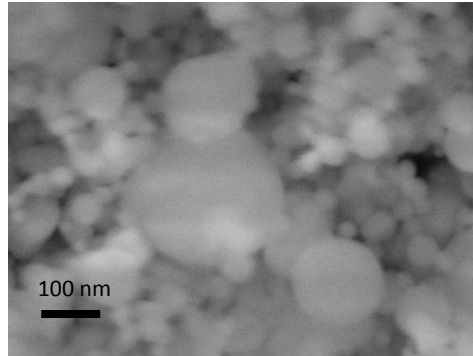


Figure 3.41. Micrograph of YAG-N powder.

The specific surface area was $20.1 \text{ m}^2/\text{g}$, corresponding with the data of the supplier ($20 \text{ m}^2/\text{g}$), and fairly larger than the first commercial powder. It can accordingly be expected that this powder will be more reactive during sintering. Using equation 3.1, the particle size was estimated at 66 nm, in agreement with the SEM observations.

The agglomeration state of this powder was also analysed. Figure 3.42 shows that even if this powder is also agglomerated, both size distribution and mean size of agglomerates ($d_{50} \sim 50 \mu\text{m}$) are smaller than those measured for the two other YAG powders.

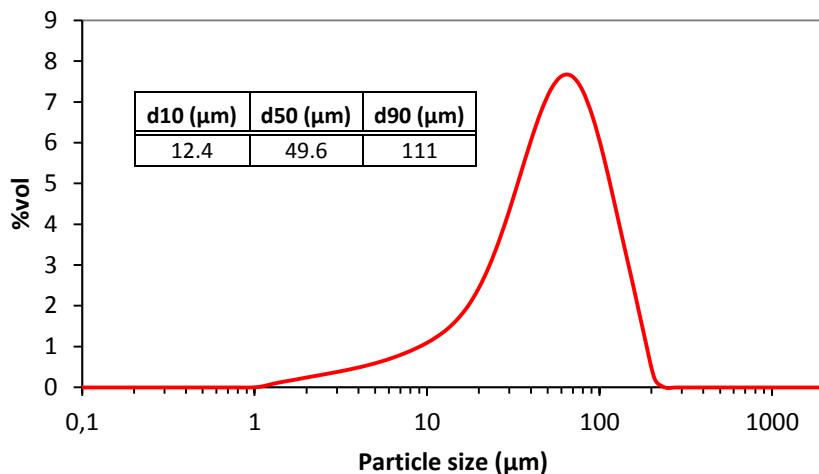


Figure 3.42. Frequency distribution (vol %) versus particle size of YAG-N powder

The XRD analysis of the Nanocerox powder (Figure 3.43) shows the hexagonal phase YAlO_3 (h- YAlO_3) as the main phase (89 wt%) and the presence of secondary phases as YAG and YAM in 7 wt% and 4 wt% respectively. It is remarkable that this powder presents a so small quantity of YAG as-received. This particularity offers the opportunity to evaluate the possibility of the conversion of intermediate phases into YAG (without addition of sintering aids) through a rapid sintering technology as SPS.

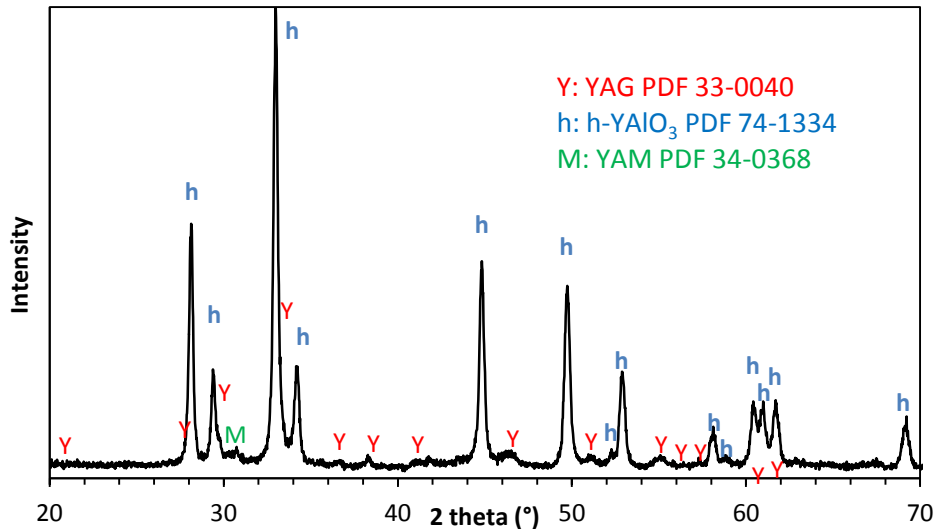


Figure 3.43. XRD of Nanocerox YAG powder.

Impurities in the YAG-N powder have been analyzed by ICP; results confirmed the high purity level of this powder with no detected impurities above 4 ppm.

3.3.2. Sintering and transparency improvement

3.3.2.1. Sintering behaviour

The sintering behaviour of YAG-N powder was evaluated by following the densification in the SPS equipment at a heating rate of 20°C/min from 500 to 1650°C under a constant pressure of 50 MPa. Result is reported in Figure 3.44.

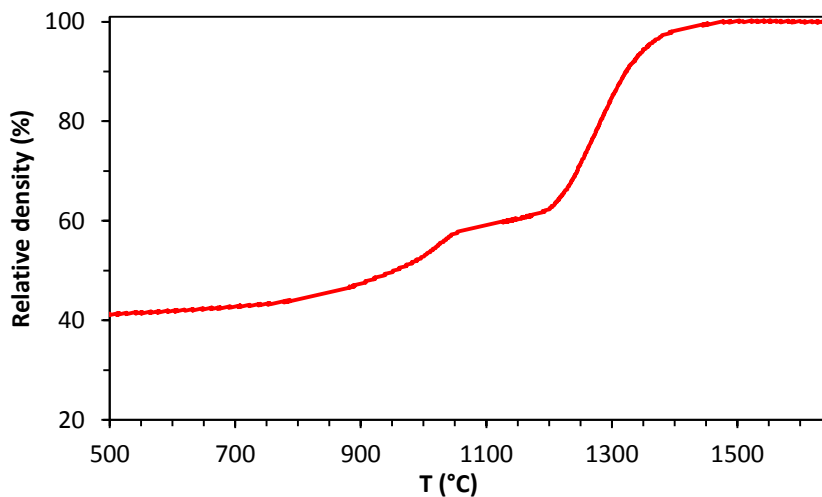


Figure 3.44. Relative density of YAG-N powder as a function of the temperature (heating rate 20°C/min, pressure 50 MPa).

YAG-N showed a densification similar to YAG-B. Nevertheless, three main differences appear. First, the relative density is 41% at 500°C, lower than YAG-B (around 53%), as a result of its higher specific surface area and sharper granulometric distribution. Second, there is a slope change between 900

and 1050°C corresponding to the transformation of h-YAlO₃ and YAM into the YAG phase [140]. This difference is noticeable owing to the large amount of h-YAlO₃ compared to the amount of secondary phases in YAG-B powder. Third, this powder is slightly more reactive than YAG-B, and reaches full density at 1450°C (vs 1500°C for YAG-B), but much less than YAG-S. This behaviour is in a good agreement with its high specific surface area too.

After this thermal cycle, the sintered sample exhibited a dark appearance. XRD semi-quantitative analyses showed that at 1650°C, YAG-N was composed of pure YAG phase. According to the Al₂O₃/Y₂O₃ phase diagram, this complete transformation of initial phases into YAG implies the presence of undetected alumina in the starting powder. It also shows that even if intermediate phases were present in large quantities, a complete conversion into pure YAG is possible, even with high heating rate and short sintering cycle.

3.3.2.2. Influence of SPS parameters on density, microstructure and visual aspect of the samples

- **Heating rate influence**

The effect of the heating rate on YAG-N densification was evaluated comparing two heating rates: 10 and 50°C/min from 1100°C up to 1400°C. The SPS cycle was the following: a pressure of 50 MPa was applied from the beginning of the thermal cycle; then a first heating step at 100°C/min up to 1100°C, followed by a step at a lower heating rate up to 1400°C and a 15-min long isothermal step. The cooling rate was fixed to 150°C/min. Figure 3.45 depicts the evolution of the relative density with the temperature, for heating rates of 10°C/min and 50°C/min. Differences in the density evolution with the temperature are observed in function of the heating rate: for a given temperature, the sample sintered at lower heating rate showed higher density. During the dwell the sample sintered at 50°C/min continues densifying while the one sintered at 10°C/min had almost achieved full density at the beginning of the dwell.

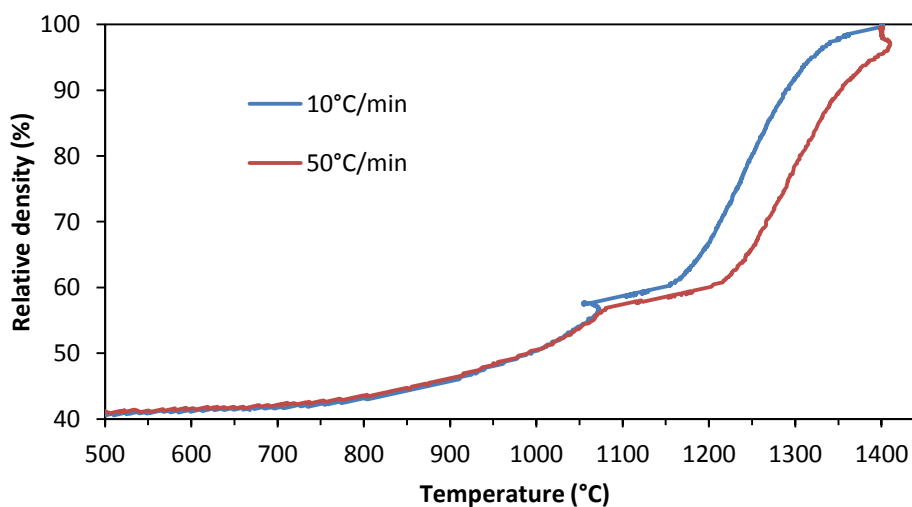


Figure 3.45. Relative density of YAG-N vs temperature for two different heating rates ($T=1400^{\circ}\text{C}$, $P=50\text{MPa}$).

XRD analysis on both samples shows only the YAG phase after sintering. Relative densities are close to 100% (99.5 and 99.9% for 50°C/min and 10°C/min, respectively). Figure 3.46 shows the appearance and microstructure of the samples. The sample sintered at the higher heating rate presents a less transparent appearance: this observation is in agreement with the porosities observed on the microstructure. These results agree with other publications ([42], [10]), where a diminution of the optical transmission with the use of high heating rates was also observed. Grain size of both samples is heterogeneous, between 100 and 800 nm, but the sample sintered at the higher heating rate presents smaller grains (mean grain size around 200 nm). Consequently, after these first results, the following samples will be sintered at a heating rate of 10°C/min.

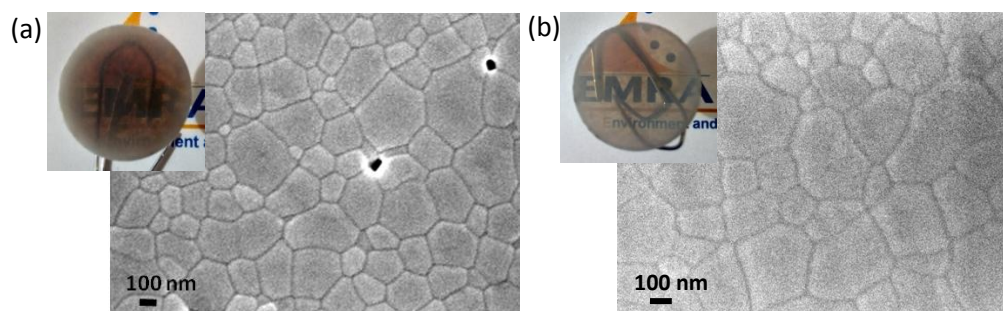


Figure 3.46. Images and microstructures of YAG-N samples sintered at 1400°C with heating rates of (a) 50°C/min and (b) 10°C/min.

- **Temperature influence**

The effect of the sintering temperature was evaluated between 1400 and 1500°C, with a pressure of 50 MPa and a heating rate of 10°C/min from 1100°C and a dwell of 15 minutes at the final temperature.

Figure 3.47 shows images of the sintered samples and their microstructure. All three samples presented a relative density of at least 99.9%, with a reduction of the darkening with the increase of the temperature.

The only phase detected in these samples after XRD analysis was the phase YAG.

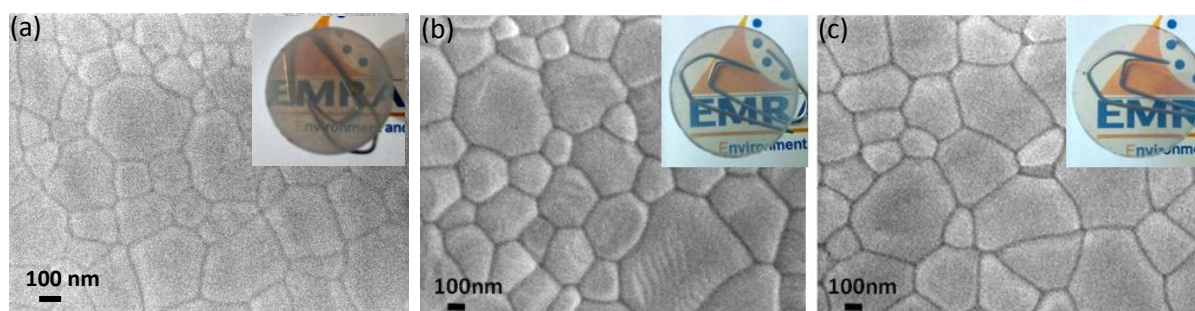


Figure 3.47. Images and microstructures of YAG-N sintered samples at (a) 1400°C; (b) 1450°C and (c) 1500°C.

The improvement of the transparency of the samples with the increase of the sintering temperature is certainly linked to the elimination of the small residual porosities (not detected in our SEM observations) inside the samples, as observed in Figure 3.46 with the effect of heating rate.

The sample sintered at 1500°C presented a very transparent appearance. In addition, this sample did not scatter light as much as LiF-doped YAG-B samples, as the text situated 15 mm under the samples can be clearly read.

Regarding the microstructure of the samples, grain size is between 200 and 800 nm in the three micrographs, with a larger proportion of larger grains at higher temperatures.

- **Pressure influence**

Once a quite transparent ceramic was obtained, the effect of the pressure on its optical transmission was assessed. We have tested pressures of 30, 50 and 70 MPa applied at the beginning of the SPS cycle with a sintering temperature of 1500°C. The other parameters were kept as defined previously.

Figure 3.48 reflects the evolution of the relative density during sintering at different pressures; an influence of the pressure on the relative density is observed since the beginning of the cycle. 70 MPa led to a higher density of the green body (45% relative density for 70 MPa vs 41% for 30 and 50 MPa) and all along the SPS cycle. There is thus an increase of the relative density with the increase of the pressure for a given temperature. But anyway, at the end of the cycle all three samples reached full density.

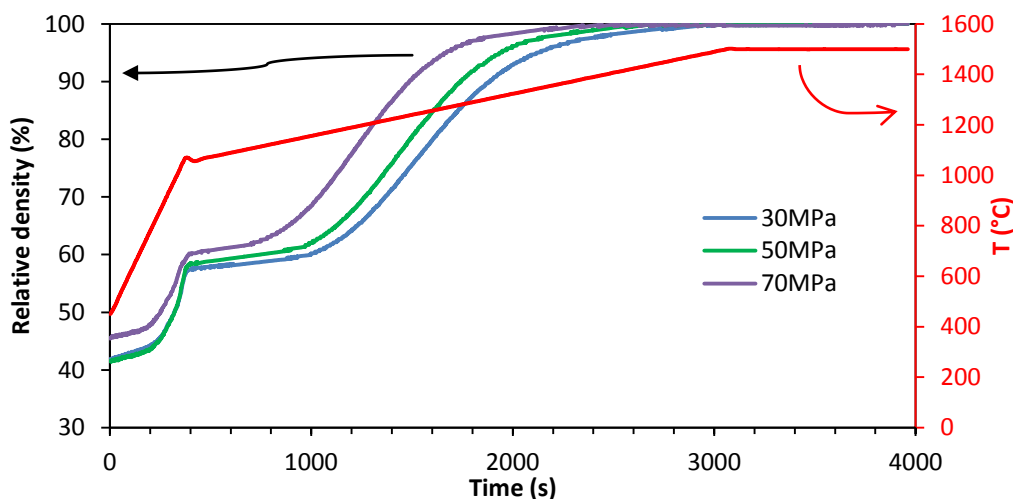


Figure 3.48. Relative density evolution of YAG-N compacts sintered at 1500°C under pressures of 30, 50 and 70 MPa.

As illustrated in Figure 3.49, all samples show a quite transparent aspect in agreement with the high density achieved. Samples sintered at 30 and 50 MPa show a homogenous transparent aspect, with visually almost no differences, while at 70 MPa a higher darkening inside the samples is observed. This aspect agrees with the results of Wang et al. [61] who described a higher darkening at higher pressures in spinel.

Wang et al. [61] pointed out that densification under external pressure can be regarded as an analogy of creep or superplastic deformation. Superplastic deformation is mostly realized through grain boundary (GB) sliding, which can be accommodated by either GB diffusion or dislocation climb from the GB. Higher deformation rate, higher stress and higher deformation temperature will facilitate the dislocation mechanism. For a porous material, the stress and strain can be easily

accommodated by the pore structures, and so there is much less possibility of generating a high dislocation density if a similar strain rate and deformation temperature are applied. Better transmission at lower pressure samples should be linked with lower levels of dislocation.

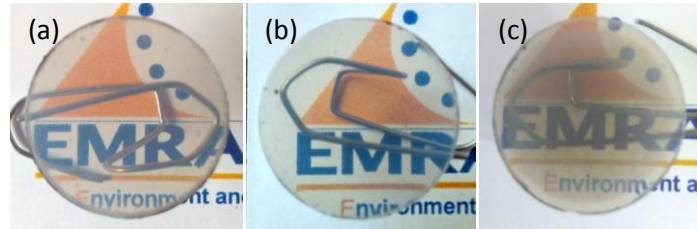


Figure 3.49. Images of samples from YAG-N sintered at 1500°C under pressures of (a) 30 MPa; (b) 50 MPa and (c) 70 MPa.

Concerning the microstructure of the samples (Figure 3.50), the increase of pressure was translated in a slight grain growth. Sample sintered at 30 MPa presented grains between and 100 and 800 nm and sample sintered at 70 MPa between 100 and 900 nm.

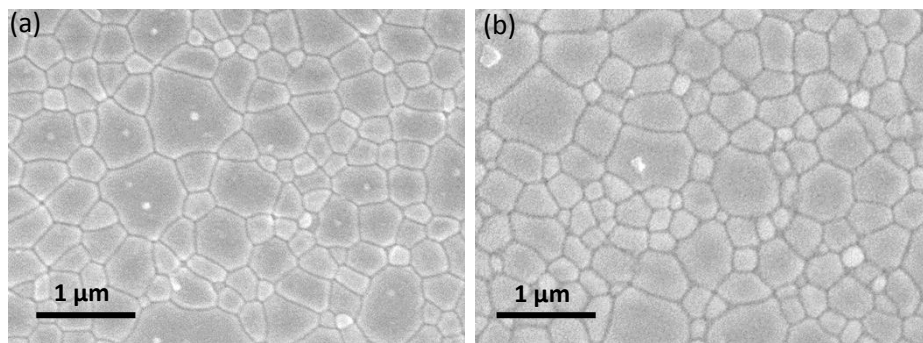


Figure 3.50. Microstructures of YAG-N sintered samples under (a) 30 MPa and (b) 70 MPa.

- Optical transmission

Figure 3.51 depicts the total forward (TFT) and real-in-line (RIT) transmission of YAG-N samples sintered at different pressures up to the temperature of 1500°C for 15 min. Transmission curves correlate with the visual aspect of the samples (Figure 3.49). For these samples, TFT and RIT values are closer owing to the smaller amount of scattering. The minor transmission losses come from the absorption ascribed to the slight darkening of the samples.

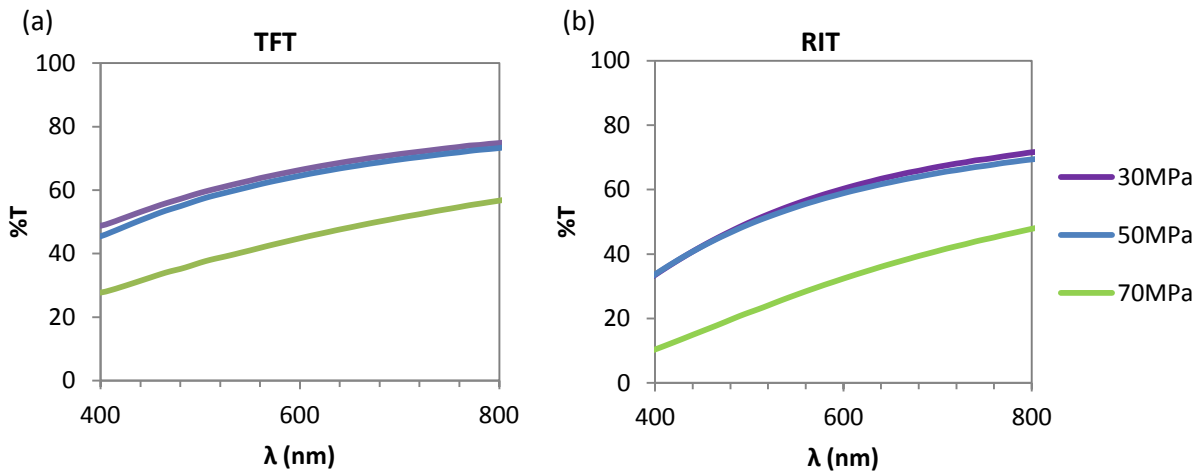


Figure 3.51. Optical transmission of samples from YAG-N sintered at 1500°C under different pressures: (a) TFT and (b) RIT values.

It is remarkable that samples from YAG-N as-sintered are very transparent, even more transparent than samples from the two other powders after annealing or post-hipping (TFT and RIT values, measured at 600 nm, are 64 and 59%, respectively). This result highlights the influence of the starting powder on the optical transmission of the samples. This powder is purer and less agglomerated and attains 100% density after sintering, with total conversion to the YAG phase, leading to more transparent samples.

3.3.2.3. Influence of pre- and post-treatments on the optical transmission

- **Annealing**

Samples of YAG-N were submitted to annealing in air in order to reduce the slight darkening they presented after sintering and further improve the optical transmission. Different temperatures and dwell times were tested. In Figure 3.52, images of some annealed samples are shown: a progressive diminution of the darkening appears with the increase of the annealing temperature and time. However, for the highest tested temperature (1200°C), no further improvement is observed.

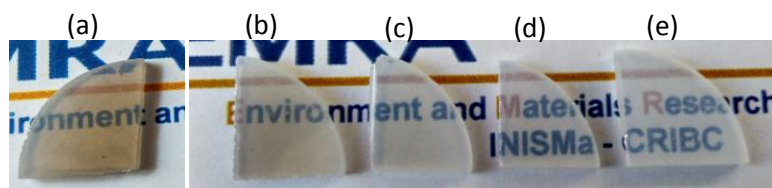


Figure 3.52. Images of YAG-N samples sintered at 1450°C, (a) before annealing; and after annealing in air at 5°C/min up to: (b) 1100°C 12 hour; (c) 1100°C 24h; (d) 1150°C 12h; (e) 1200°C 12h .

In order to quantify the benefits or disadvantages of the annealing and to deduce the best annealing conditions, the optical absorption and transmission of the samples were measured.

Figure 3.53 shows how much the absorption decreased with the increase of the annealing temperature. It is noticeable as well that the main absorption decrease happens up to 1150°C.

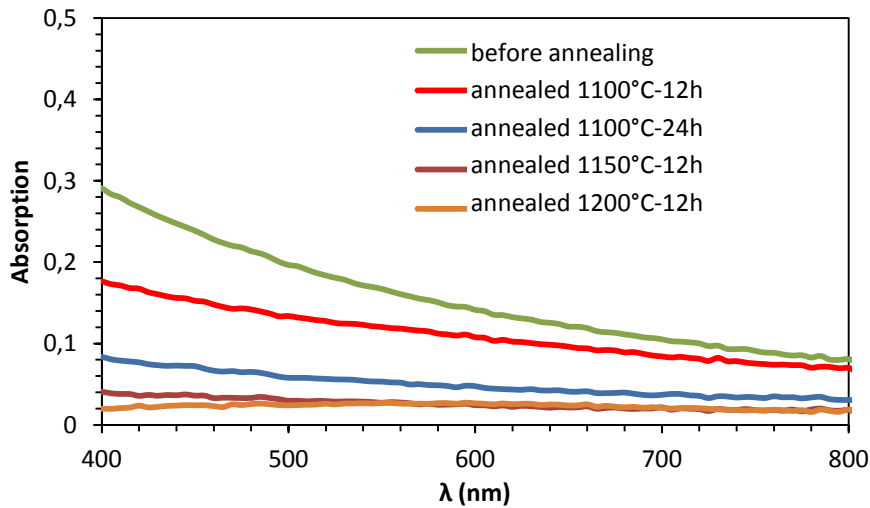


Figure 3.53. Absorption spectra of samples sintered at 1450°C after different annealing conditions.

Regarding the in-line transmission (Figure 3.54), there is a correlation with the absorption values. The RIT values increase with the increase of the annealing temperature up to 1150°C. At higher temperatures no further improvement of the transmission is observed, with even a slight decrease of RIT value at lower wavelengths.

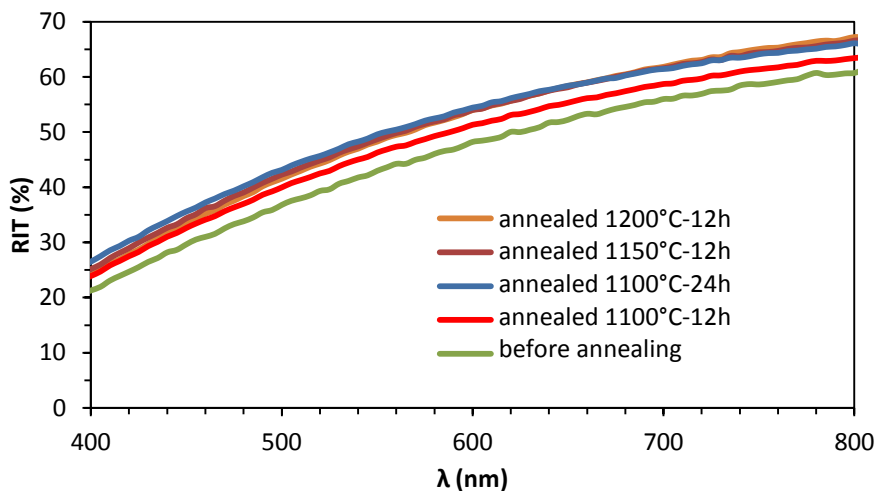


Figure 3.54. Optical transmission (RIT) of samples sintered at 1450°C after different annealing conditions.

Up to 1150°C, oxygen vacancies and graphite contamination reduce as the annealing temperature increases, but for higher temperatures, grain growth and pore arrangement start and cause an increase of scattering. For this reason, RIT did not rise, and even decrease, after annealing at 1200°C. From these results, a post-treatment in air at 1150°C for 12 hours was considered as the optimal annealing conditions.

Table 3.4 summarizes the TFT, RIT and absorption values of YAG-N samples sintered at 1450°C and 1500°C (before and after annealing). The best value, RIT of 66% at 600 nm, was obtained for a sample sintered at 1500°C after annealing. The image of the sample (1.5 mm-thick) is exhibited in Figure 3.55.

Table 3.4. Optical transmission and absorption (measured at 600 nm) of samples sintered at 1450°C and 1500°C, before and after annealing.

T _{SPS} (°C)	Annealing	TFT (%)	RIT (%)	Absorption
1450	no	61	50	0.154
1450	1150°C-12h	72	54	0.024
1500	no	63	57	0.141
1500	1150°C-12h	75	66	0.022

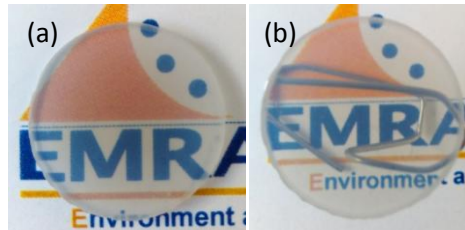


Figure 3.55. Appearance of a sample (thickness = 1.5 mm) sintered at 1500°C for 15 min after annealing in air at 1150°C for 12 hours: (a) placed on the text, (b) placed 15 mm above the text.

- **LiF addition.**

Addition of 0.2 wt% LiF to YAG-N was also tested in order to compare the results with those obtained in YAG-B. The goal was to discern if this additive improved the optical transmission of the samples or was the source of the important scattering found in YAG-B.

Figure 3.56 depicts the sintering behaviour of two samples (without and with 0.2%wt LiF) sintered by SPS at 1400°C, with an isothermal step of 15 minutes and 50 MPa applied since the beginning of the cycle. Two heating rates were used as previously, 100°C/min up to 1100°C and 10°C/min from this temperature up to the final temperature. LiF addition to YAG-N promotes its densification at lower temperatures as in the case of YAG-B. For instance, LiF-doped sample attains 99.5% relative density at 1315°C while the non-doped sample needed 1395°C to reach the same density.

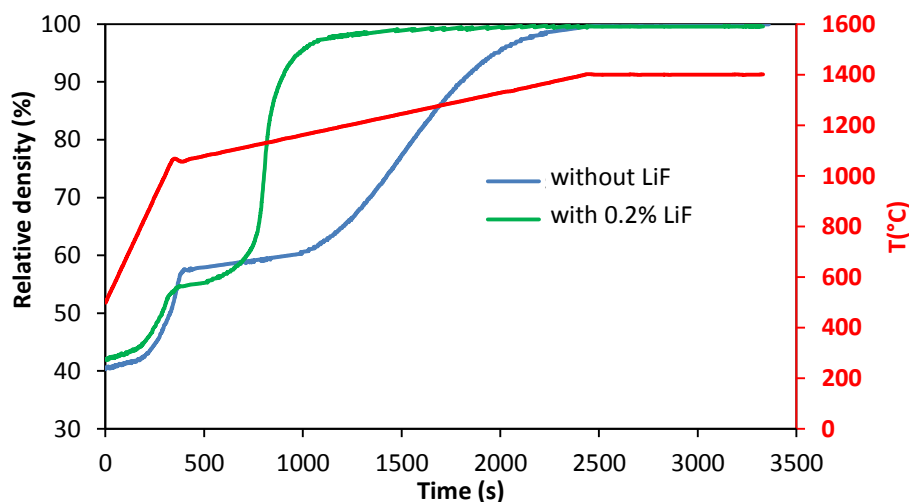


Figure 3.56. Relative density evolution of YAG-N samples sintered at 1400°C for 15 min (50 MPa), without LiF and with 0.2 wt% LiF.

Figure 3.57 reveals the appearance of the LiF-doped sample. LiF addition leads to a more transparent and homogeneous sample. Moreover, the optical scattering is low, as the text situated 15 mm under the sample can be clearly read. The relative density of the sample is near 100%. As observed for YAG-B, addition of LiF causes an important grain growth, with grains between 0.3 and 3.5 μm (average grain size was 0.2 μm for non-doped YAG-N sintered in the same conditions).

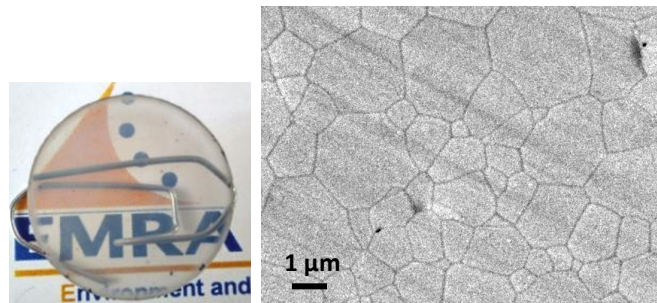


Figure 3.57. Appearance and microstructure of a YAG-N sample (thickness 1.5 mm) doped with 0.2 wt% LiF and sintered at 1400°C for 15 min.

In order to evaluate the optical transmission of the samples and compare with the best results obtained without LiF addition, a sample was also sintered at 1500°C for 15 minutes. Figure 3.58 exhibits this sample: it presents a very transparent appearance and no darkening.

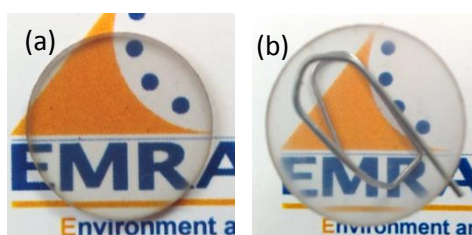


Figure 3.58. Appearance of a YAG-N sample (thickness = 1.4 mm) doped with 0.2 wt% LiF and sintered at 1500°C for 15 min (a) placed on the text, (b) placed 15 mm above the text.

The optical absorption and transmission of the LiF-doped samples were also characterized. Absorption values were almost 0. Transmission measurements (Figure 3.59) revealed that LiF addition improved the transmission of YAG-N compared to sample sintered without LiF in the same conditions. Scattering was also limited because RIT and TFT values were close. This result reinforces the hypothesis that the important scattering measured for YAG-B, with LiF addition, was not due to LiF trapping at grain boundaries or incorrect mixing of LiF and YAG powders, but rather to the residual presence of sulphur acting as source of scattering.

The transmission values of LiF-doped samples were 70% RIT and 77% TFT at 600 nm wavelength so higher than the values for the non-doped samples, especially at shorter wavelengths (this large difference at low wavelengths suggests that residual porosities or oxygen vacancies are still present in non-doped YAG-N powder).

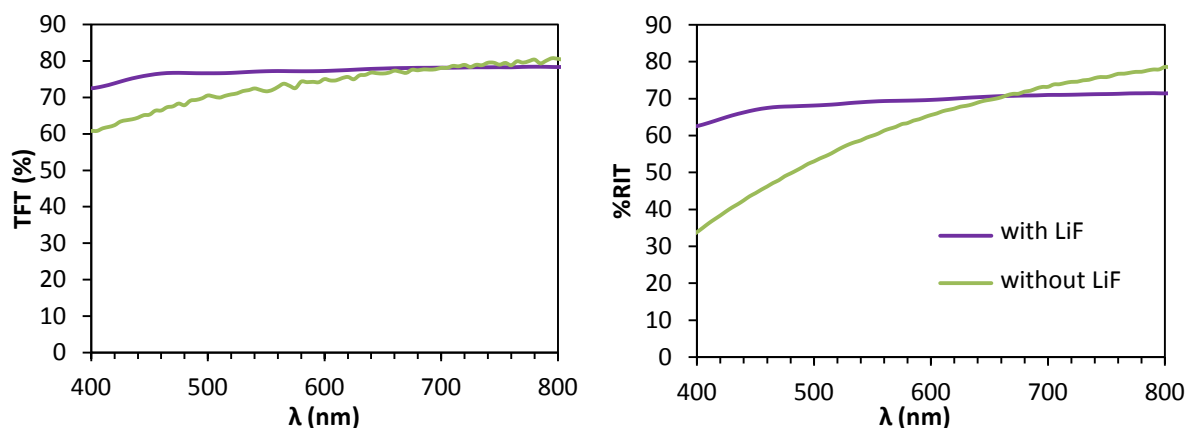


Figure 3.59. Optical transmission of YAG-N samples sintered at 1500°C without LiF and annealed (green) and with 0.2% LiF (violet).

3.3.3. Conclusions on YAG-N powder

Transmission results of YAG-N samples after Spark Plasma Sintering are better than those of the two other YAG powders. Even without any pre-treatment or post-treatment, YAG-N results were more positive, with transparent and homogeneous samples obtained as-sintered.

Complete conversion of intermediate species present initially in the powder ($h\text{-YAlO}_3$ and YAM) into pure YAG phase was possible, even with the use of short sintering cycle (high heating rate and short dwell time).

Owing to the low degree of agglomeration of the powder, the core-shell aspect was almost imperceptible and transparent ceramics were obtained without any dispersion.

SPS parameters influence the optical transmission of the samples: the use of slow heating rates and moderate pressures is beneficial to the final optical transmission.

The slight coloration of the sample, due to the presence of oxygen vacancies, can be eliminated by a post-annealing in air or addition of a small amount of lithium fluoride.

3.4. Conclusions chapter III

Three YAG powders, with different physicochemical properties (phase composition, specific surface area, agglomeration degree, purity ...) were studied in this chapter (see characteristics of the starting powders in Table 3.5).

Table 3. 5. Characteristics of the starting powders.

Powder	Phases detected by XRD	Specific surface area (m ² /g)	Agglomeration degree	Impurities
YAG-S	YAG	46 ± 0.2	Large	-
YAG-B	YAG (96%) + YAM + Y ₂ O ₃	7 ± 0.1	Large	S : 500 ± 10 ppm
YAG-N	h-YAlO ₃ (90%) + YAG + YAM	20 ± 0.2	Medium	-

YAG-S is a home-synthesized powder, composed only with YAG phase, with high purity and high specific surface area. Unfortunately, YAG-S powder is largely agglomerated, with a mean agglomerates size around 180 µm.

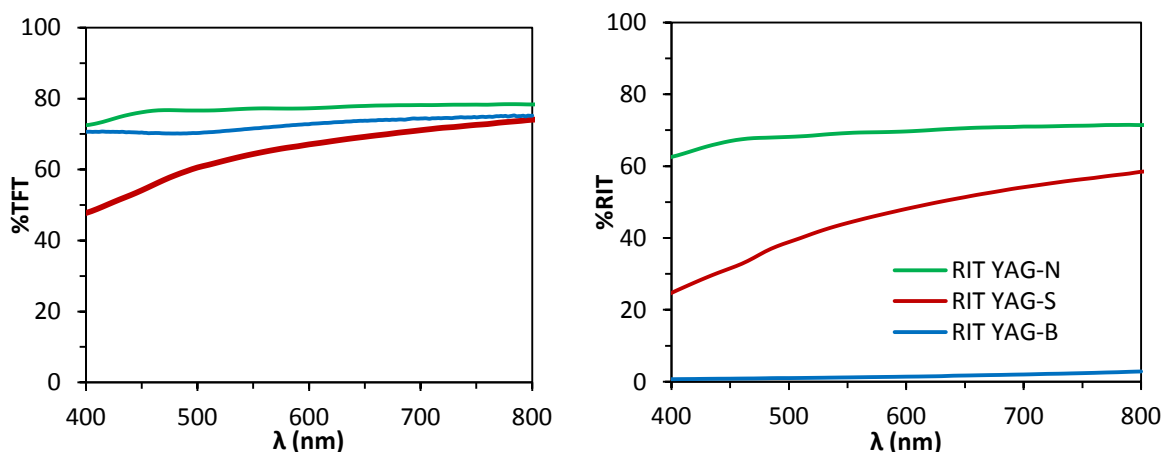
YAG-B is a commercial powder, synthesized from sulphate precursors, explaining the large amount of sulphur in the powder (~500 ppm). This powder is mainly composed of YAG phase, but traces of intermediate phases (YAM and Y₂O₃) are observed. Agglomerates size distribution is large, with a mean size around 160 µm.

Finally, YAG-N, a commercial powder synthesized by Flame Spray Pyrolysis, presents a high level of purity and a moderate agglomeration degree (mean agglomerates size around 50 µm). As received, this powder is composed mainly of intermediate phases in YAG synthesis, h-YAlO₃ and YAM, with only 7wt% of YAG.

These wide properties differences offered the opportunity to evaluate their relative effect on the final transparency of the ceramics.

After optimisation of SPS sintering parameters, pre-treatments and/or post-treatments, transparent ceramics have been obtained from each powder. Best results (TFT and RIT transmission spectra) are shown in Figure 3.60.

The highest values obtained for YAG-N were a total transmission of 77% and in-line transmission of 70% at 600 nm. The best samples obtained for YAG-S showed 67% TFT and 48% RIT at 600 nm. For YAG-B, optimised samples showed high TFT values (73% at 600 nm), but unfortunately very low RIT values.

**Figure 3.60. Comparison of the best optical transmissions for the three YAG powders sintered by SPS.**

As-sintered, samples presented some darkening, whatever YAG powder used, owing to the formation of oxygen vacancies, during vacuum sintering, and graphite contamination. However, this coloration could be, at least partially, removed by annealing in air.

Differences, in terms of sintering behaviour and final optical transmission, between powders, can be related to their physicochemical properties.

Despite the low content of YAG phase in YAG-N powder, conversion of intermediate phases into pure YAG was possible even with the use of short sintering cycles (high heating rate and short dwell time). Owing to its high purity and lower agglomeration degree, YAG-N led to transparent ceramics without pre-treatments of the powder (deagglomeration or LiF addition). However, addition of 0.2% LiF led to an improvement of the optical transmission, induced by the decrease of the small residual porosity content (not observed by SEM observations). Both TFT and RIT values were high (higher than 70%), proving that mixing between YAG-N powder and lithium fluoride was homogeneous and that Li and F are unlikely the main sources of scattering in YAG-B.

On the contrary, owing to its high degree of agglomeration, deagglomeration of YAG-S powder was necessary to obtain samples with relevant transparency level. However, even after deagglomeration, samples presented a core-shell aspect, with an opaque centre and a more transparent external part. More homogeneous samples were obtained after an optimised post-hipping cycle in air. A simple annealing in air was not sufficient to remove the core-shell aspect, it was concluded that the opaque centre was due to the presence of residual porosities (that can be removed by post-hipping, with the application of a high isostatic pressure). Comparison of the microstructures and finite element method modelling suggested that this aspect was not caused by temperature gradients inside the samples. On the contrary, this core-shell aspect was rather ascribed to the presence of stress gradients during sintering, that did not lead to noticeable microstructural heterogeneities .

Finally, for YAG-B powder, no transparent ceramics were obtained, even after powder deagglomeration. Samples were not fully densified and presence of secondary phases of YAP and YAM was detected by XRD. Addition of a small amount of LiF led to full densification, diminution of sulphur content (50 ppm), pure YAG phase and transparent ceramics. However, all LiF-doped samples presented a large amount of scattering. As the same LiF content and mixing method were used for YAG-N, this large scattering seems rather to be due to the residual sulphur content (acting as scattering centre) than to the presence of Li and F at grain boundaries. Moreover, for un-doped YAG-B samples, incomplete densification and presence of secondary phases was not linked to the short SPS sintering cycles, but to the sulphur slowing down YAG densification.

Figure 3.61 shows the best transparent ceramics obtained for each YAG powder.

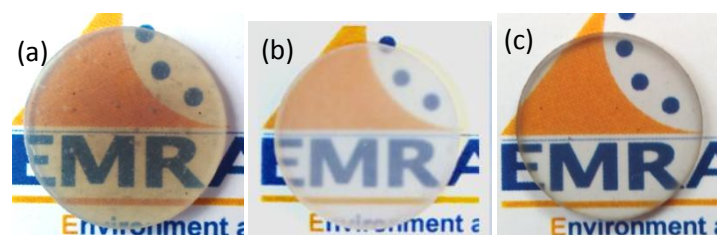


Figure 3.61. Images of best transparent samples sintered from (a) YAG-S, (b) YAG-B and (c) YAG-N powders.

Concerning transparent YAG ceramics obtained by SPS, Figure 3.62 compares some of the best results obtained to our knowledge with those obtained during this Ph. D. thesis: RIT values are high and close to the maximal values, even without LiF addition.

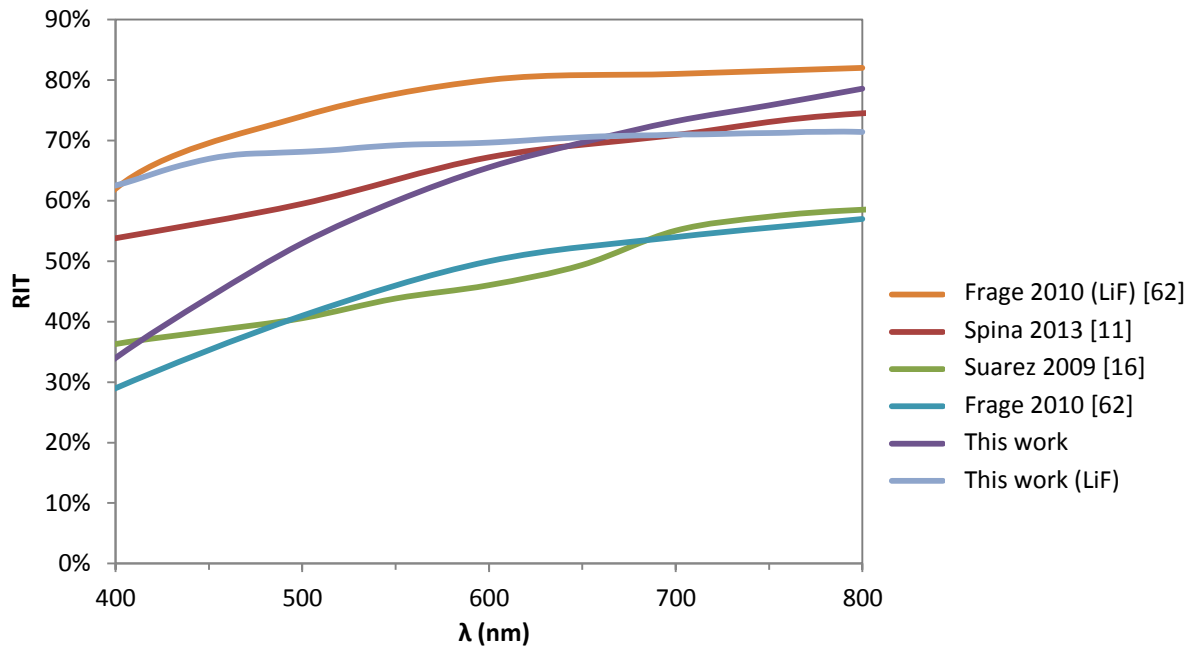


Figure 3.62. Optical transmission of transparent YAG ceramics prepared by SPS.

Thanks to the study of YAG, the influence of the starting powders and the SPS parameters on the transparency was evaluated.

Regarding the starting powders, the detrimental effect of impurities, even in a concentration as low as 50 ppm, was demonstrated. Moreover, the presence of agglomerates persistent after deagglomeration processes led to differential sintering and porosities in the sintered compacts.

Regarding the SPS parameters, the temperature should be adapted to each powder: it should be high enough to achieve full density without grain growth and coalescence of tiny pores. But, in all cases, moderate pressures (50 MPa) and low heating rates (10°C/min) offer usually the best optical results.

The procedure and conclusions obtained during the analysis of the YAG powders and compacts has allowed publishing an article in a peer-reviewed journal (Journal of Ceramic Science and Technology).

Taking the study of YAG into consideration, the following chapter will concern the study of barium titanate.

Chapter IV – Barium Titanate

Table of contents

4.1. Powders characterisations	115
4.1.1. Barium titanate	115
4.1.2. Barium strontium titanate	117
4.2. Processing dense ceramics with controlled microstructure	119
4.2.1. Barium titanate	120
4.2.1.1. Sintering behaviour	120
4.2.1.2. Influence of SPS parameters on density, microstructure and optical aspect.....	121
4.2.1.3. Powder deagglomeration	130
4.2.1.4. Conclusions	133
4.2.2. Barium strontium titanate	134
4.2.2.1. Sintering behaviour	134
4.2.2.2. Influence of SPS parameters on density, microstructure and optical aspect.....	135
4.2.2.3. Effect of powder deagglomeration	141
4.2.2.4. Conclusions	142
4.3. Functional properties	142
4.3.1. Optical properties.....	142
4.3.2. Dielectric properties	147
4.4. Conclusions chapter IV.....	158

The previous chapter highlighted the major influence of powders characteristics and of de-agglomeration and post-annealing on the optical properties of YAG ceramics prepared from three different powders.

This chapter concerns the study of barium titanate (BT) and barium strontium titanate (BST) powders. Two commercially available powders are used, a monophasic BaTiO_3 (abbreviated BT) and a $\text{Ba}_{0.8}\text{Sr}_{0.2}\text{TiO}_3$ (BST).

For each powder, the SPS parameters (temperature, pressure, heating rate ...) and the pre- and post-treatments steps were optimised to attain a dense ceramic, as transparent as possible.

The dielectric properties were also measured and results were related to the composition (influence of the strontium addition in the powder) and microstructure (homogeneity and grain size) at equivalent density.

4.1. Powders characterisations

4.1.1. Barium titanate

The barium titanate powder used in this study is a commercial powder from Inframat Advanced Materials. From the supplier's certificate of analysis (see appendix A), this is a nanometric powder (particle size 50 nm) with high purity (99.95%). No information concerning the synthesis route was available from the provider.

XRD analysis (Figure 4.1) shows the presence of BaTiO_3 with some traces of BaCO_3 , probably coming from the synthesis route. The absence of doublets in the diffractogram indicates only the cubic phase of barium titanate. However, in the case of pseudo-cubic structure, with low c/a ratio, the tetragonal phase of nanograins is difficult to observe by XRD [141]. After Rietveld refinement, the powder seems to be composed with a mixture of tetragonal and cubic phases (96% and 4%, respectively). The cell parameters for the tetragonal phase are $a = b = 4.01 \text{ \AA}$ and $c = 4.03 \text{ \AA}$ ($c/a=1.005$). The cell parameters for the cubic phase are $a = b = c = 3.99 \text{ \AA}$.

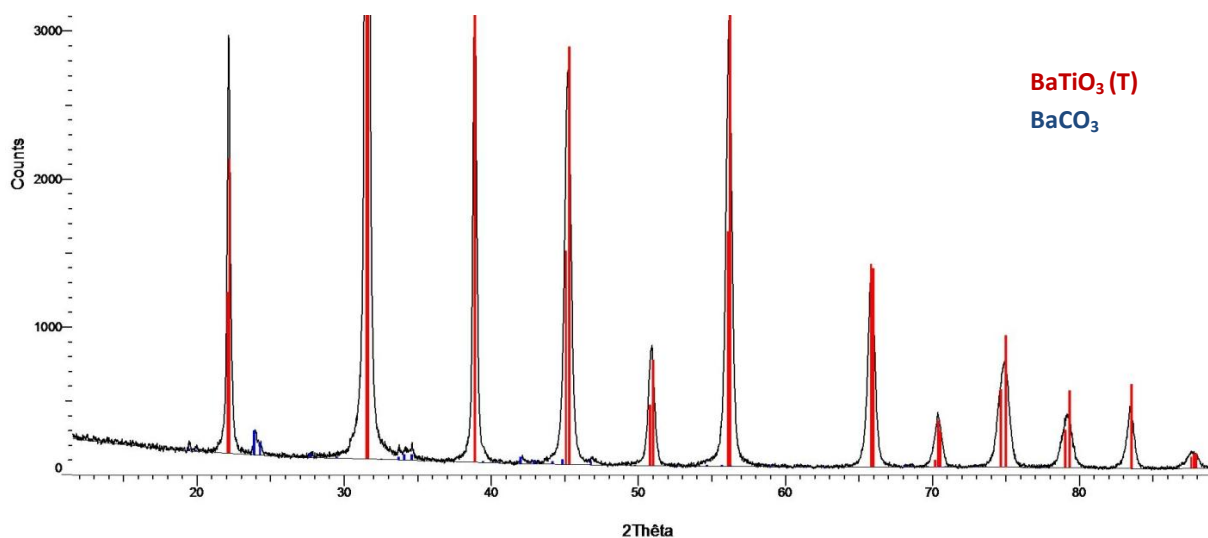


Figure 4.1. XRD of BaTiO_3 powder.

Figure 4.2 shows the Raman spectrum of the BaTiO_3 commercial powder.

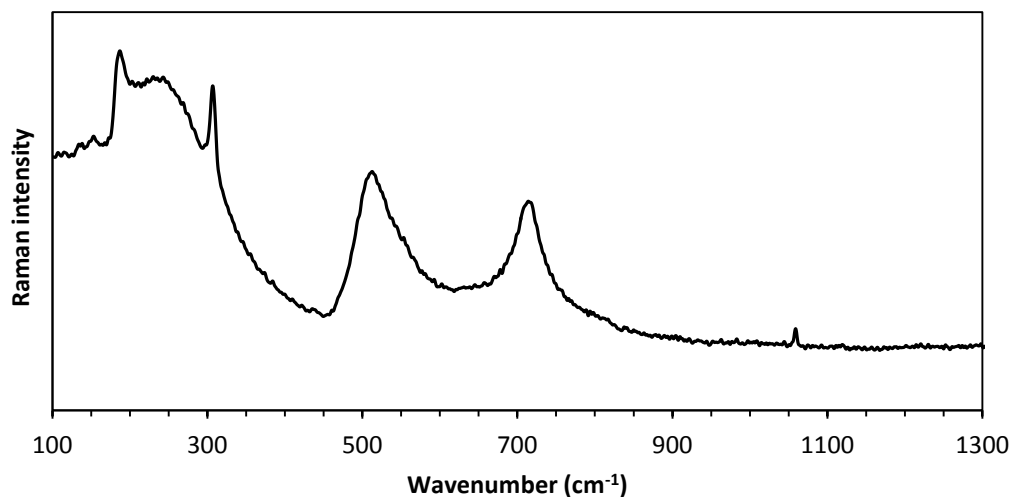


Figure 4.2. Raman spectrum of BaTiO_3 powder.

Raman spectrum of the powder confirmed the Rietveld refinement results in terms of tetragonality of the barium titanate powder: all the bands characteristic of the tetragonal structure are visible (240, 307, 514 and 717 cm^{-1}). Bands at 240 and 514 cm^{-1} are characteristic of both cubic and tetragonal phases, while bands at 305 and 715 cm^{-1} appear only in tetragonal BaTiO_3 ([141], [142]). Since the bands characteristic only for tetragonal phase are prominent in the spectrum, the tetragonal phase of BT seems to be the main phase. In addition, the line at 188 cm^{-1} is characteristic of tetragonal phase in case of a powder composed of small crystallites, which is the case with this powder.

Finally, the bands of small intensities observed at 153 and 1060 cm^{-1} are assigned to BaCO_3 [141].

Physicochemical properties of the powder have been characterised and compared to the supplier's data. ICP analysis shows high purity (over 99.9 wt%) with trace elements of Al, Co, Hf, Ni, Si and Sr. Ba/Ti ratio was checked by XRF and it corresponds to 1, indicating the perfect stoichiometry of the powder.

The specific surface area of the powder, measured using the BET method, is $18.2 \text{ m}^2/\text{g}$, close to the data of the provider ($20 \text{ m}^2/\text{g}$). The estimated primary particle size according to this specific surface area is 55 nm (using the theoretical density of BaTiO_3 , 6.02 g/cm^3).

SEM observations revealed round-shape elementary particles, smaller than 100 nm (Figure 4.3), in agreement with the size calculated from the specific surface area value. Observations at smaller magnifications show that the small particles are organised in agglomerates of different sizes, with some of them larger than $20 \text{ }\mu\text{m}$.

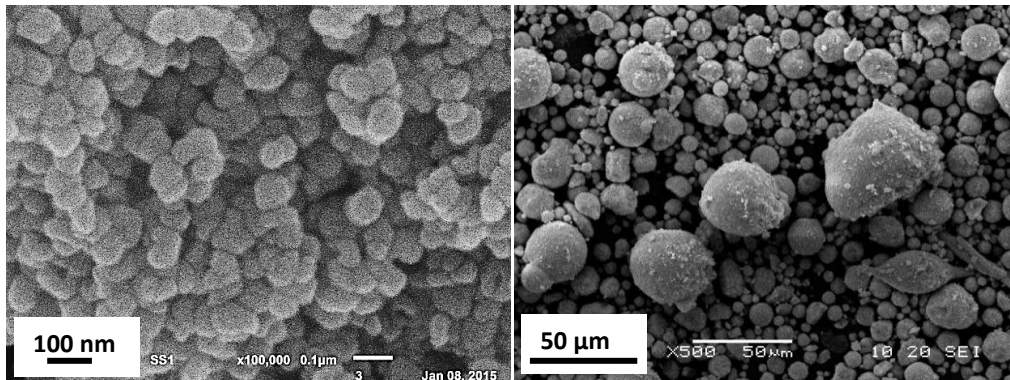


Figure 4.3. SEM images of BaTiO_3 powder at different magnifications.

These agglomerates have also been found on granulometric measurements. Figure 4.4 shows the agglomerate size distribution of the powder, with mean agglomerate size below $10 \text{ }\mu\text{m}$ and agglomerates as large as $80 \text{ }\mu\text{m}$, in agreement with the SEM observations as well.

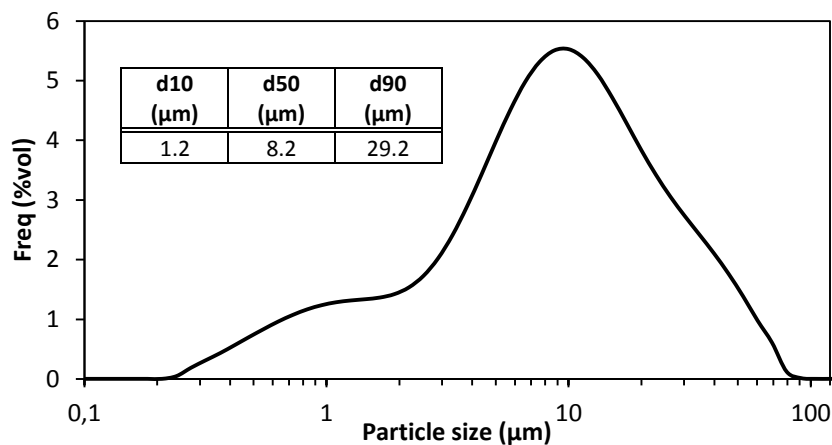


Figure 4.4. Frequency distribution (vol %) versus particle size of BaTiO_3 powder.

4.1.2. Barium strontium titanate

A barium strontium titanate (BST) powder from TPL inc., with $\text{Ba/Sr} = 80/20 \%$, was also studied in this thesis. According to the supplier's certificate of analysis (shown in appendix A), this powder, prepared by hydrothermal synthesis, is a nanometric powder with high purity ($>99.5\%$).

Several characterisations were performed on this powder to check the supplier's data.

XRD analysis shows the presence of $\text{Ba}_{0.8}\text{Sr}_{0.2}\text{TiO}_3$, apparently in its cubic phase (Figure 4.5) owing to the absence of doublets at higher angle values. Some traces of barium carbonate BaCO_3 are also detected.

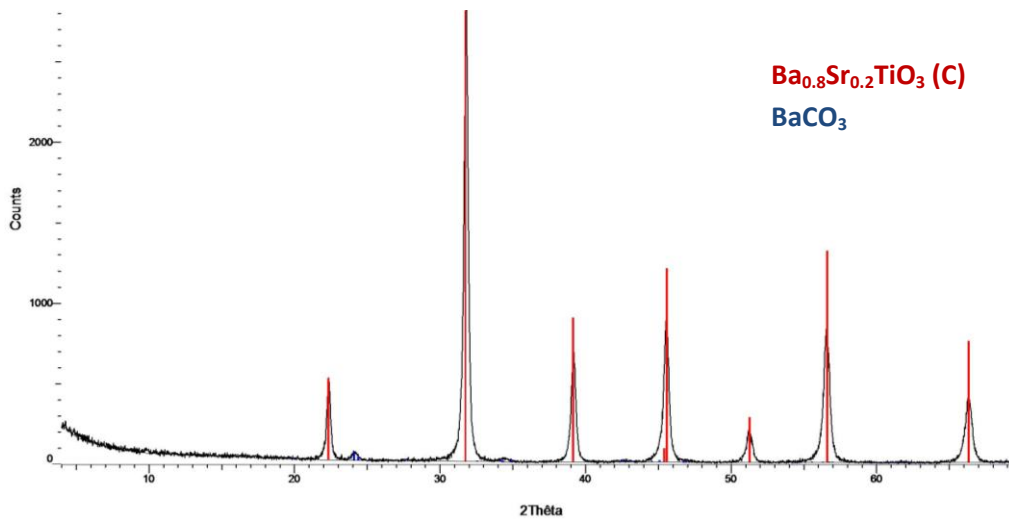


Figure 4.5. XRD of BST powder.

Ba/Ti and Sr/Ti ratios of 0.8 and 0.2, respectively, were estimated by XRF measurements, as expected according to the powder stoichiometry.

Figure 4.6 shows the Raman spectrum of the BST commercial powder. Most Raman bands are coincident with the bands characteristic of tetragonal BaTiO_3 , with the lines at 226, 304, 518 and 720 cm^{-1} . The band at 188 cm^{-1} is characteristic of tetragonal phase in case of small crystallites.

Bands at 304 and 720 cm^{-1} that appear only in tetragonal phase are observed, but are not prominent: this indicates an intrinsic phase transition towards the so-called pseudo-cubic phase (usually observed in powders or ceramics with nanometric crystalline sizes [141], [143], [144]) and explains the absence of doublets on the X-Ray diffractogram.

Bands with small intensities at 153 and 1060 cm^{-1} , also observed in BT powder, are assigned to BaCO_3 .

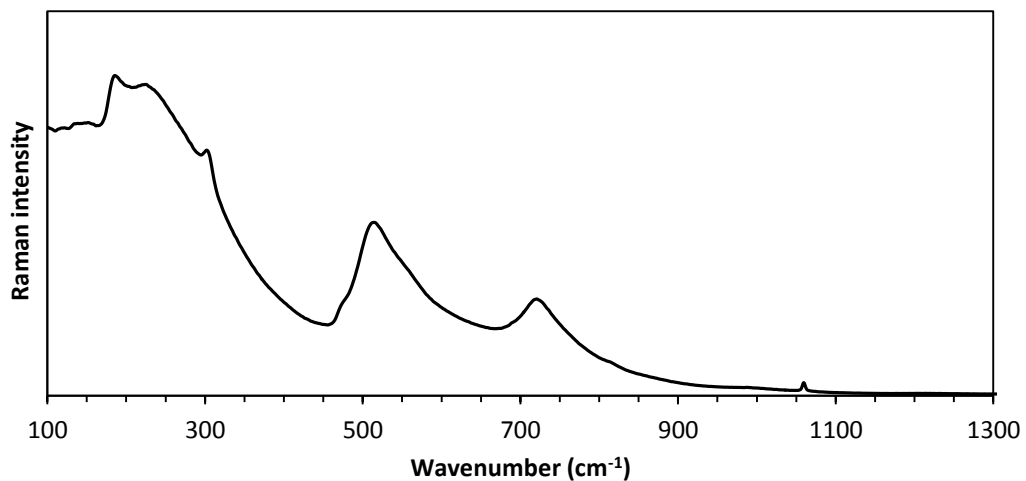


Figure 4.6. Raman spectrum of BST powder.

The high purity of the powder (over 99.9 wt%) has been confirmed by ICP analysis, with only traces of some elements detected (Ca, Fe, S, Te and V).

The measured specific surface area is $15.4 \text{ m}^2/\text{g}$, in agreement with the range of values given by the supplier, between 15 and $18 \text{ m}^2/\text{g}$. From this value, the estimated primary particle size is 67 nm , taking into account equation 3.1 and the theoretical density of BST ($5.84 \text{ g}/\text{cm}^3$).

The powder was observed by TEM: small particles with sizes under 50 nm were observed and agglomerates were also detected (Figure 4.7).

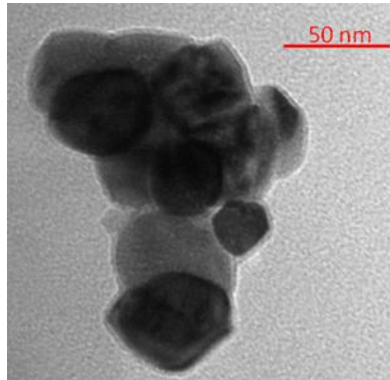


Figure 4.7. TEM images of BaSrTiO_3 powder.

Laser diffraction measurements found agglomerates in the starting powder with a size between 2 and $80 \mu\text{m}$. The mean grain size of the agglomerates was $23 \mu\text{m}$ (Figure 4.8).

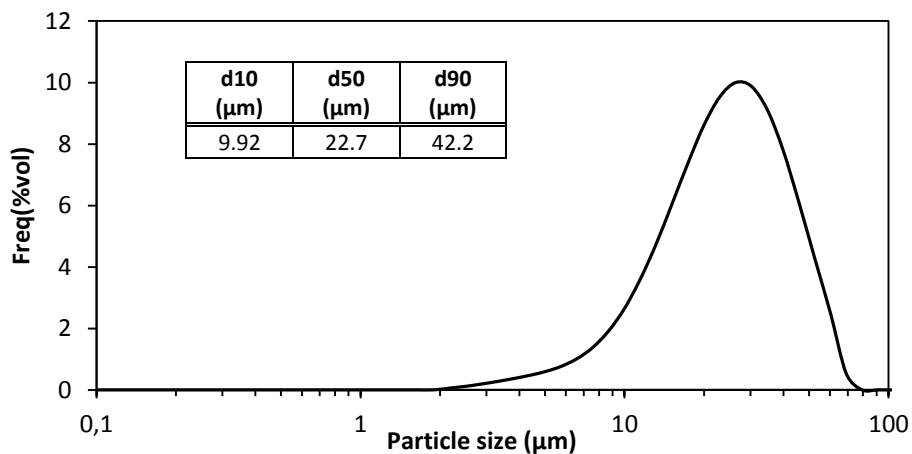


Figure 4.8. Frequency distribution (vol %) versus particle size of BaSrTiO_3 powder

4.2. Processing dense ceramics with controlled microstructure

In order to achieve the objective sought, i.e. samples as transparent as possible, dense ceramics with homogeneous microstructure and controlled grain size are a priori desired. SPS should offer the possibility to achieve these two conditions simultaneously. In this section, the influence of the SPS parameters on the density and microstructure of the BT and BST samples is analysed. In addition,

powder conditioning has been proved to be also a significant factor in the achievement of homogeneous samples, so this treatment will be also evaluated.

4.2.1. Barium titanate

4.2.1.1. Sintering behaviour

First of all, the sintering behaviour of BT powder was evaluated by measuring the punches displacement in the SPS equipment at a heating rate of 20°C/min from 500 to 1200°C, under a pressure of 50 MPa applied during the whole sintering cycle. This cycle provided information about the sintering behaviour of the powder and defined the next cycles to obtain fully dense ceramics. Punches displacement and displacement rate during the SPS cycle are reported in Figure 4.9.

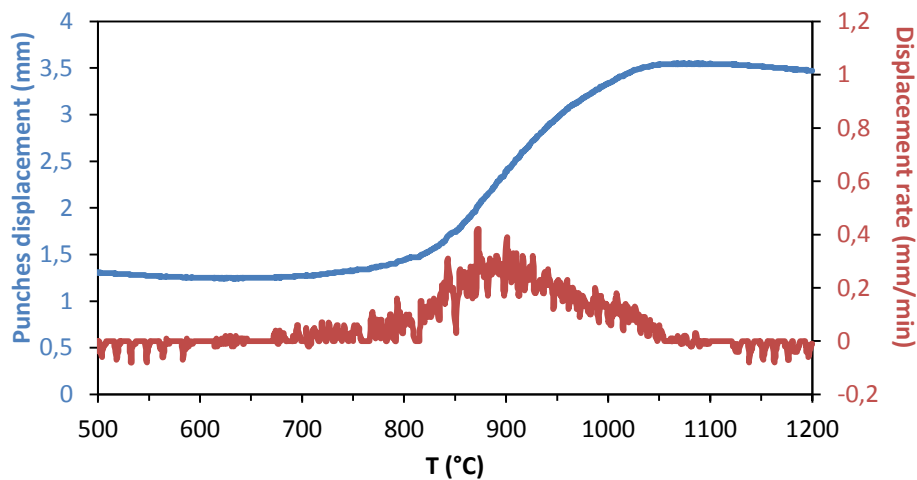


Figure 4.9. Punches displacement and displacement rate of BT powder as a function of the temperature (heating rate 20°C/min, pressure 50 MPa).

Regarding the punches displacement, up to 680°C only the thermal expansion of the system (sample + tooling) is observed. Between 680°C and 1050°C the system shrinks, the powder is sintering. Above 1050°C there is not further shrinkage of the sample, instead it appears an expansion of the system with the temperature increase. Regarding the displacement rate, it is noticeable that below 800°C, the rate is very low and around 900°C sintering rate becomes maximal.

After this thermal cycle, the relative density of the sample, measured by Archimedes' method, was 99.8%. The XRD analysis (Figure 4.10) showed that the ceramic exhibits a tetragonal structure, highlighted by the splitting of the peaks at high angle values.

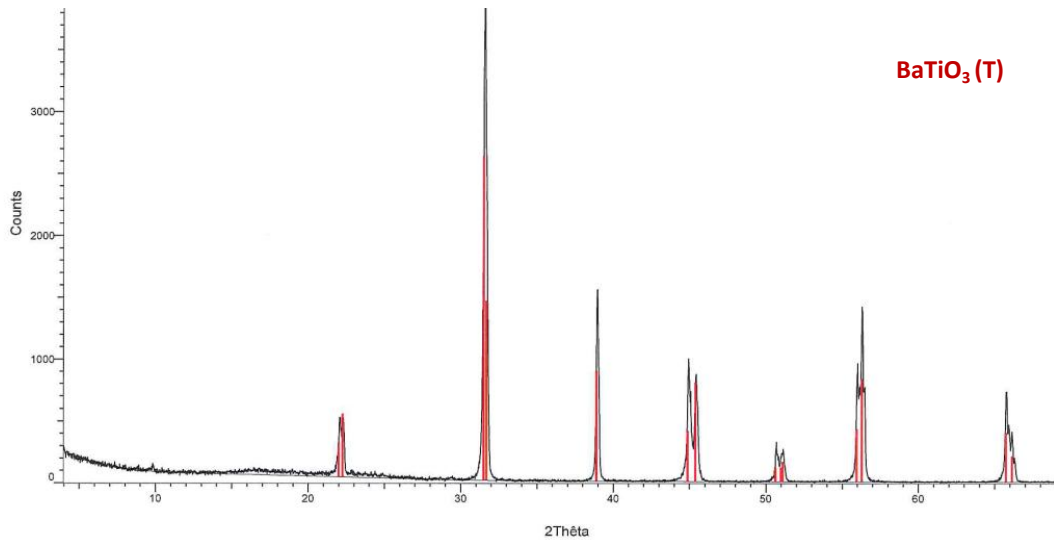


Figure 4.10. XRD patterns of BaTiO_3 after SPS at 1200°C .

4.2.1.2. Influence of SPS parameters on density, microstructure and visual aspect of the samples

Once the behaviour of BT in SPS has been evaluated, an adapted cycle with two heating rates (as in the case of YAG) was adopted: a first heating rate of $100^\circ\text{C}/\text{min}$ up to 800°C and a second one of $10^\circ\text{C}/\text{min}$ up to the final temperature. In this section, different SPS parameters (temperature, dwell time, pressure, heating rate) were evaluated to define their relative influence on density and grain size of the samples.

- **Effect of the sintering temperature**

Three different temperatures have been tested: 950 , 1000 and 1050°C . In all cases, a pressure of 50 MPa was applied before heating and maintained constant during whole cycle; the dwell time was fixed to 5 minutes. After the dwell, the electric current was switched off and the pressure was released, in order to prevent the fracture of the samples.

Figure 4.11 shows the relative density evolution of the samples sintered at 950 , 1000 and 1050°C by SPS. It illustrates the great influence of the temperature on the relative density of BT samples: in fact, densities before dwell are 90.4 , 96.4 and 99.9% , respectively at 950 , 1000 and 1050°C . So sample sintered at 1050°C was already dense before dwell. A 5 -minutes long dwell at 1000°C implies an increase of density up to 99.2% . On the contrary 5 minutes at 950°C is not enough to achieve high density and only 94.7% relative density is attained.

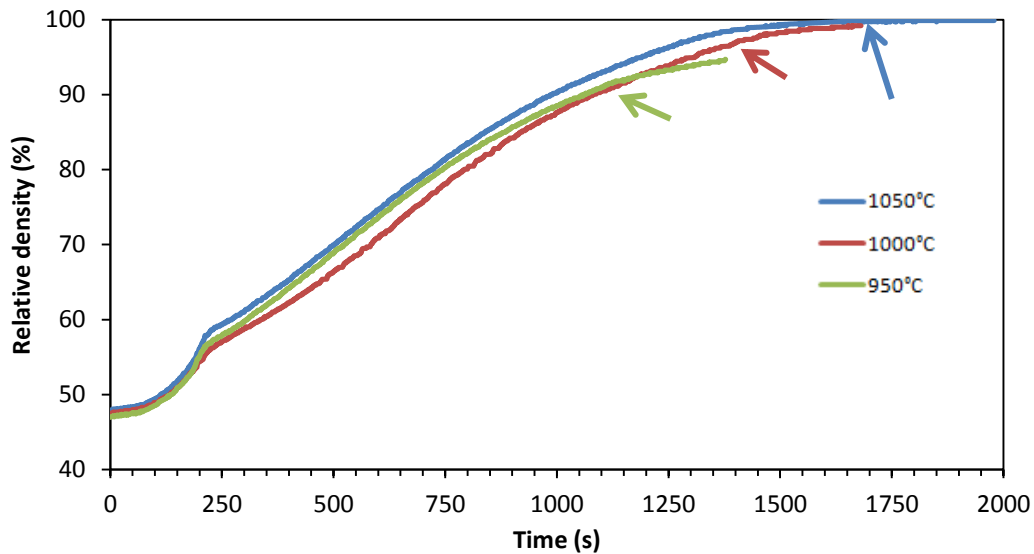


Figure 4.11. Evolution of the relative density of BT ceramics sintered at different SPS temperatures. Arrows mark the start of the dwell for each temperature (dwell: 5 minutes).

Figure 4.12 displays the images of BT samples sintered at these three temperatures. The sintering temperature not only influences the final density of the samples, but also their appearance. As the sintering temperature was increased, samples showed darkening. In BaTiO_3 samples the darkening is attributed to the presence of Ti^{3+} caused by the reducing sintering atmosphere [145], [124] added to the other sources of darkening that were already observed in YAG: graphite contamination and oxygen vacancies. A higher temperature implies more probability to produce Ti reduction and generate oxygen vacancies.

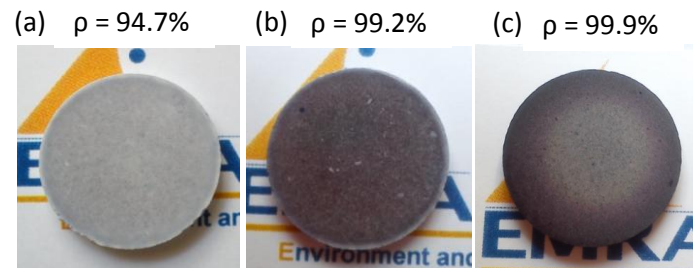


Figure 4.12. Samples of BT sintered at different temperatures: (a) 950°C, (b) 1000°C, (c) 1050°C.

XRD analysis on the three samples showed only the BaTiO_3 phase without the presence of carbonates. At the lowest temperature, 950°C, the phase seems to be cubic, but over 1000°C, some of the peaks of BaTiO_3 presented doublets characteristic of the tetragonal phase. Figure 4.13 shows, for example, the XRD patterns obtained for a sample sintered at 1000°C.

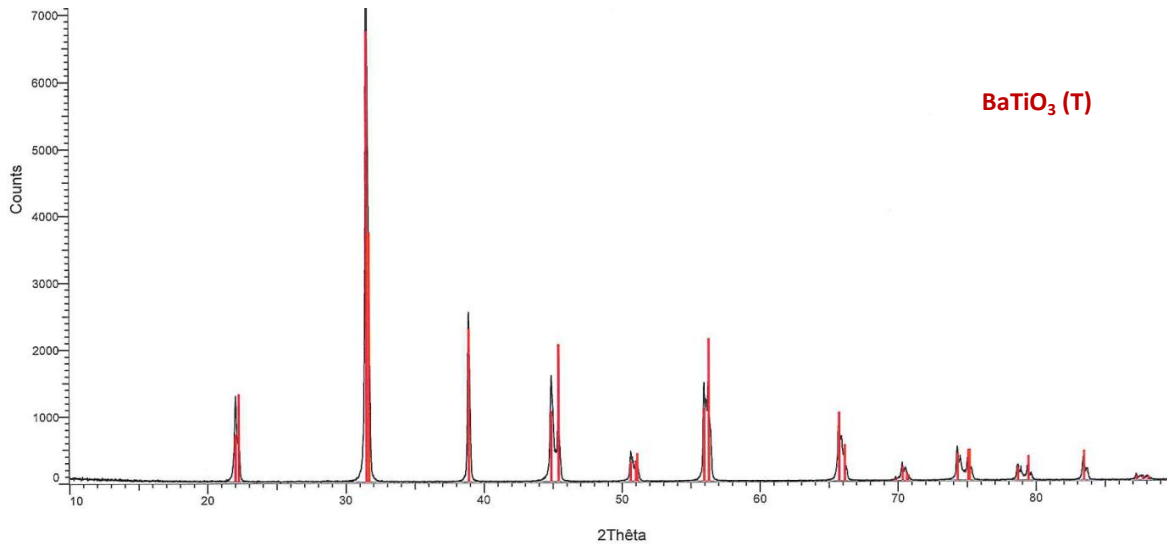


Figure 4.13. XRD patterns of BaTiO_3 after SPS at 1000°C .

Raman analysis was also performed on the samples after sintering. Whatever the sintering temperature used, all the samples present the same Raman bands and, for example, Figure 4.14 depicts the Raman spectrum of a sample sintered at 1000°C . In agreement with the XRD observations, all the bands characteristic of the tetragonal phase were present (240 , 307 , 514 and 717 cm^{-1}) and bands of BaCO_3 have disappeared. The increase in grain size with sintering can be concluded from the small negative dip (instead of band) at around 180 cm^{-1} [141].

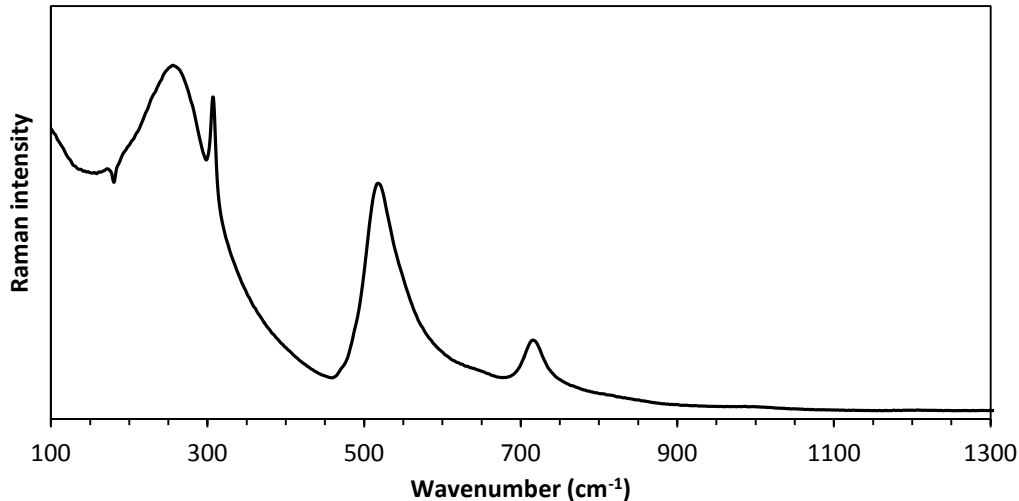


Figure 4.14. Raman spectrum of a BT sample sintered by SPS at 1000°C .

In order to analyze the influence of the temperature on the microstructure of the samples, the fracture surface of the ceramics obtained by SPS at 950°C , 1000°C and 1050°C was characterized by SEM (Figure 4.15).

Sample sintered at 950°C presents intergranular porosity. Grains are homogeneous and smaller than 200 nm . At higher temperatures, 1000°C , less porosity is observed and grains have grown, but they are still homogenous and mean grain size is around 500 nm . A coalescence phenomenon of the smaller grains appears, but no abnormal grain growth is observed. Nevertheless, increasing the

temperature by only 50°C, up to 1050°C, implies an abnormal grain growth and grains over 20 µm are observed within a matrix of smaller ones with size around 1 µm. This abnormal grain growth can be generated by Ostwald ripening owing to the higher thermodynamic stability of larger grains.

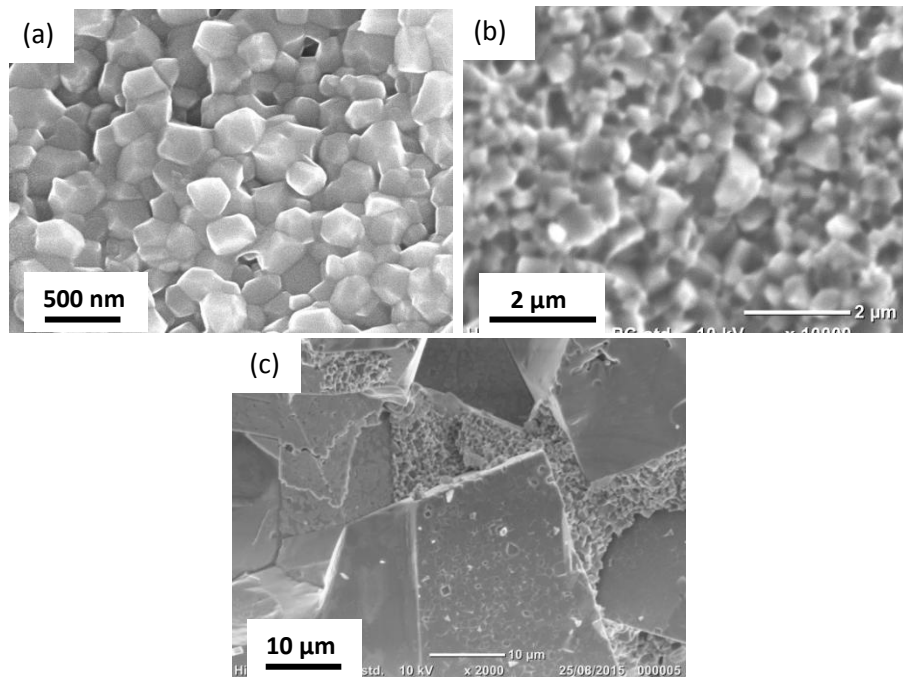


Figure 4.15. Microstructure of BT samples (fracture surfaces) sintered by SPS at (a) 950°C; (b) 1000°C and (c) 1050°C.

Some researches assigned abnormal grain growth to TiO₂ excess [146], [147], but we did not observe inhomogeneities or titanium rich zones after EDS analysis.

It is also commonly observed that rapid grain growth occurs during the final stage of micron-sized powder sintering [148, 149]. In the nano-sized porous green-bodies the grain growth seems to be driven by surface diffusion, but when the relative density reaches a value close to 99% grain growth is driven by the size difference between grains and this happens at lower temperatures in SPS samples compared to conventional sintered ones. Nevertheless relative densities close to 100% are achieved at much lower temperatures.

To attain BT transparent samples, fully dense ceramics with small and homogeneous grain size have to be obtained. In fact, contrary to YAG, barium titanate has a tetragonal structure, and grain size may influence the optical transmission of the sintered samples.

An intermediate temperature: 1025°C was also tested (keeping the rest of sintering parameters constant). Figure 4.16 shows an image of the sample and its microstructure. The sample presents also the characteristic dark colour of dense BT samples and its relative density reaches 99.9%. Its microstructure reflects that at 1025°C an abnormal grain growth already appears. Nevertheless, this effect is less pronounced than at 1050°C. At 1025°C there are less coarse grains and the matrix of 1µm-grains occupies a larger volume of the sample.

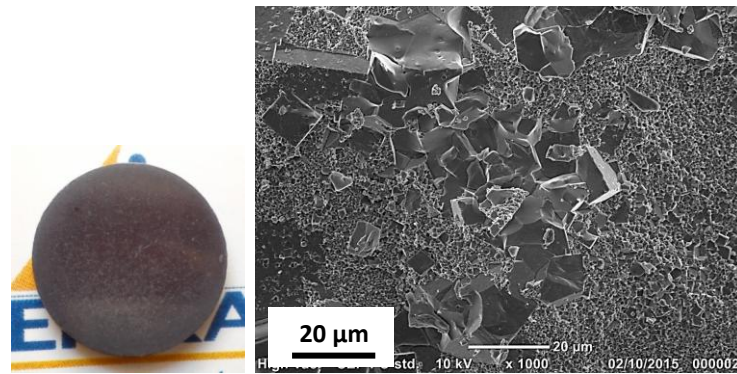


Figure 4.16. Image and microstructure of a BT sample sintered by SPS at 1025°C.

- **Effect of the dwell time.**

No abnormal grain growth was observed after sintering at 1000°C, but a 5 minutes long dwell was not enough to achieve 100% relative density. Therefore, the efficiency of longer dwell times in increasing relative density, without abnormal grain growth, was tested.

Different BT samples were obtained by SPS changing only the dwell time, the other SPS parameters were kept unchanged. Increasing the dwell from 5 to 15 minutes resulted in a sample with a relative density of 99.5%. But as shown in Figure 4.17, some coarse grains with size $\sim 5 \mu\text{m}$ were already observed within the matrix of small grains. A dwell of 25 minutes increased the density till 99.9%, but the number and size of the coarse grains increased too.

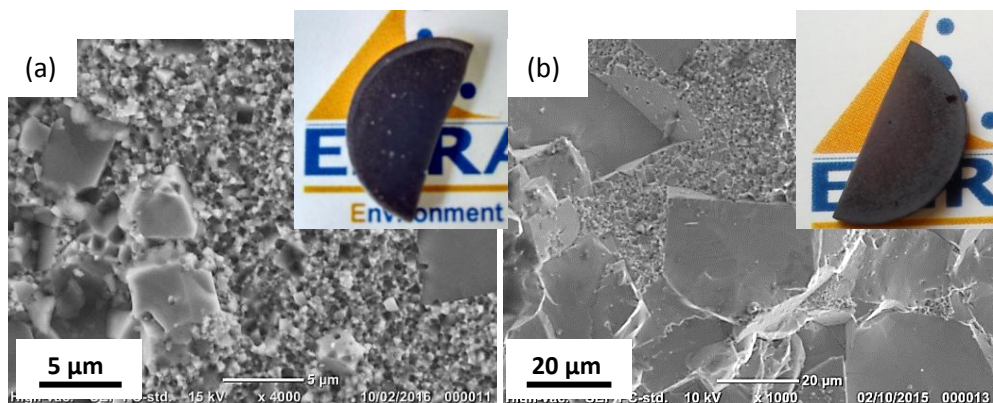


Figure 4.17. Images and microstructures of BT samples sintered by SPS at 1000°C with dwell time of (a) 15 min and (b) 25 min.

- **Effect of the pressure.**

The pressure influence was also evaluated keeping fixed the other parameters: the temperature was set to 1000°C and the dwell time to 5 minutes.

Three different pressures, maintained constant all along the sintering cycles, were evaluated: 30, 50 and 70 MPa. Figure 4.18 depicts the sintering curves at each respective pressure.

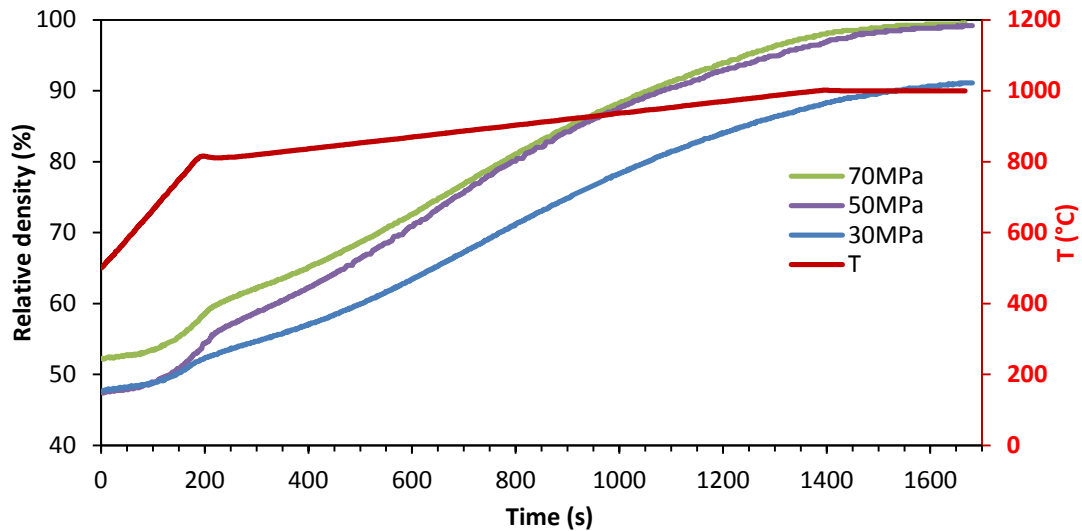


Figure 4.18. BT sintering curves at different pressures (temperature 1000°C, dwell 5min).

Increasing the pressure from 50 to 70 MPa increases slightly the green density from 48 to 52 %, respectively (no differences of the green density between 30 and 50 MPa are observed). The curve at 30 MPa keeps a lower density during the whole cycle and even at the end of the dwell it attains only 91.1%. The curve at 50 MPa starts at a lower density but from 900°C, both curves at 50 and 70 MPa are nearly superimposed. The samples obtained at 50 and 70 MPa attain quite similar densities: 99.2% and 99.4% respectively.

Figure 4.19 shows the appearance of the samples sintered at these different pressures. It is noticeable that the increase of pressure is followed by an increase of darkening. The evolution is similar to the one observed with the increase of the dwell time.



Figure 4. 19. Pictures of BT samples sintered at 1000°C by SPS at pressures of (a) 30 MPa, (b) 50 MPa and (c) 70 MPa.

Regarding the microstructure of the three samples (Figure 4.20), a slight grain growth appears as the pressure increases, but here no abnormal grain growth is observed. The microstructure remains homogeneous in all the samples.

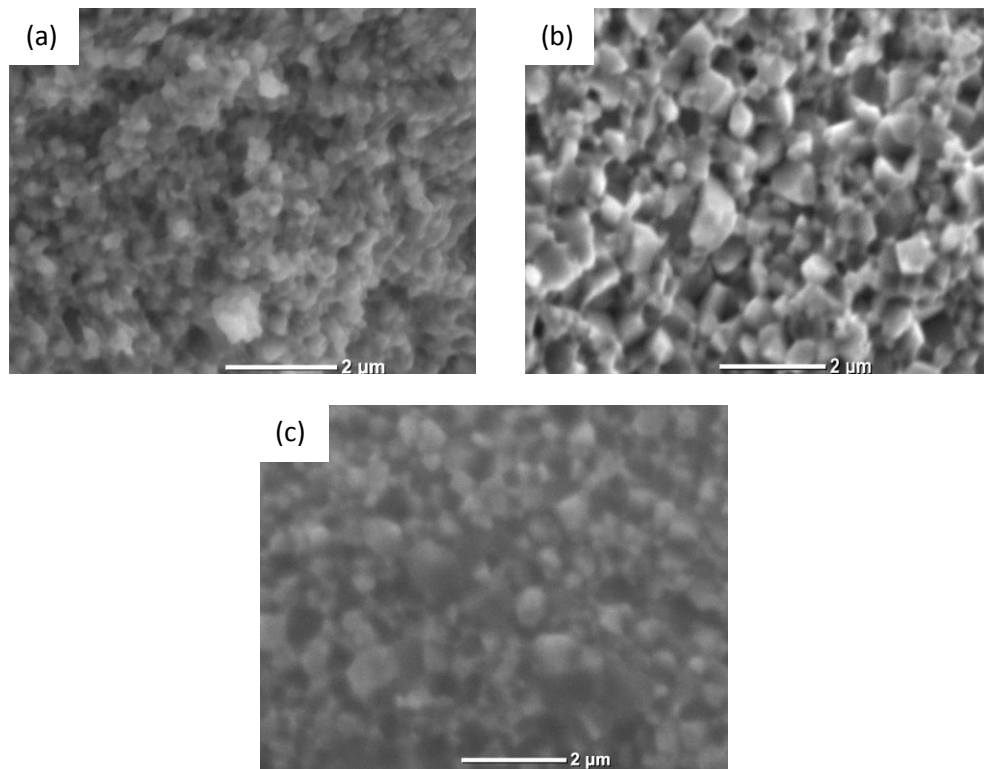


Figure 4.20. Microstructure of BT samples (fracture surfaces) sintered by SPS at 1000°C under a pressure of (a) 30 MPa; (b) 50 MPa and (c) 70 MPa.

XRD measurements showed that all samples presented only the tetragonal phase of BT.

- **Effect of heating rate.**

In order to evaluate the influence of the heating rate, three samples were sintered at 1000°C for 5 minutes but modifying the heating rate between 800 and 1000°C. Three heating rates were tested: 10, 50 and 100°C/min.

Regarding the relative density evolution versus the temperature (Figure 4.21), it is noticeable that slower heating rates results in higher densities for a fixed temperature.

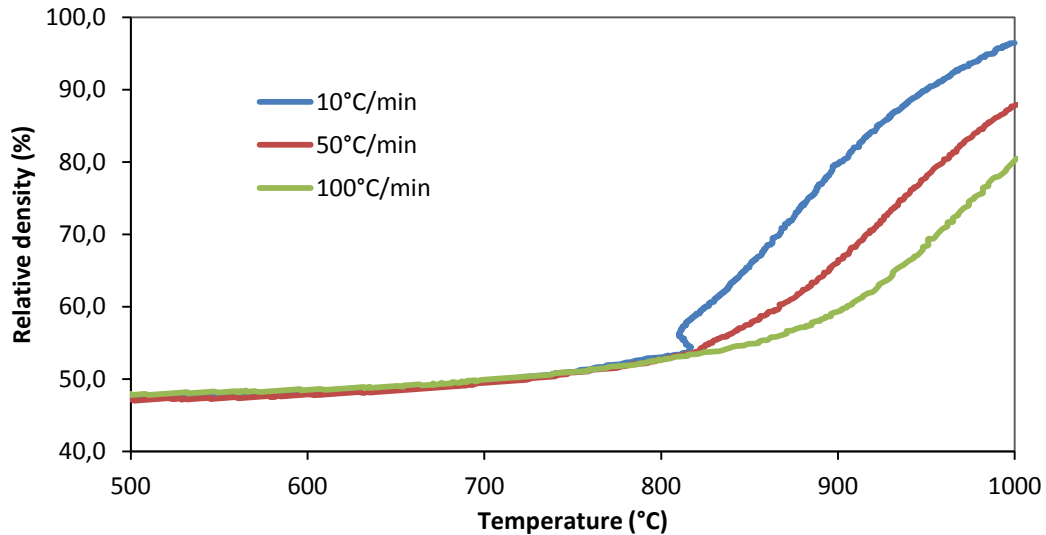


Figure 4.21. BT sintering curves at different heating rates (evolution of the relative density during dwell is not shown).

Table 4.1 shows also the evolution of density for each heating rate during dwell. At higher heating rates, there is a larger density evolution during dwell: for example, relative density increases by 17% during dwell using 100°C/min. However, despite this evolution during the dwell, slow heating cycle allows achieving higher density than the quicker ones.

Table 4.1. Relative density before and after dwell for samples sintered at different heating rates at 1000°C.

Heating rate (°C/min)	Relative density (without dwell) (%)	Relative density (after 5 min dwell) (%)	Density evolution during dwell (%)
10	96.4	99.2	2.8
50	87.7	97.9	10.2
100	79.7	96.5	16.8

Regarding the appearance of the three samples (Figure 4.22), the densest sample has the darker coloration.

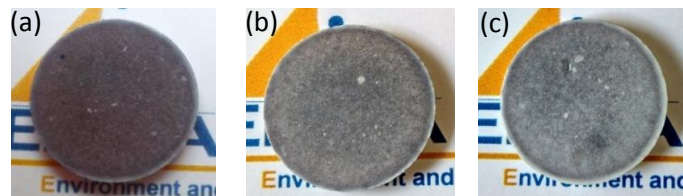


Figure 4.22. Pictures of BT samples sintered at 1000°C by SPS at heating rates of (a) 10°C/min; (b) 50°C/min and (c) 100°C/min.

At the microstructural level, the increase of the heating rate till 100°C/min results in a slightly smaller grain size of 400 nm versus 500 nm for 10°C/min (Figure 4.23).

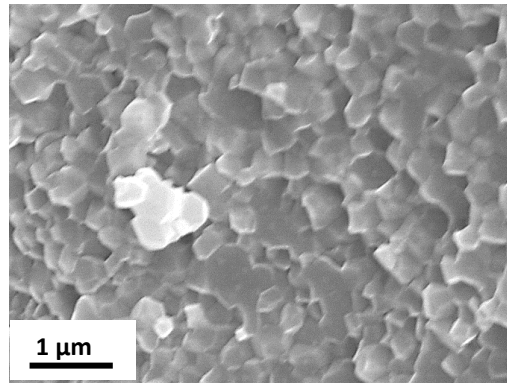


Figure 4.23. Microstructure of BT sample sintered by SPS at 1000°C with a heating rate of 100°C/min (fracture surface).

In order to try to better control the grain growth of the samples and increase density, another attempt was carried out by replacing the direct heating step by a two-step sintering in the SPS equipment.

This type of sintering is characterized by two different stages: a first high heating rate up to a temperature T_1 to obtain a high intermediate density, followed by a long dwell at a lower temperature T_2 . This dwell should finish densification avoiding grain growth. The chosen cycle is a pressure of 50 MPa applied during the whole cycle, 100°C/min up to 1025°C to obtain a high density (ideally without grain growth), a rapid cooling at 100°C/min till 950°C and finally a 45 minutes dwell.

Figure 4.24 shows relative density evolution during this two-step sintering. We can observe that at 1025°C (T_1), the sample attains 88% of relative density and during the dwell at 950°C (T_2), density increases till 99.0%. This final density is lower than expected. Another cycle with a dwell at T_2 of 90 minutes was also tested but density did not increase.

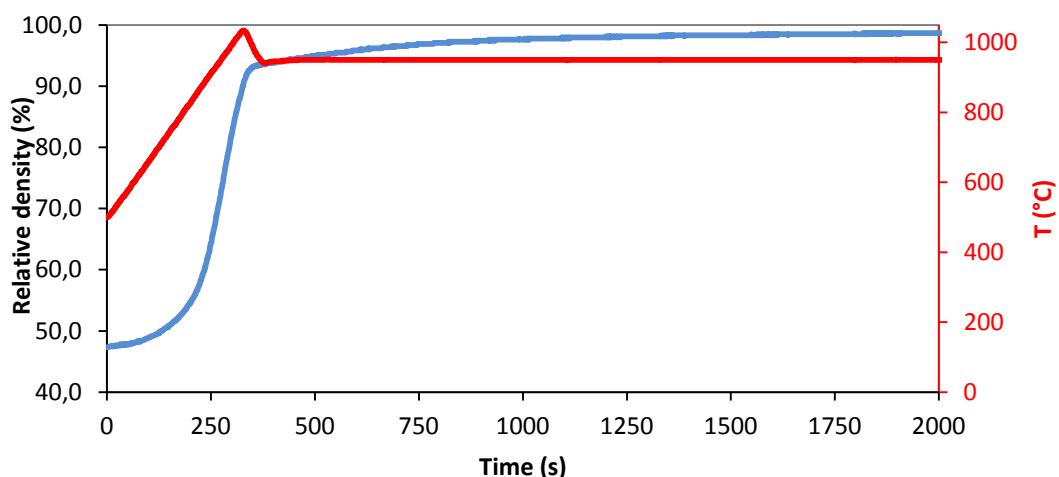


Figure 4.24. BT sintering curve with a two-step sintering cycle.

After sintering the sample showed an inhomogeneous appearance, and concerning its microstructure small grains were observed without abnormal grain growth (Figure 4.25).

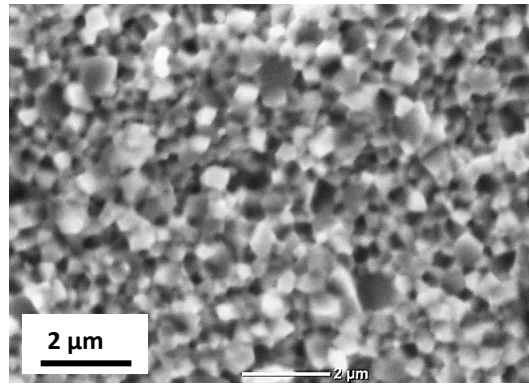


Figure 4.25. Microstructure of BT sample sintered by two-step sintering.

The study of the effect of the sintering parameters has shown that the obtaining of fully dense BT ceramics with homogeneous microstructure is a hard challenge.

In fact, the increase of temperature or dwell time implies a gain in terms of density but unfortunately also leads to abnormal grain growth. Applying higher pressures engenders only a slight improvement of the relative density. The onset temperature for grain growth seems to be between 1000 and 1025°C, therefore, the sintering window is very narrow and grain growth is hard to control.

Previous researches ([145], [150]) also found small sintering windows for barium titanate or strontium titanate powders and revealed that obtaining dense samples with grains near 1 μm by SPS is not easily controllable. This behavior explains why in most publications, when ceramics with small grains are presented, densities are very often lower than 99%. Besides, many authors are not able to get higher densities for BT ceramics, even when they do not try to control the microstructure.

In fact, most works on BT are focused only in the evaluation of the dielectric properties, and so, achieving 98% of relative density is generally enough. However, as the first objective of this study is to attain transparent ceramics, full density is requisite.

For this reason, in the following part, we have tried the efficiency of a powder pre-treatment to improve density and avoid abnormal grain growth.

4.2.1.3. Powder deagglomeration

Powder was dispersed with the aim of breaking agglomerates and having homogenous particle size which could prevent differential sintering and increase homogeneity inside the samples. Dispersion was performed in isopropanol to avoid a possible instability of BT in water due to leaching of Ba²⁺ ions [151], [152]. The dispersion was performed in a Turbula with 2mm-diameter zirconia balls.

Particle size distribution was measured by laser granulometry after different dispersion times (Figure 4.26). During the first hour of dispersion, size of agglomerates decreases strongly. Reduction of agglomerates size goes on during the following hours. Between 4 and 24 hours of dispersion, only a slight decrease of particle size is measured. Longer dispersion times did not lead to any real improvement. So, 24 hours of dispersion were considered to be sufficient to break agglomerates efficiently.

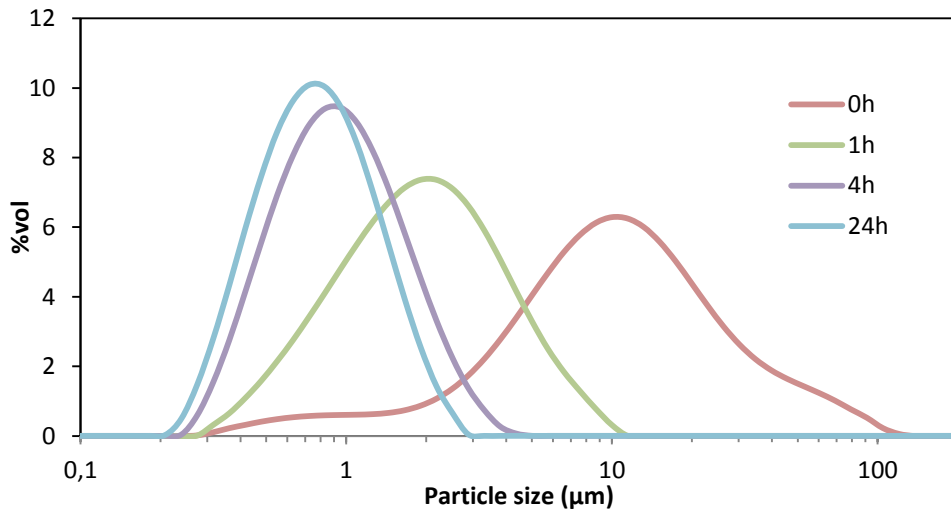


Figure 4.26. Particle size distribution of BT powder after different dispersion times.

The use of isopropanol as solvent impedes the use of freeze-drying so, after dispersion, solvent was removed with rotavapor. Finally, the dried powder was crushed in an agate mortar.

Figure 4.27 compares sintering curves of as-received and deagglomerated powder for a SPS cycle with a pressure of 50 MPa, a first heating rate at 100°C/min up to 800°C and a second one at 10°C/min up to 1000°C, followed by a 15 minutes dwell time. We do not appreciate any difference in the green density of the samples due to deagglomeration. However a different evolution of the density is noticeable: deagglomeration seems to slow down the densification process, but the deagglomerated powder after dwell attains 99.9% of relative density (95.0% at the beginning of the dwell) versus 99.5% without dispersion. Agglomerates lead to a quicker densification but also to differential sintering. Inside agglomerates, pores are smaller and particles sinter and densify early in the heating cycle, causing grain growth earlier. But between agglomerates there are larger pores more difficult to remove. This effect makes that pores stays between agglomerates and samples attain lower densities [153].

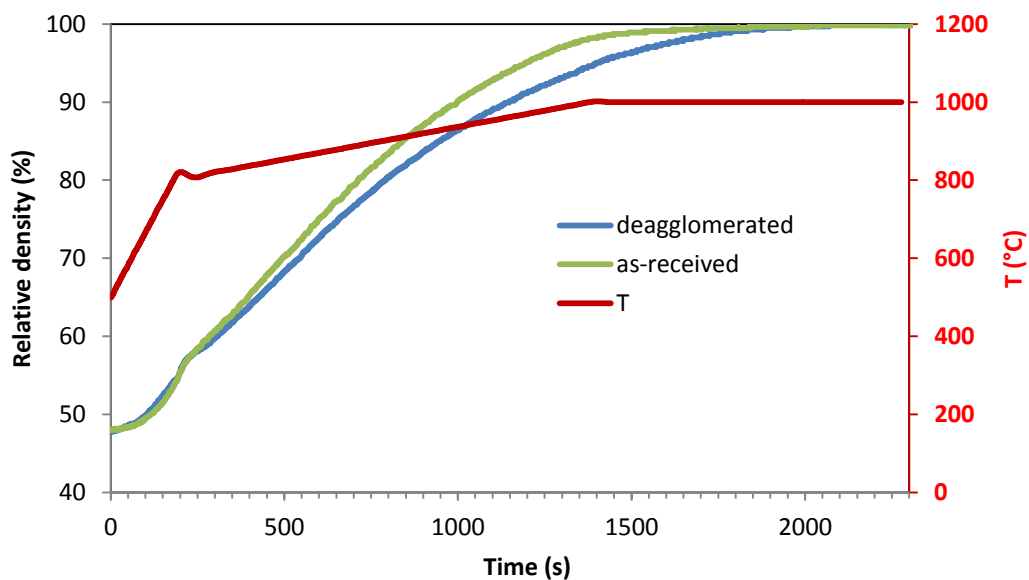


Figure 4.27. BT sintering curves of as-received and deagglomerated powders. (Pressure: 50 MPa, Temperature: 1000°C, Dwell: 15 min).

Figure 4.28 shows both an image and the microstructure of this sample: after deagglomeration, the sample presents a homogeneous dark colour and a fine microstructure, with grains around 500 nm, whereas abnormal grain growth appeared for in samples from as-received powder sintered in the same conditions (Figure 4.17).

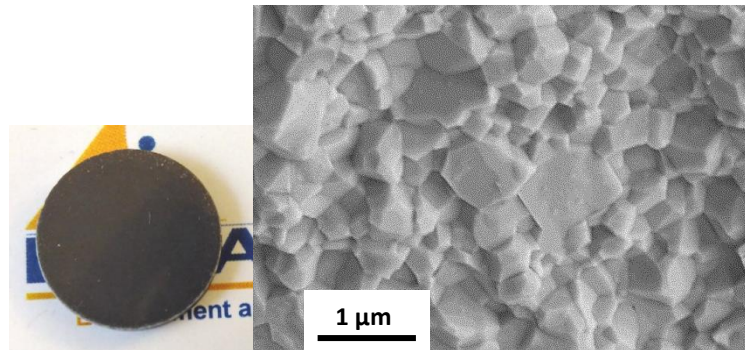


Figure 4.28. Image and microstructure of BT sample from deagglomerated powder sintered by SPS at 1000°C with dwell time of 15 min.

This result shows the benefic effect of deagglomeration in getting fully dense sample with fine microstructure. Additional sintering cycles have been performed to check if, after deagglomeration, the sintering window to avoid abnormal grain growth was larger or not.

Figure 4.29 shows the microstructures of samples sintered by SPS at 1050°C with two different dwell times: 5 and 15 minutes. In both cases, relative density is close to 100%. However, while after a 5 minute dwell, microstructure remains fine and homogeneous, with mean grain size around 1 μm, extension of the dwell to 15 minutes induces abnormal grain growth, with grains above 5 μm in a matrix of fine grains.

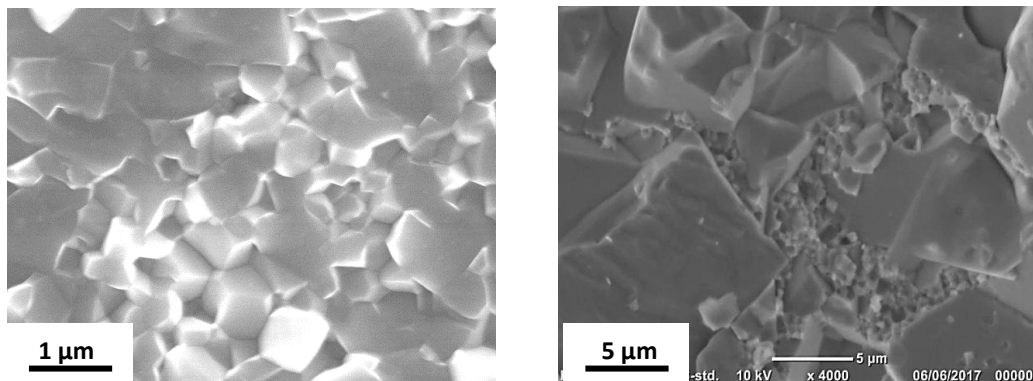


Figure 4.29. Microstructures of BT sample from deagglomerated powder sintered by SPS at 1050°C with a dwell time of (a) 5 minutes and (b) 15 minutes.

Other attempts have been performed to highlight the effect of sintering temperature. For example, if the sintering temperature is increased up to 1100°C, with only a 5 minutes dwell time, grain growth appears and microstructure presents grains over 10 μm (Figure 4.30).

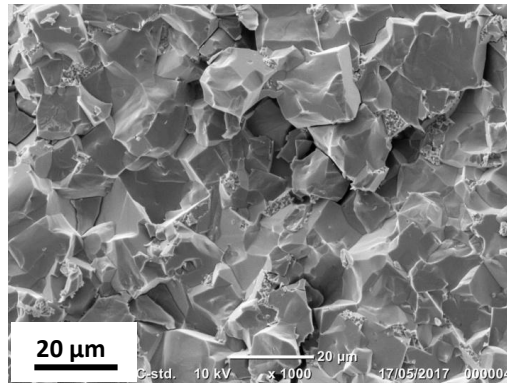


Figure 4.30. Microstructure of BT sample from deagglomerated powder sintered by SPS at 1100°C-5 minutes.

A two-step sintering was also applied to the deagglomerated powder to evaluate if it was possible to obtain dense samples with finer grain size. The sintering cycle was a pressure of 50 MPa applied during the whole cycle, a heating rate of 100°C/min up to 1025°C, a rapid cooling to 950°C, followed by a dwell at this temperature during 45 minutes (the same as the one used for the as-received powder).

Figure 4.31 shows the sample obtained this way; deagglomeration has improved density, as sample attains 99.9% of relative density. The appearance of the sample is more homogeneous and regarding its microstructure, grain size remains homogeneous, with average grain size around 400 nm. However, still some residual porosity is observed.

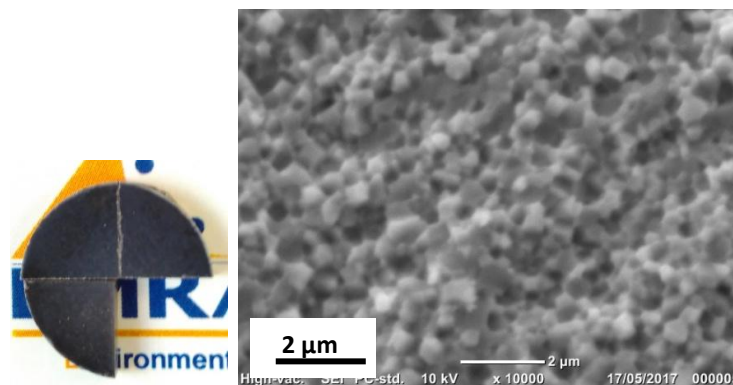


Figure 4.31. Picture and microstructure of BT sample sintered by two-step sintering from deagglomerated powder.

It is noticeable that deagglomeration of the powder has led to a better homogeneity of the sample. Moreover, deagglomeration modifies the densification of BT samples, slowing down the achievement of full density. This involves a retaining of a fine microstructure till higher temperatures and over all, allows attaining full density and retaining grains of 1 μm average size or lower.

4.2.1.4. Conclusions

In this section, the sintering behaviour of a commercial barium titanate powder has been described. BT is very sensitive to grain growth as it approaches full density. It presents a very narrow sintering

window and SPS parameters must be carefully controlled because grain growth processes take place dramatically fast. Samples prepared below the critical parameters present a fine and homogeneous microstructure but usually they do not attain full density. On the contrary, samples prepared above these critical parameters present microstructures with large grains embedded in a matrix of finer grains. The matrix of fine grains decrease as sintering conditions get away from the critical parameters. For instance, we have observed a substantial grain growth from 500 nm to 20 μm , by increasing the temperature by only 25°C or dwell time by 10 minutes.

Agglomerates make difficult attaining full density and promote abnormal grain growth at lower temperatures. Agglomerates drive to differential sintering and grain coarsening occurs quickly.

Dispersion of the powders eliminates agglomerates and allows retaining a fine microstructure up to higher temperatures. This is favourable to obtain samples with a fine microstructure and full density.

The effect of deagglomeration on functional properties of BT (optical and dielectric) will be analysed in the following parts of this chapter.

4.2.2. Barium strontium titanate

4.2.2.1. Sintering behaviour

The sintering behaviour of BST powder was evaluated by measuring the punches displacement in the SPS equipment at a heating rate of 20°C/min from 500 up to 1300°C and a pressure of 50 MPa applied during the whole sintering cycle. This cycle will provide information about the sinterability of the powder and in particular the onset temperature of sintering. Punches displacement and displacement rate are reported in Figure 4.32.

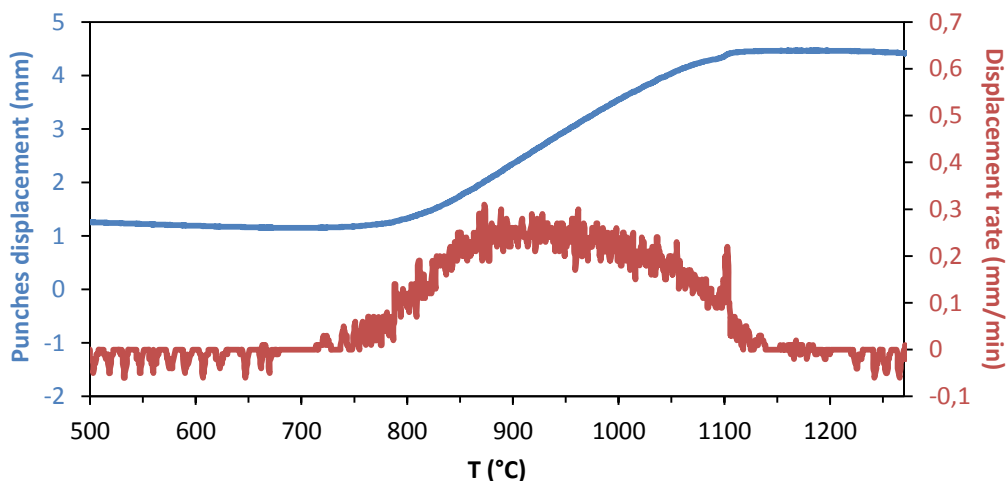


Figure 4.32. Punches displacement and displacement rate of BST powder as a function of the temperature (heating rate 20°C/min, pressure 50 MPa).

Regarding the punches displacement, the shrinkage starts at around 750°C and continues up to 1140°C. Above this temperature there is not further shrinkage of the system.

Below 800°C, the displacement rate is very slow and maximal sintering speed is found between 870 and 980°C.

After this thermal treatment, relative density of the SPSed sample is 100%. XRD analysis (Figure 4.33) corresponds to the expected phase $\text{Ba}_{0.8}\text{Sr}_{0.2}\text{TiO}_3$. Double peaks are not clearly observed but the widths of some peaks at high angle values suggest the coexistence of the tetragonal and cubic phases. Carbonates do not appear in the XRD patterns.

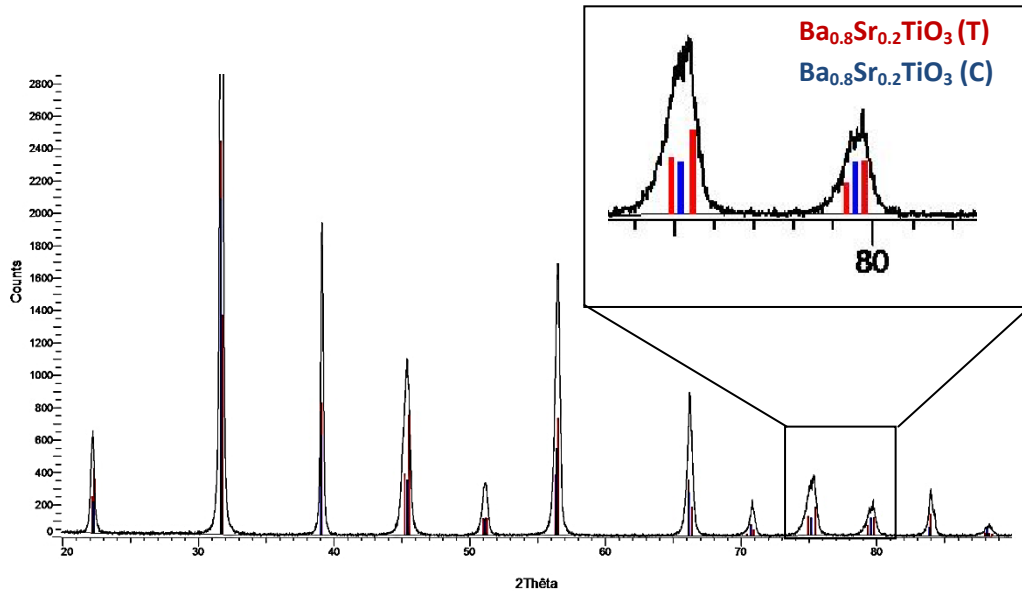


Figure 4.33. XRD patterns of Barium strontium titanate after SPS at 1300°C.

4.2.2.2. Influence of SPS parameters on density, microstructure and visual aspect of the samples

From the previous results, a sintering cycle with two different heating rates was adopted : a first heating rate of 100°C/min up to 800°C and a second one of 10°C/min till the final temperature (with a dwell of 5 minutes). In this section, different SPS parameters (temperature, dwell time, pressure) were studied to define their respective influence on density and grain size of the samples.

- **Effect of temperature**

The influence of different sintering temperatures between 1000 and 1200°C on density and microstructure was evaluated. For example, Figure 4.34 shows the density evolution of samples sintered at 1000, 1100 and 1150°C (pressure of 50 MPa is applied during whole sintering cycle).

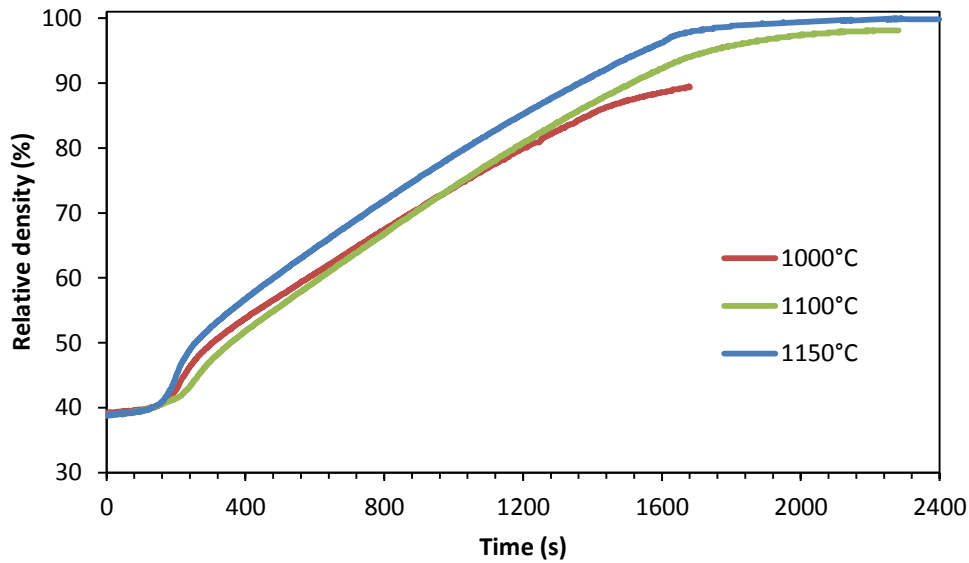


Figure 4.34. BT sintering curves for different sintering temperatures (dwell: 5 minutes included).

Green density is low, lower than 40% and compared to barium titanate powder, higher temperature is necessary to achieve full density. Table 4.2 summarizes the relative density at the beginning and at the end of the dwell for different sintering temperatures. During sintering at 1000°C, a large increase of density takes place during the 5 minutes dwell; however, it remains relatively low (89.5%). Sample sintered at 1150°C attains full density. At higher temperature, relative density decreases slightly.

Table 4.2. Relative density before and after dwell for BST samples sintered at different temperatures.

T (°C)	Relative density (without dwell)	Relative density (after 5 min dwell)
1000	84.8	89.5
1100	97.3	98.2
1150	99.9	100
1200	99.6	99.6

In Figure 4.35, it is noticeable how temperature influences the appearance of the samples. As the final temperature increases, samples go from white-yellow to grey and then to black. Here, as it happened for BT, this increasing darkening is attributed to the reduction of Ti^{4+} to Ti^{3+} and the formation of oxygen vacancies and graphite contamination. As temperature increases these effects are enhanced.

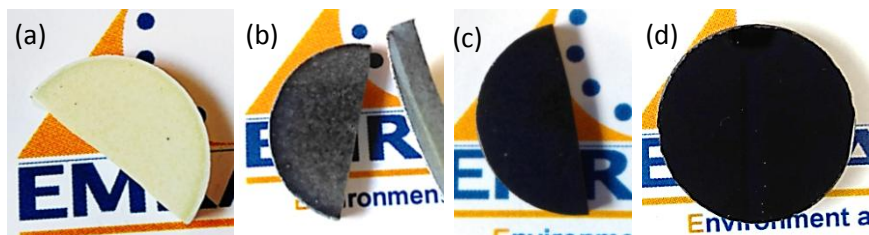


Figure 4.35. BST samples sintered at (a) 1000°C, (b) 1100°C, (c) 1150°C and (d) 1200°C by SPS.

XRD analysis on the BST samples shows only the BST phase without the presence of carbonates, whatever the sintering temperature (Figure 4.36 shows a XRD pattern of a sample sintered at 1150°C). As it happened for the sample sintered at 1300°C, no clear double peaks are observed on the diffractograms, but the widening of the peaks at high angle values suggest the presence of the tetragonal phase of BST or the possible coexistence of both cubic and tetragonal phases.

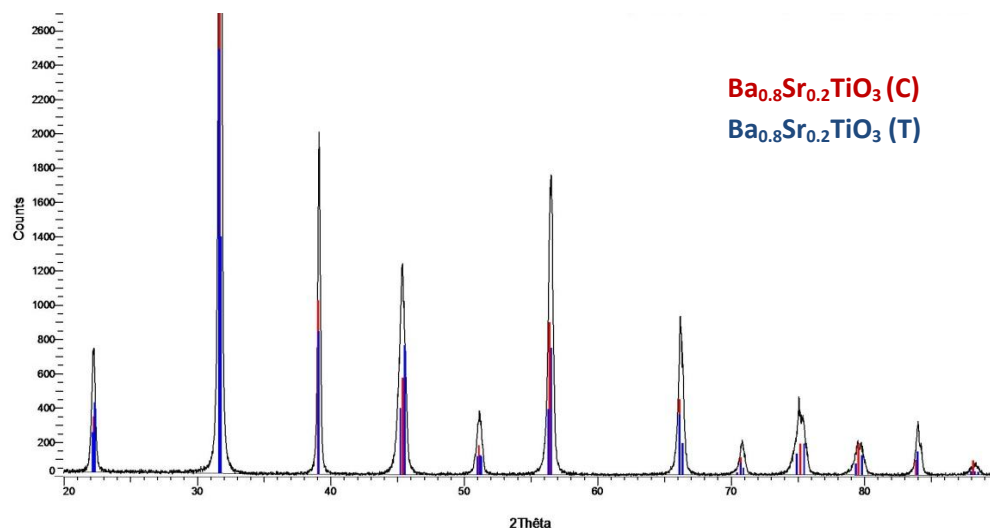


Figure 4.36. XRD patterns of BST sample sintered at 1150°C by SPS.

Raman analyses were also performed on these BST samples. Figure 4.37 depicts, as an example, the Raman spectrum of the sample sintered at 1150°C. All the bands characteristic of the tetragonal phase (226, 304, 518 and 720 cm^{-1}) are present. BaCO_3 is not detected in agreement with the XRD results.

Bands at 304 and 720 cm^{-1} , that appear only in the tetragonal phase are visible but they are not prominent, indicating an intrinsic phase transition towards the so-called pseudo-cubic phase and explaining the absence of doublets on the X-Ray diffractogram.

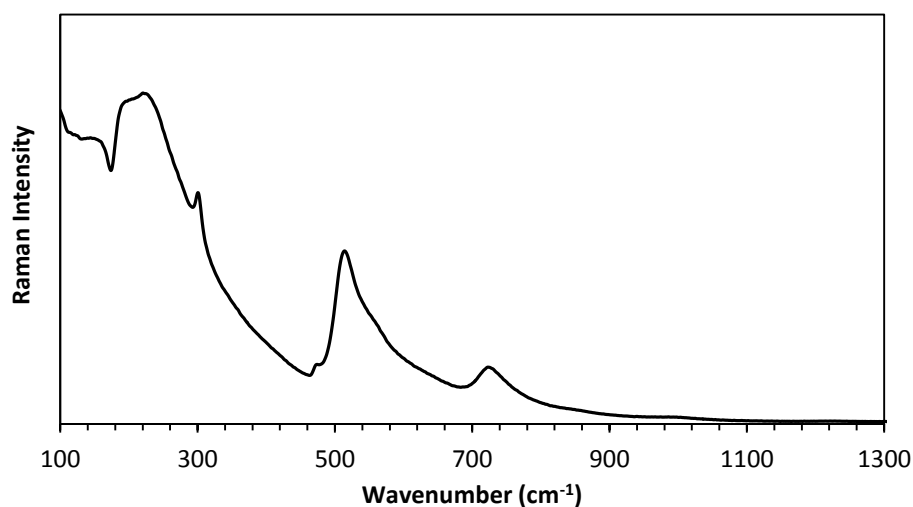


Figure 4.37. Raman spectrum of a BST sample sintered by SPS at 1150°C-5min.

The microstructure of the samples sintered by SPS at different temperatures was evaluated by SEM (Figure 4.38). Fracture surfaces of the samples were considered. Sample sintered at 1000°C present intergranular porosity and grains with a homogeneous size around 300 nm. At 1100°C, grains have slightly grown but remain under 400 nm; some porosity is still observed. At 1150°C, grains growth has been going on, but slowly, average grain size is 450 nm and no porosity is observed. At 1200°C, grain growth continues, most grains are under 1 μm but some larger grains with size over 10 μm are observed on the microstructure.

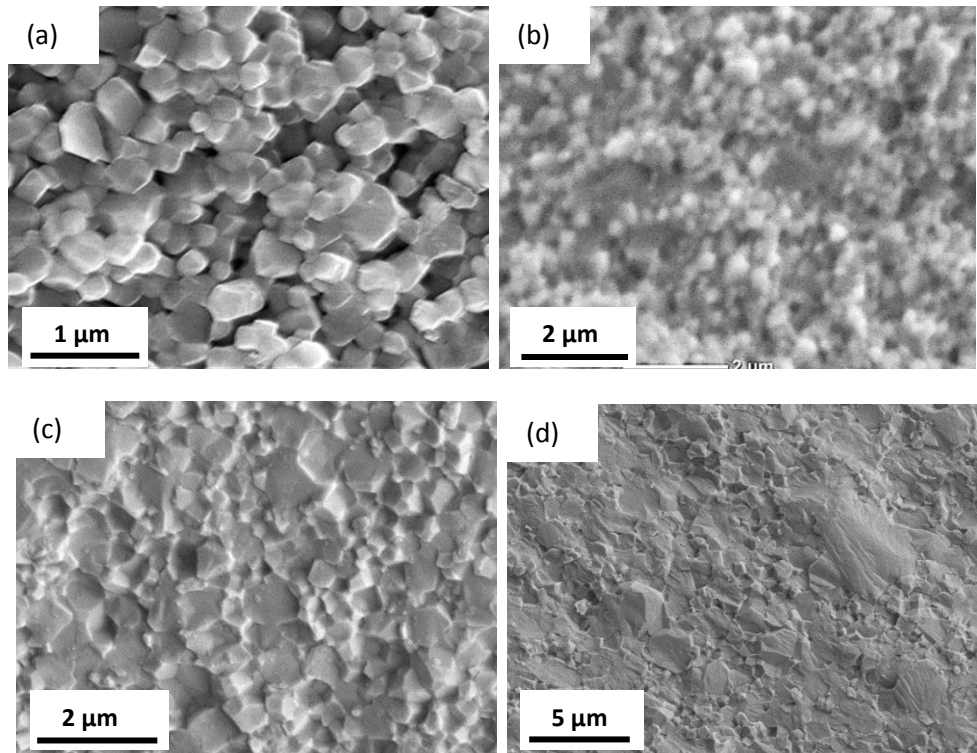


Figure 4.38. Microstructure of BST samples (fracture surfaces) sintered by SPS at (a) 1000°C; (b) 1100°C; (c) 1150°C; (d) 1200°C.

Contrary to the BT results where obtaining full density and preserving a fine microstructure was not possible without pre-treatments, BST samples presented full density and a homogenous fine microstructure, with adapted SPS parameters. In BST, abnormal grain growth can be avoided.

- **Effect of dwell time**

The influence of dwell time on density and microstructure of BST samples sintered at 1150°C was evaluated. Three different times were tested: 0, 5 and 15 minutes.

Figure 4.39 shows the visual appearance of these samples.

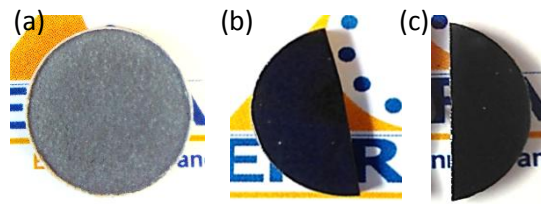


Figure 4.39. Images of BST samples sintered by SPS at 1150°C for (a) 0 min, (b) 5 min and (c) 15 min.

The sample sintered without dwell, with relative density of 99.0%, presents a grey aspect with some residual white points, characteristic of non-fully dense samples.

Dwells of 5 and 15 min lead to dark homogeneous samples, with both 100% relative density. Figure 4.40 shows the microstructure of these samples. 5-min dwell sample presents a quite homogeneous microstructure with average grain size of 450 nm. On the contrary, 15-min dwell sample presents higher degree of coarsening and some grains over 2 μm appeared within the matrix of smaller grains.

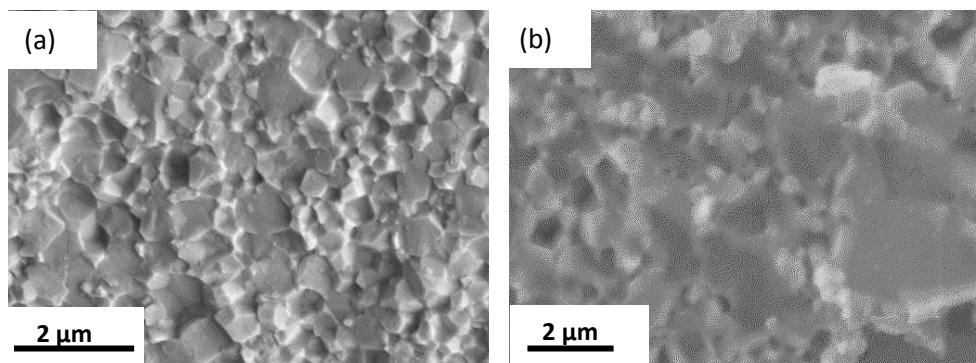


Figure 4.40. Microstructures of BST samples sintered by SPS at 1150°C with dwell time of (a) 5 min and (b) 15 min.

So, as observed in BT, the use of longer dwell times leads to very quickly abnormal grain growth and the sintering window in BST is also small.

- **Effect of pressure**

We observed previously that using a pressure of 50 MPa lead to a sample with 100% relative density, homogeneous black appearance and fine microstructure. In this section, pressures of 30 and 70 MPa were evaluated, keeping constant the rest of parameters (a first heating rate of 100°C/min up to 800°C and a second one of 10°C/min up to 1150°C with a dwell of 5 minutes).

Figure 4.41 depicts the sintering curves at 30, 50 and 70 MPa for comparison. Except a slight green density increase of sample pressed at 70 MPa (44 % vs 39%), the three sintering curves almost overlap till the end of the sintering cycle.

All samples attain similar relative densities, close to 100%.

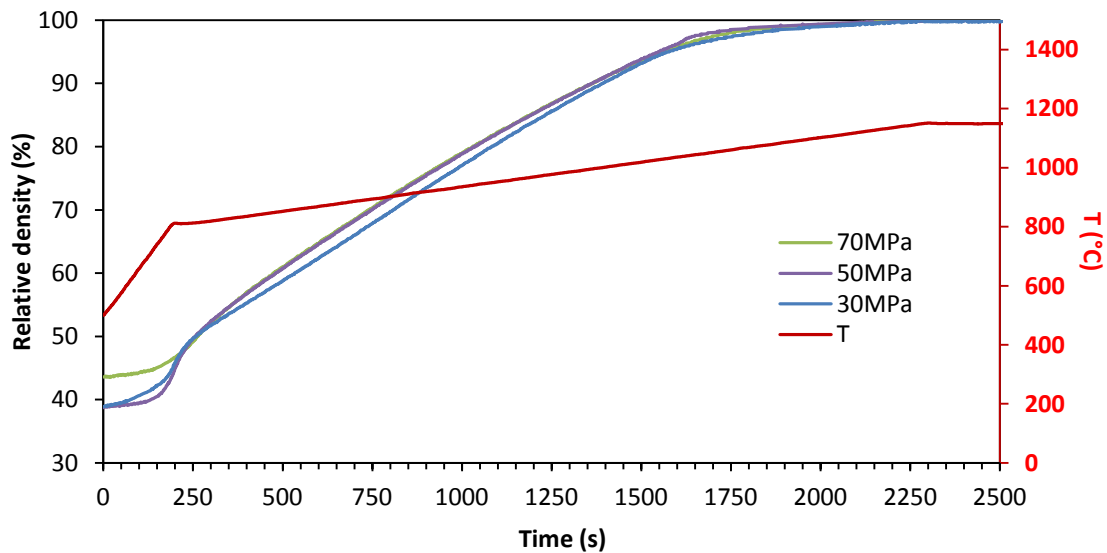


Figure 4.41. Density evolution with time of BST samples sintered at 1150°C at different pressures.

After sintering, all three samples show a similar homogeneous black appearance (Figure 4.42).

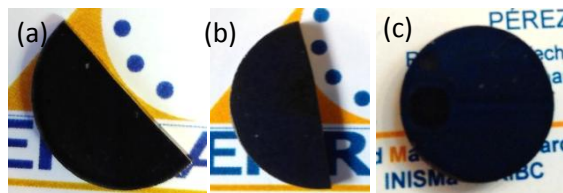


Figure 4.42. Images of BST samples sintered by SPS under a pressure of (a) 30MPa; (b) 50MPa and (c) 70MPa.

Concerning the microstructure, as in the case of BT, no influence of pressure on grain size was evidenced by SEM observations.

XRD results show that all samples present only the phase BST with larger peaks at high angle values, indicating the presence of a pseudo-cubic structure or coexistence of cubic and quadratic phases of BST.

After this parametric study, it seems that BST ceramics grain size is largely dependent of dwell time and temperature, as observed for BT powder. However, even if the sintering window to fully densify with only limited grain growth is also narrow, we were able to obtain BST samples with high density and fine microstructure without powder pretreatments.

So in BST this grain coarsening occurs in later stages of sintering compared to BT, probably due to the effect of Sr in the structure [150], the melting point of SrTiO_3 (2080°C), higher than that of BaTiO_3 (1625°C) could induce an increase in the sintering temperature of the powder and a higher stability of the structure at higher temperatures.

Nevertheless, the effect of deagglomeration of BST powder was also evaluated, with the aim of densifying at lower temperatures and retaining a finer microstructure.

4.2.2.3. Effect of powder deagglomeration

BST powder, as-received presented agglomerates as observed on Figure 4.8. With the aim of breaking these agglomerates, BST powder was dispersed in isopropanol with 2mm-zirconia balls in a Turbula and the evolution of particles size was controlled by laser granulometry.

Agglomerates size distribution was measured after 1, 4 and 24 hours of dispersion (Figure 4.43). A progressive decrease in the agglomerate size is observed with the increase of the dispersion time. After 24 hours of dispersion agglomerate size was below $7\ \mu\text{m}$ and its average size was $1.4\ \mu\text{m}$. So dispersion was quite efficient on breaking larger agglomerates.

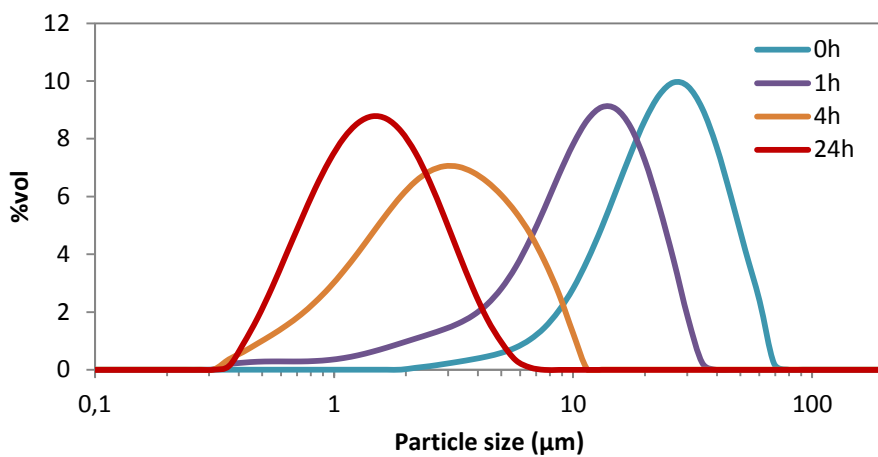


Figure 4.43. Particle size distribution of BST powder after different dispersion times.

After dispersion, the solvent was removed in a rotavapor and then, the dried powder was crushed in an agate mortar. Agglomerates were detected after drying but not as large as in the starting powder.

The deagglomerated powder was submitted to the same SPS cycle that the non-dispersed powder (50 MPa, 1150°C , 5 min). Sintering curves of as-received and deagglomerated powders overlap and both result in samples with 100% relative density.

Figure 4.44 shows the appearance and microstructure of the sample prepared from the deagglomerated powder. It presents a black-homogeneous colour, the same that the one issued of the as-received powder. Moreover, no microstructural differences are observed, average grain size is around $450\ \text{nm}$.

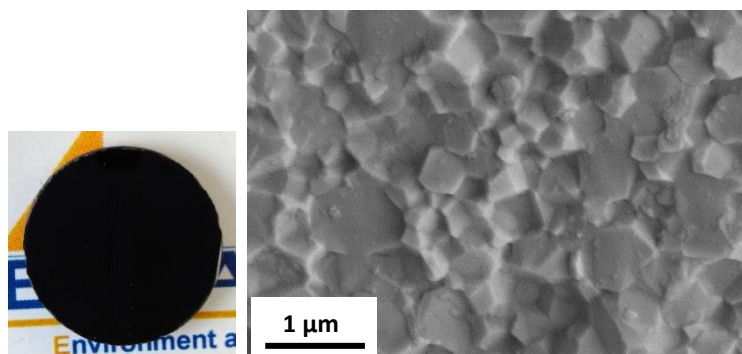


Figure 4.44. Image and microstructure of BST sample sintered up to 1150°C from a deagglomerated powder.

The eventual beneficial effect of powder deagglomeration on functional properties (optical and dielectric) will be discussed hereinafter.

4.2.2.4. Conclusions

The influence of different SPS parameters on the sintering behaviour of BST has been analysed. BST is not as sensitive to grain growth as it approaches full density as BT. Kinetic window in BST is also narrow but it happens at higher temperatures and after attaining full density, apparently the incorporation of Sr ions on the structure retards the grain growth owing to the higher melting point of BaSrTiO₃. It was possible to attain full density samples and to retain a fine microstructure on BST without using pre-treatments as dispersion or two step sintering. Dispersion was tested on BST and this allows attaining 100% relative density as well, without modification of sintering behaviour or final microstructure.

4.3. Functional properties

4.3.1. Optical properties

In the research of transparent ceramics, BT and BST samples with full density and different grain sizes were obtained in previous sections. However, after sintering by SPS, both BT and BST ceramics presented a dark colour when they attained relative densities close to 100%.

Some darkening was already observed in YAG samples, and in that case, it was attributed to the formation of oxygen vacancies and/or graphite contamination. For BT and BST, another cause can be proposed: indeed, several researches [145], [124] point out that titanium ion Ti⁴⁺ is easily reducible to ion Ti³⁺ under vacuum sintering, explaining the samples' black colour.

In order to remove this darkening, different conditions of annealing in air have been tested. Annealing was performed in a conventional furnace, with a heating rate of 10°C/min and a dwell time of 6 hours with the aim of achieving a full reoxidation of the samples.

BaTiO₃

First, annealing was performed on BT samples, sintered in different SPS conditions from as-received powder. The efficiency of annealing treatment has only been tested on samples with full density, and so with inhomogeneous grain size. It is worth to note that black coloration disappeared after annealing. For example, Figure 4.45 shows samples after annealing at 800°C: (a) sample sintered at 1025°C-5min, maximum grain size 5 µm, (b) sample sintered at 1000°C-25 min, maximum grain size 20 µm. Both samples present large inhomogeneities (as white points).

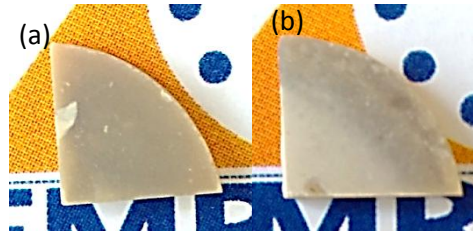


Figure 4.45. Images of samples from as-received powder after annealing at 800°C-6h (a) sintered at 1025°C-5min/50MPa (b) sintered at 1000°C-25min/50MPa.

No homogeneous nor translucent samples were obtained from the as-received powder, whatever sintering or annealing tested conditions.

Annealing treatments were also performed on samples issued from the deagglomerated powder. Several samples, with different densification rates and grain sizes, have been post-treated (800°C – 6h). Some of these samples, with their processing conditions, are summarized in Table 4.3. Images of the same samples after annealing are shown in Figure 4.46.

Table 4.3. Processing conditions, grain sizes, densities and optical transmission of BT samples issued from deagglomerated powder, after annealing at 800°C-6h.

Sample	SPS conditions			Grain size (μm)	ρ (%)	TFT (%) at 600 nm (t ~ 1 mm)
	Tf (°C)	Dwell (min)	P (MPa)			
(a)	1050/950	45	50	0.4	99.9	34
(b)	1000	15	50	0.5	100	26
(c)	1050	5	30	0.8	96.8	0
(d)	1050	5	50	1	100	35
(e)	1100	5	50	> 10	99.0	0



Figure 4.46. Images of samples from deagglomerated powder after annealing at 800°C-6h (see Table 4.3. for the legend). (Thickness ~ 2 mm).

In all samples, black or grey coloration has disappeared after annealing. However, samples with initial density lower than 99.9 % present an opaque aspect (samples c and e) and those with higher density present a translucent aspect (samples a, b and d).

For the optical transmission measurements, thickness of the samples has been reduced to 1 mm. RIT values were too low to be measured (samples present a large level of scattering indicating presence of pores and internal defects), so only TFT values are presented in Table 4.3.

As expected, samples with densities lower than 99.9% presented TFT values close to 0% in the visible range. On the contrary, for translucent samples, TFT measurements were possible and the highest TFT value, 35% at 600 nm, was obtained for a sample sintered at 1050°C during 5 minutes (Figure 4.47), which exhibited a yellow translucent aspect.

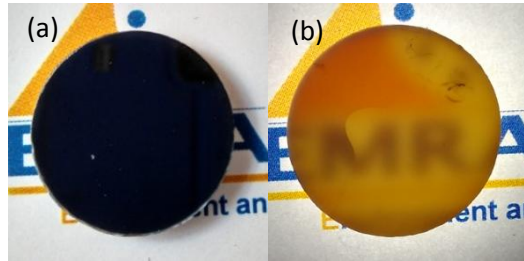


Figure 4.47. Images of a sample sintered at 1050°C-5min (50MPa) from deagglomerated powder, (a) before and (b) after annealing at 800°C-6h (thickness is 1mm and samples are backlighted).

Figure 4.48 shows the optical transmission (TFT values) of samples that presented a homogeneous and yellow aspect after annealing. Optical transmission curves of these three samples are very close. On average, on the visible and near infrared ranges, TFT values are slightly higher for the sample sintered at 1050°C. No real effect of the grain size on TFT values is observed. Sample sintered via a two-step sintering (1050°C-950°C) have TFT values in the visible range slightly lower than the two other ones: it may be explained by the presence of small residual porosities, due to the low sintering temperature used.

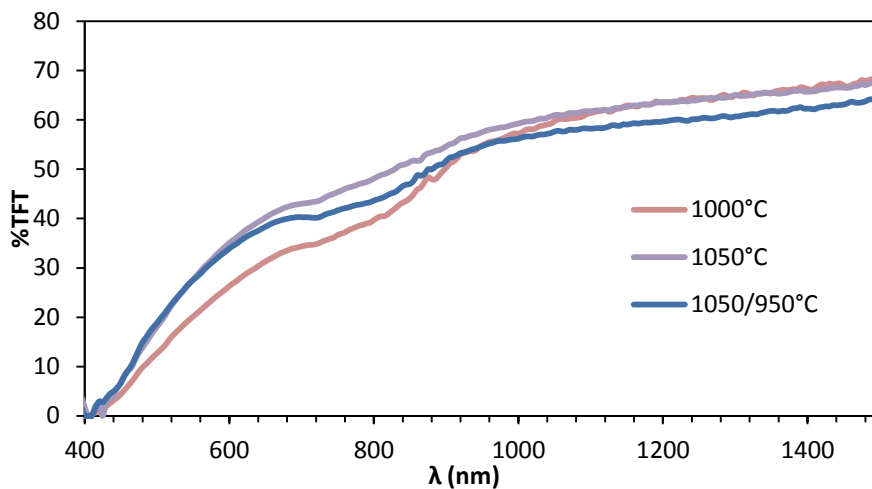


Figure 4.48. Transmission spectra of annealed BT samples sintered in different SPS conditions (thickness 1mm).

Different annealing temperatures, between 600 and 800°C, have been tested on BT samples from deagglomerated powder sintered at 1050°C-5 minutes. Dwell time was maintained 6 hours for each evaluated temperature (Figure 4.49).

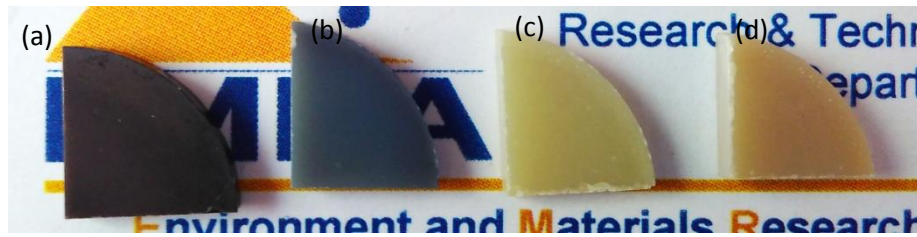


Figure 4.49. Images of (a) BT sample as-sintered and annealed samples at (b) 600°C, (c) 700°C and (d) 800°C (sintering conditions 1050°C-5 min-50MPa; thickness ~ 2mm).

Annealing in air at 600°C is not enough to restore all oxygen vacancies and/or fully reoxidise Ti^{3+} ions because the ceramic keeps its grey colour. From 700°C, annealed samples present a yellow colour indicating that oxygen vacancies and/or Ti^{3+} have been restored.

Optical transmission measurements were performed on the samples annealed at 700 and 800°C (Figure 4.50). At wavelengths lower than 600 nm, the sample annealed at 700°C presents a slightly higher transmission. This is related to the orange colour observed in the sample annealed at 800°C (at $\lambda=600$ nm both attain 35%). Above this wavelength sample annealed at 800°C overtake the one annealed at 700°C (at $\lambda=800$ nm attains 48% vs 44%). Anyway both samples present high values of transmission for a BT sample.

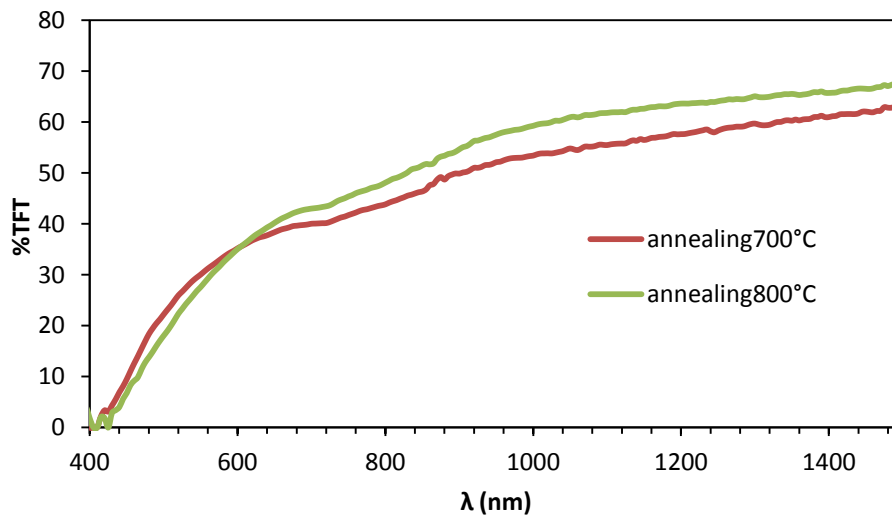


Figure 4.50. Transmission spectra of BT samples for different annealing conditions (thickness ~ 1 mm).

BaSrTiO₃

Samples from BST powder were also submitted to annealing in air at different temperatures. Only samples with a homogeneous black colour led to samples with quite high optical transmission after annealing.

The annealing conditions were a heating rate of 10°C/min and dwell time of 6 hours. Figure 4.51 shows a BST sample sintered at 50 MPa up to 1150°C for 5 min, before and after annealing at different temperatures. The annealed ceramic at 600°C presents a grey-black colour: this temperature is not enough to restore all oxygen vacancies or fully reoxidise Ti^{3+} . At 700°C the sample

has turned into a light grey indicating that most oxygen vacancies and Ti^{3+} have been restored. At 900°C, the sample presents a yellow colour indicating that oxygen vacancies and Ti^{3+} have been completely restored.

It is noticeable that in the case of BST higher temperatures are necessary in order to reoxidise the samples, compared with BT. This difference is linked to the higher temperature used in BST for obtaining dense samples.

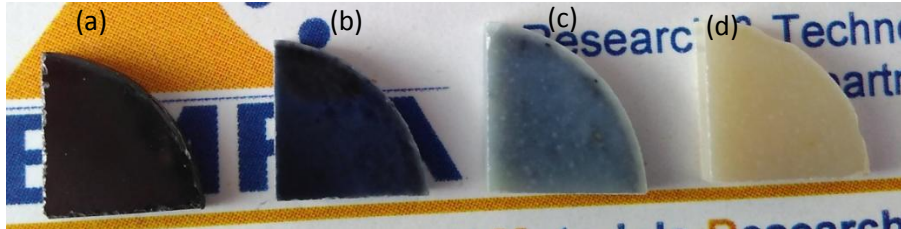


Figure 4.51. BST sample (a) as-sintered and annealed at (b) 600°C, (c) 800°C and (d) 900°C. (Thickness ~2mm).

The optical transmission of annealed BST samples (thickness reduced to 1 mm) was also measured. Figure 4.52 shows the total forward transmission and real in line transmission of a BST samples sintered at 1150°C for 5 min and annealed at 900°C. As it happened to BT, RIT in BST is very low (close to 0%), so most of the light transmitted is scattered certainly due to residual pores. The fine microstructure of the samples imply that these defects are not easily observable by SEM. Scattering also explains why we can only see through the samples when a light is situated behind them. Anyway TFT values obtained for BST (41% at a wavelength of 600 nm) are high compared to the data obtained in other researches so far [40], [133].

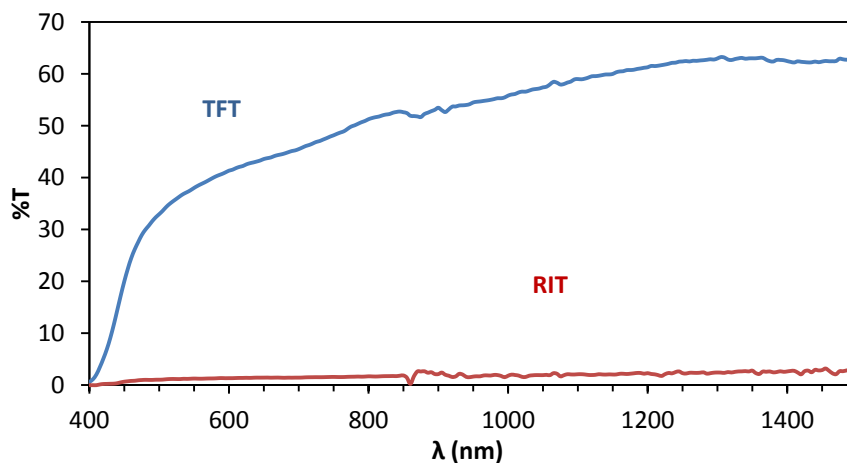


Figure 4.52. Transmission spectra of a BST sample sintered at 1150°C for 5 min and annealed at 900°C for 6 h.

The effect of the powder deagglomeration on the optical transmission of the sintered compacts was also evaluated in the case of BST. The deagglomerated powder was sintered using the same SPS conditions used for the non-dispersed powder: 1150°C for 5 minutes (50 MPa). The obtained sample presented a dark-homogeneous colour. Annealing conditions were also the same: 900°C for 6 hours. Figure 4.53 shows images of annealed BST samples without and with powder deagglomeration. Both samples looked yellowish and translucent and small differences were observed between them. In

contrast to BT, deagglomeration of BST powder did not improve the optical transmission, in agreement with the fact that BST samples attain already 100% relative density and present a fine and homogeneous microstructure without dispersion.

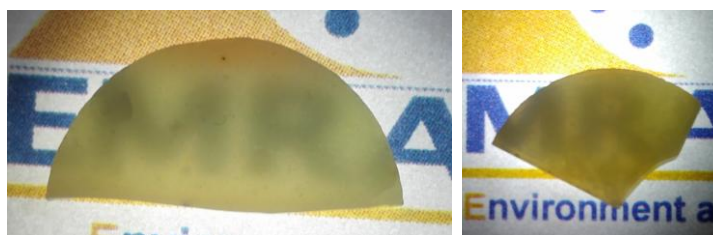


Figure 4. 53. Images of backlighted BST samples sintered at 1150°C-5min (50MPa) after annealing at 900°C-6h (a) from as-received powder, (b) after powder deagglomeration (thickness = 1mm).

Conclusions

Annealing in air allows obtaining translucent samples in BT and BST. The annealing temperature must be optimised in order to remove the oxygen vacancies originated during SPS and to fully oxidise Ti^{3+} to Ti^{4+} . Low annealing temperatures do not impact the appearance of the samples, which remain black. Intermediate temperatures lead to grey samples indicating a partial reoxidation. Optimised temperatures result in yellowish samples which present high level of optical transmission considering the results obtained so far for BT and BST [40], [133].

BST annealing temperatures are higher compared to BT owing to the higher sintering temperature of BST.

The best optical transmission obtained for $BaTiO_3$ samples attained 35% at $\lambda=600$ nm. This value is high taking into consideration the publications of BT transparent ceramics. Liu et al. [40] obtained a transmission of 20% for a BT sample of 0.87 mm of thickness so lower than our values at the same wavelength. Furthermore, they used higher heating rates and lower temperature but much higher pressures (200 MPa). In our case, a standard SPS pressure of 50 MPa was used.

The best optical transmission obtained for our $Ba_{0.8}Sr_{0.2}TiO_3$ samples attained 41% at $\lambda=600$ nm. Wu et al. [133] measured a transmission of 74% in a $Ba_{0.4}Sr_{0.6}TiO_3$ sample, with 0.3 mm thickness. However, this high value is doubtful taking into account that the maximum theoretical transmission at this wavelength is 70% (Figure 2.3) and it is obtained neglecting scattering and absorption sources, so far from a real ceramic (moreover, samples in this paper have a grey colour, suggesting a non-negligible light absorption).

In conclusion, the field of transparent BT and BST ceramics is still unexplored and the values obtained during this thesis are encouraging and open the application of these materials as optical devices.

4.3.2. Dielectric properties

After SPS, the as-sintered $BaTiO_3$ and $BaSrTiO_3$ samples were characterized by impedance measurements: permittivity and dielectric loss values were measured.

Results are compared and in the case of BT samples, the influence of grain size is discussed. The effect of the powder deagglomeration and the annealing conditions is also analysed. Finally, the temperature dependence of the dielectric properties was measured on the supposed best samples, i.e. samples with the highest permittivity values and moderate dielectric loss.

BaTiO₃

Grain size influence

Dielectric characterizations were performed on different samples prepared by SPS from the as-received BT powder. Table 4.4 summarizes the sintering conditions, density, grain size, permittivity and dielectric loss of some of these samples (their microstructures were presented earlier in this chapter).

Table 4. 4. Sintering conditions, relative density, average grain size, permittivity (ϵ) and dielectric loss (td) at 1 kHz of different BT samples prepared with the as-received powder.

SPS conditions			ρ (%)	Grain Size (μm)	ϵ (td) at 1kHz
Tf (°C)	Dwell (min)	P (MPa)			
950	5	50	95.1	0.3	10000 (0.48)
1000	5	50	99.2	0.5	9000 (0.33)
1000	15	50	99.5	5*	3400 (0.11)
1050	5	50	99.9	20*	5000 (0.15)
1000	25	50	99.9	30*	1600 (0.14)

* Inhomogeneous size, value corresponds to the largest grain size observed

Permittivity in samples sintered in reducing atmosphere, as in SPS, is enhanced by the formation of oxygen vacancies and electrons [121]. These elements can act as localized charge carriers inside the semiconducting grains or at the insulating grain boundaries under an applied electric field and create interfacial polarisation between different grains. Also these charge carriers can induce hopping dipoles inside the grains by polaron hopping and contribute as well to enhance the permittivity values of the materials [154].

Samples in Table 4.4 are characterized by different density and grain size values. Generally speaking, an increase in the permittivity is observed in the samples presenting the smallest grain size. This agrees with a larger interfacial polarisation in these samples. Samples with grains over 1 μm present inhomogeneous microstructure and it is hard to evaluate its effect on their permittivity. This might explain the fluctuation in the permittivity values. Also in SPS (or vacuum sintering), samples permittivity is very much influenced by charge carriers. The quantity of these carriers (oxygen vacancies, Ti^{3+} ions ...) is supposed to increase with temperature increase and time of sintering. Attempts have been made to quantify the amount of Ti^{3+} ions after sintering by X-ray Photoelectron Spectrometry (XPS). Unfortunately, results were unusable owing to overestimated and puzzling carbon content. Nevertheless, in our measurements grain size seems to have more influence on the permittivity values than sintering temperature.

It is also noticeable that samples presenting larger levels of porosity present as well higher values of permittivity. However, at this point, it can't be concluded if this effect is due to the lower density or

the homogeneous and smaller grain size. Moreover, the highest permittivity values also coincide with the highest dielectric losses.

Different researches [117], [118], [119] have presented the highest values of permittivity for densities higher than 95% and grain sizes near 1 μm . But they have not shown a constant density to evaluate the results. Furthermore, porosity should decrease the permittivity and increase the dielectric loss but it is not clear if 5% porosity will be enough to produce this effect when most works related to BT refers to 95% as dense samples [155], [112], [156].

In order to make clearer the influence of grain size on permittivity, Figure 4.54 depicts only the permittivity and dielectric loss of samples with a density over 99% and sintered at the same temperature of 1000°C (with the assumption that a gap of 1% of relative density would not affect too much the dielectric values).

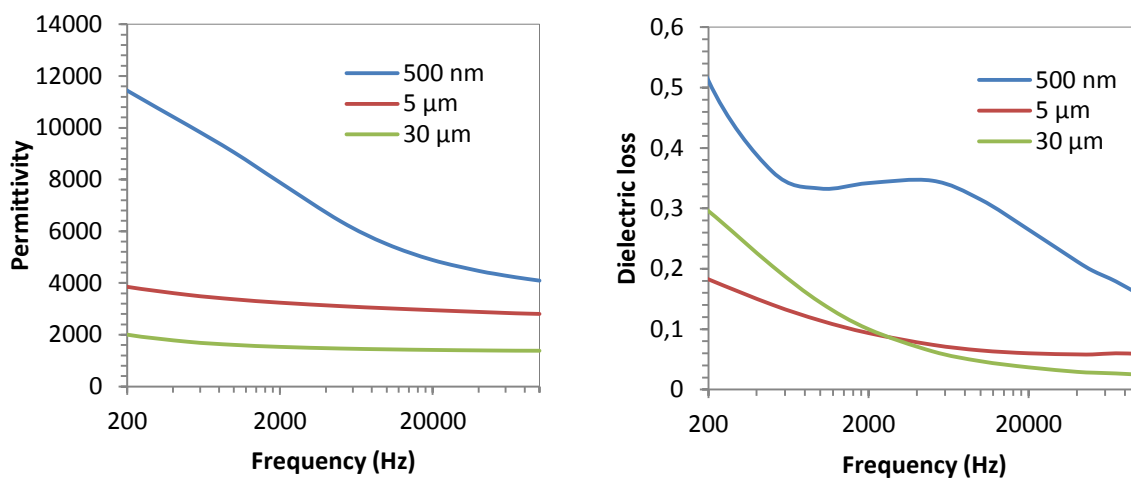


Figure 4.54. Frequency dependence of the permittivity and dielectric loss at room temperature of samples issued from the as-received powder.

A permittivity increase is observed with the decrease of the grain size. Our results agree with those of Ghosh et al. [120], who explained this effect with an enhancement of the domain wall motion as grain size approaches 1 μm .

The decrease in permittivity as the frequency increases indicates a relaxation mechanism related to the interfacial polarization (space charge) [123]. This behaviour explains why bigger grains, with fewer interfaces, induce lower permittivity. The higher permittivity observed with smaller grains and the different behaviour of the dielectric loss means that in this case two relaxation mechanisms are active: polaron hopping and interfacial polarization.

The influence of grain size was also studied after air annealing at 800°C for 6 hours of these samples. We saw in the previous part that this thermal treatment was sufficient to remove most of oxygen vacancies and reoxidise titanium ions. The frequency dependence of the permittivity and dielectric loss of BT samples after annealing is presented in Figure 4.55.

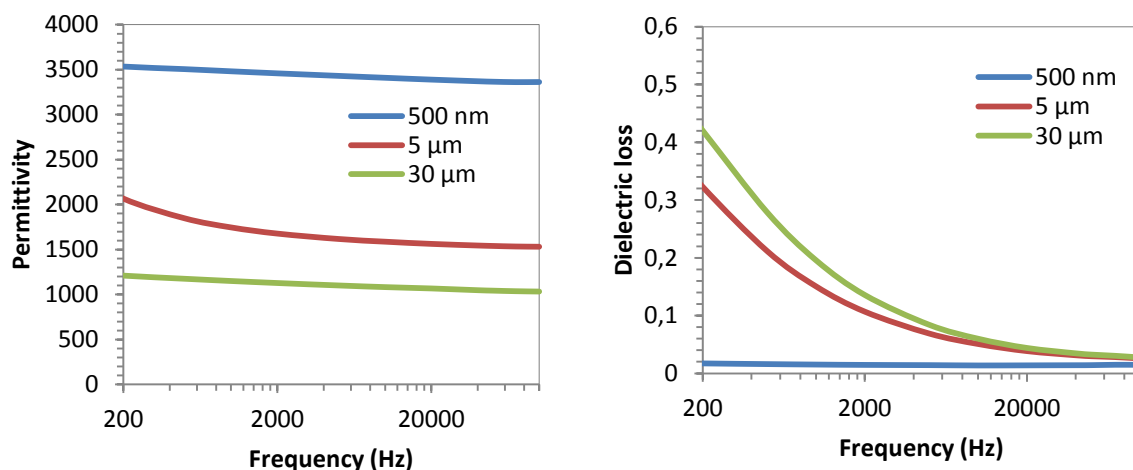


Figure 4.55. Frequency dependence of the permittivity and dielectric loss at room temperature of samples after annealing.

After annealing we observe a drop in permittivity in all samples due to the reduction of charge carriers, both the number of electrons and oxygen vacancies are reduced.

After annealing the number of charge carriers is reduced, so the contribution of the different polarisations is less active. This also explains the lower drop of the permittivity with the frequency. However, the relaxation mechanism on the dielectric loss is still evident for grains of 5 and 30 μm . In this case, dielectric losses are less linked to charge carriers, in contrast to the sample of 0.5 μm where the dielectric loss decreases dramatically after annealing.

In the case of smaller grains, the grain boundary contribution of the permittivity is displaced to frequencies lower than 200 Hz (not shown in the figure).

Pre-treatment influence

The influence of powder deagglomeration on the dielectric properties of barium titanate was also evaluated. Permittivity measurements were also carried out on samples prepared from deagglomerated powders.

Table 4.5 compares density, grain size, permittivity and dielectric loss of samples sintered by SPS at 1050°C-5 min (pressure 50MPa) from the powder as-received and after deagglomeration (microstructures were presented in Figure 4.15 and 4.29, respectively).

Table 4.5. Relative density, average grain size, permittivity (ϵ) and dielectric loss (td) at 1 kHz of a BT sample sintered at 1050°C prepared from as-received and deagglomerated powder.

Treatment	ρ (%)	Grain Size (μm)	ϵ (td) at 1kHz
As-received	99.9	>20*	5000 (0.15)
Deagglomerated	99.9	~1	16300 (0.11)

* Inhomogeneous size, value corresponds to the largest grain size observed

We observe that, in the same SPS conditions, the sample prepared from the deagglomerated powder shows values of permittivity much higher, more than three times the value of the sample obtained from the as-received powder. This huge improvement is linked to the difference in grain size between both samples (1 μm , instead of more than 20 μm) and thus the higher interfacial polarization that appears in the sample issued from the deagglomerated powder in addition to the enhancement of the domain wall motion as grain size approaches 1 μm .

Once observed the positive effect of deagglomeration in the permittivity values, the influence of grain size was analysed on samples presenting different grain sizes prepared from deagglomerated powders.

Table 4.6 describes SPS conditions used to obtain the samples, their density, grain size and dielectric properties. It is noticeable that in the case of deagglomerated powders high values of permittivity are obtained for a larger range of grain size while keeping a moderate dielectric loss. However, when the microstructure of the samples is mainly composed of grains over 10 μm , there is a pronounced drop in permittivity due to the decrease of the interfacial polarization contribution.

Table 4.6. Sintering conditions, relative density, average grain size, permittivity (ϵ) and dielectric loss (td) at 1 kHz of different BT samples issued from deagglomerated powder.

SPS conditions			ρ (%)	Grain Size (μm)	ϵ (td) at 1kHz
Tf ($^{\circ}\text{C}$)	Dwell (min)	P (MPa)			
1050/950	45	50	99.8	0.4	13000 (0.14)
1050	5	50	100	1	16300 (0.11)
1050	15	50	100	5*	14300 (0.06)
1100	5	50	99.0	15*	3900 (0.06)

* Inhomogeneous size, value corresponds to the largest grain size observed

Figure 4.56 depicts frequency dependency (200 Hz- 100 kHz) of the permittivity and dielectric loss of these samples.

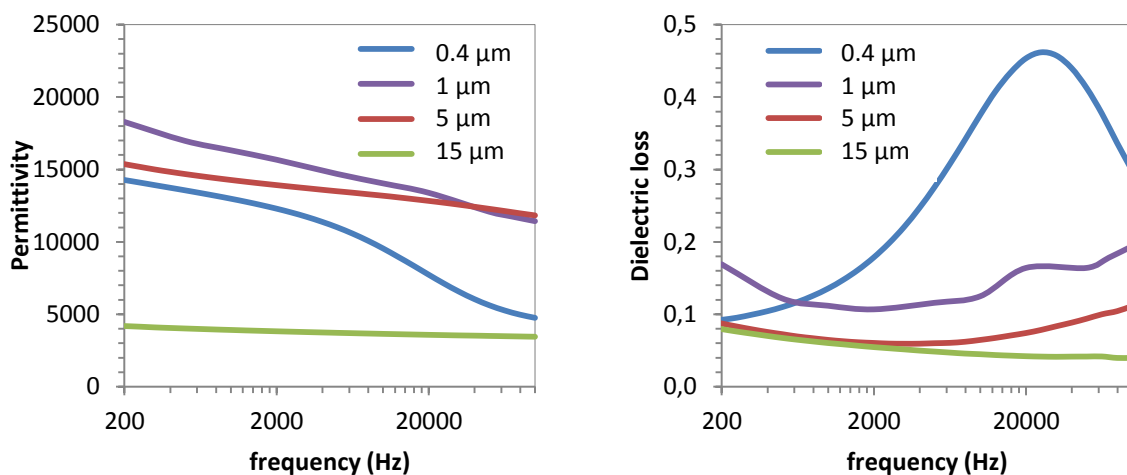


Figure 4.56. Grain size influence on the permittivity and dielectric loss at room temperature (from deagglomerated powder).

Permittivity of the sample composed of large grains remains constant over the whole range of frequencies, indicating an absence of grain boundary polarisation in this range. On the other samples, permittivity decreases as the measuring frequency increases. Sample containing 5- μm grains presents a single slope indicating some interfacial polarisation. Sample presenting 1- μm grains presents two slopes and an irregularity on the dielectric loss related to an incipient hopping polarisation effect. This is highlighted on the sample composed of smaller grains. But in this case permittivity values are lower due to the increase of insulating grain boundaries.

The influence of grain size on dielectric properties, after air annealing at 800°C for 6 hours, was also evaluated (Figure 4.57).

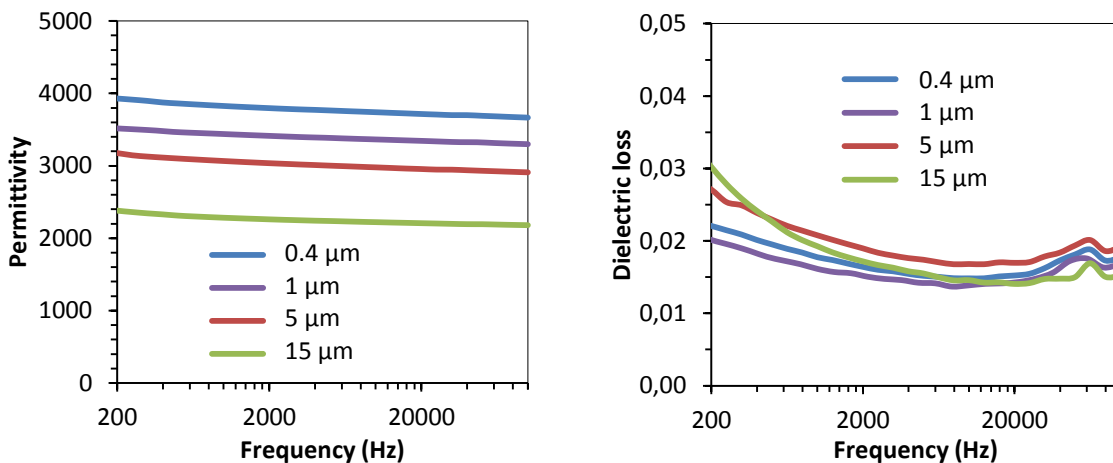


Figure 4.57. Grain size influence on the permittivity and dielectric loss at room temperature, after air annealing at 800°C-6 hours (from deagglomerated powder).

After annealing a drop in permittivity is observed in all samples due to the reduction of charge carriers, both the number of electrons and oxygen vacancies are reduced. Values of permittivity get closer and the influence of grain size is lower. Dielectric losses of the samples are very low, around 0.02, and coincident in all samples.

Annealing conditions influence

Different annealing conditions (temperatures from 600 to 800°C and dwell times of 15 minutes and 6 hours) have been evaluated to identify its influence on the permittivity of the samples.

The studied samples were prepared from deagglomerated powders and sintered at 1050°C for 5 minutes (50 MPa). Table 4.7 shows the characteristics of the samples before annealing. The frequency dependency of permittivity and dielectric loss after annealing are depicted on Figure 4.58.

After annealing at 600°C for 15 minutes, a large drop in permittivity is already observed and dielectric loss are low although the sample presents still a dark colour (Figure 4.59). Annealing for longer dwells or at higher temperatures presents a slight diminution in permittivity, but the values remain close. Dielectric losses are almost coincident for all annealing tested temperatures.

Table 4.7. Sintering conditions, relative density, average grain size, permittivity (ϵ) and dielectric loss (td) at 1 kHz before annealing.

SPS conditions			ρ (%)	Grain Size (μm)	ϵ (td) at 1kHz
Tf ($^{\circ}\text{C}$)	Dwell (min)	P (MPa)			
1050	5	50	100	1	16300 (0.11)

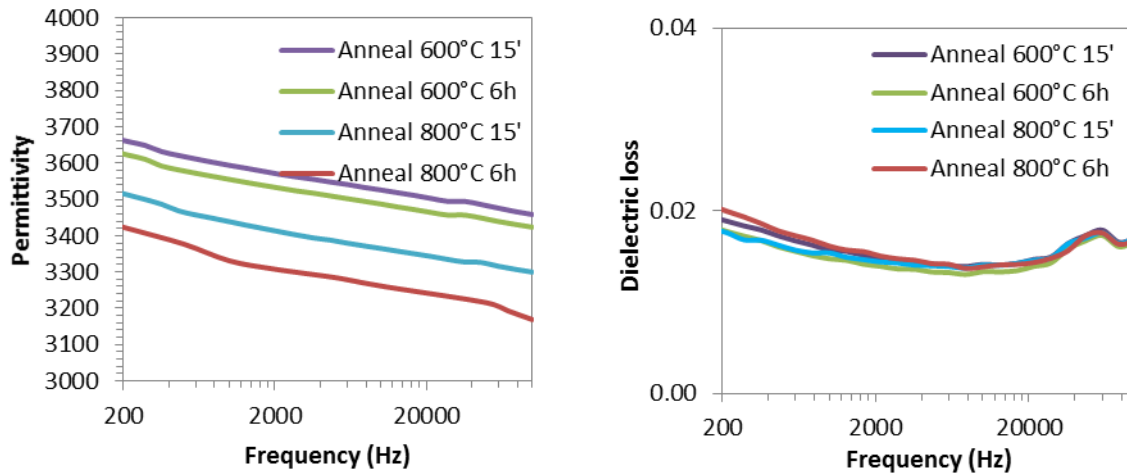


Figure 4.58. Frequency dependence of the permittivity and dielectric loss at room temperature after annealing.

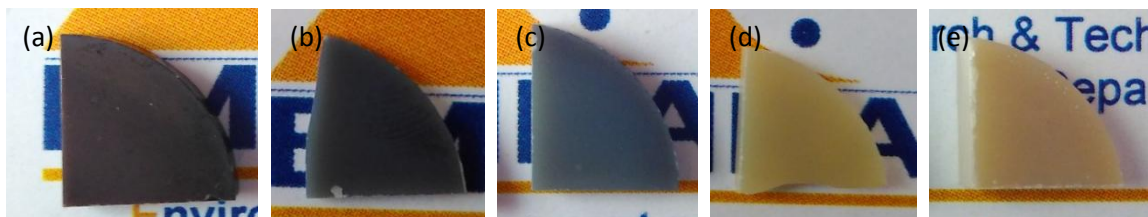


Figure 4.59. BT sample (a) as-sintered and annealed at (b) 600°C-15', (c) 600°C-6h, (d) 800°C-15' and (e) 800°C-6h.

BaSrTiO₃

The frequency and annealing dependences of the permittivity of the BST samples were also analysed.

Table 4.8 summarizes the properties (density, grain size, permittivity, dielectric loss) of a sample sintered by SPS at 50 MPa, 100°C/min up to 800°C and 10°C/min up to 1150°C with a dwell of 5 min (microstructure was presented in Figure 4.38c).

Table 4.8. Properties of a BST sample sintered by SPS at 1150°C-5 min, 50 MPa.

SPS conditions			ρ (%)	Grain Size (μm)	ϵ (td) at 1kHz
Tf ($^{\circ}\text{C}$)	Dwell (min)	P (MPa)			
1150	5	50	100	0.45	79500 (5.9)

Table 4.8 shows that permittivity values obtained are very high, but the dielectric loss is high as well, higher than 1. This dielectric loss indicates a semi-conductive behaviour of the samples. Such a high dielectric loss is not attractive in order to use BST as capacitor.

The frequency dependence of permittivity and the dielectric loss appears in Figure 4.60. Permittivity values are high (over 68000) for all the range of measured frequencies (200 Hz- 100 kHz) and only a slight decrease of permittivity appears with increasing frequency.

Regarding the dielectric loss, value diminishes as the frequency increases; the semi-conductive behaviour is less evident at high frequencies. Dielectric loss above 10 kHz remains under 1, but still over 0.2, and much higher than value obtained in BT annealed samples (0.02).

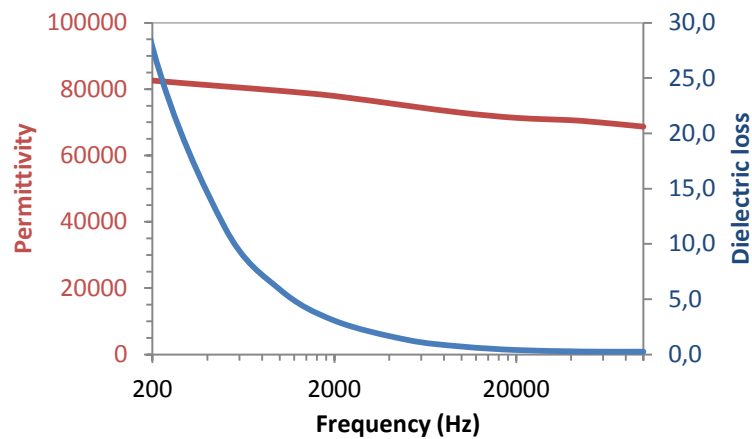


Figure 4.60. Frequency dependence of the permittivity and dielectric loss at room temperature for a BST sample.

In order to decrease the dielectric loss of BST samples, they were submitted to annealing post-treatments at different temperatures. Heating rate was fixed to 10°C/min and dwell was 6 hours.

Table 4.9 and Figure 4.61 describe the dielectric properties and appearance of samples annealed at 600, 800 and 900°C. After annealing at 600°C we observed already a large drop in permittivity, from 80000 to 40000, but the values remain still high. Dielectric loss has decreased as well; after annealing at 600°C dielectric loss remains below 1 for the whole range of frequencies. Annealing at higher temperatures leads to further decrease in permittivity values and dielectric loss. Permittivity values and dielectric losses are close in samples annealed at 800 and 900°C. Nevertheless, the charged species variation between these two temperatures is high enough to change completely the colour of the samples.

Table 4.9. Sintering conditions, relative density, average grain size, permittivity (ϵ) and dielectric loss (td) at 1 kHz after annealing.

Treatment	Annealing 600°C	Annealing 800°C	Annealing 900°C
ϵ (td) at 1kHz	43000 (0.08)	4100 (0.03)	3600 (0.04)



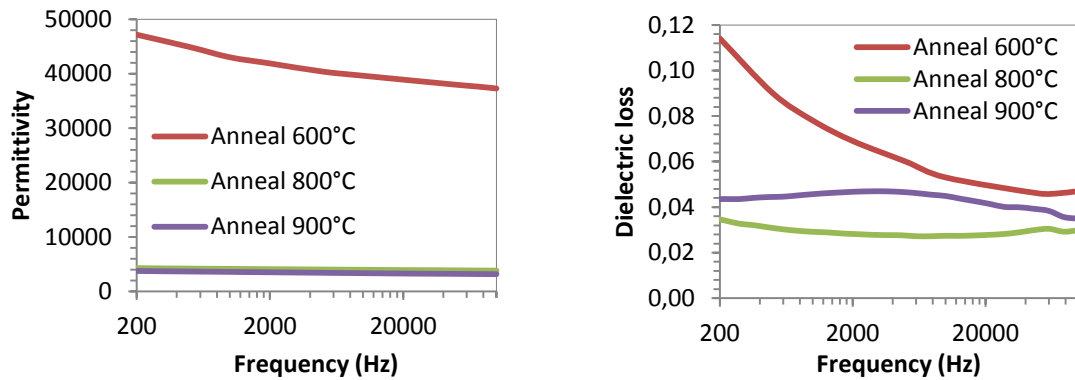


Figure 4. 61. Frequency dependence of the permittivity and dielectric loss of BST at room temperature.

Evolution of permittivity with the temperature of analysis

The temperature dependence of the permittivity and dielectric loss of BT and BST was recorded at different frequencies.

For BT, the measured sample was the one that presented the highest dielectric properties at room temperature (deagglomerated powder; 50MPa, 1050°C 5 min).

Figure 4.62 shows permittivity variation as a function of temperature. The maximum of permittivity appears around the Curie temperature, here around 140°C. This temperature is a little high for a BT ceramic, usually 130°C for samples prepared by conventional pressureless sintering [114]. This difference may be due to thermal hysteresis, as measurements were performed on heating. This transition is also diffuse and the values of permittivity and dielectric loss remain quite constant with the temperature variation. This behavior is ascribed to the small difference found between the tetragonal and cubic phases of barium titanate [124].

Permittivity values decrease as the frequency increases in the range of temperatures between 40 to 200°C as we observed in the measurements at room temperature.

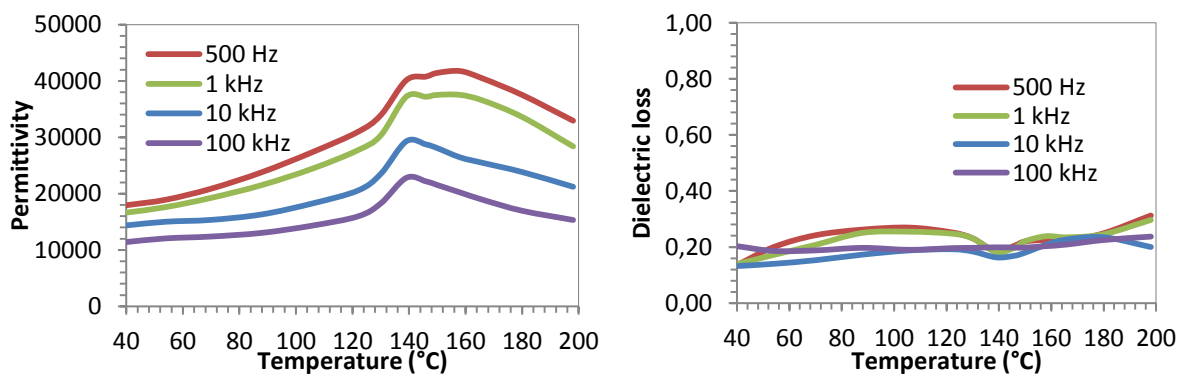


Figure 4.62. Dielectric properties of BT ceramic as a function of temperature for various frequencies.

Figure 4.63 shows the temperature dependence of the dielectric properties for a BST sample. Here a soft annealed sample (600°C) has been chosen due to the semi-conductive behavior of the as-sintered samples. However this sample presents quite high values of permittivity. Here, permittivity

shows almost no temperature dependence in the measured frequency range (0.5-100 kHz), and no discernible peak at the transition temperature is observed (for a BST with 0.2%mol. of strontium, value it should be around 70°C [125]). In BST, the high amount of charge carriers plays the main role even after soft annealing and the peak at the phase transition is unnoticeable.

As we observed for BT, in BST there is also a decrease in permittivity as the frequency increases. But the variation of the dielectric loss in BST is more dependent of the frequency, here lower dielectric losses are found at higher frequencies.

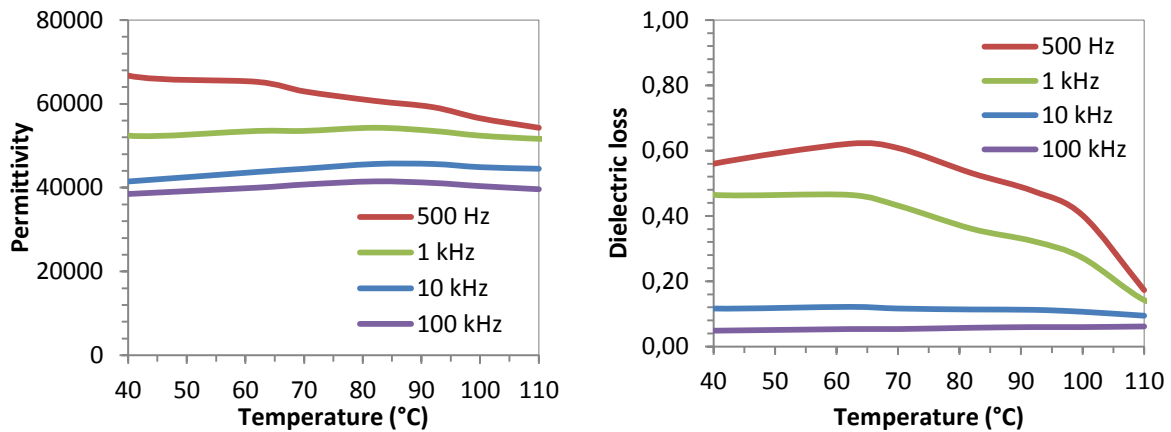


Figure 4.63. Dielectric properties of a BST ceramic as a function of temperature for various frequencies.

In order to better define the phase transition temperature of BT and BST, Raman analyses were performed as a function of the temperature. Analysed samples were sintered in the same conditions as the ones analyzed in permittivity and without annealing. No differences in the Raman spectra were found between samples before and after annealing at room temperature.

Figure 4.64 shows Raman spectra of a BT ceramic for temperatures between 80 and 170°C. It is noticeable that bands characteristic of the tetragonal phase (305 and 715 cm^{-1}) are visible up to 140°C. Above 150°C these bands almost disappear, so a diffuse transition is observed. This phase transition agrees with the previous permittivity measurements where maximum permittivity was found at 140°C.

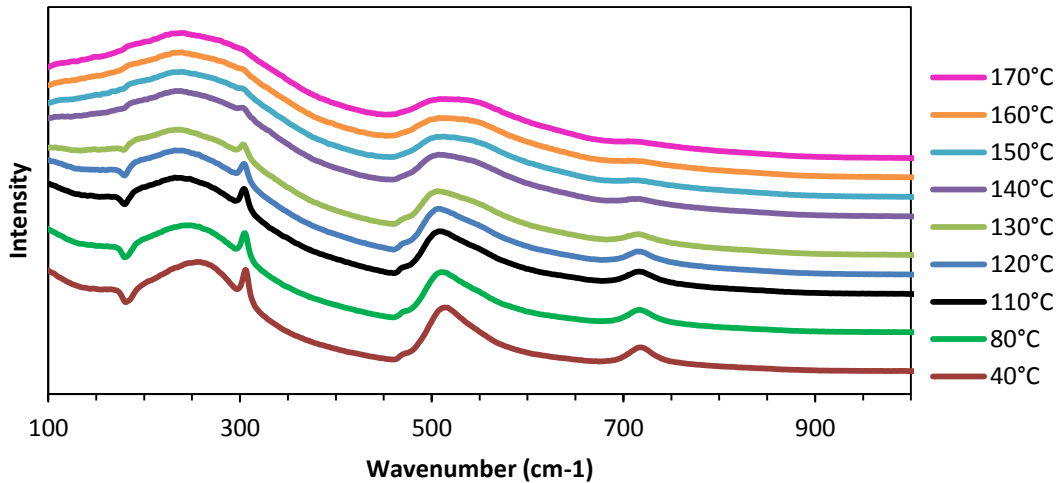


Figure 4.64. Raman spectra of BT ceramic at different temperatures.

Figure 4.65 shows Raman spectra of BST for temperatures between 20 and 100°C. In BST samples, bands characteristic of the tetragonal phase (305 and 715 cm^{-1}) are visible up to 60°C. Above 70°C these bands disappear, as expected. However also in Raman, a diffuse transition is observed.

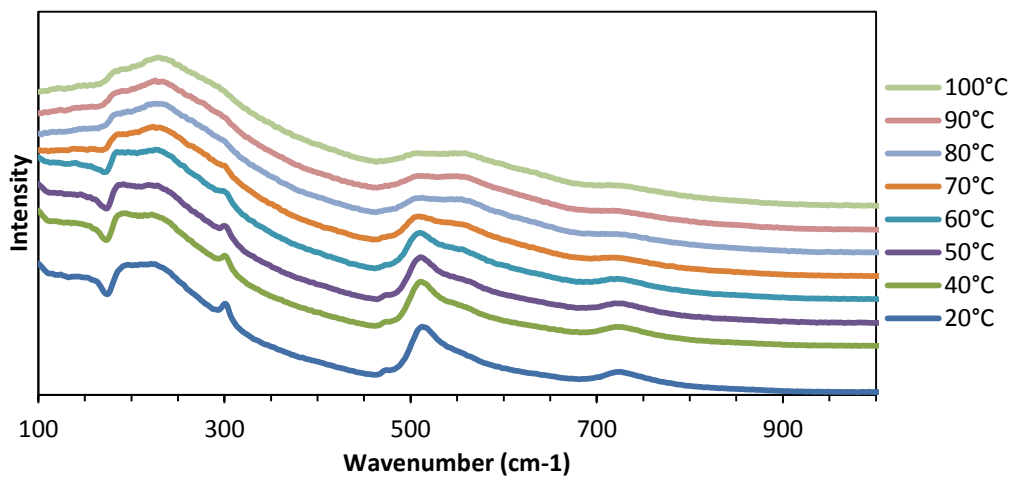


Figure 4.65. Raman spectra of BST ceramic at different temperatures.

Conclusion

Permittivity values of the as-sintered BT and BST samples are high. BT reaches values of 16000 and BST of 80000. Usually, Sr insertion to BT leads to a decrease of the permittivity values. In this work, such a behavior is not observed. This result is probably related to the synthesis origin and characteristics of the powders that both can influence the dielectric properties. BST samples present higher values of permittivity and almost frequency independent, similar to those obtained recently by Dupuis et al. [130]. Apparently in the case of BST, interfacial polarization and polaron hopping, mediated by Ti^{3+} ions and oxygen vacancies, are the main contributing mechanisms to colossal permittivity. Our explanation is that in the case of BST, more charge carriers are generated due to the

intrinsic characteristics of the powder and the higher sintering temperatures needed compared to BT.

Annealing in air at different temperatures induced a drop in permittivity. In the case of BT, this drop was already high at low temperatures (600°C) and did not evolve a lot with the increase of the annealing temperature.

In the case of BST, higher values of permittivity are obtained, almost colossal, but along with high dielectric losses. These properties indicate a higher amount of charge carriers in the samples that induce a semi-conductive behaviour. In order to recover the insulating properties of the samples, annealings at different temperatures have been performed. Annealing at lower temperatures reduces the permittivity values, which nevertheless remain quite high. Annealing also reduces the dielectric loss. This behaviour was already found by other researches ([145], [123]). They explained that as-sintered samples with colossal permittivity were slightly conductive and their dielectric loss was very high. However, with only a short annealing, the surfaces became isolating and led to a combination of colossal permittivity with relatively low dielectric losses.

Regarding the influence of grain size on the permittivity values, BT samples with grain size of 1 μm lead to the best results of permittivity. Specially before annealing, it is noticeable the contribution of interfacial and hopping polarisations owing to the charge carriers existence, and the highest contribution of these polarisations when grain size approaches 1 μm . After annealing, although the highest permittivity is also observed for grain sizes $\sim 1\mu\text{m}$, the permittivity values between samples of different grain size are closer.

The same behaviour was observed in our BT and BST samples. Permittivity is related to the amount of charge carriers induced by the SPS (oxygen vacancies and electrons), so annealing implies a reduction in the number of carriers and so the permittivity decreases. This is also linked to the colour of the samples: as long as oxygen vacancies remain, a dark colour is still present in the samples.

Unfortunately, translucent ceramics need an annealing at higher temperatures and do not present the highest permittivity values. Nevertheless they present quite high values and could be suitable for many applications.

4.4. Conclusions chapter IV

In this chapter, the sintering behaviour of BT and BST powders was described. The effect of different SPS parameters (temperature, dwell time, heating rate, pressure) was evaluated. Both powders were sensitive to abnormal grain growth and presented a very narrow sintering window where both full density and fine microstructure could be obtained. Therefore, the SPS parameters had to be carefully controlled because grain growth processes took place dramatically fast.

In the case of BT, samples from the as-received powder, sintered below the critical SPS grain growth conditions, presented a fine and homogeneous microstructure but usually without attaining full density. On the contrary, samples prepared above the critical parameters presented microstructures with large grains embedded in a matrix of finer grains. This effect was exacerbated by the presence of agglomerates. Agglomerates led to differential sintering and grain coarsening occurred quickly.

Dispersion of BT powder eliminated agglomerates and allowed retaining a fine microstructure until higher temperatures. This was favourable to obtain samples with fine microstructure and full density.

Compared to BT, BST powder was not as sensitive to grain growth as it approached full density. Its optimum sintering window was also narrow but grain growth happened at higher temperatures and after attaining full density: apparently the incorporation of Sr ions on the structure retarded grain growth. It was possible to attain full density samples and to retain a fine microstructure from the as-received BST powder. In contrast to BT, deagglomeration of BST powder did not lead to significant differences in sintering or microstructure.

BT and BST samples with 100% relative density presented a black colour attributed to oxygen vacancies, graphite contamination and/or reduction of Ti^{4+} into Ti^{3+} , originated during SPS.

These darkening sources should be removed with an annealing in air as post-treatment. The annealing temperature has to be optimised in order to remove the different sources of darkening. Optimised temperatures resulted in yellowish translucent samples which presented high level of optical transmission considering the results obtained so far for BT and BST [40], [133]. RIT values were low: despite our efforts, samples still presented defects that acted as scattering centres. But, their TFT values were quite promising.

The best optical transmission obtained for $BaTiO_3$ samples attained 35% at $\lambda=600$ nm, this value is the highest observed to date. In addition, our $Ba_{0.8}Sr_{0.2}TiO_3$ samples attained even a higher value: 41% at $\lambda=600$ nm.

Regarding the dielectric properties of our SPS samples, permittivity values of the as-sintered BT and BST samples were high. BT reached values of 16000 and BST of 80000 in samples with full density, homogeneous microstructure and grain size close to 1 μm . The influence of grain size was investigated and a drastic drop in permittivity was observed when the microstructure presented grains above 5 μm .

Annealing in air led to a diminution of the permittivity but fortunately also reduced the dielectric loss, especially on the BST samples which presented dielectric loss higher than 1 after sintering. In the case of BT, this drop in permittivity was already high at low temperature annealing (600°C) and it did not evolve more with the increase of the temperature. In contrast, annealing BST samples at 600°C reduced the dielectric loss and also the permittivity values, which however remained quite high.

Unfortunately, translucent ceramics needed an annealing at higher temperatures (800 – 900°C) and did not present the highest permittivity values. Nevertheless they presented quite high values in the frequency range 0.2- 100 kHz, they showed permittivities of 4000 and 3600 and dielectric losses of 0.02 and 0.03 for BT and BST, respectively.

In conclusion, the field of transparent BT and BST ceramics is still unexplored and the values obtained during this thesis are encouraging and open the application of these materials as optical devices. They can be suitable for optical and electrical applications and substitute more toxic components as $Pb(Zr,Ti)O_3$ (PZT).

General conclusions

This work focused on the fabrication of transparent ceramics by Spark Plasma Sintering and on a better understanding of the factors limiting the optical transmission. From the literature review, these factors may come from two different sources: the starting powder and the sintering process.

The optimisation of powder conditioning, SPS parameters and post-treatment conditions allowed the processing of transparent YAG, BaTiO₃ and Ba_{0.8}Sr_{0.2}TiO₃ compacts, with optical transmission values close or higher than those found in the literature. Moreover, the relation between final functional properties and powders characteristics and/or SPS parameters (and thus resulting microstructure) was evidenced.

In the case of YAG ceramics, three powders, a home-synthesized YAG-S and two commercial powders, YAG-B and YAG-N, were investigated. A thorough characterization of these powders has allowed highlighting their main physicochemical differences, in terms of purity, agglomeration degree and chemical composition.

- The best optical transmission results were obtained for samples sintered from YAG-N powder: RIT and TFT values, measured at 600 nm, with the addition of 0.2% Lithium fluoride, were 70 and 77%, respectively. Such high values were obtained owing to the high purity and moderate agglomeration degree of the powder. Without dispersion and LiF doping, transparent ceramic were already obtained. Addition of LiF improved slightly the RIT and TFT values by decreasing the amount of residual porosity. Moreover, although YAG phase content was very low in YAG-N starting powder, the conversion of intermediate phases (h-YAlO₃ and YAM) into pure YAG was possible during spark plasma sintering, even with the use of short sintering cycles;
- A pure and monophasic YAG powder was synthesized in this study. However, samples prepared from untreated YAG-S powder presented a significant core-shell aspect. After deagglomeration of the powder and mostly post-hipping in air, more homogeneous samples were obtained. Large temperature gradients explaining this aspect were ruled out as no difference in terms of microstructure were observed and FE modelling showed a temperature gradient of only 4°C inside the sintered compacts. This core-shell aspect was rather attributed to the high agglomeration degree of the powder and the presence of stress gradients during sintering;
- Concerning the second commercial powder, YAG-B, even after powder deagglomeration and post-annealing, ceramics were not fully densified and intermediate phases (YAP and YAM) were still detected. Addition of LiF led to fully dense samples, containing only the YAG phase and translucent ceramics: indeed, samples presented a large level of scattering. This scattering was ascribed to the residual presence of sulphur (~ 50 ppm vs 500 ppm in the initial powder, coming from the synthesis route). This result confirms the detrimental effect of impurities (even at very low concentration) in achieving highly transparent ceramics.

Regarding the influence of the SPS parameters, temperature had to be adapted to the powder and be sufficient to achieve full density. Concerning other parameters, moderate pressures (50 MPa) and low heating rates seemed more appropriate to attain high transparency level.

The study of YAG represents a thorough comparison of three different YAG powders, and the influence of the powder characteristics and sintering parameters in the obtaining of transparent ceramics. In literature, most works focus on a single powder, so the respective influence of the powder itself and the sintering conditions is hard to separate. This work offers a global view of the ensemble. In addition, it also offers different alternatives of improvement of the transparency, as deagglomeration, LiF addition, annealing or post-hipping taking into account the results obtained after sintering for each powder.

Barium titanate powder appeared very sensitive to abnormal grain growth and the sintering window (temperature, pressure and dwell time) to obtain fully dense ceramics while preserving a fine microstructure was very narrow. This effect was ascribed to the high agglomeration degree of the powder, leading to differential sintering and abnormal grain growth. After deagglomeration, fully dense samples with fine microstructure were obtained with adapted SPS parameters.

The study of the sintering of barium strontium titanate powder showed that incorporation of strontium retarded grain growth and fully dense samples with homogeneous microstructure were obtained without powder deagglomeration.

For both powders, adapted air annealing allowed removing the dark coloration and led to translucent samples. Although RIT values were very low, TFT values were significant, 35% and 41% at 600 nm, for BT and BST respectively, highest value observed to date for a BT ceramic. Dielectric properties of BaTiO_3 and $\text{Ba}_{0.8}\text{Sr}_{0.2}\text{TiO}_3$ compacts were evaluated as well. Samples with full density and a homogeneous microstructure, with average grain size near 1 μm provided the highest permittivity values and after annealing in air, low dielectric losses.

The study of the barium titanate and barium strontium titanate powders represents an important advance in the application of this type of materials to electro-optic devices. It has been shown that samples with full density and a homogeneous microstructure can be obtained from commercial powders with SPS. Moreover, the intrinsic drawbacks of SPS, vacuum sintering and graphite contamination, have been proved to be overcome with an optimised annealing in air post-treatment. The most important contribution of this study is the good level of transparency attained. The samples elaborated in this thesis present the highest values of transparency obtained so far, and encourage the research of applications of this type of materials in optical devices.

The large transparency and permittivity values obtained in BT and BST ceramics are encouraging and open the field of application of BT and BST in transparent integrated circuits, or as capacitors in solar cell modules. These advantageous characteristics make them good candidates for the substitution of more toxic, lead-based electronic components as PZT, which represent nowadays the most attractive solutions, but are harmful for the environment.

From all these results, SPS has been proven to be a good alternative to fabricate transparent ceramics despite the graphite tooling and vacuum sintering, and it is especially interesting in the sintering of materials that hardly reach full density with other sintering techniques, as BaTiO_3 .

Darkening coming from sintering conditions can be quite easily eliminated (or at least strongly reduced) by adapted annealing treatments in air.

The crucial point to obtain a transparent ceramic remains the starting powder. Presence of agglomerates can be allowed if they are relatively soft and can be removed by a deagglomeration step. On the contrary, presence of impurities (like sulphur in the case of YAG-B powder) proved to be dramatic to transparency, even in amount as low as 50 ppm.

Perspectives

Although transparent or translucent YAG and BT ceramics were obtained in this thesis, some improvements and additional analyses remain necessary.

Observations by transmission electron microscopy (TEM), more sensitive than FESEM, would allow observing the defects at the origin of the loss of transparency of certain samples. For example, TEM observations could distinguish probable differences in microstructure between the core and the shell of YAG-S samples. The detection of the presence and corresponding location of sulphur in non-doped YAG-B powder should also be possible.

Although the transmission of BT/BST samples is high compared to the literature data, it remains moderate considering their maximal theoretical value. Further investigation could be done to improve the optical transmission.

- Deagglomeration by ball milling and drying with rotavapor led to a consequent reagglomeration of the powders. So, another way could be attempted: after the dispersion step by ball milling, powders could be shaped by slip casting process. In fact, slip-casting should conserve the particles dispersed. However, slip casting implies the use of higher solid loads and so the use of an appropriate dispersant to achieve it. Hence, this dispersant should be removed before spark plasma sintering to prevent it to leave impurities in the transparent samples.
- In the literature, some researchers obtained transparent BT/BST samples with good transmission values with the application of very high pressures, around 200 MPa. However, the application of such high pressures implies the use of a tooling material different than graphite (as silicon carbide). This change of tooling material will probably need a new optimisation of SPS parameters.

Moreover, the detection of the degree of reduction of titanium, could offer more information about its influence in the permittivity values. Another possible method to detect this cation is Electron Paramagnetic Resonance spectroscopy (EPR). This technique identifies elements with unpaired electrons as Ti^{3+} .

Finally, regarding $BaTiO_3$ and $(Ba,Sr)TiO_3$, it will be interesting to evaluate other specific properties that will make these materials more attractive industrially:

- Electro-optic measurements: electro-optic devices as optical switches and optical modulators are widely used in the photonic industry to precisely control and manipulate the light. These

devices make use of materials with optical properties that are tunable with electrical signals. In ferroelectric materials, as BT, there is a change in the refractive index with the applied electric field, hence and evaluation of its electro-optic properties will made our samples very adequate for this kind of applications.

- Breakdown voltage: above a particular electric field, known as the dielectric strength, the dielectric capacitor becomes conductive. The voltage at which this occurs is called the breakdown voltage and is given by the product of the dielectric strength and the thickness of the capacitor. This voltage limits the maximum capacity of the material. Hence, the definition of the breakdown voltage of our samples would be an interesting characteristic to measure as well.

References

- [1] R. Coble, «Transparent Alumina and Method of Preparation». U.S. Brevet 3026210, 20 March 1962.
- [2] R. Apetz and M. P. Bruggen, "Transparent alumina. A light scattering model," *J. Am. Ceram. Soc.*, vol. 86, pp. 480-6, 2003.
- [3] A. Krell, J. Klimke et T. Hutzler, «Transparent compact ceramics: Inherent physical issues,» *Opt. Mater.*, vol. 31, pp. 1144-1150, 2009.
- [4] "RefractiveIndex.INFO," [Online]. Available: <http://refractiveindex.info/?shelf=main&book=BaTiO3&page=Wemple-o>. [Accessed 3 February 2014].
- [5] W. Callister, *Materials Science and Engineering. An Introduction*, John Wiley & Sons, 1997.
- [6] J. Anderson, K. Leaver, P. Leever et R. Rawlings, *Materials Science for Engineers*, Nelson Thornes Ltd., 2003.
- [7] M. Rubat du Merac, H.-J. Kleebe, M. Müller et I. Reimanis, «Fifty years of research and development coming to fruition; unraveling the complex interactions during processing of transparent MgAl₂O₄,» *J. Am. Ceram. Soc.*, vol. 96, pp. 3341-3365, 2013.
- [8] A. Krell, J. Klimke and T. Hutzler, "Advanced spinel and sub-micron alumina for transparent armour applications," *J. Eur. Ceram. Soc.*, vol. 29, pp. 275-81, 2009.
- [9] B. Kim, K. Hiraga, K. Morita et al, «Microstructure and optical properties of transparent alumina,» *Acta Materialia*, vol. 57, pp. 1319-1326, 2009.
- [10] K. Morita, B. Kim, K. Hiraga et H. Yoshida, «Fabrication of transparent MgAl₂O₄ spinel polycrystal by spark plasma sintering processing,» *Scripta Materialia*, vol. 58, pp. 1114-1117, 2008.
- [11] G. Spina, G. Bonnefont, P. Palmero, G. Fantozzi, J. Chevalier et Montanaro, «Transparent YAG obtained by spark plasma sintering of coprecipitated powder. Influence of dispersion route and sintering parameters on optical and microstructural characteristics,» *J. Eur. Ceram. Soc.*, vol. 32, pp. 2957-2964, 2012.
- [12] C. Bohren et D. Huffman, *Absorption and scattering of light by small particles*, New York: John Wiley & Sons, 1983.
- [13] M. Rubat du Merac, I. Reimanis, C. Smith, H.-J. Kleebe et M. Muller, «Effect of Impurities and LiF Additive in Hot-Pressed Transparent Magnesium Aluminate Spinel,» *Int. J. Appl. Ceram. Technol.*, vol. 10, pp. 33-48, 2013.

- [14] A. Krell, T. Hutzler, J. Klimke et A. Potthoff, «Fine-Grained Transparent Spinel Windows by the Processing of Different Nanopowders,» *J. Am. Ceram. Soc.*, vol. 93, pp. 2656-2666, 2010.
- [15] M. Suarez, *Materiales ceramicos policristalinos de Al₂O₃ y YAG con funcionalidad optica*, PhD Thesis. Universidad de Oviedo, 2008.
- [16] M. Suarez, J. Menendez et R. Torrecillas, «Transparent Yttrium Aluminium Garnet obtained by Spark Plasma Sintering of Lyophilized Gels,» *J. of Nanomaterials*, 2009.
- [17] H. Gong, J. Zhang, D.-Y. Tang, G.-Q. Xie, H. Huang et J. Ma, «Fabrication and laser performance of highly transparent Nd:YAG ceramics from well-dispersed Nd:Y₂O₃ nanopowders by freeze-drying,» *J. Nanopart. Res.*, vol. 13, pp. 3853-3860, 2011.
- [18] L. Esposito, A. Piancastelli, A. Costa, M. Serantoni, G. Toci et M. Vannini, «Experimental features affecting the transparency of YAG ceramics,» *Optical Materials*, vol. 33, pp. 713-721, 2011.
- [19] S. F. Wang, Y. Zhang, D. W. Luo et al., «Transparent ceramics : processing, materials and applications,» *Progress in solid state chemistry*, vol. 41, pp. 20-54, 2013.
- [20] X. Ba, J. Li, Y. Pan et al, «Comparison of aqueous- and non-aqueous-based tape casting for preparing YAG transparent ceramics,» *J. of Alloys and Compounds*, vol. 577, pp. 228-231, 2013.
- [21] K. Liu, D. He, H. Wang et al, «High-pressure sintering mechanism of yttrium aluminum garnet (Y₃Al₅O₁₂) transparent nanoceramics,» *Scripta Materialia*, vol. 66, pp. 319-322, 2012.
- [22] H. Mizuta, K. Oda, Y. Shibasaki et al, «Preparation of high-strength and translucent alumina by Hot Isostatic Pressing,» *J. Am. Ceram. Soc.*, vol. 72, pp. 469-73, 1992.
- [23] S.-H. Lee, E. Kupp, A. Stevenson et al., «Hot Isostatic Pressing of Transparent Nd:YAG Ceramics,» *J. Am. Ceram. Soc.*, vol. 92, n° 17, pp. 1456-1463, 2009.
- [24] J. Cheng, D. Agrawal, Y. Zhang et R. Roy, «Microwave sintering of transparent alumina,» *Materials Letters*, vol. 56, pp. 587-92, 2002.
- [25] D. Agrawal, J. Chen et R. Roy, «Microwave reactive sintering of fully transparent aluminum oxynitride (AlON) ceramics,» *Ceramics Transactions*, vol. 134, pp. 587-94, 2002.
- [26] R. S. Dohedoe, G. D. West et M. H. Lewis, «Spark plasma sintering of ceramics: understanding temperature distribution enables more realistic comparison with conventional processing,» *Advances in Applied Ceramics*, vol. 104, p. 35, 2005.
- [27] M. Omori, «Sintering, consolidation, reaction and crystal growth by the spark plasma system,» *Mat. Sci. Eng. A*, vol. 287, pp. 183-8, 2002.
- [28] R. Chaim, «Superfast densification of nanocrystalline oxide powders by spark plasma

- sintering,» *J. Mater. Sci.*, vol. 41, pp. 7862-71, 2006.
- [29] D. Jiang, D. M. Hulbert, J. D. Kuntz et al, «Spark plasma sintering: a high strain rate low temperature forming tool for ceramics,» *Mat. Sci. Eng. A*, vol. 463, pp. 89-93, 2007.
- [30] K. Inoue, «Electric-discharge sintering». U.S. Brevet 3241956, 22 March 1966.
- [31] M. Suarez, A. Fernandez, J. Menendez, R. Torrecillas, H. Kessel, J. Hennicke et al., «Challenges and Opportunities for Spark Plasma Sintering: A Key Technology for a New Generation of Materials,» chez *Sintering Applications*, InTech, 2013, pp. 319-342.
- [32] Z. Munir, D. Quach et M. Ohyanagi, «Electric current activation of sintering: A review of the pulsed electric current sintering process,» *J. Am. Ceram. Soc.*, vol. 94, n° 11, pp. 1-19, 2011.
- [33] U. Anselmi-Tamburini, S. Gennari, J. Garay et Z. Munir, «Fundamental investigations on the spark plasma sintering/synthesis process:II. Modelling of current and temperature distributions.,» *Materials Science and Engineering A*, vol. 394, pp. 139-148, 2005.
- [34] R. Chaim, M. Kalina et J. Shen, «Transparent yttrium aluminum garnet (YAG) ceramics by spark plasma sintering,» *J. Eur. Ceram. Soc.*, vol. 27, pp. 3331-3337, 2007.
- [35] B.-N. Kim, K. Hiraga, K. Morita et H. Yoshida, «Spark plasma sintering of transparent alumina,» *Scripta Materialia*, vol. 57, pp. 607-610, 2007.
- [36] K. Morita, B.-N. Kim, H. Yoshida et K. Hiraga, «Spark plasma sintering condition optimisation for producing transparent MgAlO₄ spinel polycrystal,» *J. Am. Ceram. Soc.*, vol. 92, pp. 1208-16, 2009.
- [37] M. Sokol, S. Kalabukhov, M. Dariel et N. Frage, «High-pressure spark plasma sintering (SPS) of transparent polycrystalline magnesium aluminate spinel (PMAS),» *J. Eur. Ceram. Soc.*, vol. 34, pp. 4305-4310, 2014.
- [38] B.-N. Kim, K. Hiraga, K. Morita et al., «Effects of heating rate on microstructure and transparency of spark-plasma-sintered alumina,» *J. Eur. Ceram. Soc.*, vol. 29, pp. 323-327, 2009.
- [39] M. Stuer, Z. Zhao, U. Aschauer et P. Bowen, «Transparent polycrystalline alumina using spark plasma sintering: Effect of Mg, Y and La doping,» *J. Eur. Ceram. Soc.*, vol. 30, pp. 1335-1343, 2010.
- [40] J. Liu, Z. Shen, W. Yao et al., «Visible and infrared transparency in lead free bulk BaTiO₃ and SrTiO₃ nanoceramics,» *Nanotechnology*, vol. 21, 2010.
- [41] P. Palmero, G. Bonelli, G. Fantozzi et al, «Surface and mechanical properties of transparent polycrystalline YAG fabricated by SPS,» *Materials Research Bulletin*, vol. 48, pp. 2589-2597, 2013.
- [42] N. Frage, S. Kalabukhov, N. Sverdlov et al, «Effect of the spark plasma sintering (SPS) parameters and LiF doping on the mechanical properties and the transparency of

- polycrystalline Nd-YAG,» *Ceram. Int.*, vol. 38, pp. 5513-9, 2012.
- [43] Y. Aman, V. Garnier et E. Djurado, «A Screening Design Approach for the Understanding of Spark Plasma Sintering Parameters: A Case of Translucent Polycrystalline Undoped Alumina,» *Int. J. Appl. Ceram. Technol.*, vol. 7, pp. 574-586, 2009.
- [44] L. An, A. Ito et T. Goto, «Two-step pressure sintering of transparent lutecium oxide by spark plasma sintering,» *J. Eur. Ceram. Soc.*, vol. 31, pp. 1597-1602, 2011.
- [45] A. Rothman, S. Kalabukhov, N. Sverdlov, M. Dariel et N. Frage, «The Effect of Grain Size on the Mechanical and Optical Properties of Spark Plasma Sintering-Processed Magnesium Aluminate Spinel MgAl₂O₄,» *Int. J. Appl. Ceram. Technol.*, pp. 1-8, 2012.
- [46] O. Guillon, J. Gonzalez-Julian, B. Dargatz et al., «Field-Assisted Sintering Technology/Spark Plasma Sintering: Mechanisms, Materials, and Technology Developments,» *Advanced Engineering Materials*, vol. 16, pp. 830-849, 2014.
- [47] S. Muñoz et U. Anselmi-Tamburini, «Temperature and stress fields evolution during spark plasma sintering processes,» *Journal of Materials Science*, vol. 45, pp. 6528-6539, 2010.
- [48] K. Vanmeensel, A. Laptev, J. Hennicke et al, «Modelling of the temperature distribution during field assisted sintering,» *Acta Materialia*, vol. 53, pp. 4379-4388, 2005.
- [49] S. Grasso, C. Hu, G. Maizza, B.-N. Kim et Y. Sakka, «Effects of Pressure Application Method on Transparency of Spark Plasma Sintered Alumina,» *J. Am. Ceram. Soc.*, vol. 94, pp. 1405-1409, 2011.
- [50] K. Morita, B.-N. Kim, H. Yoshida et al, «Effect of loading schedule on densification of MgAl₂O₄ spinel during spark plasma sintering (SPS) processing,» *J. Eur. Ceram. Soc.*, vol. 32, pp. 2303-2309, 2012.
- [51] R. Marder, C. Estournes, G. Chevallier et R. Chaim, «Spark and plasma in spark plasma sintering of rigid ceramic nanoparticles: A model system of YAG,» *J. Eur. Ceram. Soc.*, vol. 35, pp. 211-218, 2015.
- [52] S. Grasso, B.-N. Kim, C. Hu, G. Maizza et Y. Sakka, «Highly Transparent Pure Alumina Fabricated by High-Pressure Spark Plasma Sintering,» *J. Am. Ceram. Soc.*, vol. 93, pp. 2460-2462, 2010.
- [53] M. Sokol, S. Kalabukhov, V. Kasiyan, M. Dariel et N. Frage, «Functional properties of Nd:YAG polycrystalline ceramics processed by high-pressure spark plasma sintering (HPSPS),» *J. Am. Ceram. Soc.*, pp. 1-6, 2015.
- [54] S. Meir, S. Kalabukhov, N. Froumin, M. Dariel et N. Frage, «Synthesis and Densification of Transparent Magnesium Aluminate Spinel by SPS Processing,» *J. Am. Ceram. Soc.*, vol. 92, pp. 358-364, 2009.

- [55] G. Fantozzi, J. Le Gallet et J. Niepce, *Science & Technologies céramiques*, EDP Sciences, 2011.
- [56] J. Haussonne, C. Carry, P. Bowen et J. Barton, *Céramiques et verres: principes et techniques d'élaboration*, Presses polytechniques et universitaires romandes, 2005.
- [57] C. Marlot, *Elaboration de céramiques transparentes Er:YAG: Synthèse de poudre par co-précipitation et frittage SPS*, PhD Thesis. Université de Bourgogne, 2013.
- [58] D. Jiang, D. Hulbert, U. Anselmi-Tamburini, T. Ng, D. Land et A. Mukherjee, «Optically Transparent Polycrystalline Al₂O₃ Produced by Spark Plasma Sintering,» *J. Am. Ceram. Soc.*, vol. 91, pp. 151-154, 2008.
- [59] H. Zhang, B.-N. Kim, K. Morita, H. Yoshida, K. Hiraga et Y. Sakka, «Effect of sintering temperature on optical properties and microstructure of translucent zirconia prepared by high-pressure spark plasma sintering,» *Sci. Technol. Adv. Mater.*, vol. 12, p. 055003, 2011.
- [60] G. Bernard-Granger, N. Benameur, C. Guizard et M. Nygren, «Influence of graphite contamination on the optical properties of transparent spinel obtained by spark plasma sintering,» *Scripta Materialia*, vol. 60, pp. 164-167, 2009.
- [61] C. Wang et Z. Zhao, «Transparent MgAl₂O₄ ceramic produced by spark plasma sintering,» *Scripta Mater.*, vol. 61, pp. 193-6, 2009.
- [62] N. Frage, S. Kalabuknov, N. Sverdlov, V. Ezersky et M. Dariel, «Densification of transparent yttrium aluminum garnet (YAG) by SPS processing,» *J. Eur. Ceram. Soc.*, vol. 30, pp. 3331-3337, 2010.
- [63] W. Zhang, T. Lu, B. Ma, N. Wei, Z. Lu, F. Li, Y. Guan, X. Chen, W. Liu et L. Qi, «Improvement of optical properties of Nd:YAG transparent ceramics by post-annealing and post hot isostatic pressing,» *Optical Materials*, vol. 35, pp. 2405-2410, 2013.
- [64] R. C. Powell, *Physics of solid state laser materials*, New York: AIP, 1998.
- [65] L. Esposito, A. Piancastelli, Y. Bykov et al., «Microwave sintering of Yb:YAG transparent laser ceramics,» *Opt. Mater.*, vol. 35, pp. 261-5, 2013.
- [66] A. K. Pradhan, K. Zhang et G. B. Loutts, «Synthesis of neodymium-doped yttrium aluminum garnet (YAG) nanocrystalline powders leading to transparent ceramics,» *Mater. Res. Bull.*, vol. 39, pp. 1291-8, 2004.
- [67] J. E. Guesic, H. M. Marcos et L. G. Van Uitert, «Laser oscillations in Nd-doped yttrium aluminum, yttrium gallium and gadolinium garnets,» *Appl. Phys. Lett.*, vol. 4, p. 182, 1964.
- [68] R. Kolesov, K. Xia, R. Reuter et al, «Optical detection of a single rare-earth ion in a crystal,» *Nature Communications*, vol. 3, p. 1029, 2012.

- [69] S. M. Sim, K. A. Keller et T. I. Mah, «Phase transformation in yttrium aluminum garnet powders synthesized by chemical methods,» *J. Mater. Sci.*, vol. 35, p. 713, 2000.
- [70] G. Spina, Transparent YAG and composite ceramic materials in the system Alumina-YAG-Zirconia, Ph. D. Thesis. Politecnico di Torino-INSA Lyon, 2012.
- [71] Y. Kalisky, The physics and engineering of solid state lasers, SPIE Publications, 2006.
- [72] "Crystran," [Online]. Available: www.crystran.co.uk.
- [73] X. Xu, Z. Zhao et P. Song, «Growth of high-quality single crystal of 50 at%Yb:YAG and its spectral properties,» *J. Alloy Compd.*, vol. 364, pp. 311-4, 2004.
- [74] M. Veith, S. Mathur, A. Kareiva et al, «Low-temperature synthesis of nanocrystalline YAG and Ce-doped YAG via different sol-gel methods,» *Roy. Soc. Chem.*, vol. 9, pp. 3069-79, 1999.
- [75] J. G. Li, T. Ikegami, J. H. Lee et T. Mori, «Low-temperature fabrication of transparent yttrium aluminum garnet (YAG) ceramics without additives,» *J. Am. Ceram. Soc.*, vol. 83, pp. 961-3, 2000.
- [76] K. Takaichi, H. Yahi, J. Lu et al, «YB3+ doped-Y3Al5O12 ceramics - a solid-state laser material,» *Phys. Status Solidi A*, vol. 200, pp. R5-7, 2003.
- [77] G. Qin, J. Lu, J. F. Bisson et al, «Upconversion luminescence of Er3+ in highly transparent YAG ceramics,» *Solid Stat Commun.*, vol. 132, pp. 103-6, 2004.
- [78] S. Shikao et W. Jiye, «Combustion synthesis of Eu activated Y3Al5O12 phosphor nanoparticles,» *J Alloy Compd*, vol. 327, pp. 82-6, 2001.
- [79] X. Li, H. Liu, J. Wang et al, «Preparation of YAG:Nd nano-sized powder by co-precipitation method,» *Mat. Sci. Eng. A*, vol. 379, pp. 347-50, 2004.
- [80] Q. Zhang et F. Saito, «Mechanochemical solid reaction of yttrium oxide with alumina leading to the synthesis of YAG,» *Powder Technol.*, vol. 129, pp. 86-91, 2003.
- [81] C.-Q. Li, H.-B. Zuo, M.-F. Zhang et al, «Fabrication of transparent YAG ceramics by traditional solid-state-reaction method,» *Transnational Nonferrous Metallic Soc. China*, vol. 17, pp. 148-153, 2007.
- [82] X. Zhang, H. Liu, W. He, J. Wang, X. Li et R. Boughton, «Novel synthesis of YAG by solvothermal method,» *J. of Crystal Growth*, vol. 275, pp. 1913-1917, 2005.
- [83] G. Gowda, «Synthesis of yttrium aluminates by the sol-gel process,» *J. of Mat. Sci. Lett*, vol. 5, pp. 1029-1032, 1986.
- [84] R. Manalart et M. Rahaman, «Sol-gel processing and sintering of yttrium aluminum garnet

- (YAG) powders,» *J. Mat. Sci.*, vol. 31, pp. 3453-3458, 1996.
- [85] G. Xu, W. Zhang, W. He et al, «Preparation of highly dispersed YAG nano-sized powder by co-precipitation method,» *Material Letters*, vol. 60, n° 17, pp. 962-965, 2006.
- [86] J. Li, Y. Wu, Y. Pan, W. Liu, Y. Zhu et J. Guo, «Solid-state-reactive fabrication of Cr, Nd:YAG transparent ceramics: the influence of the raw material,» *J. Cer. Soc. Japan*, vol. 116, n° 14, pp. 572-577, 2008.
- [87] A. Aboulaich, J. Deschamps, R. Deloncie et al., «Rapid synthesis of Ce³⁺ doped YAG nanoparticles by a solvothermal method using metal carbonates as precursors,» *New J. Chem.*, vol. 36, pp. 2493-2500, 2012.
- [88] L. Wang, L. Zhang, Y. Fan et al, «Synthesis of Nd/Si codoped YAG powders via a solvothermal method,» *JACS*, vol. 89, n° 111, pp. 3570-3572, 2006.
- [89] J. Guo, J. Li et H. Kou, «Chemical preparation of advanced ceramic materials,» chez *Modern Inorganic Synthetic Chemistry*, Elsevier, 2010, pp. 249-454.
- [90] Y. Sang, H. Liu, X. Sun et al, «Formation and calcination temperature-dependent sintering activity of YAG precursor synthesized via reverse titration method,» *Journal of Alloys and Compounds*, vol. 509, pp. 2407-13, 2011.
- [91] J.-G. Li, T. Ikegami, J.-H. Lee, T. Mori et Y. Yajima, «Co-precipitation synthesis and sintering of yttrium aluminum garnet (YAG) powders: the effect of precipitant,» *J. Eur. Ceram. Soc.*, vol. 20, pp. 2395-2405, 2000.
- [92] W. Liu, W. Zhang, J. Li, H. Kou, Y. Shen et al., «Influence of pH values on (Nd + Y):Al molar ratio of Nd:YAG nanopowders and preparation of transparent ceramics,» *Journal of Alloys and Compounds*, vol. 503, pp. 525-528, 2010.
- [93] J.-G. Song, F. Wang, M.-H. Xu et al, «Effect of synthesis conditions on the particle size and morphology of YAG powder,» *Ceramic Processing Research*, vol. 13, n° 12, pp. 154-157, 2012.
- [94] B. Ma, T. Lu, S. Xiao et al, «Preparation of YAG powder by co-precipitation method in a narrow pH-change environment,» *Journal of Wuhan University of Technology-Mater*, vol. 6, pp. 379-383, 2010.
- [95] L. Wang, H. Kou, Y. Zeng et al, «The effect of precipitant concentration on the formation procedure of yttrium aluminum garnet (YAG) phase,» *Ceram. Inter.*, vol. 38, pp. 3763-71, 2012.
- [96] P. Palmero, C. Esnout, L. Montanaro et G. Fantozzi, «Influence of the co-precipitation temperature on phase evolution in yttrium-aluminium oxide materials,» *J. Eur. Ceram. Soc.*, vol. 25, pp. 1565-1573, 2005.
- [97] R. Boulesteix, A. Maitre, J. Baumard, Y. Rabinovitch et F. Reynaud, «Light scattering by pores in transparent Nd:YAG ceramics for lasers: correlations between microstructure and optical

- properties,» *Optics Express*, vol. 18, n° 114, pp. 14992-15002, 2010.
- [98] X. Qin, H. Yang, D. Shen, H. Chen, G. Zhou, S. Wang, D. Luo et D. Tang, «Fabrication and Optical Properties of Highly Transparent Er:YAG Polycrystalline Ceramics for Eye-Safe Solid-State Lasers,» *Int. J. Appl. Ceram. Technol.*, vol. 10, n° 11, pp. 123-128, 2013.
- [99] Y. Rabinovitch, C. Bogicevic, F. Karolak et al, «Freeze-dried nanometric neodymium-doped YAG powders for transparent ceramics,» *J. Mat. Proces. Technol.*, vol. 199, pp. 314-320, 2008.
- [100] R. López-Juárez, F. Gonzalez et M.-E. Villafuerte-Castrejón, «Lead-Free Ferroelectric Ceramics with Perovskite Structure,» chez *Ferroelectrics - Materials Aspects*, InTech, 2011, pp. 305-330.
- [101] D. Popovici, M. Okuyama et J. Akedo, «Barium Titanate-Based Materials - a Window of Application Opportunities,» chez *Ferroelectrics - Materials aspects*, InTech, 2011, pp. 279-280.
- [102] M. Vijatovic, J. Bobic et B. Stojanovic, «History and challenges of barium titanate: Part I,» *Science of Sintering*, vol. 40, pp. 235-244, 2008.
- [103] R. Martínez Valdés, Synthesis, Structural and Physical Characterization of Artificially Engineered Ba_{0.7}Sr_{0.3}TiO₃/La_{0.7}Sr_{0.3}MnO₃ Magnetolectric Multiferroic Thin Film Heterostructures, San Juan: Ph. D. Thesis. University of Puerto Rico, 2012.
- [104] K. Kirby et B. Wechsler, «Phase relations in the Barium Titanate-Titanium oxide system.,» *J. Am. Ceram. Soc.*, vol. 74, pp. 1841-47, 1991.
- [105] S. Lee, C. Randall et Z.-K. Liu, «Modified phase diagram for the Barium oxide-Titanium dioxide system for the ferroelectric barium titanate.,» *J. Am. Ceram. Soc.*, vol. 90, pp. 2589-2594, 2007.
- [106] D. Rase et R. Roy, «Phase equilibria in the system BaO-TiO₂,» *J. Am. Ceram. Soc.*, vol. 38, p. 102, 1955.
- [107] H. O'Bryan et J. Thomson, «Ba₂Ti₉O₂₀ Phase Equilibria,» *J. Am. Ceram. Soc.*, vol. 66, pp. 66-68, 1983.
- [108] T. Negas, R. Roth, H. Parker et D. Minor, «Subsolidus phase relations in the BaTiO₃-TiO₂ system.,» *Journal of Solid State Chemistry*, vol. 9, pp. 297-307, 1974.
- [109] Y. Tan, J. Zhang, Y. Wu, C. Wang, V. Koval, B. Shi, H. Ye, R. McKinnon et al., «Unfolding grain size effects in barium titanate ferroelectric ceramics,» *Sci. Rep.*, vol. 5, p. 9953, 2015.
- [110] "Inframat Advanced Materials," [Online]. Available: <http://www.advancedmaterials.us/5622ON-N2.htm>.
- [111] Y. He, «Heat capacity, thermal conductivity, and thermal expansion of barium titanate-based ceramics,» *Thermochimica acta*, vol. 419, pp. 135-141, 2004.

- [112] M. Buscaglia, M. Viviani, V. Buscaglia et al., «High dielectric constant and frozen macroscopic polarization in dense nanocrystalline BaTiO₃ ceramics,» *Physical Review B*, vol. 73, p. 064114, 2006.
- [113] S. Khedidja, Etude des propriétés diélectriques et structurales des céramiques du type BaTiO₃-CaTiO₃, Ph D Thesis. Université Mentouri-Constantine, 2008.
- [114] F. Maglia, I. Tredici et U. Anselmi-Tamburini, «Densification and properties of bulk nanocrystalline functional ceramics with grain size below 50 nm,» *J. Eur. Ceram. Soc.*, vol. 33, pp. 1045-1066, 2013.
- [115] T. Hoshina, Y. Kigoshi, S. Hatta, T. Teranishi, S. Takeda et T. Tsurumi, «Size Effect and Domain-Wall Contribution of Barium Titanate Ceramics,» *Ferroelectrics*, vol. 402, pp. 29-36, 2010.
- [116] G. Artl, D. Hennings et G. de With, «Dielectric properties of fine-grained barium titanate ceramics,» *J. Appl. Phys.*, vol. 58, pp. 1619-25, 1985.
- [117] H. Kim et Y. Han, «Sintering of nanocrystalline BaTiO₃,» *Ceram. Inter.*, vol. 30, pp. 1719-1723, 2004.
- [118] Z. Zhao, V. Buscaglia, M. Viviani et al., «Grain-size effects on the ferroelectric behavior of dense nanocrystalline BaTiO₃ ceramics,» *Physical Review B*, vol. 70, p. 024107, 2004.
- [119] Y. Huan, X. Wang, J. Fang et L. Li, «Grain size effect on piezoelectric and ferroelectric properties of BaTiO₃ ceramics,» *J. Eur. Ceram. Soc.*, vol. 34, pp. 1445-1448, 2014.
- [120] D. Ghosh, A. Sakata, J. Carter, P. Thomas, H. Han, J. Nino et J. Jones, «Domain Wall Displacement is the Origin of Superior Permittivity and Piezoelectricity in BaTiO₃ at Intermediate Grain Sizes,» *Adv. Func. Mater.*, vol. 24, pp. 885-896, 2014.
- [121] S. Guillemet-Fritsch, Z. Valdez-Nava, C. Tenailleau, T. Lebey, B. Durand et J.-Y. Chane-Ching, «Colossal Permittivity in Ultrafine Grain Size BaTiO_{3-x} and Ba_{0.95}La_{0.05}TiO_{3-x} Materials,» *Adv. Mater.*, vol. 20, pp. 551-555, 2008.
- [122] Z. Valdez-Nava, S. Guillemet-fritsch, C. Tenailleau et al., «Colossal dielectric permittivity of BaTiO₃-based nanocrystalline ceramics sintered by spark plasma sintering,» *Journal of Electroceramics*, vol. 22, pp. 238-244, 2009.
- [123] H. Han, C. Voisin, S. Guillemet-Fritsch, P. Dufour et al., «Origin of colossal permittivity in BaTiO₃ via broadband dielectric spectroscopy,» *J. Appl. Phys.*, vol. 113, p. 024102, 2013.
- [124] H. Han, D. Ghosh, J. Jones et J. Nino, «Colossal Permittivity in Microwave-Sintered Barium Titanate and Effect of Annealing on Dielectric Properties,» *J. Am. Ceram. Soc.*, pp. 1-6, 2012.
- [125] B. Baumert, L.-H. Chang et A. Matsuda, «Characterization of sputtered barium strontium titanate and strontium titanate thin films,» *J. Appl. Phys.*, vol. 82, pp. 2558-2566, 1997.

- [126] C. Mao, S. Yan, C. Yao, F. Cao, G. Wang, X. Dong et X. Meng, «Degraded grain size effect of barium strontium titanate ceramics under a direct current bias electric field,» *Mater. Res. Express*, vol. 4, p. 016302, 2017.
- [127] J. Ćirković, K. Vojisavljević, N. Nikolić, P. Vulić, Z. Branković et al., «Dielectric and ferroelectric properties of BST ceramics obtained by a hydrothermally assisted complex polymerization method,» *Ceram. Inter.*, vol. 41, pp. 11306-11313, 2015.
- [128] T. Hungria, M. Alguero, A. Hungria et A. Castro, «Dense, fine-grained BST ceramics prepared by the combination of mechanosynthesized nanopowders and SPS,» *Chem. Mater.*, vol. 17, pp. 6205-6212, 2005.
- [129] V. Mudinepalli, L. Feng, W.-C. Lin et B. Murty, «Effect of grain size on dielectric and ferroelectric properties of nanostructured Ba_{0.8}Sr_{0.2}TiO₃ ceramics,» *J. Adv. Ceram.*, vol. 4, pp. 46-53, 2015.
- [130] S. Dupuis, S. Sulekar, J. Kim, H. Han, P. Dufour, C. Tenailleau, J. Nino et S. Guillemet-Fritsch, «Colossal permittivity and low losses in Ba_{1-x}Sr_xTiO₃ reduced nanoceramics,» *J. Eur. Ceram. Soc.*, Vols. %1 sur %2567-575, p. 36, 2016.
- [131] H. Yamamura, H. Haneda, A. Watanabe et S. Shirasaki, «Hot-Pressing of Barium Titanate Prepared by Oxalate Method in Ethanol,» *Jap. J. Appl. Phys.*, Vols. %1 sur %224-2, pp. 433-435, 1985.
- [132] H. Shimooka, S. Kohiki, T. Kobayashi et M. Kuwabara, «Preparation of translucent barium titanate ceramics from sol-gel derived transparent monolithic gels,» *J. Mater. Chem.*, vol. 10, pp. 1511-1512, 2000.
- [133] Y. Wu, N. Wang, S. Wu et X. Chen, «Transparent barium strontium titanate ceramics prepared by spark plasma sintering,» *J. Am. Ceram. Soc.*, vol. 94, pp. 1343-45, 2011.
- [134] A. Ikesue and I. Furusato, «Fabrication of Polycrystalline, Transparent YAG Ceramics by a Solid-State Reaction Method,» *J. Am. Ceram. Soc.*, vol. 78, pp. 225-28, 1995.
- [135] Z. Lu, T. Lu, N. Wei, N. Zhang, B. Ma, J. Qi et al., «Effect of air annealing on the color center in Yb:Y₃Al₅O₁₂ transparent ceramics with MgO as sintering additive,» *Opt. Mater.*, vol. 47, pp. 292-296, 2015.
- [136] W. Pabst, J. Hostasa et L. Esposito, «Porosity and pore size dependence of the real in-line transmission of YAG and alumina ceramics,» *J. Eur. Ceram. Soc.*, vol. 34, pp. 2745-2756, 2014.
- [137] Y. Aman, V. Garnier et E. Djurado, «Influence of green state processes on the sintering behaviour and the subsequent optical properties of spark plasma sintered alumina,» *J. Eur. Ceram. Soc.*, vol. 29, pp. 3363-3370, 2009.
- [138] M. Suarez, A. Fernandez, J. Menendez, M. Nygren, R. Torrecillas et Z. Zhao, «Effect of freeze-drying treatment on the optical properties of SPS-sintered alumina,» *Ceram. Int.*, vol. 39, pp.

- 6669-6672, 2013.
- [139] T. Zawadzki, P. Apte et M. Hoare, «Effect of Sulfur on Grain Growth in UO₂ Pellets,» *J. Am. Ceram. Soc.*, vol. 67, pp. 361-364, 1984.
- [140] S.-H. Lee, S. Kochawattana et G. Messing, «Solid-State Reactive Sintering of Transparent Polycrystalline Nd:YAG Ceramics,» *J. Am. Ceram. Soc.*, vol. 89, p. 1945–1950, 2006.
- [141] A. Gajovic, P. Vukajlovic, K. Zagar et al., «Temperature-dependent Raman spectroscopy of BaTiO₃ nanorods synthesized by using a template-assisted sol-gel procedure.,» *Journal of Raman Spectroscopy*, vol. 44, pp. 412-420, 2013.
- [142] H. Hayashi, T. Nakamura et T. Ebina, «In-situ Raman spectroscopy of BaTiO₃ particles for tetragonal-cubic transformation,» *Journal of Physics and Chemistry of Solids*, vol. 74, pp. 957-962, 2013.
- [143] M. Smith, K. Page, T. Siegrist, P. Redmont and al., «Crystal structure and the paraelectric-to-ferroelectric phase transition of nanoscale BaTiO₃,» *J. Am. Chem. Soc.*, vol. 130, pp. 6955-63, 2008.
- [144] T. Hoshina, H. Kakemoto, T. Tsurumi et S. Wada, «Size and temperature induced phase transition behaviors of barium titanate nanoparticles,» *J. Appl. Phys.*, vol. 99, p. 054311, 2006.
- [145] C. Voisin, S. Guillemet-Fritsch, P. Dufour, C. Tenailleau, H. Han et J. Nino, «Influence of Oxygen Substoichiometry on the Dielectric Properties of BaTiO_{3-d} Nanoceramics Obtained by Spark Plasma Sintering,» *Int. J. Appl. Ceram. Technol.*, vol. 10, pp. E122-E133, 2013.
- [146] R. Sharma, N. Chan et D. Smyth, «Solubility of TiO₂ in BaTiO₃,» *J. Am. Ceram. Soc.*, vol. 64, pp. 448-451, 1981.
- [147] S. Zheng, X. Ma, T. Yamamoto et Y. Ikuhara, «Atomistic study of abnormal grain growth structure in BaTiO₃ by transmission electron microscopy and scanning transmission electron microscopy,» *Acta Materialia*, vol. 61, pp. 2298-2307, 2013.
- [148] J. Shi, «Relations between corasening and densification and mass transport path in solid-state sintering of ceramics: Model analysis,» *J. Mater. Res.*, vol. 14, pp. 1378-1388, 1999.
- [149] J. Shi, «Relation between corasening and densification in solid-state sintering of ceramics: Experimental test on superfine zirconia powder compacts,» *J. Mater. Res.*, vol. 14, pp. 1389-1397, 1999.
- [150] J. Liu, Z. Shen et M. Nygren, «Spark Plasma Sintering behaviour of nano-sized (Ba, Sr)TiO₃ powders: Determination of sintering parameters yielding nanostructured ceramics,» *J. Am. Ceram. Soc.*, vol. 89, pp. 2689-2694, 2006.
- [151] S. Tripathy et A. Raichur, «Dispersibility of Barium Titanate Suspension in the Presence of

- Polyelectrolytes: A Review,» *J. Disp. Sci. Technol.*, vol. 29, pp. 230-239, 2008.
- [152] Z.-G. Shen, J.-C. Chen, H.-K. Zou et J. Yun, «Dispersion of nanosized aqueous suspensions of barium titanate with ammonium polyacrylate,» *J. Col. Interf. Sci.*, vol. 275, pp. 158-164, 2004.
- [153] R. German, *Sintering: From Empirical Observations to Scientific Principles*, Elsevier Inc. , 2014.
- [154] Y. Li, L. Fang, L. Liu, Y. Huang et C. Hu, «Giant dielectric response and charge compensation of Li- and Co-doped NiO ceramics,» *Mater. Sci. Eng. B* , vol. 177, p. 673, 2012.
- [155] R. Stanculescu, C. Ciomaga, L. Padurariu, P. Galizia et al., «Study of the role of porosity on the functional properties of (Ba,Sr)TiO₃ ceramics,» *J. Alloys and Compounds*, vol. 643, pp. 79-87, 2015.
- [156] Z. Wing et J. Halloran, «Dielectric loss in porous TiO₂,» *Ceram. Int.*, vol. 43, pp. 4618-4621, 2017.

List of figures

Figure 1.1. Wavelength dependence of the refractive index of pure YAG, BaTiO ₃ and SrTiO ₃ in the visible and near infrared region.	18
Figure 1.2. Light transmission through a polycrystalline ceramic	19
Figure 1.3. Calculated transmission through a polycrystalline ceramic ($\lambda=600$ nm)	20
Figure 1.4. Fabrication variables in transparent ceramics	21
Figure 1.5. Basic configuration of a typical SPS set-up	23
Figure 1.6 Electrical current distribution during SPS of two samples: (a) alumina (insulating); (b) copper (conductive)	24
Figure 1.7. YAG relative density and mean grain size versus SPS temperature	25
Figure 1.8. Appearance of MgAl ₂ O ₄ samples sintered by SPS at different temperatures at 10°C/min	25
Figure 1.9. Effect of sintering dwell on relative density and grain size on Al ₂ O ₃ samples	26
Figure 1.10. Appearance of MgAl ₂ O ₄ samples sintered at different heating rates up to 1300°C for 20 minutes	26
Figure 1.11. Temperature distribution inside a ZrO ₂ sample (40 mm)	27
Figure 1. 12. Temperature distribution in an alumina sample (19 mm)	27
Figure 1.13. Microstructures and images of MgAl ₂ O ₄ samples as a result of pressure application at different temperatures: (a) 1000°C; (b) 1100°C; (c) 1200°C and (d) 1300°C	28
Figure 1.14. Density gradient in uniaxial pressing of ceramic powder for different L/D ratios	29
Figure 1.15. Von Mises stress distribution inside a YAG sample using (a-c) a full punch and (d-f) a drilled punch	30
Figure 1.16. Hydrostatic stress distribution inside the a) alumina and b) Cu samples	30
Figure 1.17. Influence of SPS parameters on the darkening of MgAl ₂ O ₄ SPS specimens : a) heating rate, b) sintering temperature, c) temperature of pressure application, d) applied pressure	31
Figure 1.18. Optical transmission of YAG specimens (a) with LiF; (b) without LiF	32
Figure 1.19. YAG samples after SPS (15 min, 1350 °C, 74 MPa) before annealing (left), and after air annealing at 800°C for 1h (right)	33
Figure 1.20. Optical transmission of as-sintered and annealed YAG samples	34
Figure 1.21. 1% Nd:YAG specimens doped with 0.06 and 0.14 wt% SiO ₂ , sintered for 2 h at the temperatures showed above and subsequently hot isostatic pressed at 1750°C for 2 h in 200 MPa Ar	34
Figure 1.22. Nd:YAG samples vacuum sintered at 1780°C (S1), S1+annealing at 1450°C (S2), S2+ HIP at 1700°C (S3), S3+annealing at 1250°C (S4), S3+annealing at 1350°C (S5), S3+annealing at 1450°C (S6)	35
Figure 1.23. (a) YAG unit cell. Green, white and red sites correspond to yttrium, aluminium and oxygen, respectively. (b) Surrounding of yttrium atom.....	36
Figure 1.24. Al ₂ O ₃ -Y ₂ O ₃ phase diagram.....	36
Figure 1.25. Optical transmission of transparent YAG ceramics prepared by SPS.	41
Figure 1.26. Unit cell of BaTiO ₃	42
Figure 1.27. Unit cells of the four phases of BaTiO ₃	42
Figure 1.28. BaO-TiO ₂ phase diagram	43
Figure 1.29. Permittivity of BaTiO ₃ as a function of temperature	44
Figure 1.30. Temperature dependence of permittivity of BaTiO ₃ with various grain sizes	45

Figure 1.31. a) Curie temperature of BaTiO ₃ ceramic as a function of grain size. b) Permittivity at 104 Hz as a function of temperature.	45
Figure 1.32. (a) Permittivity at 103 Hz as a function of temperature of BT ceramics with different grain sizes (b) T _c evolution as a function of grain size (GS).....	46
Figure 1.33. Variation of relative permittivity as a function of temperature for undoped BaTiO ₃ - x measured at various frequencies.....	46
Figure 1.34. Interfacial and hopping polarization model for colossal permittivity of BT ceramics	47
Figure 1.35. Phase diagram lattice parameter of BST as a function of composition	48
Figure 1.36. Curie temperature of BST as a function of composition	48
Figure 1.37. Temperature dependence of the permittivity of various BST compositions	49
Figure 1.38. Temperature dependence of the permittivity of BST (x=0.2) with different grain sizes ..	49
Figure 1.39. Temperature dependence of the permittivity of various BST compositions	50
Figure 1.40. Transmittance as a function of wavelength for hot-pressed BT	51
Figure 1.41. Appearance of a translucent BT ceramic: thickness = 0.34mm	52
Figure 1.42. Appearance of BT and ST translucent samples	52
Figure 1.43. Appearance of BST translucent samples.....	52
Figure 2.1. SPS design.....	58
Figure 2.2. Parallel plate capacitor.....	61
Figure 2.3. Maximal theoretical transmission of YAG and BST ceramics.....	63
Figure 2.4. Measurement setup for (a) total forward transmission (TFT) and (b) real in-line transmission (RIT)	64
Figure 2.5. Representation of the SPS ensemble (tooling + sample) used for FEM modelling.....	65
Figure 3.1. TG-DTA of YAG precursor from co-precipitation in AHC 0.5M.....	72
Figure 3.2. TG-DTA of YAG precursor from co-precipitation in AHC 1M.....	73
Figure 3.3. XRD evolution with temperature of YAG precursor from co-precipitation in AHC 0.5M. ..	71
Figure 3.4. XRD of synthesized YAG from co-precipitation in AHC 1M treated at 1350°C for 30 minutes.....	72
Figure 3.5. SEM images of the synthesized YAG powder calcined at 1000°C.	73
Figure 3.6. Frequency distribution (vol %) versus particle size of synthesized YAG powder.....	74
Figure 3.7. Relative density of YAG-S powder as a function of the temperature (heating rate 20°C/min, pressure 50 MPa).	75
Figure 3.8. XRD of YAG-S after SPS at 1650°C.	75
Figure 3.9. Sintering curve of a YAG-S sample sintered at 1300°C.	76
Figure 3.10. Scanning electron micrographs of YAG-S sintered at: (a) 1200°C, (b) 1250°C, (c) 1300°C, (d) 1325°C under a pressure of 50 MPa.	77
Figure 3.11. SEM images of (a) the core and (b) the shell of a sample sintered at 1300°C.	78
Figure 3.12. Temperature distribution in our SPS ensemble: tooling + sample (dwell temperature = 1300°C).....	78
Figure 3.13. "Half view" temperature distribution in a YAG sample at dwell temperature = 1300°C..	79
Figure 3.14. Sample sintered at 1300°C with a heating rate of 100°C/min.	79
Figure 3.15. Frequency distribution (vol %) versus particle size of YAG-S as-received; after 5 min and 45 min of US dispersion.....	81
Figure 3.16. SEM images of YAG-S samples sintered at 1300°C before (a) and after deagglomeration (b).	81

Figure 3.17. Samples of YAG-S sintered by SPS at 1300°C without (a) and after deagglomeration of the powder by US (b) (thickness 1.5 mm).....	82
Figure 3.18. Appearance of YAG-S samples (a) before annealing and after annealing at (b) 900°C 1h (c); 1050°C 12h (d)1100°C 24h (e) ; 1150°C 24h.	82
Figure 3.19. Sample sintered at 1300°C after annealing at 1100°C 24h.	82
Figure 3.20. YAG-S sample sintered by SPS at 1300°C and post-treated by HIP at 1250°C for 1 h.....	83
Figure 3.21. TFT and RIT values of YAG-S samples after deagglomeration, annealing and post-hip....	84
Figure 3.22. SEM Images of YAG-B.....	85
Figure 3.23. Frequency distribution (vol %) versus particle size of Baikowski YAG powder.....	86
Figure 3.24. XRD of YAG-B powder.	86
Figure 3.25. Relative density of YAG-B powder as a function of the temperature (heating rate 20°C/min, pressure 50 MPa).	87
Figure 3.26. Scanning electron micrographs of YAG-B sintered at (a) 1350°C, (b) 1400°C and (c) 1450°C under a pressure of 50MPa.	88
Figure 3.27. Microstructure of a sample sintered at 1400°C for 15 min: (a) core; (b) shell	88
Figure 3.28. Samples sintered at 1400°C with a pressure of a) 30 MPa; b) 50 MPa and c) 70 MPa.....	89
Figure 3.29. Samples sintered at 1400°C with a dwell time of a) 5min; b) 15min and c) 25min.	90
Figure 3.31. Frequency distribution (vol %) versus particle size of YAG-B as-received; after 5 min US and after 45 min US.....	91
Figure 3.32. Samples sintered at 1450°C and 50MPa (a) without dispersion and (b) dispersed 45 minutes by US and then freeze-dried.	92
Figure 3. 33. YAG-B samples after deagglomeration and SPS cycles at 50 MPa, 1450°C 15 min (a) without post-treatment; (b) after annealing at 1150°C for 12h and (c) after post-HIP at 120 MPa, 1350°C 1h (thickness 1.5 mm).....	93
Figure 3.34. Total Forward Transmission of YAG-B samples before and after post-treatments.	93
Figure 3.35. SEM image of LiF powder.....	94
Figure 3.36. Density evolution during SPS for different LiF concentrations.	95
Figure 3.37. XRD of YAG-B-0.2LiF sintered at 1400°C.	95
Figure 3.38. Optical transmission (TFT) of SPS samples of YAG-B with different LiF concentrations... ..	96
Figure 3.39. (a) Scanning electron micrograph and images of 0.2%LiF doped- YAG-B SPSed sample (1450°C, 50 MPa) (b) placed on the text and (c) 15 mm above it (1mm-thick).	97
Figure 3.40. RIT and TFT values of 0.2%LiF doped- YAG-B sample	97
Figure 3.41. Micrograph of YAG-N powder.....	99
Figure 3.42. Frequency distribution (vol %) versus particle size of YAG-N powder.....	99
Figure 3.43. XRD of Nanocerox YAG powder.	100
Figure 3.44. Relative density of YAG-N powder as a function of the temperature (heating rate 20°C/min, pressure 50 MPa).	100
Figure 3.45. Relative density of YAG-N vs temperature for two different heating rates (T=1400°C, P=50MPa).	101
Figure 3.46. Images and microstructures of YAG-N samples sintered at 1400°C with heating rates of (a) 50°C/min and (b) 10°C/min.....	102
Figure 3.47. Images and microstructures of YAG-N sintered samples at (a) 1400°C; (b) 1450°C and (c) 1500°C.	102
Figure 3.48. Relative density evolution of YAG-N compacts sintered at 1500°C under pressures of 30, 50 and 70 MPa.....	103

Figure 3.49. Images of samples from YAG-N sintered at 1500°C under pressures of (a) 30 MPa; (b) 50 MPa and (c) 70 MPa.	104
Figure 3.50. Microstructures of YAG-N sintered samples under (a) 30 MPa and (b) 70 MPa.	104
Figure 3.51. Optical transmission of samples from YAG-N sintered at 1500°C under different pressures: (a) TFT and (b) RIT values.....	105
Figure 3.52. Images of YAG-N samples sintered at 1450°C, (a) before annealing; and after annealing in air at 5°C/min up to: (b) 1100°C 12 hour; (c) 1100°C 24h; (d) 1150°C 12h; (e) 1200°C 12h	105
Figure 3.53. Absorption spectra of samples sintered at 1450°C after different annealing conditions.	106
Figure 3.54. Optical transmission (RIT) of samples sintered at 1450°C after different annealing conditions.....	106
Figure 3.55. Appearance of a sample (thickness = 1.5 mm) sintered at 1500°C for 15 min after annealing in air at 1150°C for 12 hours: (a) placed on the text, (b) placed 15 mm above the text....	107
Figure 3.56. Relative density evolution of YAG-N samples sintered at 1400°C for 15 min (50 MPa), without LiF and with 0.2 wt% LiF.	107
Figure 3.57. Appearance and microstructure of a YAG-N sample (thickness 1.5 mm) doped with 0.2 wt% LiF and sintered at 1400°C for 15 min.	108
Figure 3.58. Appearance of a YAG-N sample (thickness = 1.4 mm) doped with 0.2 wt% LiF and sintered at 1500°C for 15 min (a) placed on the text, (b) placed 15 mm above the text.	108
Figure 3.59. Optical transmission of YAG-N samples sintered at 1500°C without LiF and annealed (green) and with 0.2% LiF (violet).	109
Figure 3.60. Comparison of the best optical transmissions for the three YAG powders sintered by SPS.	110
Figure 3.61. Images of best transparent samples sintered from (a) YAG-S, (b) YAG-B and (c) YAG-N powders.....	111
Figure 3.62. Optical transmission of transparent YAG ceramics prepared by SPS.	112
Figure 4.1. XRD of BaTiO ₃ powder.....	116
Figure 4.2. Raman spectrum of BaTiO ₃ powder.	116
Figure 4.3. SEM images of BaTiO ₃ powder at different magnifications.	117
Figure 4.4. Frequency distribution (vol %) versus particle size of BaTiO ₃ powder.....	117
Figure 4.5. XRD of BST powder.....	118
Figure 4.6. Raman spectrum of BST powder.	118
Figure 4.7. TEM images of BaSrTiO ₃ powder.....	119
Figure 4.8. Frequency distribution (vol %) versus particle size of BaSrTiO ₃ powder	119
Figure 4.9. Punches displacement and displacement rate of BT powder as a function of the temperature (heating rate 20°C/min, pressure 50 MPa).....	120
Figure 4.10. XRD patterns of BaTiO ₃ after SPS at 1200°C.....	121
Figure 4.11. Evolution of the relative density of BT ceramics sintered at different SPS temperatures. Arrows mark the start of the dwell for each temperature (dwell: 5 minutes).	122
Figure 4.12. Samples of BT sintered at different temperatures: (a) 950°C, (b) 1000°C, (c) 1050°C. ..	122
Figure 4.13. XRD patterns of BaTiO ₃ after SPS at 1000°C.....	123
Figure 4.14. Raman spectrum of a BT sample sintered by SPS at 1000°C.....	123
Figure 4.15. Microstructure of BT samples (fracture surfaces) sintered by SPS at (a) 950°C; (b) 1000°C and (c) 1050°C.	124
Figure 4.16. Image and microstructure of a BT sample sintered by SPS at 1025°C.	125

Figure 4.17. Images and microstructures of BT samples sintered by SPS at 1000°C with dwell time of (a) 15 min and (b) 25 min.	125
Figure 4.18. BT sintering curves at different pressures (temperature 1000°C, dwell 5min).	126
Figure 4. 19. Pictures of BT samples sintered at 1000°C by SPS at pressures of (a) 30 MPa, (b) 50 MPa and (c) 70 MPa.....	126
Figure 4.20. Microstructure of BT samples (fracture surfaces) sintered by SPS at 1000°C under a pressure of (a) 30 MPa; (b) 50 MPa and (c) 70 MPa.	127
Figure 4.21. BT sintering curves at different heating rates (evolution of the relative density during dwell is not shown).	128
Figure 4.22. Pictures of BT samples sintered at 1000°C by SPS at heating rates of (a) 10°C/min; (b) 50°C/min and (c) 100°C/min.	128
Figure 4.23. Microstructure of BT sample sintered by SPS at 1000°C with a heating rate of 100°C/min (fracture surface).....	129 129
Figure 4.24. BT sintering curve with a two-step sintering cycle.	129
Figure 4.25. Microstructure of BT sample sintered by two-step sintering.	130
Figure 4.26. Particle size distribution of BT powder after different dispersion times.	131
Figure 4.27. BT sintering curves of as-received and deagglomerated powders. (Pressure: 50 MPa, Temperature: 1000°C, Dwell: 15 min).	131 131
Figure 4.28. Image and microstructure of BT sample from deagglomerated powder sintered by SPS at 1000°C with dwell time of 15 min.	132
Figure 4.29. Microstructures of BT sample from deagglomerated powder sintered by SPS at 1050°C with a dwell time of (a) 5 minutes and (b) 15 minutes.	132
Figure 4.30. Microstructure of BT sample from deagglomerated powder sintered by SPS at 1100°C-5 minutes.....	133
Figure 4.31. Picture and microstructure of BT sample sintered by two-step sintering from deagglomerated powder.....	133
Figure 4.32. Punches displacement and displacement rate of BST powder as a function of the temperature (heating rate 20°C/min, pressure 50 MPa).....	134
Figure 4.33. XRD patterns of Barium strontium titanate after SPS at 1300°C.	135
Figure 4.34. BT sintering curves for different sintering temperatures (dwell: 5 minutes included). .	136
Figure 4.35. BST samples sintered at (a) 1000°C, (b) 1100°C, (c) 1150°C and (d) 1200°C by SPS.	136
Figure 4.36. XRD patterns of BST sample sintered at 1150°C by SPS.....	137
Figure 4.37. Raman spectrum of a BST sample sintered by SPS at 1150°C-5min.	137
Figure 4.38. Microstructure of BST samples (fracture surfaces) sintered by SPS at (a) 1000°C; (b) 1100°C; (c) 1150°C; (d) 1200°C.....	138
Figure 4.39. Images of BST samples sintered by SPS at 1150°C for (a) 0 min, (b) 5 min and (c) 15 min.	139
Figure 4.40. Microstructures of BST samples sintered by SPS at 1150°C with dwell time of (a) 5 min and (b) 15 min.	139
Figure 4.41. Density evolution with time of BST samples sintered at 1150°C at different pressures.	140
Figure 4.42. Images of BST samples sintered by SPS under a pressure of (a) 30MPa; (b) 50MPa and (c) 70MPa.	140
Figure 4.43. Particle size distribution of BST powder after different dispersion times.	141

Figure 4.44. Image and microstructure of BST sample sintered up to 1150°C from a deagglomerated powder.	141
Figure 4.45. Images of samples from as-received powder after annealing at 800°C-6h (a) sintered at 1025°C-5min/50MPa (b) sintered at 1000°C-25min/50MPa.	143
Figure 4.46. Images of samples from deagglomerated powder after annealing at 800°C-6h (see Table 4.3. for the legend). (Thickness ~ 2 mm).	143
Figure 4.47. Images of a sample sintered at 1050°C-5min (50MPa) from deagglomerated powder, (a) before and (b) after annealing at 800°C-6h (thickness is 1mm and samples are backlighted).	144
Figure 4.48. Transmission spectra of annealed BT samples sintered in different SPS conditions..... (thickness 1mm).	144
Figure 4.49. Images of (a) BT sample as-sintered and annealed samples at (b) 600°C, (c) 700°C and (d) 800°C (sintering conditions 1050°C-5 min-50MPa; thickness ~ 2mm).	145
Figure 4.50. Transmission spectra of BT samples for different annealing conditions (thickness ~ 1 mm).	145
Figure 4.51. BST sample (a) as-sintered and annealed at (b) 600°C, (c) 800°C and (d) 900°C. (Thickness ~2mm).	146
Figure 4.52. Transmission spectra of a BST sample sintered at 1150°C for 5 min and annealed at 900°C for 6 h.	146
Figure 4. 53. Images of backlighted BST samples sintered at 1150°C-5min (50MPa) after annealing at 900°C-6h (a) from as-received powder, (b) after powder deagglomeration (thickness = 1mm).	147
Figure 4.54. Frequency dependence of the permittivity and dielectric loss at room temperature of samples issued from the as-received powder.	149
Figure 4.55. Frequency dependence of the permittivity and dielectric loss at room temperature of samples after annealing.	150
Figure 4.56. Grain size influence on the permittivity and dielectric loss at room temperature (from deagglomerated powder).	151
Figure 4.57. Grain size influence on the permittivity and dielectric loss at room temperature, after air annealing at 800°C-6 hours (from deagglomerated powder).	152
Figure 4.58. Frequency dependence of the permittivity and dielectric loss at room temperature after annealing.	153
Figure 4.59. BT sample (a) as-sintered and annealed at (b) 600°C-15', (c) 600°C-6h, (d) 800°C-15' and (e) 800°C-6h.	153
Figure 4.60. Frequency dependence of the permittivity and dielectric loss at room temperature for a BST sample.	154
Table 4.9. Sintering conditions, relative density, average grain size, permittivity (ϵ) and dielectric loss ($\tan\delta$) at 1 kHz after annealing.	154
Figure 4. 61. Frequency dependence of the permittivity and dielectric loss of BST at room temperature.	155
Figure 4.62. Dielectric properties of BT ceramic as a function of temperature for various frequencies.	155
Figure 4.63. Dielectric properties of a BST ceramic as a function of temperature for various frequencies.	156
Figure 4.64. Raman spectra of BT ceramic at different temperatures.	157
Figure 4.65. Raman spectra of BST ceramic at different temperatures.	157

List of tables

Table 1.1. Surface chemical composition (at.%) of as-sintered and annealed YAG samples	33
Table 1.2. Sintering and post-treatment conditions, grain, pore size and porosity of the 2 at.% Nd:YAG samples	35
Table 1.3. Physical and chemical properties of YAG (300K).....	37
Table 1.4. State of the art of transparent YAG ceramics.....	40
Table 1.5. Physical and chemical properties of BaTiO ₃ (300K).....	43
Table 1.6. Examples of dense titanates (barium and strontium) with nanometric grain size	51
Table 2.1. PDF cards used for the Al ₂ O ₃ -Y ₂ O ₃ system.....	59
Table 2.2. PDF cards used for the BaO-SrO-TiO ₂ system.....	60
Table 2.3. Physical properties of YAG (300K)	64
Table 2.4. Thermal and electrical conductivity of YAG	65
Table 3.1. Quantities of reagents used in YAG synthesis (for 25 g of YAG).	70
Table 3.2. Present phases in YAG precursor powders from co-precipitation in AHC 1M after thermal treatment at 600°C, 1000°C and 1350°C.....	71
Table 3.3. Evolution of the phase composition of YAG-B as a function of the sintering temperature (pressure 50 MPa, dwell time 15 minutes). XRD semi-quantitative analysis, in wt%.....	89
Table 3.4. Optical transmission and absorption (measured at 600 nm) of samples sintered at 1450°C and 1500°C, before and after annealing.	107
Table 3.5. Characteristics of the starting powders.....	110
Table 4.1. Relative density before and after dwell for samples sintered at different heating rates at 1000°C.	128
Table 4.2. Relative density before and after dwell for BST samples sintered at different temperatures.	128
Table 4.3. Processing conditions, grain sizes, densities and optical transmission of BT samples issued from deagglomerated powder.	143
Table 4.4. Sintering conditions, relative density, average grain size, permittivity (ϵ) and dielectric loss (td) at 1 kHz of different BT samples prepared with the as-received powder.....	148
Table 4.5. Relative density, average grain size, permittivity (ϵ) and dielectric loss (td) at 1 kHz of a BT sample sintered at 1050°C prepared from as-received and deagglomerated powder.	150
Table 4.6. Sintering conditions, relative density, average grain size, permittivity (ϵ) and dielectric loss (td) at 1 kHz of different BT samples issued from deagglomerated powder.....	151
Table 4.7. Sintering conditions, relative density, average grain size, permittivity (ϵ) and dielectric loss (td) at 1 kHz before annealing.....	153
Table 4.8. Properties of a BST sample sintered by SPS at 1150°C-5 min, 50 MPa.	153

Appendix A - Technical information from the suppliers

- Reagents in YAG- S synthesis

SIGMA-ALDRICH®

sigma-aldrich.com

3050 Spruce Street, Saint Louis, MO 63103, USA

Website: www.sigmaaldrich.com

Email USA: techserv@sial.com

Outside USA: eurtechserv@sial.com

Product Specification

Product Name:
Yttrium(III) chloride hexahydrate - 99.9% trace metals basis

Product Number:	211648	YCl ₃ • 6H ₂ O
CAS Number:	10025-94-2	
MDL:	MFCD00149941	
Formula:	Cl ₃ Y • 6H ₂ O	
Formula Weight:	303.36 g/mol	

TEST	Specification
Appearance (Color)	Conforms to Requirements
White to Off-White, Tan, Pink or Yellow	
Appearance (Form)	Conforms to Requirements
Crystals or Crystalline Powder and/or Chunks	
Complexometric EDTA	27.8 - 30.8 %
% Y	
ICP Major Analysis	Confirmed
Confirms Y Component	
Purity	Meets Requirements
99.9% Based On Rare Earth Analysis	
Trace Rare Earth Analysis	≤ 1500.0 ppm

Specification: PRD.0.ZQ5.10000050420

Sigma-Aldrich warrants, that at the time of the quality release or subsequent retest date this product conformed to the information contained in this publication. The current Specification sheet may be available at Sigma-Aldrich.com. For further inquiries, please contact Technical Service. Purchaser must determine the suitability of the product for its particular use. See reverse side of invoice or packing slip for additional terms and conditions of sale.

SIGMA-ALDRICH

sigma-aldrich.com

3050 Spruce Street, Saint Louis, MO 63103, USA

Website: www.sigmaaldrich.comEmail USA: techserv@sial.comOutside USA: eurtechserv@sial.com

Product Specification

Product Name:

Aluminum chloride hexahydrate – ReagentPlus®, 99%

Product Number:

237078

CAS Number:

7784-13-6

MDL:

MFCD00149134

Formula:AlCl₃ · 6H₂O**Formula Weight:**

241.43 g/mol

TEST**Specification**

Appearance (Color)

White to Off-White

Appearance (Form)

Conforms to Requirements

Crystals or Crystalline Solid and/or Chunks

ICP Major Analysis

Confirmed

Confirms Aluminum Component

Titration by AgNO₃

43.4 - 44.7 %

% Cl

Remarks:

Reviewing Chemist :

Specification: PRD.0.ZQ5.10000011132

Sigma-Aldrich warrants, that at the time of the quality release or subsequent retest date this product conformed to the information contained in this publication. The current Specification sheet may be available at Sigma-Aldrich.com. For further inquiries, please contact Technical Service. Purchaser must determine the suitability of the product for its particular use. See reverse side of invoice or packing slip for additional terms and conditions of sale.

1 of 1

SIGMA-ALDRICH®

sigma-aldrich.com

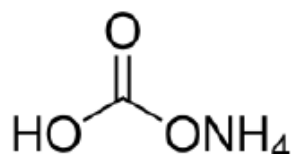
3050 Spruce Street, Saint Louis, MO 63103, USA

Website: www.sigmaaldrich.comEmail USA: techserv@sial.comOutside USA: eurtechserv@sial.com

Product Specification

Product Name:
Ammonium bicarbonate – ReagentPlus®, ≥99.0%

Product Number: A6141
 CAS Number: 1066-33-7
 MDL: MFCD00012138
 Formula: CH₅NO₃
 Formula Weight: 79.06 g/mol



TEST	Specification
Appearance (Color)	White
Appearance (Form)	Powder or Crystals
Solubility (Color)	Colorless
Solubility (Turbidity)	Clear
100 mg/mL, H ₂ O	
Purity by Titration	≥ 99.0 %
Recommended Retest Period	-----
2 years	

Specification: PRD.0.ZQ5.10000033143

Sigma-Aldrich warrants, that at the time of the quality release or subsequent retest date this product conformed to the information contained in this publication. The current Specification sheet may be available at Sigma-Aldrich.com. For further inquiries, please contact Technical Service. Purchaser must determine the suitability of the product for its particular use. See reverse side of invoice or packing slip for additional terms and conditions of sale.

- YAG- B powder



BAIKOWSKI

Les Marais Noirs Ouest, BP 501
F-74339 – LA BALME DE SILLINGY cedex
Tél. : 33 (0)4 50 22 69 02
Fax : 33 (0)4 50 22 28 92

Analysis Report

18/11/13

- Experimental -

YAG		
		21308-F
Specific Surface Area BET (m ² /g)		7.8
PSD Horiba LA950 (µm)	D10	0.09
	D50	0.15
	D90	0.29
Chemical analysis (ppm/YAG)	Na	7.8
	K	8.1
	Fe	9.0
	Si	23
	Ca	11

- YAG- N powder

 Glow Discharge Mass Spectroscopy NORTHERN ANALYTICAL LABORATORY, INC.					
13 Delta Dr., Unit #4, Londonderry NH 03053			SAMPLE NO. G59161		
Phone: (603) 434-8400		FAX: (603) 434-8500		FILE NO. 2NAN777	
www.northernanalytical.com			DATE: 23/12/2015		
Sharon Paras		YAG			
Nanocerox					
712 State Circle		PO # 10751			
Ann Arbor MI 48108		Lot # 3SP183ABulk9005			
ANALYSIS	ppmw	ANALYSIS	ppmw	ANALYSIS	ppmw
H		Zn	1.3	Pr	<0.1
Li	<0.1	Ga	0.50	Nd	0.40
Be	<0.1	Ge		Sm	0.10
B	0.90	As	<0.5	Eu	<0.1
C		Se		Gd	3.0
N		Br		Tb	0.20
O	Major	Rb		Dy	0.45
F	<5	Sr	<0.5	Ho	0.14
Na	4.5	Y	Major	Er	0.90
Mg	2.0	Zr	0.19	Tm	<0.1
Al	Major	Nb	<0.1	Yb	0.10
Si	10	Mo	≤0.1	Lu	3.4
P	8.0	Ru		Hf	<0.5
S	21	Rh		Ta	<10
Cl*	60	Pd		W	<1
K	0.80	Ag	<0.5	Re	
Ca	3.5	Cd		Os	
Sc	<0.1	In		Ir	
Ti	0.33	Sn	<1	Pt	
V	0.17	Sb	≤1	Au	
Cr	1.0	Te		Hg	
Mn	0.075	I		Tl	
Fe	1.8	Cs		Pb	<0.1
Co	<0.1	Ba	<0.1	Bi	<0.1
Ni	0.25	La	0.23	Th	<0.1
Cu	<0.5	Ce	0.12	U	<0.1

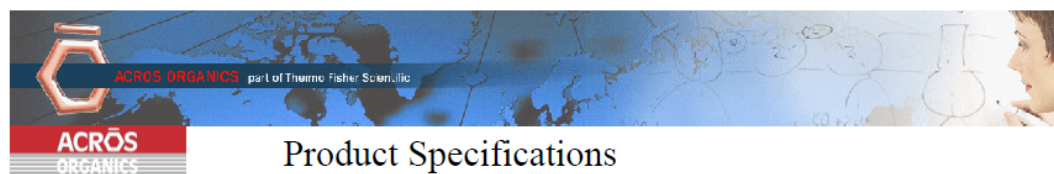
*Inhomogeneous

All other elements <0.5ppmw, each

Materials Testing
LaboratoryANALYSIS BY: William A. Guidoboni / Sr. Analytical Chemist
Name/FunctionAPPROVED BY: Richard J. Guidoboni / President
Name/Function

This test report shall not be reproduced, except in full, without the written approval of Northern Analytical Laboratory.
The recording of false, fictitious, or fraudulent statements/entries on the certificate may be punished as a felony under federal law.

- LiF powder



Product 19338
Lithium fluoride,99.98%,extra pure

General Product Data
Version 2
CAS No 7789-24-4
Molecular weight 25.93
Molecular formula F Li
Linear formula LiF

Product Specifications

Appearance (Color) White
Appearance (Form) Powder
Total trace metal impurities =<0.02 %

Acros Organics ENA23, zone 1, nr 1350, Janssen Pharmaceuticaalaa 3a, B-2440 Geel, Belgium
Tel +32 14/57.52.11 - Fax +32 14/59.34.34 Internet: <http://www.acros.com>
1 Reagent Lane, Fair Lawn, NJ 07410,USA
Fax 201-796-1329

- **BaTiO₃ powder**

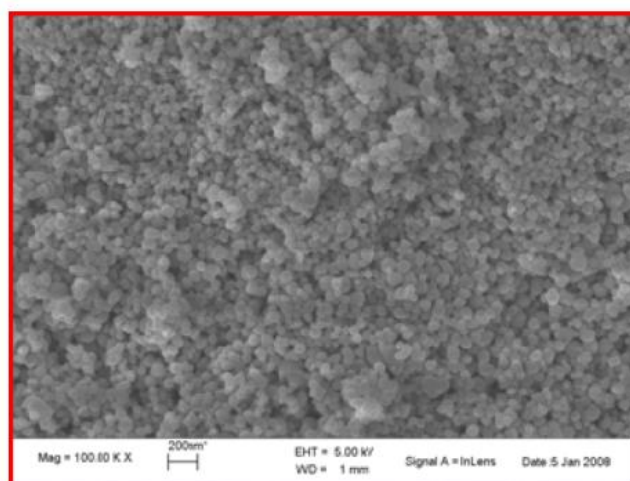
Inframat[®] Advanced Materials[™]

Plant / R & D, 151 Progress Drive, Manchester, CT 06042 Tel: (860) 432-3155, Fax: (860) 432-3722
www.advancedmaterials.us

CERTIFICATE OF ANALYSIS (Typical)

Product No: **56220N-N2**
Product #: BaTiO₃ Nano Powder

Purity	99.95%
Ba/Ti	0.99–1.01
BET Specific Surface Area	20±2 m ² /g
Average Primary Particle Size	50 nm (BET & SEM)



Typical SEM image of BaTiO₃ nano powder (50 nm)

Dimension bar: 200 nm

- (Ba, Sr)TiO₃ powder



Technologies to Products...On the Leading Edge

NanOxide™ HBS-1000 <100nm Barium-Strontium Titanate

HBS-1000 is a formulated high purity barium-strontium titanate nano-sized powder designed to meet demanding electronics applications. HBS-1000 Ba /Sr ratios of 80:20 and 50:50 are standard and are currently available from inventory. HBS-1000 is the smallest commercially available barium-strontium titanate powder on the market at 50 nanometers (nm). It is readily dispersible in aqueous and non-aqueous solvents with appropriate surfactants which are available from TPL, Inc. if necessary.

Typical Properties

Specific Surface Area	15-18 m ² /g
Nominal Size	50 nm (BET)
Loss On Ignition	<1.5%
PH (ASTM - D1208)	9.0-11.0
Chemical Analysis	
Ba + Sr:Ti (XRF)	0.995-1.010
SrO (ICP)	<0.1%
CaO (ICP)	<10 ppm
MgO (ICP)	<10 ppm
SiO ₂ (ICP)	<200 ppm
Al ₂ O ₃ (ICP)	<100 ppm
Fe ₂ O ₃ (ICP)	<10 ppm
(Ba + Sr)TiO ₃	> 99.5%

